POLITECNICO DI MILANO

Scuola di Ingegneria Industriale e dell'Informazione

Corso di Laurea Specialistica in Ingegneria Energetica

Lattice Boltzmann Methods for Single and Two-Phase
Flows in Porous Media: Theory and Applications

Relatore: Prof. Fabio Inzoli
Co-relatori: Ing. Gaël Guédon
              Prof. Pietro Asinari

Tesi di Laurea di:
Alessandro Ciani   Matr. 783130

Anno Accademico 2012-2013

A mamma e papà

Ringraziamenti

con me questo momento. Sono sicuro che sareste orgogliosi di me.

Sommario Esteso

Lo scopo principale di questa tesi è quello di esplorare le capacità dei metodi Lattice Boltzmann (LBM) nelle simulazioni di flussi monofase e bifase, con particolare focus sulle applicazioni ai mezzi porosi.

Sorti a cavallo tra gli anni ottanta e novanta, dalle ceneri del cosiddetto Lattice Gas Automaton (LGA), i metodi Lattice Boltzmann si propongono come metodi alternativi alla fluidodinamica computazionale convenzionale, basata sulla discretizzazione ed integrazione diretta delle equazioni di Navier-Stokes. Gli LBM, infatti, forniscono una descrizione su una scala inferiore rispetto a quella macroscopica, da cui però, come vedremo, emergono le equazioni che governano il mondo macroscopico. Tale scala viene comunemente detta mesoscopica, poiché intermedia fra la scala microscopica, propria ad esempio della Molecular Dynamics, e appunto macroscopica, cioè di validità dell'ipotesi del continuo su cui si basano le equazioni di Navier-Stokes.

I metodi Lattice Boltzmann fondano le loro radici nella meccanica statistica, di cui Ludwig Boltzmann ne è il padre e per questo compare nel nome stesso dei metodi. In particolare, vedremo che è stato dimostrato il legame diretto fra l'equazione di Boltzmann e la cosiddetta *"Lattice Boltzmann equation"* (LBE), seppur ciò è avvenuto storicamente dopo l'introduzione degli LBM. Il termine "Lattice" invece si riferisce alla tipica struttura della griglia di discretizzazione degli LBM, che è caratterizzata da un alto grado di simmetria. Un esempio è riportato in Fig. 1, per un caso di lattice a simmetria esagonale. Tale struttura deriva sostanzialmente da un elemento caratteristico degli LBM, cioè la discretizzazione dello spazio delle velocità. Infatti, l'oggetto della LBE sono, appunto, le funzioni di probabilità associate a tali velocità discrete.

Uno dei vantaggi fondamentali degli LBM è la semplicità dell'algoritmo, in un certo senso indotta dall'alta simmetria della griglia. In aggiunta, l'algoritmo ha un carattere puramente locale, il che permette una diretta parallelizzazione. A queste caratteristiche, si aggiungono altri vantaggi, che risultano essere particolarmente adatti al contesto dei mezzi porosi. In primis, c'è la facile gestione di geometrie complesse. Ciò è dovuto alla possibilità di modellare l'interazione con le pareti solide attraverso delle semplici condizioni
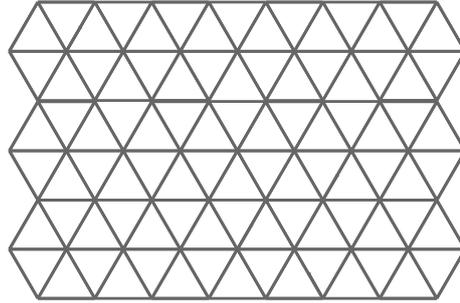
Figura 1. Esempio di lattice a simmetria esagonale.

al contorno, dette di Bounce-Back, che cercano appunto di riprodurre l'urto delle particelle con le pareti. Di fatto, la geometria di input è costituita da una semplice griglia booleana, in cui si identificano nodi di fluido e di solido. Data tale semplicità, tutte le geometrie utilizzate in questa tesi sono state generate dall'autore con semplici scripts scritti in ambiente Matlab. In seconda istanza, gli LBM consentono di simulare sistemi multifase con relativa semplicità. Il vantaggio principale è che non è necessaria una modellazione dell'interfaccia, ma la sua dinamica viene riprodotta in maniera naturale dalle forze di interazioni fra le particelle, che possono essere introdotte nel metodo. Come possiamo intuire, sia la facile gestione di geometrie complesse, sia i vantaggi nel simulare flussi multifase, derivano dalla natura mesoscopica degli LBM. Inoltre, nelle applicazioni ai mezzi porosi, diversi problemi degli LBM tendono a risolversi, date le peculiari condizioni del flusso. In definitiva, il contesto dei mezzi porosi è uno dei campi naturali di applicazione degli LBM.

In questa tesi, dunque, viene portata a termine un'analisi dei metodi Lattice Boltzmann, sia a livello teorico, che applicativo, per flussi monofase e bifase. Dopo una iniziale introduzione ai concetti fondamentali dei flussi nei mezzi porosi, che verranno utilizzati nella parte di simulazioni, i metodi Lattice Boltzmann vengono descritti riportando la loro derivazione dall'equazione di Boltzmann. Tale approccio viene preferito rispetto alla derivazione storica, in quanto fornisce una visione più moderna degli LBM, ed anche più rigorosa. Questa parte è stata inserita, poiché ritenuta necessaria per la comprensione delle tematiche sviluppate in questa tesi. In particolare, l'equazione di Boltzmann viene descritta nel dettaglio, così come il collegamento con le grandezze macroscopiche. Partendo da tali fondamenta, viene riportata la procedura di discretizzazione dell'equazione di Boltzmann, che porta alla Lattice Boltzmann equation, sottolineando i passaggi critici di tale dimostrazione. I concetti sviluppati per l'equazione di Boltzmann vengono poi traslati naturalmente nel mondo discreto degli LBM.

A valle di questa derivazione, viene mostrato il collegamento con le equa-

zioni di Navier-Stokes, mediante la cosiddetta espansione di Chapman-Enskog. Tale espansione è fondamentalmente un metodo perturbativo multi-scala, utilizzato anche per mostrare la connessione dell'equazione di Boltzmann con le equazioni macroscopiche. La procedura riportata è stata ripresa dal lavoro di Kuzmin [1], ma viene fornita una dimostrazione più generale che mostra il metodo più opportuno per l'introduzione delle forze, siano esse esterne o interagenti, nella Lattice Boltzmann equation.

Per completare l'apparato teorico degli LBM viene anche affrontato il tema delle condizioni al contorno. Innanzitutto, viene spiegato il significato delle condizioni al contorno in tale modellazione mesoscopica. Possiamo infatti intuire come le condizioni al contorno debbano riguardare le variabili della Lattice Boltzmann equation, cioè le funzioni di distribuzione associate alle velocità discrete. Ciò porta a distinguere fra due approcci. Il primo in cui si sfrutta l'interpretazione mesoscopica dei metodi; nel secondo, invece, si cerca di traslare condizioni al contorno sulle velocità o sulla pressione in termini delle funzioni di distribuzione discrete. In questa parte, solo le condizioni al contorno che verranno utilizzate nella tesi sono analizzate.

L'analisi applicativa viene svolta interamente nel caso bidimensionale. Tale scelta ha svariate motivazioni. Innanzitutto, il caso 2D permette una più semplice e veloce individuazione delle caratteristiche salienti dei metodi. In seconda istanza, data la simmetria inerente ai metodi, il passaggio alla terza dimensione è diretto e non aggiunge di fatto nulla alla trattazione. Ciò giustifica anche il fatto che la letteratura degli LBM si focalizza soprattutto su problemi bidimensionali.

Lo strumento utilizzato per le simulazioni è la libreria open-source Palabos, sviluppata recentemente da una collaborazione fra "The FlowKit Ltd. technology company" e l'Università di Ginevra. La libreria Palabos è scritta integralmente in C++, che è dunque stato l'ambiente di sviluppo di tutti i codici Lattice Boltzmann utilizzati in questa tesi.

La parte applicativa monofase ha riguardato tre casi studio:

1. il flusso di Hagen-Poiseuille in un canale bidimensionale;

2. il flusso in una schiera di dischi disposti esagonalmente;

3. il flusso in una schiera di dischi con disposizione casuale.

Il primo semplice caso di flusso laminare in un canale bidimensionale è stato utilizzato per avere una prima validazione degli LBM e per evidenziare alcune caratteristiche fondamentali, che poi si ripercuotono in qualunque applicazione più complessa. Infatti, tale flusso è sicuramente il più studiato nella letteratura degli LBM. È inoltre intuitiva l'analogia fra il flusso di Hagen-Poiseuille ed il flusso in un canale di un mezzo poroso. I risultati

sono confrontati con la soluzione analitica, nota per questo problema, ma sono anche utilizzati per verificare i risultati teorici sugli LBM descritti nella parte iniziale della tesi, mostrando, in entrambi i casi, un generale accordo.

La seconda geometria è stata invece scelta perché rappresenta un primo caso di mezzo poroso, in cui sono disponibili soluzioni semi-analitiche per la permeabilità del mezzo, che permettono, anche qui, un confronto con i risultati numerici. Inoltre, la periodicità del sistema in questione, che viene assunto infinito, consente di studiare il flusso nella sola cella elementare. Come soluzioni di riferimento sono state utilizzate le correlazioni di Drummond & Tahir [2], e quella più recente di Tamayol & Bahrami [3]. La seconda è quella che ha mostrato il migliore accordo con i risultati numerici degli LBM.

Infine, come conclusione della parte monofase, l'attenzione è volta ad una geometria più rappresentativa di un mezzo poroso reale, costituita da una schiera di dischi disposti casualmente. L'obiettivo di tale studio è quello di verificare la validità del modello di Carman-Kozeny per predire la permeabilità. Svariate geometrie random sono state generate per effettuare tale verifica, in modo da consentire una statistica dei risultati. Le simulazioni hanno confermato che il modello di Carman-Kozeny è un modello valido per tale geometria, specialmente quando la porosità del mezzo è moderata. Nella trattazione vengono anche analizzate in maniera qualitativa le cause degli scostamenti dal modello mostrati da alcune geometrie.

Alla parte applicativa monofase, segue la parte teorica di introduzione ai modelli Lattice Boltzmann (LB) per flussi multifase. Il modello utilizzato in questa tesi è quello proposto da Shan & Chen (SC) [4], che è storicamente il primo modello LB proposto per flussi multifase, ed anche il più semplice fra quelli presenti in letteratura. Inoltre, il modello di Shan & Chen risulta facilmente implementabile nell'ambiente Palabos. In questa tesi il modello di Shan & Chen verrà utilizzato solo nel caso bifase, seppure è possibile simulare anche più fasi.

L'idea principale dietro il modello di Shan & Chen risiede nell'introduzione di una forza di interazione fra un nodo del lattice e i suoi "primi vicini", capace di innescare una separazione di fase in determinate condizioni. A sua volta, possono essere distinti svariati sottomodelli dello Shan-Chen a seconda della forma assunta da tale interazione. Possiamo quindi intuire, come la modellazione multifase ottenuta con il metodo di Shan & Chen debba sottostare alle leggi che governano la separazione di fase del modello. Ad esempio, il rapporto di densità fra i due fluidi non è un parametro di input, ma va ottenuto calibrando i parametri del modello.

Caratteristica principale del modello di Shan & Chen per flussi multifase è la presenza di una interfaccia finita e diffusa, e quindi non infinitesima. Questa peculiarità è condivisa anche da altri modelli multifase Lattice

Boltzmann.

Una volta ottenuta l'equazione di stato, che consente di individuare i parametri critici del modello, la natura immiscibile del sistema viene studiata mediante applicazioni statiche, da cui si possono ottenere dei diagrammi di stato. In questa parte ci si riferisce sempre alla formulazione originale del modello di Shan & Chen. Viene anche mostrato come da semplici test sia possibile ottenere grandezze come la tensione superficiale o l'angolo di contatto. Il comportamento nelle vicinanze del punto critico del modello viene analizzato, mostrando analogie con altri fenomeni critici. Particolare enfasi è posta sui problemi di questo modello, che ne limitano le applicazioni a flussi con moderati rapporti di densità fra le due fasi. Ciò è dovuto alle cosiddette correnti spurie, delle velocità artificiali prodotte dal modello nelle vicinanze all'interfaccia. Tali correnti sono in qualche modo legate al rapporto di densità, ed essendo molto elevate, causano instabilità del modello quando tale rapporto aumenta. In aggiunta, si pone, in generale, un problema di ambiguità nella distinzione fra tali velocità artificiali e le velocità fisiche, che si manifesta anche a bassi rapporti di densità.

La letteratura sul modello di Shan & Chen si è focalizzata negli ultimi anni sulla risoluzione di questi problemi. In particolare, in questa tesi viene svolta un'analisi del metodo proposto da Yuan & Schaefer [5], che consiste sostanzialmente nel cambiare la forma dell'interazione, in modo da soddisfare equazione di stato fisiche, di cui la Peng-Robinson e la Carnahan-Starling ne sono esempi. Tale metodo viene descritto nel dettaglio ed implementato nell'ambiente Palabos. Ciò ha richiesto una espansione della libreria originale di Palabos, poiché nell'attuale versione l'incorporazione delle equazioni di stato nel modello di Shan & Chen non è direttamente disponibile. Viene quindi mostrato mediante dei test, come, fissato un rapporto di densità, sia possibile ottenere una riduzione delle correnti spurie, e come da ciò derivi un aumento del rapporto di densità limite simulabile, anche di ordini di grandezza. Tuttavia, viene puntualizzato il problema di trovare una inizializzazione stabile delle densità, che si traduce, di fatto, in una procedura di "trial and error".

Il modello viene sottoposto ad una prima validazione dinamica nel caso di flusso laminare bifase, simile al caso di flusso di Hagen-Poiseuille, per cui a sua volta è disponibile una soluzione analitica. Tale flusso è quello generalmente usato per validare il modello in letteratura e fornisce un primo esempio di flusso in un mezzo poroso. Il problema viene studiato per i tre modelli di interazione del modello di Shan & Chen esaminati, cioè la formulazione originale, e le due versioni con la equazioni di stato di Carnahan & Starling e di Peng & Robinson. È stato scelto per il confronto un rapporto di densità moderato, in modo da ottenere una configurazione stabile per tutti

i modelli. In questo caso, si evidenzia come per tale rapporto di densità il modello originale, mostri un migliore accordo con la soluzione analitica, a causa del minore spessore dell'interfaccia presentata da tale modello. Tuttavia, viene anche mostrato un primo effetto delle correnti spurie che affligge maggiormente il modello originale.

In conclusione, i metodi Lattice Boltzmann sono stati discussi sia a livello teorico che pratico, mediante diversi casi studio. Gli LBM si sono dimostrati senza dubbio uno strumento valido per lo studio dei flussi monofase nei mezzi porosi. Lo studio di flussi bifase mediante gli LBM è stato introdotto utilizzando il modello di Shan & Chen. Le caratteristiche, le potenzialità e le problematiche di tale modello sono state discusse ampiamente, analizzando i risultati delle simulazioni. Oltre al modello originale, sono stati studiati dei suoi miglioramenti implementandoli in ambiente Palabos. Sottoponendo i modelli a diversi test statici e ad una prima validazione dinamica, si è mostrato che molti problemi della formulazione originale possono essere ridotti, seppur il modello originale può essere preferibile in alcuni casi.

Le prospettive future di questa tesi sono svariate. In prima istanza, l'applicazione dei metodi Lattice Boltzmann può essere estesa a casi studio di mezzi porosi reali tridimensionali. Inoltre, i risultati teorici ottenuti per l'introduzione delle forze nella Lattice Boltzmann equation, possono essere confermati con dei test numerici. Per quanto riguarda la parte bifase, il modello di Shan & Chen può essere ulteriormente migliorato introducendo altre correzioni proposte in letteratura. In aggiunta, il modello può essere validato in un caso più complesso rispetto a quello considerato, in cui i problemi ad esso connessi potrebbero avere una maggiore influenza.

Extended Abstract

The main purpose of this thesis is to explore the capabilities of the Lattice Boltzmann methods (LBMs) for the simulation of single- and two-phase flows, with particular focus on porous media applications.

Historically, the Lattice Boltzmann methods arose between the eighties and the nineties from the ashes of the so-called Lattice Gas Automaton (LGA). They represent an alternative approach to the standard computational fluid dynamics, which is based on the direct discretization and integration of the Navier-Stokes equations. In fact, the LBMs provide a description at a lower scale compared to the macroscopic scale of the Navier-Stokes equations. However, we will see that from this description, the equations that govern the macroscopic world arise naturally. The characteristic scale of the LBMs is usually called the mesoscopic scale, because it is halfway between the microscopic scale, typical of Molecular Dynamics, and the macroscopic scale, that is the scale of validity of the continuum hypothesis, which allows to obtain the Navier-Stokes equations.

The Lattice Boltzmann methods have roots in Statistical Mechanics, whose father is certainly Ludwig Boltzmann, and for this reason, his name appears in the name of the methods. In particular, it has been proved the direct relationship between the Boltzmann equation and the *Lattice Boltzmann equation* (LBE), even though this has been achieved several years later the introduction of the LBMs. The word "Lattice" refers to the typical discretization grid of the LBMs, which is characterized by a high degree of symmetry. An example is reported in Fig.2 for the case of an hexagonal lattice. This structure is basically a consequence of a characteristic feature of LBMs, that is the discretization of the velocity space. In fact, the variables of the LBE are the probability density functions associated to these discrete velocities.

One of the main advantages of the LBMs is the simplicity of the algorithm, which is somehow induced by the high symmetry of the grid. In addition, the algorithm is purely local, which allows a direct parallelization. In the context of porous media, also other features of the LBMs seem particularly suited. In the first instance, there is the easy handling of complex
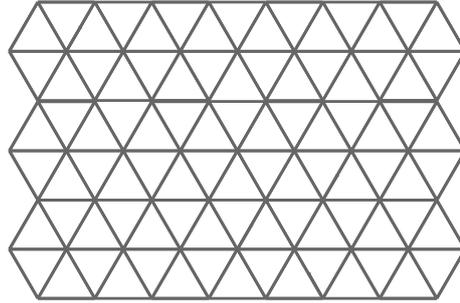
Figure 2. Example of lattice with hexagonal symmetry.

geometries. This is essentially due to the possibility of modelling the interaction of the particles with walls by means of simple boundary conditions, usually called Bounce-Back boundary conditions, which try to reproduce the collision between particles and the solid walls. As a consequence, the input geometry of the LBMs is simply a boolean grid, in which we identify fluid nodes and solid nodes. Because of this simplicity, all the geometries used in this thesis have been generated by the author with simple scripts written in the Matlab environment. In the second instance, the LBMs allow to simulate multi-phase flows with relative simplicity. In this case, the main advantage is that we do not need to model the behaviour of the interface, but its dynamics arises naturally from the interactions between particles, which can be introduced in the methods. We can say that both the easy handling of complex geometries and the advantages in simulating multiphase flows are due to the mesoscopic nature of the LBMs. Ultimately, the context of porous media is one of the natural fields of application of the LBMs.

In this thesis, a theoretical and practical analysis of the Lattice Boltzmann methods is carried out for single- and two-phase flows. After an initial introduction to the basic concepts of flows in porous media, which will be used in the simulation part, the Lattice Boltzmann method are described, reporting their derivation from the Boltzmann equation. This approach has been preferred over the historical derivation from the Lattice Gas model, because it represents the modern interpretation of the LBMs, and it is also the most rigorous procedure. This part has been included, since it was considered necessary for the understanding of the themes discussed in this thesis. In particular, the Boltzmann equation is described in details, as well as the connections to the macroscopic quantities. Starting from these solid basis, the discretization of the Boltzmann equation is reported, highlighting the critical passages of this proof, and finally the Lattice Boltzmann equation is obtained. In this way, the main concept introduced for the Boltzmann equation are naturally translated in the discrete world of the LBM.

After this derivation, the connection to the Navier-Stokes equations is

shown by means of the so-called Chapman-Enskog expansion. This expansion is basically a multi-scale perturbative method, that has been used also to show the connection between the Boltzmann equation and the macroscopic equations. The procedure here reported is similar to that described by Kuzmin [1], but it is carried out in a more general case, in order to show the most appropriate way of including the forcing term in the Lattice Boltzmann equation.

In order to complete the theoretical framework of the LBMs, also the issue of boundary conditions is analysed. First of all, an explanation of the meaning of boundary conditions in the LBMs is provided. In fact, it is intuitive that the boundary conditions should concern the variables of the LBE, i.e., the distribution functions associated to the discrete velocities. We can distinguish between two approaches to boundary conditions in LBMs. In the former, the mesoscopic nature of the methods is exploited; instead, in the latter, the macroscopic boundary conditions on velocity or pressure are expressed in terms of the distribution functions. In this part of this thesis, only the boundary conditions that will be used in the simulation part are analysed.

The application analysis is carried out entirely in two dimensions. The reason of this choice are several. First of all, the 2D case allows a quicker and easier identification of the main characteristics of the methods. Moreover, given the inherent symmetry of the lattice, the passage from two to three dimensions is straightforward and it does not add new elements. These are also the reasons why the most part of the literature about LBM is developed for the two-dimensional case.

The tool used for the simulations is Palabos, an open-source library, recently developed by a collaboration between the "The Flow Kit Ltd. technology company" and the University of Geneva. The Palabos library is written in C++, which has been the development environment of all the Lattice Boltzmann codes used in this thesis.

The single-phase part has focused on three case studies:

1. the Hagen-Poiseuille flow in a two-dimensional channel;

2. the flow over an hexagonal array of disks;

3. the flow over a random array of disks.

The first simple case of laminar flow in a two-dimensional channel has been used to obtain a first validation of the LBMs and to highlight some basic features, which characterize also any other application. In fact, this kind of flow is certainly the most studied one in the LBMs' literature. In addition, the analogy between the Hagen-Poiseuille flow and the flow in the channel

in a porous medium is evident. The results have been compared with the analytical solution, which is known for this case, but they have been also used to verify some theoretical findings about the LBMs. In both cases, the numerical results have shown a general agreement with the theory.

The second geometry has been chosen because it represents a first and more complex case of porous medium, in which semi-analytical formulas are available for the permeability, allowing even in this case a comparison with the numerical results. As reference solutions, the correlations proposed by Drummond & Thair [2] and by Tamayol & Bahrami [3] have been selected. In particular, the second one has shown the best agreement with the numerical results.

As a conclusion of the single-phase part, the attention is turned to a geometry, that is more representative of a porous medium, composed of a random array of disks. The objective of this study is to verify the validity of the Carman-Kozeny (CK) model for the prediction of the permeability. Several random geometries have been generated, in order to obtain a statistics of the results. The simulations have confirmed the validity of the CK model for this geometry, especially at moderate porosities. In the dissertation also the reasons of the discrepancies shown by some geometries is qualitatively analysed.

After the single-phase part, the theory of the Lattice Boltzmann methods for multi-phase flows is introduced. The model used in this thesis is the Shan-Chen model proposed in [4], which is the first LBM model for multi-phase flows, and also the simplest one among those available in literature. Moreover, the Shan-Chen model can be readily implemented in the current version of the Palabos library. In this thesis, the Shan-Chen model has been used to simulate only two-phase flows, even though the simulation of more phases is possible.

The basic idea behind the Shan-Chen model lies in the introduction of an interaction force between a node of the lattice and its "nearest neighbours", which is able to trigger phase separation in certain conditions. In turn, different sub-models of the Shan-Chen model can be distinguished depending on the form of this interaction. It is easy to realize, that the multi-phase modelling with the Shan-Chen model must obey the laws that govern the phase separation of the model. For instance, this means that the density ratio is not an input parameter, but has to be obtained from a preliminary calibration phase of the model.

One of the main characteristics of the Shan-Chen model for multi-phase flows is the presence of a finite and diffusive interface, and thus, not infinitesimal. This peculiarity of the Shan-Chen model is shared also by other Lattice Boltzmann models for multi-phase flows.

After obtaining the equation of state of the model, which allows to identify the critical parameter of the phase transition, the immiscible nature of the model is investigated by means of static tests, from which it is possible to obtain the phase diagrams. In this part, we refer to the original formulation of the Shan-Chen model. It is shown how, by means of simple tests, quantities like the surface tension and the contact angle can be calibrated and computed. The behaviour near the critical point is analysed, providing analogies with other critical phenomena. The drawbacks of the model, which limit its applications to problems with limited density ratio, are emphasized as well. This is mainly due to the so-called spurious currents, i.e., artificial velocities produced by the model at the interface. These currents are somehow connected to the density ratio between the two phases, and cause the instability of the model when this ratio increases. In addition, they generate also a general problem of ambiguity between physical and artificial velocities, which manifests itself even at low density ratios.

In the last years, the literature about the Shan-Chen model has focused on the solution of these problems. In particular, in this thesis, the method proposed by Yuan & Scahefer [5] is analysed. This method consists in the modification of the interaction force, in order to obtain physical equation of state, such as the Peng-Robinson (PR) and the Carnahan-Starling (CS). This method is described in details and implemented in the Palabos environment. This has required an expansion of the original library of Palabos, since in the current version, the incorporation of physical equations of state in the Shan-Chen model is not readily available. By means of simple tests, it is shown how it is possible to reduce the magnitude of the spurious velocities, given a fixed density ratio, and it is possible to simulate systems with higher density ratios, even by a orders of magnitude. However, it is also pointed out the problem of finding a stable initialization of the densities, which basically reduce the initialization to a "trial and error" procedure.

A first dynamic validation of the model is carried out in the case of a laminar co-current flow in a 2D channel, for which an analytical solution is available. This flux is in general the one used in literature to validate the model and it is a first example of flow in a channel of a porous medium. This flux is studied for the three interactions of the Shan-Chen model examined in this thesis, namely the original formulation, and the two versions with the Carnahan-Starling and Peng-Robinson equations of state. For the comparison, a case with a limited density ratio has been chosen, in order to obtain a stable configuration for all the models. The simulations have shown that for this limited density ratio, the original formulation of the Shan-Chen interaction should be preferred, because it shows a better agreement with the analytical solutions, compared to the CS and PR. This is due to the lower

thickness of the interface of the original Shan-Chen model. Nevertheless, it is also shown a first effect of the spurious currents which afflicts mainly the original model.

As a conclusion, the Lattice Boltzmann methods have been discussed at the theoretical and practical level, by means of several case studies. The LBMs have proved to be without doubts a valid tool for the study of single-phase flows in porous media. The study of two-phase flows has been introduced using the Shan-Chen model. The characteristics, the potentialities and the drawbacks of this model have been highlighted, analysing the results of the numerical simulations. Some improvements of the original model have been implemented in the Palabos library. By means of static tests and a first dynamic validation, it has been shown how many problems of the original formulation can be reduced, even though the original model might be more advisable in some cases.

The future perspectives of this thesis are several. In the first instance, the application of the Lattice Boltzmann methods may be extended to real three-dimensional porous media. In addition, the theoretical results obtained for the introduction of the forcing term in the LBE might be confirmed by numerical tests. About the two-phase part, further improvements of the Shan-Chen model might be implemented in the Palabos library. Moreover, the model needs a validation in a more complex case than the 2D co-current flow, in which the problems of the Shan-Chen model may have a greater influence on the solution.

Contents

List of Figures

List of Tables

Sommario

In questa tesi, i metodi Lattice Boltzmann (LBM) vengono analizzati ed utilizzati per simulare flussi monofase e bifase. In particolare, gli esempi applicativi riguarderanno lo studio di flussi in mezzi porosi, che rappresenta uno dei campi applicativi naturali degli LBM. Le simulazioni numeriche sono realizzate utilizzando la libreria open-source Palabos.

Gli LBM vengono inizialmente introdotti riportando la derivazione della Lattice Boltzmann equation (LBE) a partire dall'equazione di Boltzmann [6, 7]. In seguito, viene mostrato il collegamento con le equazioni di Navier-Stokes, utilizzando l'espansione di Chapman-Enskog [1]. In tale procedura, viene anche discusso il metodo più appropriato di introdurre i termini forzanti nella LBE.

La parte applicativa monofase riguarda tre casi studio bidimensionali. Il flusso di Hagen-Poiseuille viene utilizzato, oltre che per fornire una prima validazione dei metodi, anche per confrontare diversi modelli e per mostrare l'andamento dell'errore. Il secondo caso studio è quello di un flusso in una schiera esagonale di dischi, per cui sono disponibili formule semi-analitiche, che permettono una ulteriore validazione. La parte monofase è conclusa utilizzando gli LBM per verificare la validità del modello di Carman-Kozeny per predire la permeabilità di un mezzo poroso.

Il modello LBM per simulazioni di flussi bifase analizzato è quello proposto da Shan & Chen [4]. Le sue caratteristiche sono messe in evidenza da simulazioni di casi statici. Un particolare problema di tale modello è la presenza di correnti artificiali all'interfaccia che limita i rapporti di densità simulabili. Per ridurlo, è stato implementato in ambiente Palabos il metodo di Yuan & Scahefer [5], che consiste nell'incorporare equazioni di stato fisiche, quali la Carnahan-Starling e la Peng-Robinson, nel modello. Viene mostrato come, in tal modo, sia possibile ottenere una riduzione delle correnti spurie e simulare rapporti di densità più alti, seppur con problemi di inizializzazione. Infine, il modello di Shan & Chen è sottoposto ad una prima validazione dinamica nel caso di flusso laminare bifase in un canale bidimensionale.

Parole Chiave: *Metodi Lattice Boltzmann, Mezzi Porosi, Flussi Monofase, Flussi Bifase.*

Abstract

In this thesis, the Lattice Boltzmann methods (LBMs) are analysed and employed for the simulation of single- and two-phase flows. In particular, the examples of application will concern the study of flows in porous media, which represents one of the natural field of application of the LBMs. The numerical simulations are performed using the open-source Palabos library.

Initially the LBMs are introduced reporting the derivation of the Lattice Boltzmann equation (LBE), starting from the Boltzmann equation [6, 7]. Afterwards, the connection with the Navier-Stokes equations is shown, by means of the Chapman-Enskog expansion [1]. In this procedure, it is also shown the correct way of introducing the forcing terms in the LBE.

In the single-phase part, three two-dimensional test cases are considered. The Hagen-Poiseuille flow is used to provide a first validation of the methods, and also to compare different models and to show the behaviour of the error. In the second case study, the flow over a hexagonal array of disks is taken into account. For this geometry, semi-analytical formulas are available, which allow a further validation. The single-phase part is concluded by using the LBMs to verify the validity of the Carman-Kozeny model for the prediction of the permeability of a porous medium.

The LBM model for the two-phase simulations analysed in this thesis is the Shan-Chen model [4]. Its main features are highlighted through the simulation of static tests. A particular problem of this model is the presence of artificial velocities at the interface, which limits the achievable density ratios. In order to reduce this problem, the method proposed by Yuan & Schaefer [5] has been implemented in the Palabos library. This method consists in the inclusion of physical equations of state, such as the Peng-Robinson and the Carnahan-Starling in the Shan-Chen model. In this way, it is shown how it is possible to reduce the magnitude of the spurious currents and to reach higher density ratios, even though with some initialization issues. Finally, a first dynamic validation of the Shan-Chen model is provided in the case of a laminar 2D co-current flow.

Keywords: *Lattice Boltzmann Methods, Porous Media, Single-Phase Flows, Two-Phase Flows.*

Chapter 1

Introduction

The study of flows in porous media has always been a field of intense research. In fact, in nature and technology, we can identify many phenomena involving flows in material that can be characterized as porous media.

The filtration of water in soil, as well as the flow of groundwater in aquifers are first straightforward examples. In petroleum engineering, the rocks of an oil reservoir can be considered a porous medium, as they have some void space and they are not consolidated. Thus, in this field, the understanding of the fluid transport inside the reservoir is fundamental to figure out the amount of unrecovered oil and the technical parameters to be used in the design of the extraction system. Accordingly, the study of flows in oil reservoir has been subject of strong research in literature [8, 9] and it has been definitely the field of application, which has given the greatest contribution in the development of porous media theory. A further and most recent application of porous media theory in energy enegineering is the study of flows through the porous electrodes of Fuel Cells [10].

In biology, plants and trees are able to uptake and transport water in their pore structure thanks to capillary effects. Moreover, many biological tissues can be numbered among porous media, justifying the growing applications of porous media theory to biotechnology [11, 12]. In general, a huge variety of problems which involves flows in porous media can be figured out.

In the classical theory of porous media, the flow properties are analysed by means of a high-level approach. The aim of the porous media study is not to obtain a detailed pore scale description of the flow, that would be experimentally unfeasible, but to focus on its macroscale characteristics, by defining appropriate macroscopic quantities. This macroscopic description deals with the study of a big enough sample of the porous medium, that is able to represent the effect of the underlying pore structure. The Darcy's law, introduced by Henry Darcy during the 19th century, is based on this approach. It basically states that, when the system has achieved a steady

state, the flow rate of a fluid through a porous medium is proportional to the ratio between the pressure gradient and the dynamic viscosity of the fluid. The proportionality constant is the most important quantity in porous media, that is, the permeability. In this very simple law, the pore structure manifests itself at the macroscopic level to the extent that it influences the permeability. Thus, the permeability is related by constitutive equations to parameters that describe the structure of the porous medium. An example of these consitutive equations is the Carman-Kozeny equation [8], in which the permeability is related to the porosity of the medium, a shape factor and a new quantity called tortuosity.

In case of multi-phase flow in porous medium, the Darcy's law can be extended by means of the concept of relative permeability, which tries to take into account the effect of the presence of the other fluids. In this case, an important effect is given by the wetting conditions of the porous medium, and also by other dimensionless parameters.

Historically, the influence of different parameters on permeability and relative permeability has been determined empirically. However, for reasons that will be clear later on, even for the single-phase case, parameters such as the above-mentioned tortuosity are very difficult to evaluate due to their complex definition.

In recent years, the improvement of the calculating capacity of computers and the development of new numerical schemes have made it possible to approach the study of fluid dynamics problem by solving directly the governing equations. This branch of fluid dynamics is called Computational Fluid Dynamics (CFD). In this context, the description of the fluid dynamics system is richer than the experimental one, since we obtain approximate solutions of velocity and pressure in each point of the discretized domain. In addition, the study of the fluid dynamics problem by means of CFD is definitely cheaper and less time consuming compared to the empirical approach.

As we know, the governing equations of fluid dynamics are the Navier-Stokes equations. The Navier-Stokes equations are basically the translation of the mass conservation principle and Newton's second law of dynamics to fluid systems, where the fluid is assumed as a continuum. Given their complex nature, the analytical solution of these partial differential equations can be obtained only in very simple cases and, in general, the solution can only be obtained numerically. Thus, the starting point of standard computational fluid dynamics is the discretization of the Navier-Stokes equations. For instance, this discretization is needed to obtain the Finite Volume, Finite Element and Finite Difference methods.

Nevertheless, all these methods seems to struggle when dealing with flows in porous media. In particular, the complex geometry of the porous medium

is difficult to handle with these models. Moreover, the study of multi-phase flows requires an interface tracking algorithm [13], which rather complicates the numerical scheme, particularly when complex geometries are involved.

1.1   Literature Review of LBM

In the last twenty-five years, a new approach to CFD, called the Lattice Boltzmann method (LBM), has been proposed and developed. In this new model, the attention is shifted from the Navier-Stokes equations to the so-called Lattice Boltzmann equation (LBE), which involves appropriate statistical particle distribution functions. From these particle distribution functions, it is possible to define macroscopic quantities, such as density and momentum. It can be shown that these macroscopic quantities satisfy the Navier-Stokes equations in the continuous limit. Thus, the LBM provides a lower level description compared to the Navier-Stokes equations, but a higher level description with respect to Molecular Dynamics, in which the particle collisions are directly taken into account. For these reasons, the Lattice Boltzmann method is said to be a mesoscopic model, in order to distinguish it between the macroscopic scale of the Navier-Stokes equations and the microscopic scale of Molecular Dynamics.

The LBM has basically originated from the ashes of the Lattice Gas Automata (LGA) [14, 15, 16] developped during the seventies and the eighties. The first Lattice Boltzmann model was introduced by McNamara & Zanetti [17] in 1988 in order to overcome the main drawbacks of the LGA. Thus, the idea behind the LBM in its origin, was the same behind the LGA and can be summarised by the following statement:

> *If the domain of the system is discretized with a sufficient degree of symmetry, it is possible to define a simplified dynamics, in which the only requirements are that mass and momentum must be conserved during collision, that is able to recover the macroscopic Navier-Stokes in the continuum limit.*

The collision term used in [17] was the Bhatnagar-Gross-Krook (BGK) with one parameter, called relaxation parameter, already used to model collision in the Boltzmann Equation (BE) [18, 19]. This is a first clue of the connection between the BE and the LBE.

The procedure to obtain the macroscopic equations is a multi-scale mathod called Chapman-Enskog (CE) [20] expansion. An example of CE for the LBE can be found in [21]. It is worth pointing out that the CE procedure has been originally developped to recover the macroscopic equations for the Boltzmann equation (BE) in [20], which is another evidence of the connection with the

Boltzmann equation. This relationship has been made explicit by He & Luo in [7], in which it is shown that the LBE can be seen as a proper discretization of the BE. This work has provided strong theoretical foundations to LBM, which somehow lacked in the original formulation derived from the LGA. Nowadays, the LBM is connected to the LGA only for historical reasons and the interpretation given in [7] is the most widely adopted.

From its introduction, the LBM has been subject of active research and development. The key ingredients of its success are:

- the simplicity of coding;

- the inherent parallelization;

- the easy handling of complex geometry.

However, it is worth pointing out that the control of the simulations and the interpretation of the result are not trivial.

The research has mainly focused on three issues of the LBM:

1. the development of proper boundary conditions;

2. the development of more stable and flexible collision terms;

3. the development of multi-phase models.

In LBM, the boundary conditions shall be translated for the particle distribution functions. The wall boundary conditions are usually achieved by means of the so-called Bounce-Back scheme [22], which is very simple and one of the reasons of the success of LBM when dealing with complex geometries. More elaborate schemes have also been proposed [23]. Several schemes are available for pressure and velocity boundary conditions [24, 25, 26, 27].

In order to overcome some drawbacks of the BGK collision term, the Multiple-Relaxation-Time (MRT) collision model has been introduced [28, 29, 30]. By tuning the parameters of this model, it is possible to improve the stability and to eliminate some annoying effects of the BGK model, such as the unphysical dependency of the simulated geometry on the relaxation parameter.

As far as multi-phase models are concerned, the main advantages of the LBM mesoscopic approach for multi-phase flow is that we do not need to track the interface location, but the behaviour of the interface arises naturally from the underlying lattice, if proper interactions between particles are taken into account. Even in this case, a very simplified scheme such as that proposed by Shan & Chen [4], based on a fictitious interaction potential, is able to produce phase separation. Another, LBM model has been developped by Swift *et al.* [31] and it is based on the definition of a Free-Energy

functional. Both methods shared similar shortcomings: spurious currents at the interface and limited density ratios. Hence, the research has focused on the solution of these problems.

For the Shan-Chen model, improvements have been obtained either by extending the range of the interactions [32] or by changing the form of the interaction potential [5], while the free energy model has been improved in [33], by solving the original problem of the violation of Galilean invariance.

Most recent multi-phase models, like that proposed by Lee & Lin [34], seem to be very promising in terms of achievable density ratios, but the price to be paid is a higher complexity and computational cost.

From this brief review of the literature, we are already able to realize that a natural field of application of LBM is to flows in porous media. In fact, the easy implementation of the wall boundary conditions by means of the Bounce-Back rule allows to handle complex geometries easily, where standard CFD schemes fail. The problem of interface tracking is solved, since the dynamics of the interface arises naturally from the scheme. In addition, as we will see, all the LBM theory is valid in the low Mach number limit; a condition that is certainly matched by flows in porous media.

Many scientific articles in literature have dealt with the study of fluid flow in porous media by means of the Lattice Boltzmann methods. Some examples are given in what follows.

In [35], LBM are applied to the study of the permeability of a cubic array of spheres and a random array of spheres, comparing the results of different collision terms. The use of randomly generated porous media is in general very wide in literature. A concrete application for single phase flow can be find in [36], where a study of the permeability of a reconstructed Fontainebleau sandstone is carried out. The Shan-Chen single-component model has been used in [37] to study the dependency of the relative permeability on several parameters, such as the contact angle and the viscosity ratio, in a random array of squares in two dimensions. The two-components Shan-Chen model has been used in [38] to obtain the capillary pressure-saturation curve and the results compared to experimental data. The Free-Energy method has been applied in [39] to investigate the relative permeability of a cubic pack of sphere and of a carbon paper gas diffusion layer. Finally, an application of the Lee-Lin model for two-phase flow in porous media can be found in [40].

1.2 Motivations and organization of the thesis

The main purpose of this thesis is to explore the capabilities of the Lattice Boltzmann methods for single-phase flows and two-phase flows, with a particular focus on the applications to porous media. In fact, we have already pointed out that the study of flows in porous media is the natural field of application of the LBMs, since they are able to overcome several drawbacks which affects the standard CFD methods, based on the discretization of the Navier-Stokes equations. The easy handling of complex geometries, achieved by means of the Bounce-Back boundary conditions, and the capability of simulating multi-phase flow without an interface tracking algorithm, due to its mesoscopic nature, are the main reasons of success of LBM. In addition, as we will see, the algorithm remains rather simple, even though its understanding is not trivial.

In this thesis, the Lattice Boltzmann method is analysed always in two dimensions. The reasons of this choice are twofold. In the first instance, the two-dimensional case allows an easier and quicker analysis of the main characteristics of the methods. In the second instance, the characteristics of LBM in two dimensions are basically the same of the three-dimensional case. Due to its high degree of symmetry, the extension to 3D problems is straightforward. For these reasons, the most part of the related literature is developed in two dimensions, while concrete applications are obviously in three dimensions.

In what follows, an outline of the thesis organisation is provided.

The second chapter is devoted to a general introduction to flows in porous media. In this chapter, only the concepts that will be used in the application part of the thesis will be reported. Thus, the aim of chapter two is not to cover the whole theory regarding porous media, which of course would require hundreds of pages, but to introduce the necessary ingredients for the understanding of the simulation part. In particular, starting from the Navier-Stokes equations, the limiting case of Stokes flow is identified, which is the typical flow condition in porous media. Then the most important law of porous media, i.e., the Darcy's law, is introduced, along with the consequent concept of permeability and the Carman-Kozeny equation [8], that is a model to predict the permeability of porous media. Then the attention is turned on some basic concepts of multi-phase flows, such as the surface tension and the contact angle, and the extension of the Darcy's law to multi-phase flows, with the definition of the relative permeability.

In chapter three, the Lattice Boltzmann methods is described in details. After a brief review of the historical development of the LBM, in which the

connection to the Lattice Gas Automata (LGA), is provided, the connection with the Boltzmanne equation is shown, carrying out its discretization, as done in [6] and [7]. In particular, the main ideas of the Boltzmann equation are introduced, showing the proper definition of the macroscopic quantities and how the macroscopic equations can be obtained [19]. This part was considered necessary, because only in this way, the definition of the macroscopic quantities in the LBM and the restoration of the Navier-Stokes equations would appear clear. At the end of this derivation, the Lattice Boltzmann equation with the single-parameter Bhatnagar-Gross-Krook (BGK) collision model. In the last section of chapter three, the Multiple-Relaxation-Time (MRT) model is described [29, 28], which has been basically introduced to overcome some drawbacks of the original BGK model, such as the fixed ratio between dynamic and bulk viscosities and the dependency of the simulated geometry on the parameter of the BGK model.

Chapter four is devoted to the recovery of the Navier-Stokes equations by means of the Chapman-Enskog expansion. Taking inspiration from the proof given by Kuzmin in [1], the expansion is carried out in a more general case at the beginning, in order to show the proper way of incorporating the forcing term into the LBE. In particular, the scheme proposed by Guo *et al.* is shown to be the best method. At the end of the chapter, the different sources of errors in the LBM will definitely appear clear. The issue of boundary conditions in LBM is the topic of chapter five. Here again, only the boundary conditions that will be used in the simulations are described. First of all, the meaning of boundary conditions in LBM is explained. Particular attention is given to the Bounce-Back scheme, the most popular way of simulating the wall interaction. In fact, this scheme when coupled with the BGK model is the cause of the previously mentioned dependency of the simulated geometry on the relaxation parameter of the BGK model. The explanation of this phenomenon is reported in details, as well as its solution by means of the MRT model. About pressure and velocity boundary conditions we report the scheme proposed by Zou & He [24], that will be used in the simulations.

In chapter six, the LBM is applied to study three test cases in two dimensions, providing also a first validation. In order to carry out the simulations the C++ Palabos library has been used. In the chapter, there is also a brief description of this library.

The first test case is the Hagen-Poiseuille flow in a straight channel. The solution of this problem is known analytically, and for this reason, it is certainly the most widely studied flow in the LBM literature. In addition, it also shows connections with flows in porous media, given its laminar flow conditions. This test case is used to compare three different collision models, namely, the original BGK model [17], the Two-Relaxation-Time model

(TRT) and the Multiple-Relaxation-Time model with improved stability [41]. In addition, also a comparison between two different kind of scalings, i.e., the diffusive and convective scaling, is carried out in terms of accuracy and computational time. Then, we start to turn the attention to more complex geometries with the analysis of the flow over a hexagonal array of disks, or infinite cylinders in three dimensions, which is a first example of porous medium. For this case, semi-analytical formulas are available [3, 2], which allow a comparison with the numerical results. Finally, the last case taken into account is the random array of disks, where a verification of the Carman-Kozeny equation is carried out.

Chapter seven deals with the topic of the LBM for multi-phase flows. The LBM multi-phase model used in this analysis is the Shan-Chen model introduced in [4]. This model has been chosen because it is the first and most simple multi-phase model for LBM, and in addition, because it is the easiest model to implement within the Palabos library. The Free-Energy method [31] is not implemented in the current version of Palabos, while the Lee-Lin model [34] is available, but only in three dimensions. The main idea behind the Shan-Chen model is the definition of a simplified interaction force between particles, which is able to trigger phase separation in certain conditions. Starting from the original formulation of the Shan-Chen model [4], its miscible/immiscible behaviour is analysed for the single-component and the multi-component case by means of static tests, highlighting also the main issues of concern of this model, i.e., the diffusive nature of the interface and the presence of artificial spurious currents. In particular, the issue of spurious currents is the cause of the instability of the model at high density ratios, which limits its applicability to physical problems where the density ratio (or the dynamic viscosity ratio) does not play an important role. However, the literature about the Shan-Chen model has focused on the solution of this problem, trying to reduce the magnitude of these spurious currents. Yuan & Schaefer [5] have shown that a way to achieve higher density ratio is to incorporate physical Equation of State (EOS) in the interaction potential of the Shan-Chen model, for example the Peng-Robinson EOS [42] or the Carnahan-Starling EOS [43]. This procedure is illustrated in details. In the current version of Palabos, the incorporation of EOS into the Shan-Chen model is not readily available. Nevertheless, it was decided to explore this possibility and the library expanded, writing the code to implement the EOS. The results obtained for the static tests by means of the implementation of EOS are compared to those of the original Shan-Chen model. Finally, comparison is carried out for a dynamic application, namely the case of a co-current flow two-dimensional channel, for which an analytical solution is available.

Chapter 2

Fluid flow in porous media

The flow in porous media can be basically viewed either as a flow around many and random obstacles, or as a flow inside very small and intricate conduits. The former approach is more suited for porous media with high porosities, while, the latter is more appropriate for low porosities [8]. In the case of high porosities, we are allowed to say that the reference case is the free flow, and the presence of few obstacles represents a small deviation from the free flow condition. On the contrary, for low porosities the basic case is the Hagen-Poiseuille flow and again, the flow inside the porous media can be considered as a perturbation of this flow. As shown in [8], different models have arisen from these approaches.

However, there are also other models which cannot be included in these two broad approaches. These are:

- Empirical models

- Direct solution of the Navier-Stokes equations.

In particular, the last one regards special cases in which the geometry is characterized by a certain degree of symmetry, and an the solutions are valid under some approximations. Some of these solutions will be introduced in Chap. 6 for the study of a porous media made up of an array of disks.

Initially, in this chapter, the incompressible Navier-Stokes equations are analysed, showing the typical conditions which marks out the flow in porous media. Afterwards, the analytical solution of the Hagen-Poiseuille flow is obtained. In fact, this simple flow will be studied in detail in Chap. 6 via the Lattice Boltzmann method, since it is definitely the most studied flow in the related literature. The fundamental Darcy's law is introduced in Sec. 2.3 along with the consequent concept of permeability of a porous media. The single-phase analysis is concluded by describing the Carman-Kozeny model to obtain the permeability of a porous media. The approach

(a) $\phi = 0.8$

(b) $\phi = 0.45$
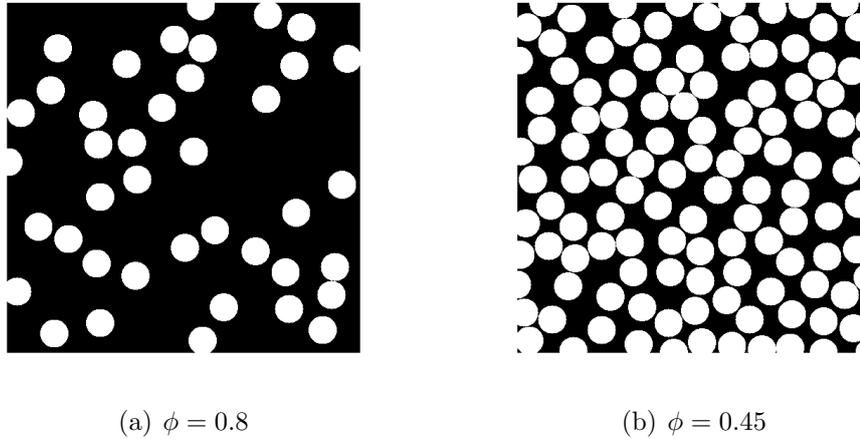
Figure 2.1. Examples of porous media made up of a random array of disks with different porosities.

followed by this model is definitely that of "flow inside conduits" and in fact it is basically derived by making some flow assumptions and then by using the Hagen-Poiseuille equation. Moreover, this model introduces the concept of tortuosity which we will describe in details.

The second part of the chapter is devoted to the introduction of the main features of multi-phase flows, with particular emphasis to flow in porous media. The general concepts of surface tensions and wettability are explained in details. Then, the focus is shifted towards porous media dealing with the issues of saturation and relative permeability.

It is worth pointing out that in this chapter only the quantities and the concepts that will be used in the simulation part will be introduced.

2.1 The Navier-Stokes equations

The starting point of any fluid dynamics study is definitely the analysis of the Navier-Stokes equations. They represent basically the translation of mass conservation principle and Newton's second law to a fluid system. The usual approach to obtain them is to assume the fluid as a continuum. The discrete nature of matter is not taken into account, but in each point of the fluid system appropriate averaged macroscopic quantities are defined: the density ρ, the velocity $\boldsymbol{u} = (u, v, w)$, the pressure P and the stress tensor $\bar{\bar{\boldsymbol{\sigma}}}$. The real nature of this assumption is to be found in Statistical Mechanics, and it will be more clear when in Chap. 3 we will illustrate the statistical description of macroscopic quantities.

Under the assumptions of incompressible flow, Newtonian fluid and absence of external forces, the mass conservation principle and the Newton's second law are respectively translated into [44]:

$$\nabla \cdot \boldsymbol{u} = 0, \tag{2.1a}$$

$$\rho \frac{\partial \boldsymbol{u}}{\partial t} + \rho \nabla \cdot (\boldsymbol{u}\boldsymbol{u}) = -\nabla P + \mu \nabla^2 \boldsymbol{u}, \tag{2.1b}$$

where μ is the dynamic viscosity of the fluid, here assumed as constant.

In order to understand the governing parameters of Eqs. (2.1), let us obtain their non-dimensional form. Let us take a characteristic reference length L_0 and a characteristic reference velocity U_0 of the problem we are considering. For example, in the case of a flow inside a conduit, the reference length might be the conduit's diameter, while the reference velocity might be chosen as the average cross sectional velocity. However, for more complex geometries, like porous media for instance, several lengths and velocities might be taken as reference. Therefore, it is very important to define these quantities properly and clearly, otherwise they might be source of confusion. Throughout this thesis, these choices will always be made explicit.

The definitions of L_0 and U_0 bring about the definition of a reference time $t_0 = L_0/U_0$ and a reference pressure $P_0 = \rho U_0^2$, as well. Thus, we define the following non-dimensional quantities:

$$\hat{\boldsymbol{x}} = \frac{1}{L_0}\boldsymbol{x}, \quad \hat{\boldsymbol{u}} = \frac{1}{U_0}\boldsymbol{u}, \quad \hat{t} = \frac{U_0}{L_0}t, \quad \hat{P} = \frac{1}{\rho U_0^2}P. \tag{2.2}$$

Using Eqs. (2.2) into Eqs. (2.1), we finally obtain the non-dimensional form of the Navier-Stokes equation:

$$\nabla_{\hat{\boldsymbol{x}}} \cdot \hat{\boldsymbol{u}} = 0, \tag{2.3a}$$

$$\frac{\partial \hat{\boldsymbol{u}}}{\partial_{\hat{t}}} + \nabla_{\hat{\boldsymbol{x}}} \cdot (\hat{\boldsymbol{u}}\hat{\boldsymbol{u}}) = -\nabla_{\hat{\boldsymbol{x}}}\hat{P} + \frac{1}{Re}\nabla_{\hat{\boldsymbol{x}}}^2\hat{\boldsymbol{u}}, \tag{2.3b}$$

where the symbol $\nabla_{\hat{\boldsymbol{x}}}$ specifies that they are derivatives respect to $\hat{\boldsymbol{x}}$ and we have introduced the Reynolds Number Re defined as:

$$Re = \frac{\rho U_0 L_0}{\mu}. \tag{2.4}$$

Hence, the Reynolds Number is definitely the governing parameter of the incompressible Navier-Stokes equations. In fact, if two different fluid systems satisfy the geometric similarity, i.e. the geometries of the two domains are the same except for a scale factor, the same non-dimensional initial and boundary conditions are applied, and the Reynolds Number is the same,

then they share the same non-dimensional solution and they are said to be in similarity condition.

In addition, the Reynolds Number plays another important role in fluid dynamics. It is the ratio between the order of magnitude of inertia forces and viscous forces. Inertia forces are taken into account in Eqs. (2.1) by the term $\rho\nabla(\boldsymbol{uu})$, while the term responsible for viscous forces is definitely $\mu\nabla^2\boldsymbol{u}$. Thus:

$$\frac{\rho\nabla(\boldsymbol{uu})}{\mu\nabla^2\boldsymbol{u}} \sim \frac{\rho U_0^2/L_0}{\mu U_0/L_0^2} = Re. \tag{2.5}$$

Moreover, it is straightforward to verify that also the ratio between the term $\rho\partial\boldsymbol{u}/\partial t$ and the viscous term is proportional to Re.

Accordingly, when $Re \to \infty$, viscous forces are negligible compared to inertia forces and the flow is said to be completely turbolent, with the limiting case of inviscid flow. On the contrary, if $Re \to 0$, viscous forces take over and the flow is organised in parallel layers. This kind of flow is known as laminar flow, with the limiting case of Stokes flow. Actually, there is always a range of Reynolds Number in which we witness a transition from laminar to turbulent flow. For the case of flow inside a straight smooth pipe with circular cross section, the transition regime takes place when the Reynolds Number is approximately between 2000 and 10000 [45]. The laminar-turbulent transition has been studied for the first time in 1883 by O. Reynolds in [46], where he carried out his famous experiment.

2.2 The Hagen-Poiseuille flow

In this section we will obtain the analytical solution of the Hagen-Poiseuille flow for the two-dimensional case [45]. The existence of an analytical solution has driven the attention towards this kind of flow, because it is straightforward to compare the analytical solution with the numerical one and then to obtain the error. In particular, when dealing with Lattice Boltzmann methods, the Hagen-Poiseuille flow is very useful to highlight some of the drawbacks of LBM, which will be better explained later on, and also to analyse how the error vanishes when the grid resolution is increased. Moreover, as pointed out at the beginning of this chapter, the Hagen-Poiseuille equation is very important for the study of flow in porous media and it is the starting point of the Carman-Kozeny model that we will introduce in Sec. 2.4.

Let us consider a flow in a two-dimensional straight channel of height H, like in Fig. 2.2, with the following assumptions:

- The Reynolds Number is sufficiently low have laminar flow condition; in this case streamlines are parallel and the velocity in the y-direction v is zero in each point.
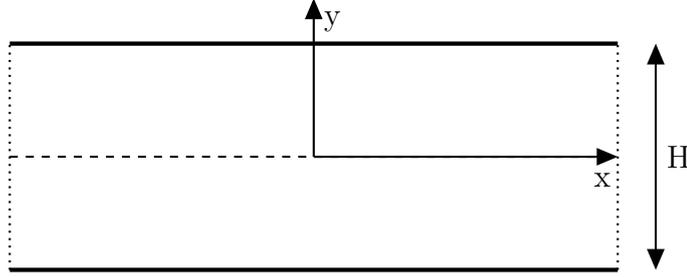
Figure 2.2. Two-dimensional straight conduit.

- The flow is stationary: $\partial \boldsymbol{u}/\partial t = 0$.

- There are no variations in the x-direction, i.e., $\partial \boldsymbol{u}/\partial x = 0$. In this case we say that the flow is fully developed.

Eqs. 2.1 turn into:

$$\frac{\partial v}{\partial y} = 0, \tag{2.6a}$$

$$-\frac{\partial P}{\partial x} + \mu \frac{\partial^2 u}{\partial y^2} = 0, \tag{2.6b}$$

$$-\frac{\partial P}{\partial y} = 0. \tag{2.6c}$$

Placing the origin of the y-axis at the centre of the channel, we set the typical no-slip boundary conditions at the upper and lower wall:

$$\begin{cases} \boldsymbol{u}(x, R) = 0, \\ \boldsymbol{u}(x, -R) = 0, \end{cases} \tag{2.7}$$

where $R = H/2$.

It is easy to verify that the solution of the system composed by Eqs. (2.6) and Eqs. (2.7) is:

$$\begin{cases} u = -\frac{1}{2\mu}\frac{\partial P}{\partial x}(R^2 - y^2), \\ v = 0. \end{cases} \tag{2.8}$$

We can see that x-component of velocity u shows a parabolic profile with a maximum at the centre $y = 0$:

$$u_{max} = -\frac{R^2}{2\mu}\frac{\partial P}{\partial x}. \tag{2.9}$$

Moreover, it is easy to prove that the average cross sectional velocity, that we denote by q, is given by:

$$q = \frac{1}{2R}\int_{-R}^{+R} u(y)\, dy = -\frac{R^2}{3\mu}\frac{\partial P}{\partial x} = \frac{2}{3}u_{max}. \tag{2.10}$$

If we turn our attention to the three-dimensional case of flow through a cylindrical pipe of radius R, with the same hypothesis as before, we obtain:

$$u = -\frac{1}{4\mu}\frac{\partial P}{\partial x}(R^2 - r^2), \qquad (2.11)$$

which gives an average velocity

$$q = -\frac{R^2}{8\mu}\frac{\partial P}{\partial x}. \qquad (2.12)$$

2.3 Stokes flow and Darcy's law

The flow in porous media is usually charachterized by small Reynolds numbers. In general both the reference length L_0 and velocity U_0 are very low, indeed. In this case, we are allowed to neglect the inertia contributions, which appear in the incompressible Navier-Stokes equation Eqs. (2.1). Thus, we obtain:

$$\nabla \cdot \boldsymbol{u} = 0, \qquad (2.13a)$$
$$-\nabla P + \mu \nabla^2 \boldsymbol{u} = 0. \qquad (2.13b)$$

Eqs. 2.13 are usually called the Stokes equations, while the flow which obeys to these equations is known as Stokes flow or creeping flow.

The Stokes flow has two basic features which immediately emerge from Eqs. (2.13)

1. The flow has no memory. Since there is no time derivative into the equations, the solution is time independent. In addition, if at a certain time t there is a variation of boundary conditions, a new solution is established which does not depend on the previous one.

2. The flow responds instantaneously to perturbations, since it has no inertia. A typical example is a sphere entering a fluid. If Stokes conditions are maintained, the sphere reaches immediately the characteristic terminal velocity.

However, when dealing with flow in porous media, in most cases we are in conditions in which the flow obeys to the so-called Darcy's law. The Darcy's law was introduced empirically by H. Darcy during the 19th century and it has been recently derived theoretically by means of volume averaging [47].

The Darcy's law makes a more general statement on the flow compared to the Stokes equations. In order to introduce the Darcy's law, let us consider a porous medium, like those shown in Fig. 2.1, and let us suppose that a

pressure gradient is applied between the left and the right boundary. In addition, we denote by L the length of the porous medium and we define the pressure difference as $\Delta P = P_{out} - P_{in}$. The Darcy's law states that:

$$q = -\frac{k}{\mu}\frac{\Delta P}{L}, \tag{2.14}$$

where q is the average cross sectional velocity, and the cross section A is to be intended as the total area including both pore and solid contribution; this means that the volumetric flow rate Q, which flows in the direction of the applied pressure gradient, is given by $Q = qA$. In Eq. (2.14), it appears for the first time the permeability of a porous media k, which is only dependent on the geometry of the porous medium. Comparing Eq. (2.14) to Eq. (2.10) and to Eq. (2.12), it is clear that the permeability of a two dimensional straight conduit is $k = R^2/3$, while the permeability of a cylindrical pipe is $R^2/8$. A flow obeying to Eq. (2.14) is called a Darcy's flow, and the velocity q is known as the Darcy's velocity.

For the sake of generality, the permeability of a porous medium is a tensor, indeed. If we apply a pressure gradient along the x-direction, we can of course compute the average velocity q_x, but also the induced pressure gradients along the y- and z-directions, and the consequent q_y and q_z. Obviously, for each direction we have a permeability k_{xx}, k_{xy} and k_{xz}. The same operation can be carried out applying a pressure gradient along the y- or z-direction. Hence, the most general formulation of the Darcy's law is:

$$\boldsymbol{q} = -\frac{\bar{\bar{\boldsymbol{k}}}}{\mu}\nabla P, \tag{2.15}$$

where $\bar{\bar{\boldsymbol{k}}}$ is the permeability tensor. However, in most cases we are interested in the diagonal components of $\bar{\bar{\boldsymbol{k}}}$.

As we have mentioned before, the permeability of a porous medium does not depend on the applied pressure gradient, but it is just function of the geometry. This is the main feature of a Darcy's flow.

As a matter of fact, in general the Darcy's law is valid when the pressure gradient is sufficiently low, i.e. the Reynolds number is low. We can identify a Reynolds Number for which the relationship between the Darcy's velocity and the pressure gradient begins to deviate from linearity and thus, the permeability is not constant any more. This is a first effect of inertia forces, but it shall not be confused with the transition from laminar to turbulent flow, but just as a transition from Darcy to non-Darcy flow. In particular, the Darcy's law underestimates the pressure gradient needed to obtain a certain flow rate. In order to take into account the inertia effects, the Forchheimer equation has been proposed which adds a further term into the Darcy's law [8].

2.4 The Carman-Kozeny equation

The Carman-Kozeny equation is a model to predict the permeability of a porous medium, which approaches the porous medium as an intricate system of small conduits. In order to introduce this model, we will refer to [8].

The Carman-Kozeny model is also known as "hydraulic radius theory", because the starting point is to assume that the fluid flows inside a conduit, whose diameter is given by:

$$D_H = \frac{4V_f}{S_{wet}}, \tag{2.16}$$

where V_f is the volume occupied by the fluid and S_{wet} is the solid surface wetted by the fluid [1]. At this point, an Hagen-Poiseuille like flow is assumed inside this fictitious channel, which gives an average velocity:

$$u_{HP} = -\frac{\Delta P}{L_e}\left(\frac{D_H^2}{\beta_0 \mu}\right), \tag{2.17}$$

where L_e is an appropriate average length of the path of a fluid particle, which we will define better in Subsec. 2.4.1, and β_0 is a factor which depends only on the grains' shape. The velocity u_{HP} is assumed to be related to the Darcy's velocity q by the following relation:

$$u_{HP} = \frac{qL_e}{\phi L}, \tag{2.18}$$

in which ϕ is the porosity of the porous medium, i.e the ratio between the volume occupied by the fluid and the total volume $\phi = V_f/V$.

The insertion of Eqs. (2.14) and (2.17) into Eq. (2.18) allows to obtain the expression of the Carman-Kozeny permeability:

$$k_{CK} = \frac{\phi D_H^2}{\beta_0 (L_e/L)^2}. \tag{2.19}$$

If we call S_0 the ratio between the wet surface and the volume occupied by the solid, $S_0 = S_{wet}/V_s$, we can express the hydraulic diameter as:

$$D_H = \frac{4\phi}{S_0(1-\phi)}. \tag{2.20}$$

---

[1] In the two-dimensional case, of course V_f is substituted by the area occupied by the fluid A_f, while S_{wet} becomes a wet perimeter P_{wet}. Furthermore, it is wise to change the factor 4 with 2, so that in case of a straight conduit D_H would be equal to the height of the channel.

Hence, we can rewrite Eq. (2.19) as:

$$k_{CK} = \frac{\phi^3}{\beta(L_e/L)^2(1-\phi)^2 S_0^2},\qquad(2.21)$$

where the new shape factor β is related to the previous β_0 simply by $\beta = \beta_0/16$.

Eq. (2.21) allows to figure out directly the relationship between permeability and porosity in the Carman-Kozeny model.

2.4.1 Tortuosity

The quantity L_e/L which appears into the Carman-Kozeny equation is known as tortuosity and it is usually denoted by T. In order to understand this quantity, we definitely need to define rigorously the length L_e.

Let us suppose that a pressure gradient is applied along the x-direction of a two-dimensional porous medium of length L. L_e is defined as [48]:

$$L_e = \frac{\int_A u(y)\lambda(y)\,dy}{\int_A u(y)\,dy},\qquad(2.22)$$

where the integration is carried out over a generic cross section A, and $\lambda(y)$ is the length of the streamline which passes through A at y. Thus, L_e can be viewed as the weighted average of the length of the streamlines over whichever cross section, where the weight are the infinitesimal flow rates $u(y)\,dy$. The extension to the three-dimensional case is straightforward. It is also worth pointing out that, by means of similar reasoning to those used for permeability, the tortuosity is a tensor, indeed.

It is rather obvious that $T \geq 1$. However, we recognize that the tortuosity of a porous media is not known *ex ante* the solution of the flow. Besides, it depends on the porosity, the shape of the grains, their distribution and the flow condition. In particular, we expect that porous media with high porosities are charachterized by lower tortuosities.

Thus, it is very difficult to obtain tortuosity via experiments and this is the main limit of the Carman-Kozeny model.

Anyway, from the point of view of computational fluid dynamics, reasonable estimates of the integrals of Eq. (2.22) can be obtained during the post-processing phase. Therefore, CFD allows to know the tortuosity of a porous medium and thus, to investigate the validity of the Carman-Kozeny equation and the dependency of tortuosity on the various parameters. The way in which tortuosity is computed from the numerical solution should always be well defined, since it could be source of confusion in literature.
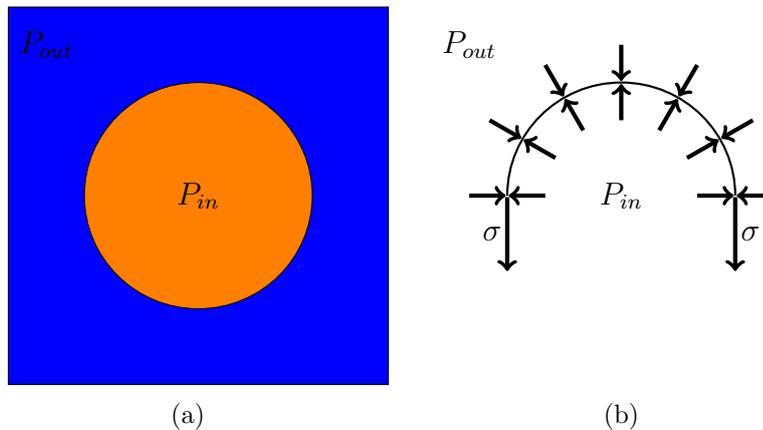
Figure 2.3. Interface force balance for a bubble.

2.5 Multi-phase flow

Up to now, we have only considered single-phase flows in porous media and introduced the main concepts and quantities which characterize these kinds of flows. However, when dealing with flows in porous media, we are mostly interested in multi-phase flows. For instance, in petroleum engineering, we always witness at least a two-phase flow, i.e. water and oil inside an oil reservoir, but we might be interested also in studying three-phase flows, in case of enhanced oil recovery techniques. In hydrology and geology, instead, we usually deal with an air-water system, for example the flow of water into the ground. In general in every day life, we can figure a variety of situations which involve multi-phase flow, and in particular multi-phase flow in porous media. A trivial example is the wetting of an handkerchief, where air is displaced by water.

In what follows, the main parameters and physical phenomena which govern the flow in porous media will be introduced, with particular insights on flows in porous media.

2.5.1 Laplace's law

When many phases coexist in a system, they are separated by a thin surface. In the opinion of the author, the best way to understand the nature of this interface, and the associated concept of surface tension, is to make an example from daily life. Let us imagine to create a soap bubble, or to blow up a balloon. Initially, the interface between the external environment is little, but when we blow up, the interfacial surface increases. It is intuitive, that when we blow the bubble through the small opening, or when we blow inside the balloon, we are just doing work, by increasing the pressure of the air,

against a certain force which try to contrast the surface generation. Thus, we realize that the infinitesimal work δW done against this force is proportional to the created surface dS:

$$\delta W = \sigma dS, \tag{2.23}$$

where σ is called the surface tension. Consequently the surface tension can be interpreted either as an energy per unit of area [2] or as a force per unit of length. In fact, if we imagine to apply an incision of length l on the surface of the soap bubble or the balloon, we expect that a force proportional to l arise, which tends to separate the two strips.

Let us now consider the case of a spherical bubble of radius r inside a surrounding fluid, as in Fig. 2.3, and to carry out the force balance for an hemisphere. It is straightforward to realize that the pressure inside the bubble is forced to be higher than the one of the surrounding fluid. From the force balance, we want to obtain an equation for the pressure difference $P_c = P_{in} - P_{out}$, which is usually called capillary pressure. The force balance at interface reads:

$$P_{in}\pi r^2 = \sigma 2\pi r + P_{out}\pi r^2, \tag{2.24}$$

which yields:

$$P_c = \frac{2\sigma}{r}. \tag{2.25}$$

Eq. (2.25) is known as theLaplace's law. Actually, in the most general case of a non-spherical bubble, the Laplace's law is given by [8]:

$$P_c = \sigma \left(\frac{1}{r_1} + \frac{1}{r_2} \right), \tag{2.26}$$

where r_1 and r_2 are the principal radii of curvature.

Since in this thesis we will carry out simulations in two dimensions, we report the Laplace's formula for a circular disk:

$$P_c = \frac{\sigma}{r}. \tag{2.27}$$

2.5.2 Wettability and capillary effects

The next step in the understanding of multi-phase flows is to introduce the interaction with the solid surface and the concept of wettability. In Fig. 2.4, we can see the typical scheme of a drop on a solid surface, surrounded by a gas. In this case, we have to consider the surface tension between gas

---

[2]This interpretation explains the tendency of the bubble to assume a spherical shape. In fact, it is known that the sphere is the shape that minimize the surface given a fixed volume.
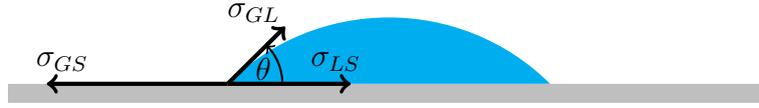
Figure 2.4. Contact angle at solid surface. In this case the contact angle is lower than 90° and the liquid is the wetting phase.
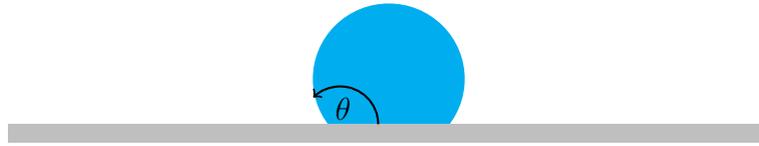
Figure 2.5. The liquid is the non-wetting phase.

and liquid, σ_{GL}, but also the surface tensions between solid and liquid, σ_{LS}, and between solid and gas, σ_{GS}. These surface tensions act to minimize the respective interfacial surfaces. This justifies the directions of the vectors in Fig. 2.4.

At the contact point between the three phases, the force balance in the horizontal direction is simply:

$$\sigma_{GS} = \sigma_{GL} \cos\theta + \sigma_{LS}, \qquad (2.28)$$

where θ is called contact angle and it consequently satisfies:

$$\cos\theta = \frac{\sigma_{GS} - \sigma_{LS}}{\sigma_{GL}}. \qquad (2.29)$$

Assuming the circularity of the drop or bubble, the contact angle can be evaluated geometrically as:

$$\theta = \arctan\frac{b/2}{r-h}, \qquad (2.30)$$

where b is the base, h is the height and r is the radius of the drop/bubble. In turn, the radius r is given by $r = b^2/(8h) + h/2$.

If the contact angle, here referred to the liquid, is lower than 90°, as in Fig. 2.4, the liquid is said to *"wet"* the solid surface. On the contrary, it is said to be the *non-wetting* phase, if the contact angle is greater than 90°, like in Fig. 2.5.

From everyday life, we know that when oil spreads over a solid surface, if successively water is poured over the surface, water shows a behaviour
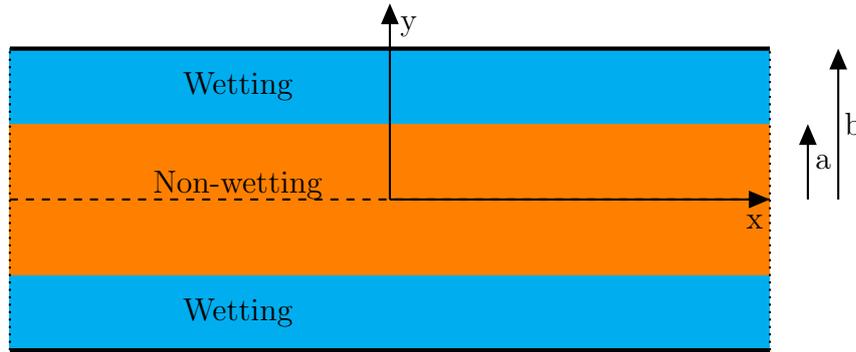
Figure 2.6. Co-current two-phase flow in a 2D channel.

similar to that displayed in Fig 2.5. The explanation of this phenomenon is that since water and oil are not affine, which is of course supported by the immiscibility of the oil-water mixture, the previous spreading of oil on the solid surface causes the increase of the term σ_{LS}, leading to a high contact angle.

2.5.3 Relative Permeability

When dealing with multi-phase flows in porous media, the Darcy's law can be extended using the concept of relative permeability. In fact, considering a two-phase system, it is easy to realize that the presence of the non-wetting fluid (NW) influences the permeability of the wetting fluid (W) and vice versa. The Darcy's laws for the two fluids becomes [8]:

$$q_w = -\frac{k_{r,w}k}{\mu_w}\frac{\Delta P}{L}, \tag{2.31a}$$

$$q_{nw} = -\frac{k_{r,nw}k}{\mu_{nw}}\frac{\Delta P}{L}. \tag{2.31b}$$

Thus, the relative permeabilities $k_{r,w}$ and $k_{r,nw}$, of the W and NW phases respectively, appear in the Darcy's law, as coefficients acting on the permeability of the porous medium k. The products $k_{r,w}k$ and $k_{r,nw}k$ may also be considered as the effective permeabilities. In general, the relative permeabilities are expressed as a function of the wetting saturation S_w, defined as the ratio between the volume occupied by the W phase and the total volume occupied by the fluid:

$$S_w = \frac{V_w}{V_w + V_{nw}}. \tag{2.32}$$

The definition is analogous for the non-wetting saturation, and hence, $S_{nw} = 1 - S_w$.

As an example, let us consider the case of a co-current Poiseuille-like two-phase flow, like that displayed in Fig. 2.6. For this kind of fluid dynamics

problem, there exists an analytical solution [49]. In particular, for the W fluid the velocity is given by:

$$u(y) = -\frac{\Delta P}{2L\mu_w}(b^2 - y^2), \qquad |a| \leq |y| \leq |b|; \qquad (2.33)$$

while for the NW fluid:

$$u(y) = -\frac{\Delta P}{2L\mu_w}(b^2 - a^2) - \frac{\Delta P}{2L\mu_{nw}}(a^2 - y^2), \qquad |0| \leq |y| \leq |a|. \qquad (2.34)$$

From these analytical solutions, the relative permeabilities of the W and NW phase can be obtained as [49]:

$$k_{r,w} = \frac{1}{2}S_w^2(3 - S_w), \qquad (2.35a)$$

$$k_{r,nw} = S_{nw}(\frac{3}{2}M + S_{nw}^2(1 - \frac{3}{2}M)), \qquad (2.35b)$$

where M is the dynamic viscosity ratio $M = \mu_{nw}/\mu_w$. Obviously, given the presence of analytical formulas, this problems is widely used for validation of numerical multi-phase methods. As an example, it has been used in [37, 50, 39] to validate the respective Lattice Boltzmann multiphase model. For this reason it will be used in Chap.7.

In Fig. 2.7, we can see the typical relative permeability curves for the Poiseuille-like two-phase flow. Similar curves can be obtained for more complex porous media.

In Fig. 2.7, it is clear that the relative permeability of the non-wetting phase is strongly influenced by the dynamic viscosity ratio M. At a first glance, we would expect that $k_{r,nw}$ should always decrease (and hence always be lower than 1) with the increase of the saturation S_w due to the reduction of the cross section of the NW phase. Nevertheless, the NW fluid takes also advantage of the *"lubricating"* effect caused by the W phase, which avoids the contact of the NW fluid with the boundary walls. This effect is particularly important in this case, as we can see in Fig. 2.7(b), in which the $k_{r,nw}$ initially increases with S_w.

However, the importance of the effect of the dynamic viscosity ratio in practical applications has been debated for a long time. As pointed out by Dullien in [8]:

> "The question whether the effective permeabilities are independent of the viscosities of the fluid pair employed is of considerable practical significance".
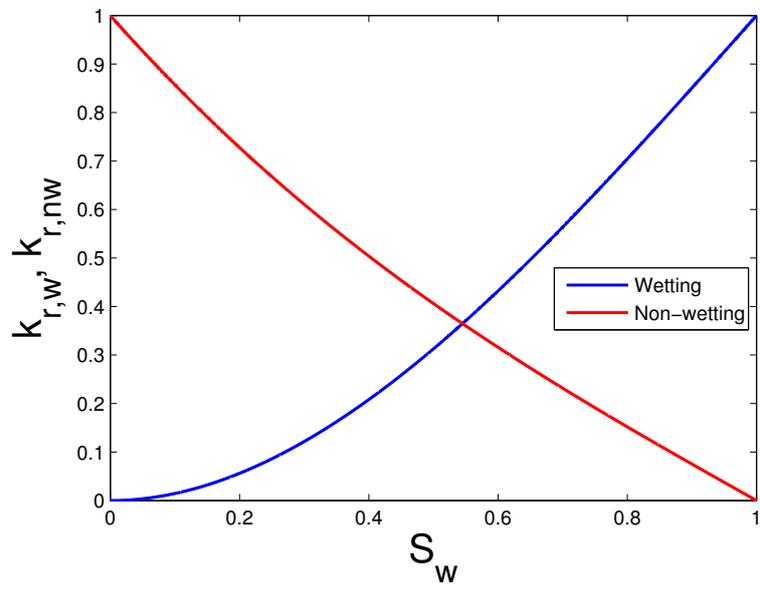
(a) $M = 0.5$
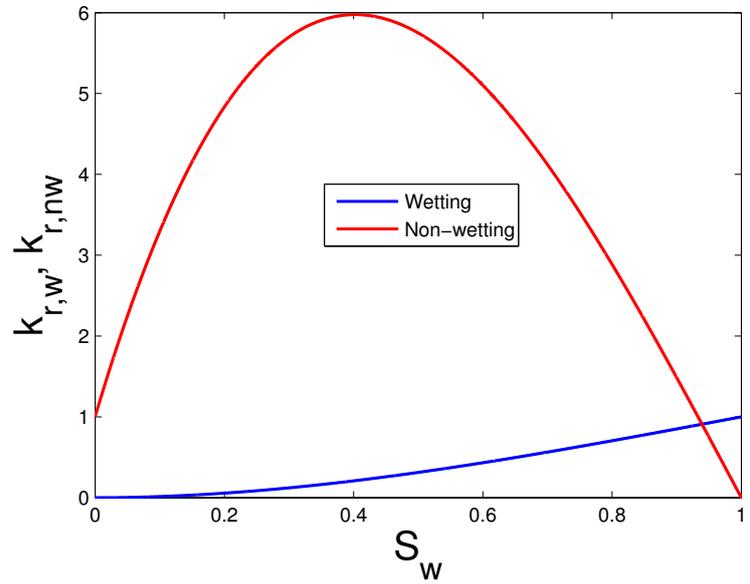
(b) $M = 10$

Figure 2.7. Relative permeability curve for the co-current two-phase flow with different values of the dynamic viscosity ratio M.

We could also add that it is of considerable *computational* significance.

Discussions about this argument can be found in [8, 9], where contradictory studies have been reported for the case of an oil-water system, such as [51, 52]. Dou & Zhou in [50] have carried out a Lattice Boltzmann study for the case of a random array of squares. They showed that the importance of the viscosity ratio may also be function of the heterogeneity of the porous medium.

Obviously, there are also other factors that influence the permeability of a porous medium. In the first instance, it is clear that relative permeabilities are influenced by the wetting conditions, i.e., by the contact angle. Basically, the wettability has effects on the distribution of the two (or more) phases inside the porous medium [9]. In particular, we expect the wetting phase to fill preferentially smaller pores (see [53] for an interesting explanation of this phenomenon), allowing the non-wetting phase to flow over the larger pores. Thus, we expect the relative permeability of the non-wetting phase to increase with the decrease of the contact angle at a fixed saturation. The opposed phenomenon is expected for the wetting phase.

The effects of viscous and capillary forces are incorporated in a dimensionless group called Capillary Number (Ca), defined as [53]:

$$Ca = \frac{U_0 \mu_w}{\sigma}, \qquad (2.36)$$

where U_0 is a characteristic velocity of the flow and σ is the surface tension. In the first instance, the Capillary Number plays a key role, as it determines the validity of the modified Darcy's law for multiphase flows Eqs. (2.31). In fact, it has been shown [52], that at high Ca, the relative permeability depends on the flow rate, and accordingly on the pressure gradient, which is a clear violation of the assumptions of the Darcy's law. Hence, the Darcy's law for multiphase flow is valid under the assumptions of low Capillary Numbers $Ca \ll 1$ [3]. A typical value in oil reservoir for waterflooding is $Ca \approx 10^{-6}$ [9].

The influence of the Capillary Number on the relative permeabilities curves can be readily understood. Let us suppose to vary the surface tension, thus increasing the strength of capillary forces. In this case, the wetting phase preferentially fills the smaller pores as usual, but in addition we expect an higher pressure gradient in order to cause the same flow rate of the wetting phase, because we have to cope with higher capillary pressures, which tend to impede the flow of the wetting phase. In turn, the non-wetting phase is slowed down by the lower velocity of the wetting one. The opposite behaviour

---

[3]Of course, we have to consider also the assumption of low Reynolds Number, which is the regime of validity of the single-phase Darcy' law

can be obtained by increasing the strength of the viscous forces. In fact, the viscous forces tends to cause a uniform distribution of the two phases in the pore spaces, preventing the effect of capillary forces. It is worth pointing out, that the dependency of the relative permeability on the Capillary Number has not to be intended as a direct dependency on the applied pressure gradient. The dependency is purely on the Capillary Number, even though the pressure gradient influences this value by controlling the magnitude of the viscous forces. In case the relative permeability depends explicitly on the pressure gradient, the Darcy's law is not valid. From, this brief explanation, we realize that a way to increase the relative permeabilities, or in general to increase the flow rates of the W and NW phases, is to increase the Capillary Number. The easiest way to do it is by decreasing the surface tension σ and in fact, one of the main Enhanced Oil Recovery techniques consists in the injection of surfactants, which are supposed to decrease the surface tension.

Chapter 3

The Lattice Boltzmann method

Historically, the Lattice Boltzmann method (LBM) was originated as an evolution of the Lattice Gas Automata (LGA) [14]. The main idea behind the Lattice Gas was that a simplified microdynamics, in which particles with discrete velocities collide only at the lattice sites and, at the following stage, stream to the connected node, is sufficient to recover the macroscopic Navier-Stokes equations if mass and momentum are conserved during collisions, and the lattice geometry is characterized by a certain degree of symmetry, as shown in [54], [55].

However, the Lattice Gas suffered several diseases such as lack of Galilean invariance, statistical noise and anomalous dependence of velocity on pressure [55], [56]. In order to overcome these shortcomings, the Lattice Boltzmann method was introduced by McNamara and Zanetti [17] in 1988. In the LBM, the particle population in each node, and for each discrete velocity, is replaced by a continuous distribution function. This allows to substitute the LGA Fermi-Dirac equilibrium distribution function, which was the basic cause of the Galilean invariance violation [56], with a Maxwellian, typical of kinetic theory of gases [19]. Another consequence of the continuous distribution function was the elimination of statistical noise. In addition, the collisions were replaced by a Bhatnagar-Gross-Krook (BGK) collision term [57], in a similar approximation of the collision integral of the Boltzmann equation (BE).

In this context, we can understand the intimate relationship between the LBM and the BE. In fact, it was shown recently by He and Luo [6], [7] that the Lattice Boltzmann equation (LBE) can be seen as a special discretization of the BE. This discovery established the basis for a more rigorous and deep understanding of LBM.

In this chapter, firstly, we will describe in general the Lattice Gas microdynamics. In the second instance, we will present the derivation of the Lattice Boltzmann equation starting from the Boltzmann BGK Equation,
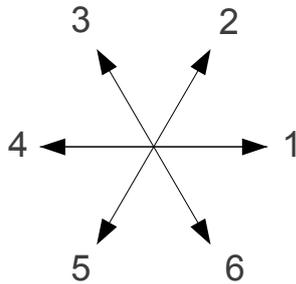
Figure 3.1. FHP lattice structure

and also the Multiple Relaxation Time (MRT) collision model will be introduced.

3.1 The ancestor: Lattice Gas Automaton

The first Lattice Gas Automaton was proposed by Hardy, de Pazzis, and Pomeau (HPP) [15] in 1973 and it is named by its authors. It was based on a square lattice with four possible discrete velocities. However, this model does not recover the macroscopic Navier-Stokes equations. For this reason we will consider the Lattice Gas Automaton proposed by Frisch, Hasslacher, and Pomeau (FHP) [16, 54], which was the first LGA with the required degree of symmetry to satisfy the macroscopic conservation equations, even though with some shortcomings, mainly, lack of Galilean invariance, statistical noise and anomalous dependence of velocity on pressure.

The FHP is build on an hexagonal lattice with six discrete velocities $\{e_i | i = 1, 2, \ldots, 6\}$, each pointing to the connected neighbour. Therefore, in each lattice node, there are six cells related to the discrete velocities, as we can see in Fig. 3.1, and in lattice units they are given by

$$e_i = \left(\cos \frac{(i-1)\pi}{3}, \sin \frac{(i-1)\pi}{3} \right). \tag{3.1}$$

A node can be occupied by at most one particle and, consequently, its state is described by a Boolean number $\{0, 1\}$ called occupation number n_i; it is straightforward that the number of possible state of a lattice site is 2^6. As pointed out in [55], a *Pauli exclusion principle* for Lattice Gases holds.

The evolution of the LGA dynamics consists of two steps: collision and streaming. When two or more particles are simultaneously in a lattice node, a collision can occur. The *conditio sine qua non* to simulate the macroscopic dynamics is that collisions must preserve the same physical quantity as real world collisions, i.e. mass and momentum. If also kinetic energy is conserved, we expect that an ideal gas behaviour should be recovered, since the basic

hypotheses are identical. Nevertheless, for ideal gases the equilibrium distribution function is a Maxwellian, different from the Fermi-Dirac distribution implied by the exclusion principle of LGA. In the FHP model, two, three and four particle interactions can take place, and they conserve mass, momentum and kinetic energy. After the collision step, particles simply stream to the connected node, according to their velocity. An example of streaming step can be seen in Fig. (3.3). The concepts of collision and streaming steps will be inherited by the Lattice Boltzmann methods. It should be noted that collisions are fully local, and streaming consists only on a shift of particles. We can understand how the algorithm is computationally easy to handle and also inherently parallelizable.

In order to complete the description of LGA, we will now briefly show the mathematical formulation of the evolution of the FHP model, and how the macroscopic quantities are defined. For further information see [54, 16, 58, 55, 59].

The LGA evolution equation, assuming lattice spacing and time step as units, can be written as

$$n_i(\boldsymbol{x} + \boldsymbol{e_i}, t + 1) = n_i(\boldsymbol{x}, t) + C_i(\{n_\beta\}), \qquad i = \{1, 2. \ldots, 6\}, \qquad (3.2)$$

where n_i is the occupation number and C_i is the collision term, which is function of the state of the lattice node. Here we start to become familiar with a common practice in LGA and LBM literature, that is the use of lattice units. In this system of units, the time step δt is chosen as the time unit, while the lattice spacing δx is set as the space unit. We could say that the use of these units is justified by the symmetry of the lattice structure and by the collision-streaming interpretation of the LBM and LGA.

It is easy to recognize that C_i can assume only the values $\{-1, 0, 1\}$. Since the collision operator preserves mass, momentum and kinetic energy, the following equalities hold

$$\sum_i C_i = 0, \qquad (3.3a)$$

$$\sum_i \boldsymbol{e_i} C_i = 0, \qquad (3.3b)$$

$$\sum_i e_i^2 C_i = 0. \qquad (3.3c)$$

From the particle population n_i we can obtain the macroscopic density of mass and of momentum as follows,

$$\rho(\boldsymbol{x}, t) = m \sum_i n_i(\boldsymbol{x}, t), \qquad (3.4a)$$

$$\rho\boldsymbol{u}(\boldsymbol{x}, t) = m \sum_i \boldsymbol{e_i} n_i(\boldsymbol{x}, t), \qquad (3.4b)$$
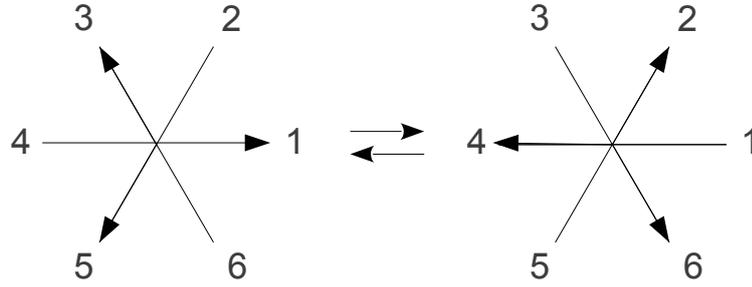
Figure 3.2. Example of three particle collision in FHP

(a) *Particle population at time t*   (b) *Particle population at time t + δt*
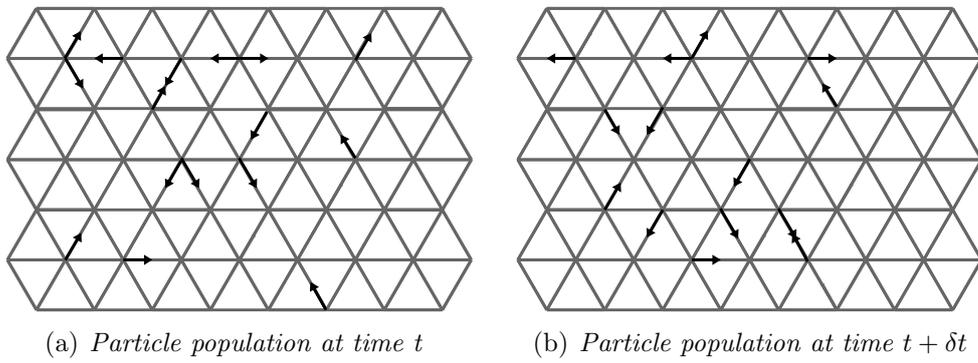
Figure 3.3. Streaming in FHP

where m is the mass of one particle. Actually, several random initial distribution are generated [54], and we can define a suitable ensemble averaged distribution function $f_i = \langle n_i \rangle$ that can be computed, and an evolution equation for this function can be obtained,

$$f_i(\boldsymbol{x} + \boldsymbol{e_i}, t + 1) = f_i(\boldsymbol{x}, t) + \Omega_i(f), \tag{3.5}$$

where $\Omega_i(f)$ is the collision operator for f_i. The hydrodynamic quantities can now be calculated from the f_i as:

$$\rho(\boldsymbol{x}, t) = \sum_i f_i(\boldsymbol{x}, t), \tag{3.6a}$$

$$\rho\boldsymbol{u}(\boldsymbol{x}, t) = \sum_i \boldsymbol{e_i} f_i(\boldsymbol{x}, t), \tag{3.6b}$$

The crucial step which lead to the establishment of the Lattice Boltzmann method was the substitution of $\Omega_i(f)$, with a BGK collision term [60].

From now on, the Lattice Boltzmann methods will be approached from a totally different point of view, but the basic ideas of the Lattice Gas will remain embedded in its structure.

3.2   The Boltzmann Equation

Assuming that molecules are particles obeying the laws of classical mechanics, the state of a system with N particles is defined by a $6N$-dimensional vector $\boldsymbol{z}$, which stores the position $\boldsymbol{x_i}$ and the velocity $\boldsymbol{\xi_i}$ of each particle. Thus, in this context, the phase space of a system is the $6N$-dimensional space composed by the $3N$ components of the N positions $\boldsymbol{x_i}$, and the $3N$ components of the N velocities $\boldsymbol{\xi_i}$. Particles evolve on time according to Newton's law, and consequently also the representative vector $\boldsymbol{z}$.

It is easy to recognize that the determination of the evolution of the vector $\boldsymbol{z}$ is practically impossible for a system with many particles, since the knowledge of all the positions and velocities is needed, and also every forces acting on a particle should be taken into account. For this reason, the aim of Statistical Mechanics is not to determine the evolution of $\boldsymbol{z}$, but to study the governing equation for the probability density function $P^{(N)}(\boldsymbol{z})$ in phase space, such that $P^{(N)}(\boldsymbol{z})\,d\boldsymbol{z}$ represents the probability of finding $\boldsymbol{z}$ between $\boldsymbol{z}$ and $\boldsymbol{z} + d\boldsymbol{z}$ [1]. As shown in [19], the equation satisfied by $P^{(N)}(\boldsymbol{z})$ is:

$$\frac{\partial P^{(N)}}{\partial t} + \nabla \cdot (P^{(N)}\boldsymbol{Z}) = 0, \tag{3.7}$$

where $\boldsymbol{Z}$ is a $6N$-dimensional vector, whose components are the $3N$ components of the N velocities $\boldsymbol{\xi_i}$ and the $3N$ components of the N forces acting on each particle $\boldsymbol{F_i}$. Eq. (3.7) is called the Liouville equation.

From the definition of the probability density function $P(\boldsymbol{z})$, the definition of the s-particle distribution function follows as:

$$P^{(s)} = \int P^{(N)} \prod_{i=s+1}^{N} d\boldsymbol{x_i}\,d\boldsymbol{\xi_i}, \tag{3.8}$$

with $s = \{1, 2, \ldots, N-1\}$. Thus, $P^{(s)}(\boldsymbol{x_1}, \boldsymbol{\xi_1}, \ldots, \boldsymbol{x_s}, \boldsymbol{\xi_s}) \prod_{i=1}^{s} d\boldsymbol{x_i}\,d\boldsymbol{\xi_i}$ represents the probability of finding s randomly chosen molecules with $\boldsymbol{x_1} \in [\boldsymbol{x_1}, \boldsymbol{x_1} + d\boldsymbol{x_1}], \boldsymbol{\xi_1} \in [\boldsymbol{\xi_1}, \boldsymbol{\xi_1} + d\boldsymbol{\xi_1}], \ldots, \boldsymbol{x_s} \in [\boldsymbol{x_s}, \boldsymbol{x_s} + d\boldsymbol{x_s}], \boldsymbol{\xi_s} \in [\boldsymbol{\xi_s}, \boldsymbol{\xi_s} + d\boldsymbol{\xi_s}]$. However, we are usually interested in computing the 1-particle distribution function, from which we are able to define the macroscopic quantities as we will show later on.

Let us consider a system of rigid sphere of diameter σ, with no external forces acting on the particles, in the hypothesis that particles can interact

---

[1]Please notice that the symbol $\boldsymbol{z}$ indicates both the random variable and "the value assumed by the random variable". A distinction has not been made in order to not burden the notation, but it should be kept in mind in what follows.

only with elastic collisions which satisfies

$$\boldsymbol{\xi_1} = \boldsymbol{\xi'_1} - \boldsymbol{n}[\boldsymbol{n} \cdot (\boldsymbol{\xi'_1} - \boldsymbol{\xi_2})], \quad (3.9a)$$

$$\boldsymbol{\xi_2} = \boldsymbol{\xi'_2} - \boldsymbol{n}[\boldsymbol{n} \cdot (\boldsymbol{\xi'_2} - \boldsymbol{\xi_1})], \quad (3.9b)$$

where $\boldsymbol{\xi'_1}$ and $\boldsymbol{\xi'_2}$ are the velocities before collision, while $\boldsymbol{\xi_1}$ and $\boldsymbol{\xi_2}$ those after collision, and $\boldsymbol{n}$ is the unit vector directed along the line joining the two centres. As proved in [19], for this system, starting from the Liouville equation Eq. (3.7), an equation for the s-particle distribution function $P^{(s)}$ can be obtained.

For the 1-particle distribution function the equation is:

$$\frac{\partial P^{(1)}}{\partial t} + \boldsymbol{\xi} \cdot \nabla_{\boldsymbol{x}} P^{(1)} = (N-1)\sigma^2 \int [P^{(2)'} - P^{(2)}] |(\boldsymbol{\xi} - \boldsymbol{\xi_*}) \cdot \boldsymbol{n}| \, d\boldsymbol{n} \, d\boldsymbol{\xi_*}, \quad (3.10)$$

where $d\boldsymbol{n}$ is the infinitesimal element of solid angle, $P^{(2)'} = P^{(2)}(\boldsymbol{x}, \boldsymbol{\xi'}, \boldsymbol{x_*}, \boldsymbol{\xi'_*}, t)$ and $P^{(2)} = P^{(2)}(\boldsymbol{x}, \boldsymbol{\xi}, \boldsymbol{x_*}, \boldsymbol{\xi_*}, t)$, with $\boldsymbol{\xi'}, \boldsymbol{\xi'_*}, \boldsymbol{\xi}$ and $\boldsymbol{\xi_*}$ satisfying Eqs. (3.9).

We can notice that in Eq. (3.10), the 2-particle distribution function $P^{(2)}$ is involved. This implies that in order to obtain $P^{(1)}$, we need $P^{(2)}$, but, in turn, the equation regarding $P^{(2)}$ involves the 3-particle distribution $P^{(3)}$, and so on. At the end, we would come back to the original Liouville equation.

To overcome this drawback, L. Boltzmann introduced the famous and controversial [61] "*stosszahlansatz*", i.e., the molecular chaos hypothesis [18, 20]. This consists on the assumption that no correlations exists between two particle. The following equation mathematically translates the previous statement:

$$P^{(2)}(\boldsymbol{x}, \boldsymbol{\xi}, \boldsymbol{x_*}, \boldsymbol{\xi_*}, t) = P^{(1)}(\boldsymbol{x}, \boldsymbol{\xi}, t) P^{(1)}(\boldsymbol{x_*}, \boldsymbol{\xi_*}, t). \quad (3.11)$$

Inserting Eq. (3.11) into Eq. (3.10), in the limit of high N, we finally obtain the Boltzmann equation:

$$\frac{\partial P}{\partial t} + \boldsymbol{\xi} \cdot \nabla_{\boldsymbol{x}} P + \boldsymbol{a} \cdot \nabla_{\boldsymbol{\xi}} P = (N\sigma^2) \int (PP'_* - PP_*) |(\boldsymbol{\xi} - \boldsymbol{\xi_*}) \cdot \boldsymbol{n}| \, d\boldsymbol{n} \, d\xi_*, \quad (3.12)$$

where, for the sake of simplicity, we have substituted $P^{(1)}$, with P, and we have taken into account the presence of an external force per unit of particle mass $\boldsymbol{a}$.

However, usually the Boltzmann equation is introduced in a different form, in which the unknown function is the mass distribution function f related to P, by this simple relationship:

$$f = NmP = MP, \quad (3.13)$$

where m is the particle's mass and M is the total mass of the system. From the normalization condition on P, it follows that:

$$\int f \, d\boldsymbol{x} \, d\boldsymbol{\xi} = M. \tag{3.14}$$

It is straightforward to derive the Boltzmann equation involving f:

$$\frac{\partial f}{\partial t} + \boldsymbol{\xi} \cdot \nabla_{\boldsymbol{x}} f + \boldsymbol{a} \cdot \nabla_{\boldsymbol{\xi}} f = \frac{\sigma^2}{m} \int (ff'_* - ff_*)|(\boldsymbol{\xi} - \boldsymbol{\xi}_*) \cdot \boldsymbol{n}| \, d\boldsymbol{n} \, d\xi_*. \tag{3.15}$$

From now on, we will refer to Eq (3.15) as the Boltzmann equation and the integral on the right side will be called the collision term or collision integral. In order to unburden the notation, the collision term is often replaced by the symbol $Q(f, f)$.

3.3 Collision invariants and equilibrium distribution

The collision integral of Eq. 3.15 satisfies simple properties, which have a clear physical meaning and also an important role in the path to derive the macroscopic equations. Let us define a "collision invariant" a function $\varphi(\boldsymbol{\xi})$ that satisfies the following equation:

$$\int Q(f, f)\varphi(\boldsymbol{\xi}) \, d\boldsymbol{\xi} = 0. \tag{3.16}$$

It is shown in [19, 62], that for all the functions $\varphi(\boldsymbol{\xi})$ which satisfy Eq. (3.16), the equality

$$\varphi(\boldsymbol{\xi}) + \varphi(\boldsymbol{\xi}_*) = \varphi(\boldsymbol{\xi}') + \varphi(\boldsymbol{\xi}'_*) \tag{3.17}$$

holds. Hence, the interpretation of Eq. (3.17) is clear: collision invariants are all the functions $\varphi(\boldsymbol{\xi})$ preserved during an elastic collision.

It can be proved, that the general form of a collision invariant is a linear combination of the physical quantities conserved by an elastic collision, i.e., mass, momentum and kinetic energy [19, 62]:

$$\varphi(\boldsymbol{\xi}) = a + \boldsymbol{b} \cdot \boldsymbol{\xi} + c\,\xi^2, \tag{3.18}$$

where a and c are constants and $\boldsymbol{b}$ is a constant vector. Thus, the functions $\varphi_0 = 1, (\varphi_1, \varphi_2, \varphi_3) = \boldsymbol{\xi}, \varphi_4 = \xi^2$ are linearly independent, and represent a basis for the space of the collision invariants $\varphi(\boldsymbol{\xi})$.

Let us now consider a system without external forces, with particles interacting only by means of elastic collisions and in which the time derivative

$\partial f / \partial t$ is equal to zero, and in addition the system is spatially homogeneous, i.e., $\nabla_{\boldsymbol{x}} f = 0$. Carefully, we say that this condition represents "equilibrium state". For a more detailed discussion on the intrinsic meaning of equilibrium in Statistical Mechanics and the analysis of the necessary conditions for equilibrium to be reached, see [19]. With these assumptions the Boltzmann equation Eq. (3.15) becomes:

$$Q(f, f) = 0. \tag{3.19}$$

As explained in [19, 62], a necessary and sufficient condition to satisfy Eq. (3.19) is

$$f' f'_* = f f_*, \tag{3.20}$$

and considering the logarithms:

$$\ln f' + \ln f'_* = \ln f + ln f_*. \tag{3.21}$$

Hence, in this condition, the logarithm of f fits the definition of collision invariant. Using Eq. (3.18), we obtain that in an equilibrium state:

$$f^{eq}(\boldsymbol{\xi}) = \exp(a + \boldsymbol{b} \cdot \boldsymbol{\xi} + c \, \xi^2), \tag{3.22}$$

which is known as a "Maxwellian" distribution.

3.4 From mesoscopic to macroscopic description

The macroscopic quantities typical of fluid dynamics can be defined as proper averages of the 1-particle distribution function P [19]. From Sec. 3.2, we know that $P(\boldsymbol{x}, \boldsymbol{\xi}, t) \, d\boldsymbol{x} \, d\boldsymbol{\xi}$ represents the probability of finding a particle with position and velocity, respectively, in infinitesimal neighbourhoods of $\boldsymbol{x}$ and $\boldsymbol{\xi}$. Hence, if we call $P_{\boldsymbol{x}}$ the spatial probability density function, such that $P_{\boldsymbol{x}}(\boldsymbol{x}, t) \, d\boldsymbol{x}$ is the probability of finding a particle whose position lies in an infinitesimal neighbourhood of $\boldsymbol{x}$, whatever its velocity is, by means of basic statistical notions [63], it is clear that

$$P_{\boldsymbol{x}} = \int P \, d\boldsymbol{\xi} \tag{3.23}$$

Therefore, using Eq. (3.13) the infinitesimal expected mass $d \, M(\boldsymbol{x}, t)$ is given by:

$$d \, M = N m \, P_{\boldsymbol{x}} \, d\boldsymbol{x} = d\boldsymbol{x} \int f \, d\boldsymbol{\xi}. \tag{3.24}$$

Thus, the definition of density $\rho(\boldsymbol{x}, t)$ from the statistical point of view is:

$$\rho(\boldsymbol{x}, t) = \int f \, d\boldsymbol{\xi}. \tag{3.25}$$

For the sake of simplicity, from now on we will omit the arguments of the functions. From similar considerations, we can also derive the expression for momentum density, that is:

$$\rho \boldsymbol{u} = \int \boldsymbol{\xi} f \, d\boldsymbol{\xi} \tag{3.26}$$

As we will show in the next lines, it is useful to decompose the molecular velocity ξ as:

$$\boldsymbol{\xi} = \boldsymbol{u} + \boldsymbol{c}, \tag{3.27}$$

where $\boldsymbol{c}$ represents the deviation from the macroscopic velocity $\boldsymbol{u}$.

Let us now introduce the flux $P_{\alpha\beta}$ of the β-th component of the momentum vector over the surface whose normal is directed along the x_α-axis; its expression is:

$$P_{\alpha\beta} = \int \xi_\alpha (\xi_\beta f) \, d\boldsymbol{\xi} \tag{3.28}$$

Accordingly, the momentum flux tensor $\bar{\bar{\boldsymbol{P}}}$, whose components are all the possible momentum fluxes, is a symmetric tensor of second-rank. Using the decomposition of ξ, Eq. (3.27), we obtain:

$$P_{\alpha\beta} = \rho u_\alpha u_\beta + \int c_\alpha c_\beta f \, d\boldsymbol{\xi} \tag{3.29}$$

By the analysis of Eq. (3.29), we see that the momentum flux tensor is split into two parts, i.e., the macroscopic momentum flux tensor, which appears in the derivation of the Navier-Stokes equations [44, 45], and another contribution due to the fluctuating velocity component. This term is actually what in the macroscopic description we call the "stress tensor", and accordingly, we recognize that the momentum flux associated to the random molecular velocity is the cause of the surface forces. Hence, we define

$$\sigma_{\alpha\beta} = \int c_\alpha c_\beta f \, d\boldsymbol{\xi} \tag{3.30}$$

as the stress in the x_β-direction acting on a surface normal to the x_α direction. From the previous considerations, we understand also why the stress tensor $\bar{\bar{\boldsymbol{\sigma}}}$ proves to be symmetric [44], since from Eq. (3.30) immediately follows that $\sigma_{\alpha\beta} = \sigma_{\beta\alpha}$.

Applying the same procedure for the energy density E we obtain

$$E = \frac{1}{2} \int \xi^2 f \, d\boldsymbol{\xi} = \frac{1}{2}\rho u^2 + \frac{1}{2} \int c_\alpha c_\alpha f \, d\boldsymbol{\xi} = \frac{1}{2}\rho u^2 + \frac{1}{2}\sigma_{\alpha\alpha}, \qquad (3.31)$$

where we have used the Einstein notation, in which if an index appears twice in a single term, summation of that term over all the possible values of the index is implied. From now on, we will use widely the Einstein notation because of its simplicity and to align ourselves with literature. Again, we see that energy is divided in two components: the macroscopic kinetic energy and a term due to velocity fluctuations. The second term represents what we usually call the "internal energy", and hence, we define its density ρe as:

$$\rho e = \frac{1}{2} \int c_\alpha c_\alpha f \, d\boldsymbol{\xi}. \qquad (3.32)$$

Since the pressure is defined as the isotropic part of the stress tensor $P = \sigma_{\alpha\alpha}/3$, we have:

$$P = \frac{2}{3}\rho e \qquad (3.33)$$

which represents the state equation of the gas. As pointed out in [19], from Eq. (3.33) we recognize that the ratio P/ρ remains constant if e is fixed. It is easy to connect this result to the ideal gas law:

$$P = \rho R T, \qquad (3.34)$$

where T is the absolute temperature and $R = k_b/m$ is the ideal gas constant, with k_b the Boltzmann's constant and m the mass of one molecule. The insertion of Eq. (3.34) into Eq. (3.33) gives

$$e = \frac{3}{2}RT. \qquad (3.35)$$

Finally, for the energy flux over a surface normal to the x_α-axis, Q_α we have:

$$Q_\alpha = \frac{1}{2} \int \xi_\alpha \xi^2 f \, d\boldsymbol{\xi} = u_\alpha(\frac{1}{2}\rho u^2 + e) + u_\beta \sigma_{\alpha\beta} + \frac{1}{2}q_\alpha, \qquad (3.36)$$

where:

- $u_\alpha(\frac{1}{2}\rho u^2 + e)$ is the macroscopic flow of kinetic and internal energy;

- $u_\beta \sigma_{\alpha\beta}$ is the work done by the stresses per unit of time;

- $q_\alpha = \int c_\alpha c_\beta c_\beta f \, d\boldsymbol{\xi}$ represents the heat flux.

The macroscopic conservation equations can be obtained recalling the concept of collision invariant introduced in Sec. (3.16). In fact, by multiplying the Boltzmann equation, Eq. (3.15), by the five elementary collision invariants φ_i with $i = 0, 1, \ldots, 4$, integrating over $d\boldsymbol{\xi}$ and taking into account Eq. (3.16), we have:

$$\frac{\partial}{\partial t} \int \varphi_i f \, d\boldsymbol{\xi} + \frac{\partial}{\partial x_\beta} \int \xi_\beta \varphi_i f \, d\boldsymbol{\xi} + F_\beta \int \varphi_i \frac{\partial f}{\partial \xi_\beta} \, d\boldsymbol{\xi} = 0, \qquad (3.37)$$

where we have assumed that F_α does not depend on velocities. Using Eqs. (3.25), (3.26), (3.29), (3.30), (3.32) and (3.36), and inserting successively the elementary collision invariants φ_i, we obtain the macroscopic conservation equations [19]:

$$\frac{\partial \rho}{\partial t} + \frac{\partial}{\partial x_\beta}(\rho u_\beta) = 0 \qquad (3.38a)$$

$$\frac{\partial}{\partial t}(\rho u_\alpha) + \frac{\partial}{\partial x_\beta}(\rho u_\beta u_\alpha + \sigma_{\alpha\beta}) = \rho a_\alpha, \quad \alpha = 1, 2, 3 \qquad (3.38b)$$

$$\frac{\partial}{\partial t}[\rho(\frac{1}{2}u^2 + e)] + \frac{\partial}{\partial x_\beta}[\rho u_\beta(\frac{1}{2}u^2 + e) + \sigma_{(\beta\alpha)}u_\alpha + q_\beta] = \rho a_\beta u_\beta. \qquad (3.38c)$$

These equations are affected by the well-known problem that the number of variables, that in this case are ρ, e, the three components of the vector $\boldsymbol{u}$, the three components of the vector $\boldsymbol{q}$ and the six components of the tensor $\bar{\bar{\boldsymbol{\sigma}}}$, for a total of 14, is greater than the number of equations, which are 6, considering also the state equation Eq. (3.33). Hence, if we consider only Eqs. (3.38) and Eq. (3.33), we need to add other equations that relate $\bar{\bar{\boldsymbol{\sigma}}}$ and $\boldsymbol{q}$ to ρ, e and $\boldsymbol{u}$. An example is given by the hypothesis of Newtonian fluid [44, 45] and Fourier's law [64].

However, from the point of view of Statistical Mechanics this modelling is not needed. In fact, all the information are stored in the distribution function f which satisfies the Boltzmann equation Eq. (3.15). The modelling of the Boltzmann equation lies in the approximation of particle-particle interaction via elastic collision. If we considered long range interactions, the function f would obey to a different form of the Boltzmann equation [19]. Once the Boltzmann equation is solved, we can compute all the macroscopic quantities, but solving the Boltzmann equation is definitely not an easy task, since it is a non-linear integro-differential equation.

Finally, it should be noted that applying Eqs. (3.25), (3.26) and (3.32) to the definition of the Maxwellian distribution function given in Sec. (3.3) we obtain:

$$f^{eq} = \frac{\rho}{(2\pi\theta)^{\frac{D}{2}}} \exp\left[-\frac{(\boldsymbol{\xi} - \boldsymbol{u})^2}{2\theta}\right], \qquad (3.39)$$

where, for the sake of generality, we have made the space dimension D explicit, and introduced $\theta = k_b T/m$, that can be interpreted as the "thermal energy" per unit of mass and its squared root as a characteristic molecular velocity. If we analyse Eq. (3.39), we recognize that the equilibrium distribution function, and hence, the equilibrium state, is univocally determined by ρ, $\boldsymbol{u}$ and e. Furthermore, the following fundamental equalities holds:

$$\rho \;=\; \int f^{eq}\, d\boldsymbol{\xi}, \tag{3.40a}$$

$$\rho \boldsymbol{u} \;=\; \int \boldsymbol{\xi} f^{eq}\, d\boldsymbol{\xi}, \tag{3.40b}$$

$$\rho e \;=\; \frac{1}{2}\int c_\alpha c_\alpha f^{eq}\, d\boldsymbol{\xi}. \tag{3.40c}$$

3.5 The dimensionless Boltzmann equation: the Knudsen number

In order to understand the relative order of magnitude of different terms in a physical partial differential equation, it is very useful to analyse the dimensionless form of the equation. The non-dimensionalization of the Boltzmann equation [65] is very similar to that of the Navier-Stokes equations [44, 45], in which the Reynolds number stands out as the governing parameter.

Let us consider a typical length scale L_0, a typical density ρ_0 and a typical temperature T_0, which defines also a thermal energy per unit of mass θ_0. From these reference quantities, we can also define a characteristic molecular velocity $\xi_0 = \sqrt{\theta_0}$ and a characteristic time scale $t_0 = L_0/\xi_0$. Thus, we introduce the dimensionless variables, that we denote with the circumflex:

$$\hat{\boldsymbol{x}} = \frac{1}{L_0}\boldsymbol{x}, \quad \hat{t} = \frac{\xi_0}{L_0}t \quad \hat{\boldsymbol{\xi}} = \frac{1}{\xi_0}\boldsymbol{\xi} \quad \hat{\boldsymbol{F}} = \frac{L_0}{\xi_0^2}\boldsymbol{F}, \quad \hat{f} = \frac{\xi_0^3}{\rho_0}f. \tag{3.41}$$

The insertion of Eqs. (3.41) in the Boltzmann equation Eq. (3.15) the dimensionless Boltzmann equation gives:

$$\frac{\partial \hat{f}}{\partial \hat{t}} + \hat{\boldsymbol{\xi}}\cdot\nabla_{\hat{\boldsymbol{x}}}\hat{f} + \hat{\boldsymbol{F}}\cdot\nabla_{\hat{\boldsymbol{\xi}}}\hat{f} = \frac{1}{Kn}\hat{Q}(\hat{f},\hat{f}), \tag{3.42}$$

where

$$\hat{Q}(\hat{f},\hat{f}) = \int (\hat{f}'\hat{f}'_* - \hat{f}\hat{f}_*)|(\hat{\boldsymbol{\xi}} - \hat{\boldsymbol{\xi}}_*)\cdot\boldsymbol{n}|\, d\boldsymbol{n}\, d\hat{\boldsymbol{\xi}}_*, \tag{3.43}$$

and the dimensionless number Kn, known as the Knudsen number, is given by:

$$Kn = \frac{m}{L_0\rho_0\sigma^2} = \frac{\Lambda}{\mathsf{L}_0}, \tag{3.44}$$

where Λ can be considered the mean free path of a particle. Thus, we can distinguish between two limiting cases, i.e. $Kn \to \infty$ and $Kn \to 0$. The case of high Knudsen number corresponds to a rarefied gas and, by means of intuition, we can understand how the description in terms of macroscopic quantity is not sufficient to describe the gas conveniently. On the other hand, when $Kn \to 0$, the system is completely described by ρ, $\boldsymbol{u}$ and e. In fact, when Eq. (3.42) turns into Eq. (3.19), we are allowed to say that in every point of the system we have a Maxwellian distribution function, univocally defined by the above-mentioned macroscopic quantities. It should be noted that this does not mean that the system is completely uniform, without gradients, because Eq. (3.19) does not imply that f does not vary on time and space. However, in this condition the system evolution is totally determined by the gradients of ρ, $\boldsymbol{u}$ and e .

Thus, we know the solution of the Boltzmann equation for a particular value of the Knudsen. The basic idea of perturbative theory [66, 67] is to expand the unknown function around the exact solution of a related problem, as a power series of a small small parameter, which quantifies the deviation from the known solution. The Chapman-Enskog expansion [20] is a particular multi-scale method, which applied to the Boltzmann equation gives the conservation equations and in addition allows to render explicit an expression for the transport coefficient. We will not perform the Chapman-Enskog expansion for the Boltzmann equation, but we will apply it for the Lattice Boltzmann equation.

3.6   The BGK approximation

It is clear that the main obstacle in the solution of the Boltzmann equation is the complicated form of the collision integral. For this reason, alternative collision operators $J(f)$ have been proposed to substitute the collision term with a simpler one. The basic idea behind these models is that a collision model must satisfy two fundamental properties to recover the same behaviour of the collision integral [19]:

1. the collision invariants must remain the same.

2. the collision term $J(f)$ must satisfy

$$\int log f \, J(f) \, d\boldsymbol{\xi} \leq 0, \qquad (3.45)$$

   where equality holds only if f is a Maxwellian.

The first requirement is needed to guarantee the same macroscopic equations, Eqs. (3.38), while the second one expresses the tendency to a Maxwellian.

The simplest and most widely used collision model is certainly the BGK operator [57], whose idea is that the effect of collision is proportional to the deviation from the Maxwellian. Thus, the form of the BGK collision term is:

$$J(f) = \frac{f^{eq} - f}{\lambda},$$ (3.46)

where λ is a relaxation time. Obviously, in each point of the system a Maxwellian distribution function is defined by ρ, $\boldsymbol{u}$ and e, univocally determined by f. From now on, we will consider the BGK Boltzmann equation to deduce the Lattice Boltzmann equation.

3.7 From BE to LBE

As we know from Sec. 3.1, historically the Lattice Boltzmann method has arisen from the ashes of the Lattice Gas model, in order to overcome its limits. However, it has been shown [6, 7, 59], that the Lattice Boltzmann equation can be rigorously viewed as a special discretization of the Boltzmann equation. In this framework, the LBE gains a new independent interpretation, apart from the concept of LGA.

The procedure that yields the LBE, starting from the BE, requires three basic steps:

1. resolution of the BE as an Ordinary Differential Equation (ODE) in the time variable and time discretization via Taylor expansion.

2. low Mach number expansion of the equilibrium distribution function.

3. discretization of the velocity space $\boldsymbol{\xi}$ by means of Gauss-Hermite quadrature and consequent discretization of the position space $\boldsymbol{x}$.

At the end of this procedure, the lattice structure will directly induced by the finite set of velocities $\{\boldsymbol{\xi_i}\}$ obtained in the third step. Moreover, we will be able to detect the different sources of error during the derivation.

In the following subsections, for the sake of simplicity, we will carry out these three steps for the Boltzmann equation with a BGK collision term and in absence of external forces, referring to [6, 7, 59]. The inclusion of the force term in the Lattice Boltzmann equation will be analysed later on in Chap. 4. Hence, our starting point is:

$$\frac{\partial f}{\partial t} + \boldsymbol{\xi} \cdot \nabla_{\boldsymbol{x}} f = \frac{f^{eq} - f}{\lambda}.$$ (3.47)

3.7.1 BE as an ODE

Let us suppose to follow the trajectory of a particle over time. From this point of view, the position of the particle $\boldsymbol{x}$ is obviously function of time $\boldsymbol{x} = \boldsymbol{x}(t)$. Thus, if we restrict the Boltzmann BGK equation Eq. (3.47) along this path, the mass distribution f becomes function of time only $f = f(\boldsymbol{x}(t), \boldsymbol{\xi}, t)$, and by means of the chain rule for computing the derivative of composite functions, we can rewrite Eq. (3.47) as

$$\frac{df}{dt} + \frac{1}{\lambda} f = \frac{1}{\lambda} f^{eq}, \tag{3.48}$$

where df/dt represents the total derivative of f respect to time t. By means of simple knowledge of Ordinary Differential Equation [68], we recognize that Eq. (3.48) is a linear non-homogeneous ODE of first order with constant coefficient $1/\lambda$, and its integration over a time step δt gives:

$$f(t + \delta t) = f(\boldsymbol{x} + \boldsymbol{\xi}\delta t, \boldsymbol{\xi}, t + \delta t) = e^{-\delta t/\lambda} f(\boldsymbol{x}, \boldsymbol{\xi}, t)$$
$$+ \frac{1}{\lambda} e^{-\delta t/\lambda} \int_0^{\delta t} e^{\delta t'/\lambda} f^{eq}(\boldsymbol{x} + \boldsymbol{\xi}t', \boldsymbol{\xi}, t + t') \, dt'. \tag{3.49}$$

The next step is to write the Taylor expansion up to first order in δt, around $\delta t = 0$ for:

$$e^{-\delta t/\lambda} = 1 - \frac{1}{\lambda} \delta t + \mathcal{O}(\delta t^2), \tag{3.50a}$$

$$\frac{1}{\lambda} e^{-\delta t/\lambda} \int_0^{\delta t} e^{\delta t'/\lambda} f^{eq}(\boldsymbol{x} + \boldsymbol{\xi}t', \boldsymbol{\xi}, t + t') \, dt' =$$
$$\frac{1}{\lambda} f^{eq}(\boldsymbol{x}\boldsymbol{\xi}, t) \delta t + \mathcal{O}(\delta t^2). \tag{3.50b}$$

The insertion of Eqs. (3.50) into Eq. (3.49) gives:

$$f(\boldsymbol{x} + \boldsymbol{\xi}\delta t, \boldsymbol{\xi}, t + \delta t) - f(\boldsymbol{x}, \boldsymbol{\xi}, t) = -\frac{1}{\tau}(f(\boldsymbol{x}, \boldsymbol{\xi}, t) - f^{eq}(\boldsymbol{x}, \boldsymbol{\xi}, t)) + \mathcal{O}(\delta t^2), \tag{3.51}$$

where $\tau = \lambda/\delta t$. We notice that we have already introduced a source of error, i.e., the discretization of time.

3.7.2 Low Mach number expansion of the equilibrium distribution

Let us recall the form of the Maxwellian equilibrium distribution function defined in Sec. 3.4:

$$f^{eq} = \frac{\rho}{(2\pi\theta)^{\frac{D}{2}}} \exp\left[-\frac{(\boldsymbol{\xi} - \boldsymbol{u})^2}{2\theta}\right].$$

This equation can be viewed as

$$f^{eq} = \frac{\rho}{(2\pi\theta)^{\frac{D}{2}}} \exp\left[-\frac{\boldsymbol{\xi}^2}{2\theta}\right] exp\left[-\frac{\boldsymbol{u}^2}{2\theta} + \frac{\boldsymbol{\xi}\cdot\boldsymbol{u}}{\theta}\right], \tag{3.52}$$

and it is expanded in the parameter $u/\sqrt{\theta}$, using the Taylor formula up to second order around $u/\sqrt{\theta} = 0$. This is a low Mach number expansion, indeed. In fact, since the speed of sound for an ideal gas, assuming an isentropic process, is given by $c_s = (\partial P/\partial\rho)_s = \sqrt{\gamma R T}$ [44], with γ the ratio between isobaric and isochoric specific heats, the Mach number, i.e., the ratio between the macroscopic velocity and the speed of sound, is proportional to $u/\sqrt{\theta}$. Moreover in what follows, we will consider isothermal processes, and thus, the speed of sound c_s is rigorously equal to $\sqrt{\theta}$. We will better analyse the issue of the sound speed in LBM, after the derivation of the Lattice Boltzmann equation.

Hence, the expansion of Eq (3.52) gives:

$$f^{eq} = \frac{\rho}{(2\pi\theta)^{\frac{D}{2}}} \exp\left[-\frac{\boldsymbol{\xi}^2}{2\theta}\right]\left[1 + \frac{\boldsymbol{\xi}\cdot\boldsymbol{u}}{\theta} + \frac{(\boldsymbol{\xi}\cdot\boldsymbol{u})^2}{2\theta^2} - \frac{\boldsymbol{u}^2}{2\theta}\right] + \mathcal{O}(Ma^3). \tag{3.53}$$

As pointed out in [59], many shortcomings of the Lattice Boltzmann methods are related to this expansion. In fact, according to [69], and references therein, instability is often attributed to this polynomial expansion and it can also cause the equilibrium distribution function to be negative. Nevertheless, as we will see, it is necessary for the discretization of the velocity space.

3.7.3 Discretization of the velocity space

We now come to the crucial passage in the derivation of the Lattice Boltzmann equation, that is the discretization of the velocity space and, accordingly, of the coordinate space as well. In order to understand this key step, we have to keep in mind how the macroscopic conservation equations Eqs. (3.38) were obtained from the Boltzmann equation. In practice, the Boltzmann equation was multiplied by each elementary collision invariants introduced in Sec. 3.3 and integrated over the velocity space. Then, we have exploited the definition of collision invariant Eq. (3.16) and macroscopic quantities Eqs. (3.25), (3.26), (3.29), (3.30), (3.32) and (3.36).

Before introducing the basic idea behind the discretzation of velocity space, let us define a moment of order k of the mass distribution function f as:

$$I_k = \int \xi_x^n \xi_y^m f \, d\boldsymbol{\xi}, \tag{3.54}$$

where $k = n + m$, and for the sake of simplicity we have considered the two-dimensional case. We will also consider moments of the mass distribution function, linear combinations of I_k, i.e., also the polynomial in $\boldsymbol{\xi}$. It is straightforward that the macroscopic quantities are moments of f. The discretization of velocity space consists in the computation of the moments of f, by means of a suitable weighted sum over a finite set of $\{f(\boldsymbol{x}, \boldsymbol{\xi}_i, t)\}$, related to peculiar velocities $\{\boldsymbol{\xi}_i\}$, where $i = 0, 1, \ldots, n-1$, with n, the number of velocities of the model. Hence, after the discretization, the moments of the distribution function will be computed as:

$$I_k = \sum_{i=0}^{n-1} W_i \xi_{ix}^n \xi_{iy}^m f(\boldsymbol{x}, \boldsymbol{\xi}_i, t), \tag{3.55}$$

where W_i is the relative weight. Consequently, also the macroscopic quantities such as ρ, $\rho\boldsymbol{u}$, ρe, etc. will be obtained according to Eq. (3.55):

$$\rho = \sum_{i=0}^{n-1} W_i f(\boldsymbol{x}, \boldsymbol{\xi}_i, t), \tag{3.56a}$$

$$\rho\boldsymbol{u} = \sum_{i=0}^{n-1} W_i \boldsymbol{\xi} f(\boldsymbol{x}, \boldsymbol{\xi}_i, t), \tag{3.56b}$$

$$\rho e = \sum_{i=0}^{n-1} W_i c_\alpha c_\alpha f(\boldsymbol{x}, \boldsymbol{\xi}_i, t). \tag{3.56c}$$

The idea is to obtain the conservation equations Eqs. (3.38) by sum over the discrete set of velocity Eq. (3.51), and not by integration. In particular (see Chap. 4), in Eq. (3.51) the left side represents the approximation of the term $\partial f/\partial t + \boldsymbol{\xi} \cdot \nabla_{\boldsymbol{x}} f$, while the right side is the approximation of the BGK collision term.

In Eq. (3.55), we have only introduced a general weighted sum, but we have not specified neither the discrete velocities $\{\boldsymbol{\xi_i}\}$, nor the weights W_i, thus far. However, in order to obtain the macroscopic equation, it is necessary that the elementary collision invariants of the collision term in Eq. (3.49) do not change. Thus, considering Eqs. (3.56), this means:

$$\rho = \sum_{i=0}^{n-1} W_i f(\boldsymbol{x}, \boldsymbol{\xi}_i, t)^{eq}, \tag{3.57a}$$

$$\rho\boldsymbol{u} = \sum_{i=0}^{n-1} W_i \boldsymbol{\xi} f(\boldsymbol{x}, \boldsymbol{\xi}_i, t)^{eq}, \tag{3.57b}$$

$$\rho e = \sum_{i=0}^{n-1} W_i c_\alpha c_\alpha f(\boldsymbol{x}, \boldsymbol{\xi}_i, t)^{eq}. \tag{3.57c}$$

Eqs. (3.57) implies that we need an appropriate quadrature scheme to approximate the moment of the equilibrium distribution function up to second order. Actually, in this way we would obtain the conservation equation, but the microscopic dynamics would not be sufficient to recover the Navier-Stokes equations with the hypothesis of Newtonian fluid, in the limit of low Knudsen number. In practice, the relationship between the stress tensor and the velocity would not be the correct one, and, in general, it is never fully correct, since we would need to compute exactly the moments of any order, and consequently come back to the Boltzmann equation. Anyway, as we will show in Chap. 4 via the Chapman-Enskog expansion, in order to recover the isothermal Navier-Stokes equations in the limit of low Knudsen number and low Mach number, we need to preserve the moments of f^{eq} up to third order. We have already approximated f^{eq} in Eq. (3.53) with a low Mach number expansion, and so, we want to compute by quadrature the moments up to third order of the approximated f^{eq} [2]:

$$I_k^{eq} = \int e^{-\boldsymbol{\xi}^2/2\theta} \psi_{k+2}(\boldsymbol{\xi}) \, d\boldsymbol{\xi} = \sum_{i=0}^{n-1} W_i e^{-\boldsymbol{\xi}_i^2/2\theta} \psi_{k+2}(\boldsymbol{\xi_i}), \quad 0 \le k \le 3 \quad (3.58)$$

where $\psi_{k+2}(\boldsymbol{\xi})$ is a polynomial of degree $k + 2$, since we have to take into account the polynomial of degree 2 in $\boldsymbol{\xi}$ of the approximated f^{eq}.

Let us consider the integral of Eq. (3.58) for a generic monomial in $\boldsymbol{\xi}$ of degree at most 5:

$$I_{m+n}^{eq} = \int_{-\infty}^{+\infty} \left(\int_{-\infty}^{+\infty} \exp\left[-\frac{\xi_x^2 + \xi_y^2}{2\theta} \right] \xi_x^m \xi_y^n \, d\xi_x \right) d\xi_y,$$
$$0 \le m + n \le 5. \quad (3.59)$$

Operating the change of variable $\zeta_{x,y}^2 = \xi_{x,y}^2/2\theta$ we have:

$$I_{m+n}^{eq} = (\sqrt{2\theta})^{(m+n+2)} \bar{I}_m \bar{I}_n, \quad (3.60)$$

where in general

$$\bar{I}_\gamma = \int_{-\infty}^{+\infty} e^{-\zeta^2} \zeta^\gamma \, d\zeta. \quad (3.61)$$

The most appropriate quadrature formula for computing $\bar{I}_\gamma$ is definitely the Gauss-Hermite quadrature (see Appendix A.1). In fact, by considering $k = 3$ nodes of integration, Gauss-Hermite formula evaluates exactly integrals of the

---

[2]It is clear that using the approximated f^{eq}, the moments of the correct Maxwellian will be approximated as well.

form of Eq. (3.61) up to $\gamma = 2n - 1 = 5$ [70]. As a matter of fact, the low Mach number expansion of f^{eq} has been specifically conceived to exploit this quadrature. Therefore, we are allowed to write:

$$\bar{I}_\gamma = \sum_{j=1}^{3} \omega_j \zeta_j^\gamma, \tag{3.62}$$

and the abscissas and the weights of the quadrature are:

$$\zeta_1 = -\sqrt{3/2}, \qquad \zeta_2 = 0, \qquad \zeta_3 = \sqrt{3/2}; \tag{3.63a}$$
$$\omega_1 = \sqrt{\pi}/6, \qquad \omega_2 = 2\sqrt{\pi}/3, \qquad \omega_3 = \sqrt{\pi}/6. \tag{3.63b}$$

Considering Eq. (3.62), Eq. (3.60) we have:

$$I_{m+n}^{eq} = \left(\sum_{j=1}^{3} \omega_j \zeta_j^m \sum_{k=1}^{3} \omega_k \zeta_k^n \right) = 2\theta \left(\sum_{j=1}^{3} \omega_j \xi_j^m \sum_{k=1}^{3} \omega_k \xi_k^n \right). \tag{3.64}$$

After some simple algebra, we finally obtain:

$$I_{m+n}^{eq} = 2\theta [\omega_2^2 \xi_1^m \xi_2^n + \omega_1 \omega_2 (\xi_1^m \xi_2^n + \xi_2^m \xi_1^n + \xi_2^m \xi_3^n + \xi_3^m \xi_2^n)$$
$$+ \omega_1^2 (\xi_1^m \xi_1^n + \xi_1^m \xi_3^n + \xi_3^m \xi_1^n + \xi_3^m \xi_3^n)]. \tag{3.65}$$

Eq. (3.65) induces the following nine velocities:

$$\boldsymbol{\xi_i} = \begin{cases} (\xi_2, \xi_2) \\ (\xi_{1,2}, \xi_{1,2}) \\ (\xi_{1,3}, \xi_{1,3}) \end{cases} = \begin{cases} (0, 0), & i = 0 \\ [(\pm 1, 0)\sqrt{3\theta}, (0, \pm 1)\sqrt{3\theta}] & i = 1, 2, 3, 4, \\ [(\pm 1, \pm 1)\sqrt{3\theta}] & i = 5, 6, 7, 8, \end{cases} \tag{3.66}$$

At this point, we introduce the discretization of the coordinate space $\boldsymbol{x}$, according to the discretization of velocity space and time, setting the space travelled by one particle in a time step δt equal to $\sqrt{3\theta}$:

$$c = \frac{\delta x}{\delta t} = \sqrt{3\theta}. \tag{3.67}$$

Consequently we can write Eq. (3.66) as:

$$\boldsymbol{\xi_i} = \begin{cases} (0, 0), & i = 0 \\ [(\pm 1, 0)c, (0, \pm 1)c] & i = 1, 2, 3, 4, \\ [(\pm 1, \pm 1)c] & i = 5, 6, 7, 8, \end{cases} \tag{3.68}$$

This space discretization generates the lattice called D2Q9 showed in Fig. 3.4 and hence, we understand how the lattice structure is a direct consequence
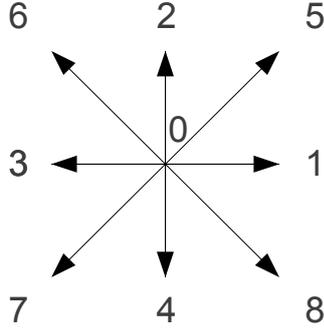
Figure 3.4. D2Q9 lattice structure

of the quadrature formula we have chosen and the constraint imposed by the preservation of the moments up to third order. Via a similar procedure other appropriate lattices can be derived such as the D3Q27 in three dimensions. Moreover, it should be noted that, according to this space discretization, the speed of sound of the model c_s, which as already mentioned in Subsec. 3.53 is equal to $\sqrt{\theta}$, is related to c by:

$$c_s = \frac{c}{\sqrt{3}} = \frac{1}{\sqrt{3}}\frac{\delta x}{\delta t}. \tag{3.69}$$

Actually, it is common practice in literature to assume the space step δx and the time step δt to be unity. In this case we will talk of "lattice units" and obviously in this system of unit $c_s = 1/\sqrt{3}$.

According to Eqs. (3.65) and (3.66), if we consider a generic polynomial of degree $k + 2$, like in Eq (3.58), we have:

$$I_k^{eq} = 2\theta\left[\omega_1^2\psi_k(\boldsymbol{\xi_0}) + \sum_{i=1}^{4}\omega_1\omega_2\psi_k(\boldsymbol{\xi_i}) + \sum_{i=5}^{8}\omega_1^2\psi_k(\boldsymbol{\xi_i})\right]. \tag{3.70}$$

The comparison between Eq. (3.70) and Eq. (3.58), allows to evaluate the weights W_i introduced in Eq. (3.58) as:

$$W_i = 2\pi\theta\exp\left[\frac{\boldsymbol{\xi_i^2}}{2\theta}\right]w_i, \tag{3.71}$$

where,

$$w_i = \begin{cases} 4/9, & i = 0, \\ 1/9, & i = 1, 2, 3, 4, \\ 1/36, & i = 5, 6, 7, 8. \end{cases} \tag{3.72}$$

Taking into account the weights of Eq. (3.71), we introduce the weighted mass distribution functions f_i:

$$f_i(\boldsymbol{x}, t) = W_i f(\boldsymbol{x}, \boldsymbol{\xi_i}, t), \tag{3.73}$$

and consequently according to Eq. (3.58), the moments f can be computed as a sum over the f_i of the related polynomial $\psi_k(\boldsymbol{\xi_i})$:

$$I_k = \sum_{i=0}^{8} \psi_k(\boldsymbol{\xi_i}) f_i. \tag{3.74}$$

It is easy to verify that the equilibrium distribution function of the weighted f_i is given by:

$$f_i^{eq}(\boldsymbol{x}, t) = W_i f^{eq}(\boldsymbol{x}, \boldsymbol{\xi_i}, t) = \rho w_i \left[1 + \frac{3\boldsymbol{\xi_i} \cdot \boldsymbol{u}}{c^2} + \frac{9(\boldsymbol{\xi_i} \cdot \boldsymbol{u})^2}{2c^4} - \frac{3\boldsymbol{u}^2}{2c^2} \right]. \tag{3.75}$$

Finally, we are able to derive the Lattice Boltzmann equation. In fact, we have to consider Eq. (3.51) for the discrete velocity $\boldsymbol{\xi}_i$ and multiply it for the related weight W_i:

$$f_i(\boldsymbol{x} + \boldsymbol{\xi_i}\delta t, t + \delta t) - f_i(\boldsymbol{x}, t) = -\frac{1}{\tau}(f_i(\boldsymbol{x}, t) - f_i^{eq}(\boldsymbol{x}, t)), \quad i = 0, 1, \ldots, 8, \tag{3.76}$$

which is known as the BGK Lattice Boltzmann equation.

After this derivation, an analysis of Eq. (3.76) and how it was obtained is certainly needed. We see that the Lattice Boltzmann equation is a simple and explicit scheme, despite its complex origin. Basically the concept of collision and streaming introduced for the LGA in Sec. 3.1 are inherited by the Lattice Boltzmann method, but applied to the distribution functions. We can enlist the key steps of the LBM algorithm:

1. At t=0, the lattice is initialised by means of suitable distribution functions dependent on the particular problem we are dealing with. For example, if density ρ and velocity $\boldsymbol{u}$ are known, the simplest way is to set initial $f_i(\boldsymbol{x}, 0)$ at equilibrium, using Eq. (3.75). For more details on the initialization procedures see [71].

2. The collision term $J(f_i) = -1/\tau(f_i - f_i^{eq})$ on the right side of Eq. (3.76) is evaluated on each lattice site and for each velocity, of course.

3. The post-collision value of f_{ip} in $\boldsymbol{x}$ can now be computed as $f_{ip}(\boldsymbol{x}, t) = f_i(\boldsymbol{x}, t) + J(f_i)$.

4. The f_{ip} of the node $\boldsymbol{x}$ are simply streamed along the relative connected nodes $f_i(\boldsymbol{x} + \boldsymbol{\xi_i}\delta t, t + \delta t) = f_{ip}(\boldsymbol{x}, t)$.

5. Now, in each node, we can compute ρ and $\boldsymbol{u}$, and, thus the new equilibrium distribution functions and start again from point 2.

Actually, the issue of boundary conditions in LBM has been voluntarily overlooked thus far, since we will talk about it later on.

Thus, the LBM shares the inherent parallelization typical of LGA. The collision term is evaluated locally and so it does not need communication at all, while the streaming step is just a shift operation.

Furthermore, it is clear that LBM are inherently transient solvers. Therefore, we cannot simulate a steady state directly, but it will be always viewed as the limit of a related transient problem. In general, we need to define an appropriate parameter in order to understand whether the steady state can be considered reached or not.

Differently from other conventional CFD scheme such as Finite Volume Methods [72] in the Lattice Boltzmann methods we witness the coupling between velocity and coordinate spaces, which forces the grid structure to have a certain degree of symmetry. Thus, we are not allowed to construct arbitrary structured meshes, but it is possible to realize a local grid refinement [73, 74], though this possibility will not be explored in this thesis. However, LBM proves to be surprisingly accurate and also guarantees an easy handle, when dealing with complex geometries [73] and, for this reason, they are very suited for flow in porous media.

In Subsec. 3.7.2 we have touched on the issue of the sound speed in the Lattice Boltzmann methods (see also [75, 76]). As a matter of fact, in the model presented we are considering an isothermal process and thus, the speed of sound is equal to the derivative of pressure with respect to density at constant temperature $c_s = (\partial P/\partial \rho)_T = \sqrt{\theta}$. This assumption is fundamental in order to obtain the regular lattice structure induced by Eq. (3.66) and without it, we could not be able to obtain the numerical method itself. If θ is not kept constant, we will draw just a weird model, without physical meaning. Nevertheless, as we know, sound waves are basically adiabatic and the isothermal case is an unlikely situation. Consequently, if we want to use the LBM with BGK collision term, for simulations of compressible flows, we have to deal with this isothermal speed of sound, instead of the most appropriate isentropic one. However, if we want to simulate an incompressible flow we are not interested in compressibility effects and sound waves, but we want to keep them as limited as possible, indeed. In fact, similarly to other compressible schemes [77], in order to approximate the incompressible Navier-Stokes equations, the Mach number should be very low, since it is the parameter that governs the compressibility effects. In particular, as pointed out in [78], LBM with BGK recovers compressible Navier-Stokes equation, which in turn are used to approximate an incompressible flow with an error $\mathcal{O}(Ma^2)$ on the continuity equation and $\mathcal{O}(Ma^3)$ in the momentum equations.

The Lattice Boltzmann equation with BGK collision term suffers some

drawbacks due to the BGK approximation. In particular, the simulated gas shows a fixed Prandtl number (equal to 1) and a fixed ratio between shear and bulk viscosity [29]. Moreover, it can be proved that the BGK LBE coupled with the usual Bounce-Back boundary conditions on walls, that we will introduce later on, produces a slip velocity dependent on the relaxation parameter τ [79]. In the context of incompressible flows in porous media, this implies that permeability does not remain constant and becomes dependent on viscosity ν, simply because the geometry representation varies with τ. In fact, we will show in Chap. 4 that the viscosity of the model is given by:

$$\nu = c_s^2 \left(\frac{2\tau - 1}{2} \right) \delta t = \frac{2\tau - 1}{6} \frac{\delta x^2}{\delta t}, \qquad (3.77)$$

and it follows necessarily that $\tau > 1/2$, in order to obtain a positive viscosity.

3.8   The Multiple-Relaxation-Time model

The main reason for the shortcomings of the BGK model presented in Subsec. 3.7.3 is the single relaxation parameter of the collision term. As a matter of fact, with a single relaxation time constant, we cannot tune independently the macroscopic transport coefficients, such as bulk and shear viscosities. In order to increase the number of tunable coefficients, we definitely need more relaxation parameters. The Multiple-Relaxation-Time (MRT) model has been introduced for the first time in [28] and its aim is to overcome the main deficiencies of the BGK model.

Let us consider a general Lattice Boltzmann model defined by a set of N velocities $\{\boldsymbol{\xi}_i\}$ where $i = 0, 1, \ldots, N - 1$, connecting each lattice node to its neighbours, and the corresponding distribution functions $\{f_i\}$. Obviously, also a set of equilibrium distribution functions is defined $\{f_i^{eq}\}$, depending on the the local conserved quantities as usual. In the most generic case, the evolution equation is given by:

$$|f(\boldsymbol{x} + \boldsymbol{\xi}\delta t, t + \delta t)\rangle - |f(\boldsymbol{x}, t)\rangle = -\bar{\bar{\boldsymbol{S}}}[|f(\boldsymbol{x}, t)\rangle - |f^{eq}(\boldsymbol{x}, t)\rangle], \qquad (3.78)$$

where we have used the ket notation $|\,\rangle$ to denote column vectors, while the bra notation $\langle\,|$ will be used to denote row vectors; $\bar{\bar{\boldsymbol{S}}}$ represents a collision matrix, whose eigenvalues are all between 0 and 2 in order to attain linear stability [28]. Within this framework, the BGK model can be regarded as a special case of the MRT model, in which $\bar{\bar{\boldsymbol{S}}} = \omega\bar{\bar{\boldsymbol{I}}}$, where $\bar{\bar{\boldsymbol{I}}}$ is the identity matrix and $\omega = 1/\tau$ is called the relaxation frequency. As a matter of fact, the constraint on linear stability for the BGK model is actually a request for positive viscosity.

However, in the MRT model, the collision step is basically carried out in the space of moments of the distribution function, and the relaxation parameters corresponds to relaxation frequencies towards equilibrium of certain "hydrodynamic modes". In order to understand the previous statement we need to examine in depth the concept of moments introduced in Subsec. 3.7.3.

In continuous kinetic theory a moment of order n of f is a tensor of rank n defined as [80]:

$$\boldsymbol{I}_n(\boldsymbol{x}, t) = \int \underbrace{\boldsymbol{\xi} \ldots \boldsymbol{\xi}}_{n\,times} f(\boldsymbol{x}, \boldsymbol{\xi}, t) \, d\boldsymbol{\xi}. \tag{3.79}$$

It is easy to recognize that the number of independent components of a moment of order n, in a D-dimensional space, is given by the combination with repetition of D element taken n times, that is equal to $C_{D,n} = (D + n - 1)!/[(D - 1)!n!]$. Thus, in $2D$ it is equal to $n + 1$. For the sake of simplicity, from now on we will consider the 2-dimensional case.

However, in discrete kinetic theory, the moments are computed as a sum over a specific set of N velocities $\{\boldsymbol{\xi_i}\}$ [80]

$$\boldsymbol{I}_n(\boldsymbol{x}, t) = \sum_{i=0}^{N-1} \underbrace{\boldsymbol{\xi_i} \ldots \boldsymbol{\xi_i}}_{n\,times} f_i(\boldsymbol{x}, t). \tag{3.80}$$

In general, we can view a component of a moment of order n $I_{\gamma_1 \ldots \gamma_n}$ as the scalar product between the column vector of the distribution function $|f\rangle$ and a N-dimensional row vector $\langle m_{\gamma_1 \ldots \gamma_n}|$, characteristic of the elementary moment considered. Hence:

$$I_{\gamma_1 \ldots \gamma_n} = \langle m_{\gamma_1 \ldots \gamma_n} | f \rangle, \tag{3.81}$$

where the components of $\langle m_{\gamma_1 \ldots \gamma_n}|$ are obviously of the form $\xi_x^m \xi_y^l$ with $m + l = n$. Hence, the moment $M_{\gamma_1 \ldots \gamma_n}$ is basically represented by a vector of $\mathbb{R}^N$. Now we can extend the definition of moment, considering also linear combination of elementary moments, i.e., the polynomial, and consequently the moment space $\mathbb{M} \equiv \mathbb{R}^N$. The number of independent discrete moments is therefore equal to N. It is obvious now that, regardless of the velocities chosen, if $N < n + 1$, the correct model will not be able to represent the moments up to order n, since the independent moments would be different from the continuous one. However, this is just a necessary condition to represent the continuous moments correctly, but it is very useful because for instance, it allows to say immediately that a 2-dimensional model with 3 velocities cannot be able to recover the Navier-Stokes equation, since in Subsec. 3.7.3 we required the preservation of moments up to third order.

Let us consider the lattice D2Q9. For this discrete model we can choose the following elementary independent moments [81]. The first four moments are the collision invariants:

$$m'_1 = \rho = \sum_{i=0}^{8} f_i, \tag{3.82a}$$

$$m'_2 = \rho u_x = j_x = \sum_{i=0}^{8} \xi_{ix} f_i, \tag{3.82b}$$

$$m'_3 = \rho u_y = j_y = \sum_{i=0}^{8} \xi_{iy} f_i, \tag{3.82c}$$

$$m'_4 = \rho(e + \frac{1}{2}\boldsymbol{u}^2) = \sum_{i=0}^{8} (\xi_{ix}^2 + \xi_{iy}^2) f_i. \tag{3.82d}$$

As we know, pressure P is defined as the arithmetic mean of the diagonal stresses, i.e., in 2-dimensions $P = 1/2(\sigma_{xx} + \sigma_{yy}) = 1/2(\sum_i \xi_{ix}^2 f_i + \sum_i \xi_{iy}^2 f_i)$. Thus, we define the diagonal deviatoric components of the stress tensor as $p_{xx,yy} = \sigma_{xx,yy} - P = \sum_i 1/2(\xi_{ix,y}^2 - \xi_{iy,x}^2) f_i$, while the off-diagonal components are $p_{xy} = \sigma_{xy} = p_{yx} = \sigma_{yx}$. We can add two independent moments related to the stress tensor to those of Eqs. (3.82):

$$m'_5 = 2p_{xx} = \sum_{i=0}^{8} \frac{1}{2}(\xi_{ix}^2 - \xi_{iy}^2) f_i, \tag{3.83a}$$

$$m'_6 = p_{xy} = \sum_{i=0}^{8} \xi_{ix} \xi_{iy} f_i. \tag{3.83b}$$

In fact, we can consider as independent moments only the one between s_{xx} and s_{yy}, because from the moments of Eqs. (3.82), we can compute the pressure P, by means of the state equation Eq. (3.33), and therefore s_{xx} and s_{yy} are not independent.

As m'_7 and m'_8 we set the energy fluxes along x, y of the kinetic energy corresponding to $\xi_{x,y}$:

$$m'_7 = \phi_{xy} = \sum_{i=0}^{8} \xi_{ix} \xi_{iy}^2 f_i, \tag{3.84a}$$

$$m'_8 = \phi_{yx} = \sum_{i=0}^{8} \xi_{iy} \xi_{ix}^2 f_i. \tag{3.84b}$$

Finally, we set the last independent moment

$$m'_9 = \epsilon = \sum_{i=0}^{8} \xi_{ix}^2 \xi_{iy}^2 f_i, \tag{3.85}$$

that can be regarded as a higher order energy transport term [81].

Thus, we denote with $\langle \eta'_j|$ the vectors in the moment space $\mathbb{M}$, corresponding to the moments of Eqs. (3.82), (3.83), (3.84) and (3.85). For the lattice D2Q9 they are given by:

$$
\bar{\bar{M}}' = \begin{bmatrix} \langle \eta'_1| \\ \langle \eta'_2| \\ \langle \eta'_3| \\ \langle \eta'_4| \\ \langle \eta'_5| \\ \langle \eta'_6| \\ \langle \eta'_7| \\ \langle \eta'_8| \\ \langle \eta'_9| \end{bmatrix} = \begin{bmatrix} \langle \rho| \\ \langle j_x| \\ \langle j_y| \\ \langle \rho(e+1/2u^2)| \\ \langle 2p_{xx}| \\ \langle p_{xy}| \\ \langle \phi_{xy}| \\ \langle \phi_{yx}| \\ \langle \epsilon| \end{bmatrix} = \begin{bmatrix} 1 & 1 & 1 & 1 & 1 & 1 & 1 & 1 & 1 \\ 0 & 1 & 0 & -1 & 0 & 1 & -1 & -1 & 1 \\ 0 & 0 & 1 & 0 & -1 & 1 & 1 & -1 & -1 \\ 0 & 1 & 1 & 1 & 1 & 2 & 2 & 2 & 2 \\ 0 & 1 & -1 & 1 & -1 & 0 & 0 & 0 & 0 \\ 0 & 0 & 0 & 0 & 0 & 1 & -1 & 1 & -1 \\ 0 & 0 & 0 & 0 & 0 & 1 & -1 & -1 & 1 \\ 0 & 0 & 0 & 0 & 0 & 1 & 1 & -1 & -1 \\ 0 & 0 & 0 & 0 & 0 & 1 & 1 & 1 & 1 \end{bmatrix}
$$
(3.86)

Although these vectors are independent, they are not orthogonal. In order to obtain orthogonal vectors $\langle \eta_j|$, we have to apply the Gram-Schmidt procedure, which, taking as starting vector $\langle \rho|$, yields:

$$
\bar{\bar{M}} = \begin{bmatrix} \langle \eta_1| \\ \langle \eta_2| \\ \langle \eta_3| \\ \langle \eta_4| \\ \langle \eta_5| \\ \langle \eta_6| \\ \langle \eta_7| \\ \langle \eta_8| \\ \langle \eta_9| \end{bmatrix} = \begin{bmatrix} \langle \rho| \\ \langle j_x| \\ \langle j_y| \\ \langle e| \\ \langle 2p_{xx}| \\ \langle p_{xy}| \\ \langle q_x| \\ \langle q_y| \\ \langle \varepsilon| \end{bmatrix} = \begin{bmatrix} 1 & 1 & 1 & 1 & 1 & 1 & 1 & 1 & 1 \\ 0 & 1 & 0 & -1 & 0 & 1 & -1 & -1 & 1 \\ 0 & 0 & 1 & 0 & -1 & 1 & 1 & -1 & -1 \\ -4 & -1 & -1 & -1 & -1 & 2 & 2 & 2 & 2 \\ 0 & 1 & -1 & 1 & -1 & 0 & 0 & 0 & 0 \\ 0 & 0 & 0 & 0 & 0 & 1 & -1 & 1 & -1 \\ 0 & -2 & 0 & 2 & 0 & 1 & -1 & -1 & 1 \\ 0 & 0 & -2 & 0 & 2 & 1 & 1 & -1 & -1 \\ 4 & -2 & -2 & -2 & -2 & 1 & 1 & 1 & 1 \end{bmatrix}
$$
(3.87)

Let us denote with η_j the moment identified by the vector in moment space $|\eta_j\rangle$, i.e., $\eta_j = \langle m_j|f\rangle$ and with $|\eta\rangle$ the corresponding row vector. Accordingly, we can write:

$$
|\eta\rangle = \bar{\bar{M}} \, |f\rangle \rightarrow |f\rangle = \bar{\bar{M}}^{-1} \, |\eta\rangle . \tag{3.88}
$$

Thus, there is a linear relationship between the vector of moments $|\underline{\eta}\rangle$ and the vector of the distribution functions $|f\rangle$, described by the matrix $\bar{\bar{M}}$. At this point the idea is to consider a particular collision matrix $\bar{\bar{S}}$ (introduced in Eq. (3.78)), such that its eigenvectors are the row vectors of $\bar{\bar{M}}$. In this way, the collision step can be carried out in the moment space, by means of

a diagonal collision matrix $\bar{\bar{\hat{S}}}$:

$$
\begin{bmatrix}
\delta\rho \\
\delta j_x \\
\delta j_y \\
\delta e \\
\delta 2p_{xx} \\
\delta p_{xy} \\
\delta q_x \\
\delta q_y \\
\delta\varepsilon
\end{bmatrix}
=
\begin{bmatrix}
s_\rho & 0 & 0 & 0 & 0 & 0 & 0 & 0 & 0 \\
0 & s_{j_x} & 0 & 0 & 0 & 0 & 0 & 0 & 0 \\
0 & 0 & s_{j_y} & 0 & 0 & 0 & 0 & 0 & 0 \\
0 & 0 & 0 & s_e & 0 & 0 & 0 & 0 & 0 \\
0 & 0 & 0 & 0 & s_{p_{xx}} & 0 & 0 & 0 & 0 \\
0 & 0 & 0 & 0 & 0 & s_{p_{xy}} & 0 & 0 & 0 \\
0 & 0 & 0 & 0 & 0 & 0 & s_{q_x} & 0 & 0 \\
0 & 0 & 0 & 0 & 0 & 0 & 0 & s_{q_y} & 0 \\
0 & 0 & 0 & 0 & 0 & 0 & 0 & 0 & s_\varepsilon
\end{bmatrix}
\begin{bmatrix}
\rho - \rho^{eq} \\
j_x - j_x^{eq} \\
j_y - j_y^{eq} \\
e - e^{eq} \\
p_{xx} - p_{xx}^{eq} \\
p_{xy} - p_{xy}^{eq} \\
q_x - q_x^{eq} \\
q_y - q_y^{eq} \\
\varepsilon - \varepsilon^{eq}
\end{bmatrix}
\quad (3.89)
$$

Now we have to represent this collision in terms of the distribution functions using Eq. (3.88) and finally, the Lattice Boltzmann equation for the MRT models turns into:

$$
|f(\boldsymbol{x} + \boldsymbol{\xi}\delta t, t + \delta t)\rangle - |f(\boldsymbol{x}, t)\rangle = -\bar{\bar{\boldsymbol{M}}}^{-1}\bar{\bar{\hat{\boldsymbol{S}}}}[|f(\boldsymbol{x}, t)\rangle - |f^{eq}(\boldsymbol{x}, t)\rangle], \quad (3.90)
$$

where the equilibrium moments can be computed by means of the equilibirum distribution function introduced in Eq. (3.75). The parameters of $\bar{\bar{\hat{S}}}$ are now related to the "hydrodynamic modes", which possess a macroscopic meaning and, clearly, we can set $s_\rho = s_{j_x} = s_{j_y} = 0$, since ρ, j_x and j_y are preserved during a collision. Tuning the six parameters left, we are able to set the various transport coefficients. In fact, as shown in [29], if we set $s_{p_{xx}} = s_{p_{xy}} = s_\nu = 1/\tau$, the viscosity of the model has exactly the same expression of Eq. obtained for the BGK model, but we are allowed to control also the bulk viscosity ζ, which is determined by $s_e = s_\zeta$:

$$
\zeta = \frac{2}{9}\left(\frac{1}{s_\zeta} - \frac{1}{2}\right). \quad (3.91)
$$

Moreover, the parameters of the MRT model can be properly chosen in order to achieve optimal stability [41] or to attain a well-defined no-slip condition when using the Bounce-Back rule [82].

Chapter 4

The Chapman-Enskog expansion

In this chapter, we will initially discuss how the forcing term can be included in the Lattice Boltzmann equation, analysing different methods. Afterwards, the Chapman-Enskog procedure will be applied to the BGK Lattice Boltzmann equation with the forcing term, in order to restore the Navier-Stokes equations. At the end of this procedure, the relationship between the macroscopic coefficients and the relaxation parameter will be definitely clear. Moreover, we will be able to show the error sources. In our analysis, we will generally refer to Kuzmin's work [1], but the Chapman-Enskog procedure will be applied to a more general case than the one considered in [1], providing insights on the correct way of including the forcing term.

4.1 The role of δt

Let us write again the Lattice Boltzmann equation introduced in Sec. 3.7, that is Eq. (3.76)

$$f_i(\boldsymbol{x} + \boldsymbol{\xi_i}\delta t, t + \delta t) - f_i(\boldsymbol{x}, t) = -\frac{1}{\tau}(f_i(\boldsymbol{x}, t) - f_i^{eq}(\boldsymbol{x}, t)), \quad i = 0, 1, \ldots, N-1.$$

The starting point of the Chapman-Enskog expansion is the assumption of convective scaling, $\delta t \sim \delta x$, which introduces a precise relationship between δx and δt. From Eqs. (3.68), we realize that under this assumption the discrete velocities $\boldsymbol{\xi_i}$ are kept constant during the scaling.

The consequence of the convective scaling is that for the Lattice Boltzmann equation, the role of the Knudsen number, introduced in Sec. 3.5, can be carried out by δt. However, this assumption is not trivial. In fact, at first sight, it seems straightforward that for $\delta t \to 0$ the solution is $f_i \to f_i^{eq}$. However, in Subsec. 3.7.1, we have seen that actually $\tau = \lambda/\delta t$, where λ

is the relaxation parameter of the continuous BGK Boltzmann equation [1]. Consequently, the right side of Eq. (3.76) goes to zero when $\delta t \to 0$, without necessarily requiring that $f_i \to f_i^{eq}$. To solve this contradiction, we need to draw an analogy with the continuous Boltzmann BGK equation. Basically, since the LBE is a discretization of the BE, in order to recover the Navier-Stokes equations we need to be in the same conditions, which allow this recovery starting from the BE, that is, the low Knudsen number condition. As shown in [1], the Knudsen number for the BGK collision term $Kn \sim \lambda$. Accordingly, we need to assume that $\delta t \sim Kn \sim \lambda$. In this way, $\tau = \lambda/\delta t$ remains constant in this procedure, and thus we are allowed to say that when $\tau \to 0$, $f_i \to f_i^{eq}$. However, we will see at the end of this derivation that these assumptions on the Chapman-Enskog expansion applied to the LBE may be controversial. For this reason, in literature, different methods to recover the Navier-Stokes equations from the LBE have been attempted, which will be briefly discussed in the last section of this chapter.

In what follows, we will perform the Chapman-Enskog expansion around the solution f^{eq}, taking δt as the parameter of the expansion. In addition, we will denote $\varepsilon = \delta t$ in order to highlight that it is the small parameter of the perturbative method.

4.2 Inclusion of the forcing term

The inclusion of external or internal forces into the Lattice Boltzmann equation is carried out adding the term εF_i:

$$f_i(\boldsymbol{x} + \boldsymbol{\xi_i}\varepsilon, t + \varepsilon) - f_i(\boldsymbol{x}, t) = -\frac{1}{\tau}(f_i(\boldsymbol{x}, t) - f_i^{eq}(\boldsymbol{x}, t)) + \varepsilon F_i. \qquad (4.1)$$

The idea behind this additional term is that it should be proportional to ε; in fact if we consider a collision in a finite time ε in presence of forces, according to Newton's second law, the total momentum will change proportionally to ε.

In the second instance, in the case of external forces, the force functions F_i should be constructed so that the macroscopic forcing term is equal to $\boldsymbol{F} = \rho\boldsymbol{a}$ as in Eqs. (3.38). As a matter of fact, in this process we go through an opposite direction with respect to what we have done so far, namely we design the mesoscopic dynamics starting from the macroscopic one. This does not happen with the Boltzmann equation, in which the forcing term emerges naturally from the conservation equations. In a certain sense starting from the Boltzmann equation, we derive the macroscopic equations and,

---

[1]It should be noted that in lattice units $\lambda = \tau$ since $\delta t = 1$ in this system of units

consequently, the expression of the forcing term, and then we impose to obtain the same term in the LBE conservation equations. Also the presence of an hypothetical mass source M can be handled with F_i, as we will see in what follows.

However, the generation of the forcing term could be not only caused by the force functions F_i, but also by the collision term, redefining the density and momentum used in the computation of f_i^{eq} [83].

From the previous observations, we recognize that what really matters is that in mass and momentum equations:

$$\varepsilon\mathcal{M} - \sum_i \frac{f_i}{\tau} + \sum_i \frac{f_i^{eq}}{\tau} = \varepsilon M, \tag{4.2a}$$

$$\varepsilon\mathcal{F}_\alpha - \sum_i \frac{\xi_{i\alpha}f_i}{\tau} + \sum_i \frac{\xi_{i\alpha}f_i^{eq}}{\tau} = \varepsilon F_\alpha, \tag{4.2b}$$

where $\mathcal{M} = \sum_i F_i$ and $\mathcal{F}_\alpha = \sum_i \xi_{i\alpha}F_i$ are moments of F_i. Thus:

$$\varepsilon\mathcal{M} - \frac{\rho}{\tau} + \frac{\rho^{eq}}{\tau} = \varepsilon M, \tag{4.3a}$$

$$\varepsilon\mathcal{F}_\alpha - \frac{\rho u_\alpha}{\tau} + \frac{\rho^{eq}u_\alpha^{eq}}{\tau} = \varepsilon F_\alpha. \tag{4.3b}$$

We will prove that within this framework, the macroscopic density and momentum, which take part in the restoration of macroscopic equations are:

$$\rho^m = \rho + \varepsilon\frac{M}{2}, \tag{4.4a}$$

$$\rho^m u_\alpha^m = \rho u_\alpha + \varepsilon\frac{F_\alpha}{2}, \tag{4.4b}$$

where "m" stands for macroscopic. Three specific cases are worth mentioning [1]

1. $\rho = \rho^{eq}$, $\rho^{eq}u_\alpha^{eq} = \rho u_\alpha$: the forcing term is only due to the moments of F_i (scheme I);

2. $\rho^{eq} = \rho^m$, $\rho^{eq}u_\alpha^{eq} = \rho^m u_\alpha^m$: the forcing term is distributed between the moments of the collision term and the moments of F_i (scheme II);

3. $\rho^{eq} = \rho + \varepsilon M\tau$, $\rho^{eq}u_\alpha^{eq} = \rho u_\alpha + \varepsilon F_\alpha\tau$: the forcing term is generated only by the moments of the collision term (scheme III).

Actually, we will prove that the correct model is the second one, which is that proposed by Guo in [84]. Only with this model, ρ^m and $\rho^m u_\alpha^m$ represent

properly the macroscopic density and momentum into the recovered Navier-Stokes equations, while the others introduce additional sources of error. In addition, we identify the third method as the method of shifting velocity proposed by Shan & Chen in [4]. In this paper an interaction force is introduced between particles, in order to allow phase separation. We will explain in details the Shan-Chen model in Chap. 7, but for now we have to keep in mind that it introduces the forcing term by means of scheme III.

4.3 The Chapman-Enskog multi-scale expansion

The first step of the Chapman-Enskog procedure for the LBE is the Taylor expansion of the left side of Eq. (4.1):

$$f_i(\boldsymbol{x} + \boldsymbol{\xi_i}\varepsilon, t + \varepsilon) - f_i(\boldsymbol{x}, t) = \sum_{n=0}^{+\infty} \frac{(\partial_t + \xi_{i\beta}\partial_\beta)^n}{n!} \varepsilon^n f(\boldsymbol{x}, t), \qquad (4.5)$$

where we have used the notation ∂_t to denote the partial derivative with respect to time t, and ∂_β to denote the partial derivative with respect to the coordinate x_β.

The Chapman-Enskog expansion is a multiscale method in which both the unknown function f_i and the time variable are expanded as a polynomial in the small parameter ε. For $\varepsilon \to 0$ the solution is obviously f_i^{eq}, which is our known solution. Hence, f_i and t are expanded as follows:

$$f_i = f_i^{(0)} + \varepsilon f_i^{(1)} + \varepsilon^2 f_i^{(2)} + \cdots = \sum_{k=0}^{+\infty} \varepsilon^k f_i^{(k)}, \qquad (4.6a)$$

$$t = t_0 + \varepsilon t_1 + \varepsilon^2 t_2 + \cdots = \sum_{k=0}^{+\infty} \varepsilon^k t_k, \qquad (4.6b)$$

and accordingly

$$\partial_t = \partial_{t_0} + \varepsilon \partial_{t_1} + \varepsilon^2 \partial_{t_2} + \cdots = \sum_{k=0}^{+\infty} \varepsilon^k \partial_{t_k}. \qquad (4.7)$$

Thus, the time derivative of a generic function g will be given by $\partial_t g = \partial_{t_0} g + \varepsilon \partial_{t_1} g + \varepsilon^2 \partial_{t_2} g + \dots$. According to the previous statements $f_i^{(0)} = f_i^{eq}$.

The insertion of Eqs. (4.5) and (4.6) into Eq. (4.1) gives:

$$\sum_{n=0}^{+\infty} \frac{(\sum_{k=0}^{\infty} \varepsilon^k \partial_{t_k} + \xi_{i\beta}\partial_\beta)^n}{n!} \varepsilon^n (f_i^{(0)} + \varepsilon f_i^{(1)} + \varepsilon^2 f_i^{(2)} + \dots) = -\frac{\sum_{n=1}^{+\infty} \varepsilon^n f_i^{(n)}}{\tau} + \varepsilon F_i.$$

$$(4.8)$$

4.4 Restoration of macroscopic equations

Let us introduce an approximation of order n of Eq. (4.8), considering terms of order at most ε^n. In particular, we are interested in approximations of order ε^1 and ε^2 (the approximation of order ε^0 is trivial) for which it is easy to verify the following results:

$$\varepsilon^1 : (\partial_{t_0} + \xi_{i\beta}\partial_\beta)f_i^{(0)} = -\frac{f_i^{(1)}}{\tau} + F_i, \tag{4.9a}$$

$$\varepsilon^2 : \partial_{t_1}f_i^{(0)} + (\partial_{t_0} + \xi_{i\beta}\partial_\beta)f_i^{(1)} + \frac{(\partial_{t_0} + \xi_{i\beta}\partial_\beta)^2 f_i^{(0)}}{2} = -\frac{f_i^{(2)}}{\tau}. \tag{4.9b}$$

It is worth pointing out that these successive approximations are not affected by errors. In fact, we can simply assume that $f_i^{(1)}$ and $f_i^{(2)}$ satisfy respectively Eq. (4.9a) and Eq. (4.9b), and in general $f_i^{(k)}$ satisfies the approximation of order ε^k. It is easy to verify that this procedure is consistent, since if these successive equations hold, the Lattice Boltzmann equation is consequently satisfied. In general, within the Chapman-Enskog framework, the moments of f can be also viewed as an expansion in ε. For example, considering ρ and ρu_α:

$$\rho = \sum_i f_i = \sum_i f_i^{(0)} + \varepsilon \sum_i f_i^{(1)} + \varepsilon^2 \sum_i f_i^{(2)} + \cdots =$$
$$\rho^{(0)} + \varepsilon\rho^{(1)} + \varepsilon^2\rho^{(2)} + \ldots, \tag{4.10a}$$

$$\rho u_\alpha = \sum_i \xi_{i\alpha} f_i = \sum_i \xi_{i\alpha} f_i^{(0)} + \varepsilon \sum_i \xi_{i\alpha} f_i^{(1)} + \varepsilon^2 \sum_i \xi_{i\alpha} f_i^{(2)} + \cdots =$$
$$\rho^{(0)}u_\alpha^{(0)} + \varepsilon\rho^{(1)}u_\alpha^{(1)} + \varepsilon^2\rho^{(2)}u_\alpha^{(2)} + \ldots, \tag{4.10b}$$

A direct consequence of Eqs. (4.2) is that ρ and $\rho\boldsymbol{u}$ are certainly due only to $f_i^{(0)}$ and $f_i^{(1)}$. Hence, we can write Eqs. (4.2) as:

$$\rho = \rho^{(0)} + \varepsilon\tau(\mathcal{M} - M), \tag{4.11a}$$

$$\rho u_\alpha = \rho^{(0)}u_\alpha^{(0)} + \varepsilon\tau(\mathcal{F}_\alpha - F_\alpha), \tag{4.11b}$$

which by comparison with Eqs. (4.10) allows to identify

$$\rho^{(1)} = \tau(\mathcal{M} - M) \tag{4.12a}$$

$$\rho^{(1)}u_\alpha^{(1)} = \tau(\mathcal{F}_\alpha - F_\alpha), \tag{4.12b}$$

and consequently:

$$\rho = \rho^{(0)} + \varepsilon\rho^{(1)}, \tag{4.13a}$$

$$\rho u_\alpha = \rho^{(0)}u_\alpha^{(0)} + \varepsilon\rho^{(1)}u_\alpha^{(1)}. \tag{4.13b}$$

It is obvious that direct consequences of Eqs (4.13) are $\sum_i f_i^{(k)} = 0$ and $\sum_i \xi_{i\alpha} f_i^{(k)} = 0$ for $k \geq 2$.

The macroscopic equations we would like to obtain via the Chapman-Enskog expansion are those of a compressible and Newtonian fluid, in which the relationship between stresses and velocities (or better their gradients) is given by:

$$\sigma_{\alpha\beta} = -\left[\mu\left(\frac{\partial u_\alpha}{\partial x_\beta} + \frac{\partial u_\beta}{\partial x_\alpha}\right) + \delta_{\alpha\beta}\left(\zeta \frac{\partial u_\gamma}{\partial x_\gamma} - P\right) \right], \tag{4.14}$$

where μ and ζ are respectively the dynamic and bulk viscosities; $\delta_{\alpha\beta}$ is the Kronecker delta. In Eq. (4.14) we have assumed the conventions induced by Eqs. (3.38). In this case the Navier-Stokes equations we want to restore are:

$$\partial_t \rho + \partial_\alpha(\rho u_\alpha) = M, \tag{4.15}$$

$$\partial_t(\rho u_\alpha) + \partial_\beta(\rho u_\beta u_\alpha) = -\partial_\alpha P + \partial_\beta(\mu \partial_\beta u_\alpha) + \partial_\beta((\mu + \zeta)\partial_\alpha u_\beta) + F_\alpha. \tag{4.16}$$

In Eq. (4.15) we have also considered a mass source term, due for example to a chemical reaction.

4.4.1 Mass equation

Let us consider the Lattice Boltzmann equation in the ε^1 approximation Eq. (4.9a). By summing over i and taking into account Eqs. (4.12) it is easy to derive:

$$\varepsilon^1 : \partial_{t_0}\rho^{(0)} + \partial_\alpha(\rho^{(0)} u_\alpha^{(0)}) = M. \tag{4.17}$$

The same operations applied to the ε^2 approximation Eq. (4.9b) yields:

$$\partial_{t_1}\rho^{(0)} + \partial_{t_0}\rho^{(1)} + \partial_\alpha(\rho^{(1)} u_\alpha^{(1)}) + \sum_i \frac{(\partial_{t_0} + \xi_{i\alpha})^2 f_i^{(0)}}{2} = 0. \tag{4.18}$$

The insertion of Eq. (4.17) into Eq. (4.18) leads to:

$$\partial_{t_1}\rho^{(0)} + \partial_{t_0}\rho^{(1)} + \partial_\alpha(\rho^{(1)} u_\alpha^{(1)}) + \sum_i \frac{(\partial_{t_0} + \xi_{i\alpha})(-\frac{f_i^{(1)}}{\tau} + F_i)}{2} = 0. \tag{4.19}$$

After some simple algebra and remembering the definitions of $\mathcal{M}$ and $\mathcal{F}_\alpha$ given in Sec. 4.2, Eq. (4.19) finally turns into:

$$\varepsilon^2 : \partial_{t_1}\rho^{(0)} + \left(1 - \frac{1}{2\tau}\right)\partial_{t_0}\rho^{(1)} + \left(1 - \frac{1}{2\tau}\right)\partial_\alpha(\rho^{(1)} u_\alpha^{(1)}) + $$
$$\frac{1}{2}\partial_{t_0}\mathcal{M} + \frac{1}{2}\partial_\alpha \mathcal{F}_\alpha = 0. \tag{4.20}$$

Multiplying Eq. (4.20) by ε and summing it with Eq. (4.17) we obtain:

$$\partial_{t_0}\left(\rho^{(0)} + \varepsilon\left(1 - \frac{1}{2\tau}\right)\rho^{(1)} + \varepsilon\frac{\mathcal{M}}{2}\right) +$$
$$\partial_\alpha\left(\rho^{(0)}u_\alpha^{(0)} + \varepsilon\left(1 - \frac{1}{2\tau}\right)\rho^{(1)}u_\alpha^{(1)} + \varepsilon\frac{F_\alpha}{2}\right) + \varepsilon\partial_{t_1}\rho^{(0)} = M, \tag{4.21}$$

which taking into account Eqs. (4.11) and (4.12) becomes:

$$\partial_{t_0}\left(\rho + \varepsilon\frac{M}{2}\right) + \partial_\alpha\left(\rho u_\alpha + \varepsilon\frac{F_\alpha}{2}\right) + \varepsilon\partial_{t_1}\rho^{(0)} = M. \tag{4.22}$$

At this point, we would like to adopt the second order approximation in ε of the time derivative $\partial_t = \partial_{t_0} + \varepsilon\partial_{t_1} + \mathcal{O}(\varepsilon^2)$, in order to obtain the derivative of a macroscopic density with respect to time. Clearly, the only correct way is to set $\rho^{(0)} = \rho^m = \rho + \varepsilon M/2$, that is the method denoted as scheme II. With this assumption, no further sources of errors are introduced. Of course we identify also $\rho^m u_\alpha^m = \rho u_\alpha + \varepsilon F_\alpha/2$ and finally we obtain:

$$\partial_t\rho^m + \partial_\alpha(\rho^m u_\alpha^m) = M + \mathcal{O}(\varepsilon^2). \tag{4.23}$$

However, from Eqs. (4.3) and (4.4), we notice that we can write:

$$\rho^{eq} = \varepsilon M(\tau - \frac{1}{2}) - \tau\varepsilon\mathcal{M} + \rho^m. \tag{4.24}$$

This means that by summing and subtracting the term $\varepsilon M(\tau - 1/2) - \tau\varepsilon\mathcal{M}$ into Eq. (4.22) we can obtain:

$$\partial_t\rho^m + \partial_\alpha(\rho^m u_\alpha^m) = M - \varepsilon\partial_{t_1}(\varepsilon M(\tau - \frac{1}{2}) - \tau\varepsilon\mathcal{M}) + \mathcal{O}(\varepsilon^2). \tag{4.25}$$

We notice that the additional source of error is due a partial derivative with respect to the time scale t_1, which is rigorously zero, if the mass source M and the the zero-th order moments of $\mathcal{M}$ of F_i do not depend on time. Anyway scheme II is definitely the most appropriate. Furthermore, we notice that the additional source of error shows a dependency on the relaxation parameter τ. Similar considerations can be found in the paper of Guo *et al.* [84].

4.4.2 Momentum Equation

Now our goal is to obtain the macroscopic momentum equation. Basically the procedure is similar to that adopted in Subsec. 4.4.1, but the derivation is lengthier and more complex. In particular new sources of error will arise.

Thus, let us consider the equation for ε^1 Eq. (4.9a). Multiplying it by $\xi_{i\alpha}$ and summing over i we obtain:

$$\varepsilon^1 : \partial_{t_0}(\rho^{(0)} u_\alpha^{(0)}) + \partial_\beta \left(\sum_i \xi_{i\alpha} \xi_{i\beta} f_i^{(0)} \right) = F_\alpha, \tag{4.26}$$

where we have also used Eq. (4.12b). The same procedure applied to Eq. (4.9b) yields:

$$\varepsilon^2 : \partial_{t_1}(\rho^{(0)} u_\alpha^{(0)}) + \left(1 - \frac{1}{2\tau} \right) \partial_{t_0}(\rho^{(1)} u_\alpha^{(1)}) + \left(1 - \frac{1}{2\tau} \right) \partial_\beta \left(\sum_i \xi_{i\alpha} \xi_{i\beta} f_i^{(1)} \right) +$$
$$\frac{1}{2} \partial_{t_0} \mathcal{F}_\alpha + \frac{1}{2} \partial_\beta \left(\sum_i \xi_{i\alpha} \xi_{i\beta} F_i \right) = 0. \tag{4.27}$$

The multiplication of Eq. (4.27) by ε and its summation to Eq (4.26) gives:

$$\partial_{t_0} \left(\rho^{(0)} u_\alpha^{(0)} + \varepsilon \left(1 - \frac{1}{2\tau} \right) \rho^{(1)} u_\alpha^{(1)} + \frac{\varepsilon}{2} \mathcal{F}_\alpha \right) + \varepsilon \partial_{t_1}(\rho^{(0)} u_\alpha^{(0)}) +$$
$$\partial_\beta \left(\sum_i \xi_{i\alpha} \xi_{i\beta} f_i^{(0)} + \varepsilon \left(1 - \frac{1}{2\tau} \right) \sum_i \xi_{i\alpha} \xi_{i\beta} f_i^{(1)} + \frac{\varepsilon}{2} \sum_i \xi_{i\alpha} \xi_{i\beta} F_i \right) = F_\alpha. \tag{4.28}$$

Using Eqs. (4.11) and (4.12) we finally obtain:

$$\partial_{t_0} \left(\rho u_\alpha + \frac{\varepsilon}{2} \mathcal{F}_\alpha \right) + \varepsilon \partial_{t_1}(\rho^{(0)} u_\alpha^{(0)}) +$$
$$\partial_\beta \left(\sum_i \xi_{i\alpha} \xi_{i\beta} f_i^{(0)} + \varepsilon \left(1 - \frac{1}{2\tau} \right) \sum_i \xi_{i\alpha} \xi_{i\beta} f_i^{(1)} + \frac{\varepsilon}{2} \sum_i \xi_{i\alpha} \xi_{i\beta} F_i \right) = F_\alpha. \tag{4.29}$$

In analogy with Subsec. 4.4.1 we recognize that the most reasonable way to introduce the approximation $\partial_t = \partial_{t_0} + \varepsilon \partial_{t_1} + \mathcal{O}(\varepsilon^2)$ is to set $\rho^{(0)} u_\alpha^{(0)} = \rho^m u_\alpha^m = \rho u_\alpha + \varepsilon F_\alpha / 2$. It is easy to verify that assuming $\rho^{eq} = \rho^m$ and $\rho^{eq} u_\alpha^{eq} = \rho^m u_\alpha^m$, the zeroth and first order moments of F_i shall satisfy:

$$\sum_i F_i = M \left(1 - \frac{1}{2\tau} \right), \tag{4.30a}$$

$$\sum_i \xi_{i\alpha} F_i = F_\alpha \left(1 - \frac{1}{2\tau} \right). \tag{4.30b}$$

Hence, we are allowed to write:

$$\partial_t(\rho^m u_\alpha^m) + \partial_\beta \left(\sum_i \xi_{i\alpha} \xi_{i\beta} f_i^{(0)} + \varepsilon \left(1 - \frac{1}{2\tau} \right) \sum_i \xi_{i\alpha} \xi_{i\beta} f_i^{(1)} + \right.$$
$$\left. \frac{\varepsilon}{2} \sum_i \xi_{i\alpha} \xi_{i\beta} F_i \right) = F_\alpha + \mathcal{O}(\varepsilon^2). \tag{4.31}$$

Again, the considerations made for the mass equation in Subsec. 4.4.2 are the same for the momentum equation. In fact, if we did not set $\rho^{(0)}u_\alpha^{(0)} = \rho^m u_\alpha^m$, we would obtain an additional source of error and Eq. 4.31 would become:

$$\partial_t(\rho^m u_\alpha^m) + \partial_\beta\bigg(\sum_i \xi_{i\alpha}\xi_{i\beta}f_i^{(0)} + \varepsilon\bigg(1 - \frac{1}{2\tau}\bigg)\sum_i \xi_{i\alpha}\xi_{i\beta}f_i^{(1)} +$$
$$\frac{\varepsilon}{2}\sum_i \xi_{i\alpha}\xi_{i\beta}F_i\bigg) = F_\alpha - \varepsilon\partial_{t_1}(\varepsilon F_\alpha(\tau - \frac{1}{2}) - \tau\varepsilon\mathcal{F}_\alpha) + \mathcal{O}(\varepsilon^2). \tag{4.32}$$

Similarly to the mass equation, these terms are rigorously zero, if F_α and $\mathcal{F}_\alpha$ do not depend purely on time. However, we will see that also other sources of error arise if $\rho^{(0)}u_\alpha^{(0)} \neq \rho^m u_\alpha^m$.

We notice that in Eq. (4.31), higher order moments of $f_i^{(0)}$, $f_i^{(1)}$ and F_i begin to come up and their computation will be the main problem in what follows.

Thus, we have to derive the expression of these moments in terms of macroscopic density and velocity. In particular, let us focus on the moments of $f_i^{(1)}$. According to Eq. (4.9a) we can write $f_i^{(1)}$ as:

$$f_i^{(1)} = \tau(F_i - \partial_{t_0}f_i^{(0)} - \xi_{i\gamma}\partial_\gamma f_i^{(0)}). \tag{4.33}$$

Accordingly, the second order moment of $f_i^{(1)}$, which appears in Eq. (4.31), can be expressed in terms of the moments of $f_i^{(0)}$ and F_i as:

$$\sum_i \xi_{i\alpha}\xi_{i\beta}f_i^{(1)} = \tau\bigg(\sum_i \xi_{i\alpha}\xi_{i\beta}F_i - \partial_{t_0}\sum_i \xi_{i\alpha}\xi_{i\beta}f_i^{(0)} - \partial_\gamma\sum_i \xi_{i\alpha}\xi_{i\beta}\xi_{i\gamma}f_i^{(0)}\bigg). \tag{4.34}$$

Consequently Eq. (4.31) turns into:

$$\partial_t(\rho^m u_\alpha^m) + \partial_\beta\bigg[\sum_i \xi_{i\alpha}\xi_{i\beta}F_i + \varepsilon\bigg(\tau - \frac{1}{2}\bigg)\bigg(\sum_i \xi_{i\alpha}\xi_{i\beta}F_i - $$
$$\partial_{t_0}\sum_i \xi_{i\alpha}\xi_{i\beta}f_i^{(0)} - \partial_\gamma\sum_i \xi_{i\alpha}\xi_{i\beta}\xi_{i\gamma}f_i^{(0)}\bigg) + \frac{\varepsilon}{2}\sum_i \xi_{i\alpha}\xi_{i\beta}F_i\bigg] = F_\alpha + \mathcal{O}(\varepsilon^2). \tag{4.35}$$

It is now explained the reason why in Subsec. 3.7.3 we required the quadrature formula to preserve the moments of the low Mach number expansion of the Maxwellian up to third order. In fact, we notice that in Eq. (4.35) a third order moment of $f_i^{(0)}$ appears and we would like to compute it correctly. Actually, as properly explained in Appendix A.2, these moments corresponds to those of a Maxwellian neglecting the terms of order $\mathcal{O}(Ma^3)$. This is intuitive indeed, as the Maxwellian distribution function is expanded up to

second order in the Mach number and thus, the expansion is characterized by an error $\mathcal{O}(Ma^3)$. As shown in Appendix A.2, the second and third order moments of $f_i^{(0)}$ are given by:

$$\sum_i \xi_{i\alpha}\xi_{i\beta} f_i^{(0)} = \delta_{\alpha\beta}c_s^2\rho^{(0)} + \rho^{(0)}u_\alpha^{(0)}u_\beta^{(0)}, \tag{4.36a}$$

$$\sum_i \xi_{i\alpha}\xi_{i\beta}\xi_{i\gamma} f_i^{(0)} = c_s^2\rho^{(0)}(\delta_{\alpha\beta}u_\gamma^{(0)} + \delta_{\alpha\gamma}u_\beta^{(0)} + \delta_{\beta\gamma}u_\alpha^{(0)}). \tag{4.36b}$$

Even in this case we realize the importance of setting $\rho^m = \rho^{(0)}$ and $\rho^m u_\alpha^m = \rho^{(0)}u_\alpha^{(0)}$, otherwise we would obtain additional errors. For example, let us consider the case of scheme III, that is the method of shifting velocity in the equilibrium distribution function [4]. For the sake of simplicity, let us also consider $M = 0$ in this example, which means that $\rho = \rho^m = \rho^{eq}$. In this case, it is easy to obtain from Eqs. (4.3) and (4.4) that:

$$u_\alpha^{eq} = u_\alpha^m + \frac{\varepsilon F_\alpha}{\rho}\left(\tau - \frac{1}{2}\right). \tag{4.37}$$

Now, if we insert the previous relationship into the equation of the second order moments, Eq. (4.36a), we obtain:

$$\sum_i \xi_{i\alpha}\xi_{i\beta} f_i^{(0)} = \delta_{\alpha\beta}c_s^2\rho + \rho\left[u_\alpha^m + \frac{\varepsilon F_\alpha}{\rho}\left(\tau - \frac{1}{2}\right)\right]\left[u_\beta^m + \frac{\varepsilon F_\beta}{\rho}\left(\tau - \frac{1}{2}\right)\right]. \tag{4.38}$$

It is clear that extra sources of error arise if we do not set $u_\alpha^m = u_\alpha^{eq}$. Huang *et al.* have shown that these additional terms may play an important role, especially when dealing with multi-phase flows [85]. Thus, from now on we will set $\rho^{(0)} = \rho^m$ and $u_\alpha^{(0)} = u_\alpha^m$.

The insertion of Eqs. (4.36) into Eq. 4.35 yields:

$$\partial_t(\rho^m u_\alpha^m) + \partial_\beta\left(\delta_{\alpha\beta}c_s^2\rho^m + \rho^m u_\alpha^m u_\beta^m\right) + \varepsilon\left(\tau - \frac{1}{2}\right)\partial_\beta\left\{\sum_i \xi_{i\alpha}\xi_{i\beta}F_i -\right.$$

$$\partial_{t_0}(\delta_{\alpha\beta}c_s^2\rho^m + \rho^m u_\alpha^m u_\beta^m) - \partial_\gamma(c_s^2\rho^m[\delta_{\alpha\beta}u_\gamma^m + \delta_{\alpha\gamma}u_\beta^m + \delta_{\beta\gamma}u_\alpha^m])\Big\} + \tag{4.39}$$

$$\partial_\beta\left(\frac{\varepsilon}{2}\sum_i \xi_{i\alpha}\xi_{i\beta}F_i\right) = F_\alpha + \mathcal{O}(\varepsilon^2).$$

Let us focus on the following terms:

$$\partial_\beta\partial_{t_0}(c_s^2\delta_{\alpha\beta}\rho^m) = c_s^2\partial_\alpha\partial_{t_0}\rho^m = c_s^2\partial_\alpha(M - \partial_\gamma\rho^m u_\gamma^m), \tag{4.40}$$

where we have inserted Eq. 4.17.

In addition:

$$\partial_\beta \partial_{t_0}(\rho^m u_\alpha^m u_\beta^m) = \partial_\beta[u_\alpha^m \partial_{t_0}(\rho^m u_\beta^m) + u_\beta^m \partial_{t_0}(\rho^m u_\alpha^m) - u_\alpha^m u_\beta^m \partial_{t_0}\rho^m] =$$
$$= \partial_\beta\{u_\beta^m[F_\alpha - \partial_\alpha(c_s^2\rho^m) - \partial_\gamma(\rho^m u_\alpha^m u_\gamma^m)]+ \tag{4.41}$$
$$u_\alpha^m[F_\beta - \partial_\beta(c_s^2\rho^m) - \partial_\gamma(\rho^m u_\beta^m u_\gamma^m) - u_\alpha^m u_\beta^m[M - \partial_\gamma(\rho^m u_\gamma^m)]\},$$

neglecting the terms of order $\mathcal{O}(u^3)$, i.e., $\mathcal{O}(Ma^3)$, we finally obtain:

$$\partial_\beta\partial_{t_0}(\rho^m u_\alpha^m u_\beta^m) = \partial_\beta[(u_\alpha^m F_\beta + u_\beta^m F_\alpha)-$$
$$c_s^2(u_\alpha^m \partial_\beta \rho^m + u_\beta^m \partial_\alpha \rho^m) - u_\alpha^m u_\beta^m M] + \mathcal{O}(Ma^3). \tag{4.42}$$

Thus, we have introduced a further source of error related to the Mach number. This approximation is necessary indeed, because, as it was previously mentioned, in the low Mach number expansion of the Maxwellian we are not capable of recovering the terms of third or higher order in Ma.

The last term we analyse is:

$$\partial_\beta\partial_\gamma[c_s^2\rho^m(\delta_{\alpha\beta}u_\gamma^m + \delta_{\alpha\gamma}u_\beta^m + \delta_{\beta\gamma}u_\alpha^m)] =$$
$$= \partial_\beta[c_s^2(\rho^m\partial_\beta u_\alpha^m + u_\alpha^m\partial_\beta\rho^m)] + \partial_\beta[c_s^2(\rho^m\partial_\alpha u_\beta^m + u_\beta^m\partial_\alpha\rho^m))] + \partial_\alpha[c_s^2\partial_\alpha(\rho^m u_\gamma^m)]. \tag{4.43}$$

The substitution of these terms into Eq. 4.39 gives:

$$\partial_t\rho^m u_\alpha^m + \partial_\alpha(c_s^2\rho^m) + \partial_\beta(\rho^m u_\alpha^m u_\beta^m) + \varepsilon\tau\partial_\beta\left(\sum_i \xi_{i\alpha}\xi_{i\beta}F_i\right)-$$
$$\varepsilon\left(\tau - \frac{1}{2}\right)\left\{\partial_\alpha[c_s^2(M - \partial_\gamma(\rho^m u_\gamma^m))] - \partial_\beta[(u_\alpha^m F_\beta + u_\beta^m F_\alpha)-\right.$$
$$c_s^2(u_\alpha^m\partial_\beta\rho^m + u_\beta^m\partial_\alpha\rho^m) - u_\alpha^m u_\beta^m M] - \partial_\beta[c_s^2(\rho^m(\partial_\beta u_\alpha^m + \partial_\alpha u_\beta^m)+ \tag{4.44}$$
$$\left. u_\alpha^m\partial_\beta\rho^m + u_\beta^m\partial_\alpha\rho^m)] - \partial_\alpha[c_s^2\partial_\gamma(\rho^m u_\gamma^m)]\right\} = F_\alpha + \mathcal{O}(\varepsilon^2) + \mathcal{O}(Ma^3).$$

At this point, we neglect the term $\varepsilon(\tau-1/2)\partial_\beta(u_\alpha^m u_\beta^m M)$ that is $\mathcal{O}(Ma^2)\mathcal{O}(\varepsilon)$. It should be noted that this term is rigorously zero if $M = 0$. Moreover, we also set a further constraint on F_i:

$$\tau\partial_\beta\left(\sum_i \xi_{i\alpha}\xi_{i\beta}F_i\right) = \left(\tau - \frac{1}{2}\right)[\partial_\alpha(c_s^2 M)] + \partial_\beta(u_\alpha^m F_\beta + u_\beta^m F_\alpha), \tag{4.45}$$

so that these terms cancel each other out into Eq. (4.44). Thus, the F_i should satisfy Eqs. (4.30) and (4.45) and it can be shown that these constraints are fulfilled by [1]:

$$F_i = w_i\left(1 - \frac{1}{2\tau}\right)\left(M + \frac{\boldsymbol{F}\cdot\boldsymbol{\xi_i}}{c_s^2} + \frac{\xi_{i\alpha}\xi_{i\beta} - c_s^2\delta_{\alpha\beta}}{2c_s^4}F_\alpha u_\beta\right). \tag{4.46}$$

As a consequence, Eq. (4.44) turns into:

$$\partial_t(\rho^m u_\alpha^m) + \partial_\beta(\rho^m u_\alpha^m u_\beta^m) = -\partial_\alpha(c_s^2 \rho^m) + \partial_\beta\left[\varepsilon\left(\tau - \frac{1}{2}\right)c_s^2\rho^m\partial_\beta u_\alpha^m\right] +$$
$$\partial_\beta\left[\varepsilon\left(\tau - \frac{1}{2}\right)c_s^2\rho^m\partial_\alpha u_\beta^m\right] + F_\alpha + \mathcal{O}(\varepsilon^2) + \mathcal{O}(Ma^3) + \mathcal{O}(Ma^2)\mathcal{O}(\varepsilon). \tag{4.47}$$

The comparison between Eq. (4.47) and Eq. (4.16) allows the identification of the dynamic viscosity of the model:

$$\mu = \varepsilon\left(\tau - \frac{1}{2}\right)c_s^2\rho^m, \tag{4.48}$$

which was already anticipated in Subsec. 3.7.3. Therefore, the viscosity depends on the following parameters:

- the time step size δt and the spatial step size δx, since $c_s^2 \sim \delta x^2/\delta t^2$;

- the relaxation parameter τ;

- the lattice model, which defines the proportionality constant between c_s and $\delta x/\delta t$ (for the D2Q9 it is $1/\sqrt{3}$).

Finally, the BGK Lattice Boltzmann method recovers the following momentum equation:

$$\partial_t(\rho^m u_\alpha^m) + \partial_\beta(\rho^m u_\alpha^m u_\beta^m) = -\partial_\alpha(c_s^2 \rho^m) + \partial_\beta(\mu\partial_\beta u_\alpha^m) +$$
$$\partial_\beta(\mu\partial_\alpha u_\beta^m) + F_\alpha + \mathcal{O}(\varepsilon^2) + \mathcal{O}(Ma^3) + \mathcal{O}(Ma^2)\mathcal{O}(\varepsilon). \tag{4.49}$$

Comparing again Eq. (4.49) to Eq. (4.16), it is clear that the BGK model predicts a zero bulk viscosity (assuming the definition given in Eq. (4.14)).

From Eq. (4.48), we clearly see the problem of the Chapman-Enskog expansion applied to the LBE. In fact, at the beginning of the procedure we have pointed out that, in order to ensure a mathematical consistency of the method, we need to assume $\tau = \lambda/\delta t = const$, along with the assumption of convective scaling $\delta x \sim \delta t$. This means that when $\delta t \to 0$, also $\mu \to 0$. Thus, by means of the Chapman-Enskog expansion, we have actually shown that the LBE is able to recover the compressible Navier-Stokes equation in the limit of low viscosity. In order to obtain more general results, different methods have been proposed in literature, which will be briefly described in the next section.

As a concluding remark, it is worth pointing out that in this procedure the effect of boundary conditions has not been taken into account.

4.5 Beyond the Chapman-Enskog expansion

By means of the Chapman-Enskog expansion, the Lattice Boltzmann equation is able to recover the macroscopic Navier-Stokes equations. However, we have also pointed out that this procedure is based on the assumption of convective scaling $\delta t \sim \delta x$ and in addition, it is rigorously valid in the limit of low viscosity. This has lead to employ different methods to recover the Navier-Stokes equation from the LBE.

Junk [86] identified the diffusive scaling $\delta t \sim \delta x^2$ as the natural choice for the analysis of the LBE. However, even this method is based on an asymptotic analysis. Holdych *et al.* [87] attempted to recover the Navier-Stokes equations without requiring a further relationship between its parameters, in order to obtain a general order of convergence of the methods. In particular, these parameters are $\tau, \delta x$ and δt, but they are not independent because of the viscosity relationship Eq. 3.8. In addition, in [87], no asymptotic analysis are employed in this procedure. In this case, considering δx and δt as the independent parameters in the viscosity relationship Eq. 3.8, the error of the LBE in the continuity equation, denoted by C.E. (Continuity Error) and momentum equation, denoted by M.E. (Momentum Error) should be given in the $\mathcal{O}$ notation and in the incompressible limit by:

$$C.E. = \mathcal{O}(\delta x^4) + \mathcal{O}(\delta t^2) + \mathcal{O}((\delta t/\delta x)^2), \tag{4.50a}$$

$$M.E. = \mathcal{O}(\delta x^2) + \mathcal{O}(\delta t^2) + \mathcal{O}((\delta t/\delta x)^2), \tag{4.50b}$$

where $\delta t/\delta x$ is clearly proportional to Ma. This result has been obtained in [87] without considering the presence of a forcing term and the influence of boundary conditions. The details of the sources of error can be found in [87]. In the case of diffusive scaling $\delta t \sim \delta x^2$ it is clear that the error on the continuity equation and the momentum equation becomes both $\mathcal{O}(\delta x^2)$.

Chapter 5

Boundary conditions in LBM

As for any other numerical method, boundary conditions play a key role for the success of Lattice Boltzmann methods. Boundary conditions are needed to solve any partial differential equation, and they are supposed to model the interaction between the system and the external environment. Thus, it is not surprising that also Lattice Boltzmann methods require boundary conditions, as in Chap. 3 we have shown in details how the Lattice Boltzmann equation can be viewed as a special discretization of the Boltzmann equation.

In this chapter, initially, the answer to the question *"what do boundary conditions mean for LBM?"* is provided, analysing also the different philosophies of boundary conditions.

Then, we will analyse the Bounce-Back rule, which is the most widely used scheme to model the interaction with solid boundaries for its simplicity of coding. In particular, some drawbacks of the Bounce-Back rule, when used together with the BGK model, are shown. These shortcomings are particularly annoying for porous media applications and should be carefully tackled.

The periodic boundary conditions are also presented, because they will be used in the numerical simulations.

Afterwards, we will focus on the issue of imposing macroscopic quantities, such as pressure and velocity, on a boundary node. A general and rather simple analysis inspired by Bennett's work [88] will help us to understand which macroscopic quantities shall be imposed simultaneously and which not. In this framework, we will present the Zou-He boundary conditions, which have proved to be very efficient especially for the 2D case.
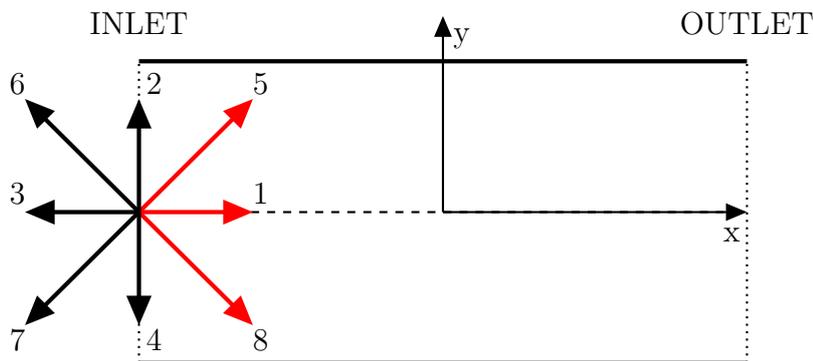
Figure 5.1. Inlet node of a two-dimensional channel with the D2Q9 lattice model. The red arrows identify the velocities, whose distribution functions are unknown.

5.1   Meaning of boundary conditions in LBM

In order to understand what boundary conditions mean in Lattice Boltzmann methods, let us refer to the D2Q9 lattice model and let us consider an inlet node of a two-dimensional channel, as shown in Fig. 5.1. It is clear that after a streaming process in this node the distribution functions f_0, f_2, f_3, f_4, f_6 and f_7 are known, while f_1, f_5 and f_8, which come from the external environment, are still to be determined. Thus, what boundary conditions do in LBM is nothing but providing a rule, i.e., a set of equations, to determine the incoming distribution functions. Obviously, similar considerations can be drawn for outlet nodes and wall nodes.

From the macroscopic point of view, we are certainly allowed to state that in LBM, boundary conditions have not got a straightforward physical meaning. In conventional fluid dynamics, where the Navier-Stokes equations are solved directly, boundary conditions regard pressure and velocity, which take part to the equations. In LBM, instead, boundary conditions for the unknown distribution functions need to be prescribed.

From an analysis of the different schemes proposed in literature, a categorisation into two broad categories of boundary conditions is suggested:

- Boundary conditions which try to model the interaction between the gas and external environment. The Bounce-Back scheme, described in the following section, and reflection schemes, such as the one proposed in [89], belong to this category.

- Boundary conditions which try to translate the macroscopic conditions in terms of the distribution functions. We number among this category the Inamuro boundary condition [26], the finite difference scheme proposed by Skordos [25], the regularized boundary dynamics developed

by Lätt [27] and the aforementioned Zou-He method [24].

It is worth pointing out that methods such as those proposed by Lätt and Skordos do not prescribe only the unknown distribution functions, but they provide a new value to all the f_i at the boundary node. Moreover, all these methods are developed for straight boundaries, while in practical problems we may deal with curved boundaries. In this case, the rigid lattice structure of LBM represents a drawback indeed, because we are not free to adapt the mesh to the geometry as it happens with finite volume methods. For this reason, interpolation or extrapolation methods are needed for these boundaries. Examples of boundary conditions for curved boundaries are the schemes proposed by Mei *et al.* in [90] and by Bouzidi *et al.* in [91].

5.2 Wall interaction: the Bounce-Back rule

The Bounce-Back rule is a scheme supposed to model the interaction between the gas and the solid wall boundary. The idea behind this rule is rather simple and also suggested by the name itself: particles in these nodes reverse their velocities and are reinjected into the fluid domain.

From this basic idea, several Bounce-Back schemes have come out [22]. Here, we will focus only on the one used in this thesis. This scheme is illustrated in Fig. 5.2 and it is translated mathematically by the following equation:

$$f_{\bar{q}}(\boldsymbol{x_b}, t + \delta t) = f_q^*(\boldsymbol{x_b}, t), \tag{5.1}$$

where $\boldsymbol{x_b}$ is the coordinate vector of a fluid node bordering a Bounce-Back node; $\bar{q}$ denotes a generic inward distribution function, while q its outward counterpart; the symbol * means that the distribution function is evaluated after the collision step.

In Fig. 5.2, the Bounce-Back nodes are the black ones. They shall not be considered as fluid nodes, but "logic" nodes, indeed. When a particle try to access these nodes through a natural streaming process, they are reinjected into the fluid domain according to the aforementioned rule.

Thus, the Bounce-Back rule is certainly a very simple to code and this is its main strong point.

5.2.1 Geometry dependency on relaxation parameters
Though its simplicity of coding, the Bounce-Back rule does not lack drawbacks and the main one is certainly a slip-velocity dependent on the relaxation parameters of the model. If we consider a two-dimensional Hagen-Poiseuille flow and we assume that the wall is placed half-way between the last fluid node and the Bounce-Back node, the slip velocity at the wall is

(a) *Time t: before collision*

(b) *Time t: after collision*

(c) *Time t + δt*
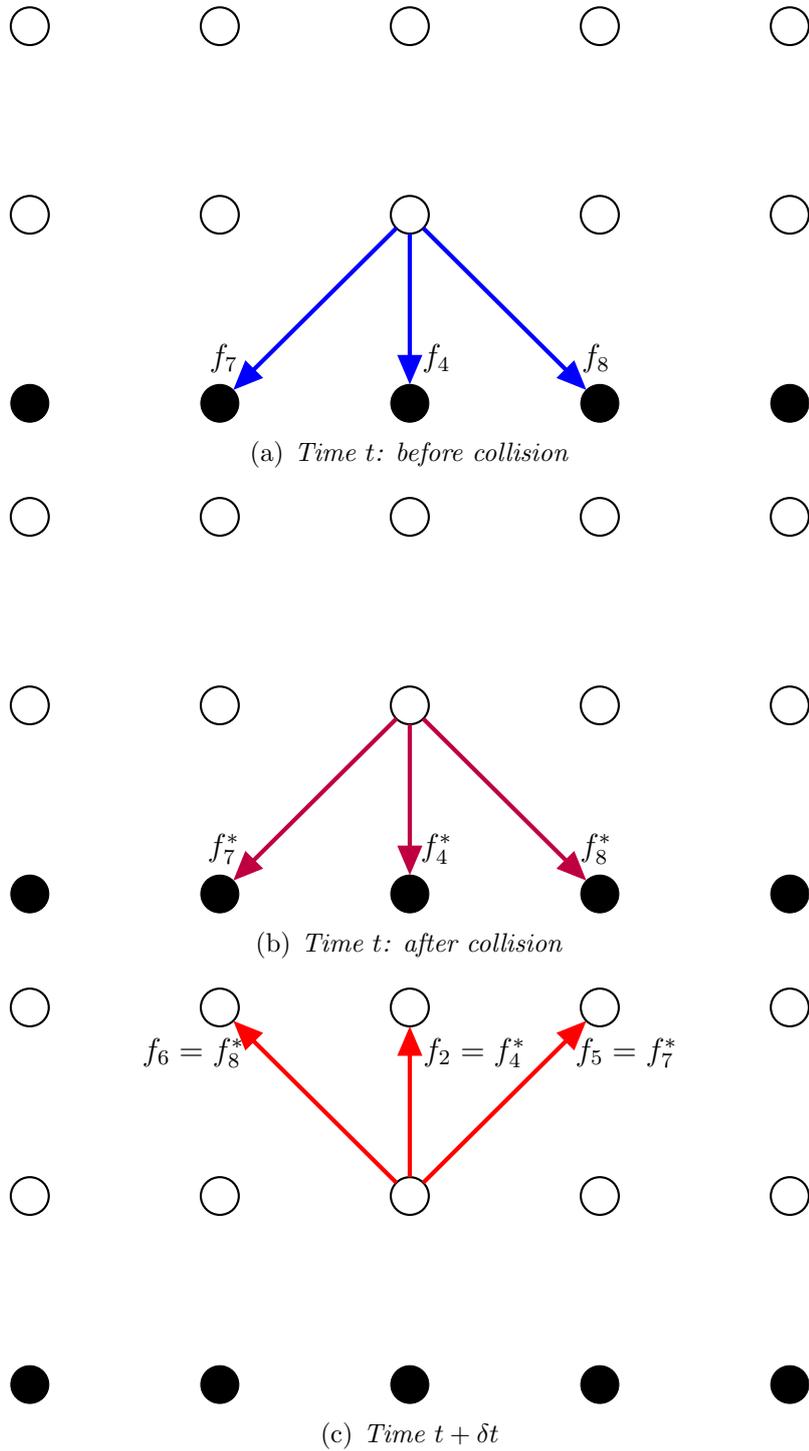
Figure 5.2. Sketch of the Bounce-Back process for a bottom wall node: during the streaming step, the unknown inward distributions f_2, f_5 and f_6 are set equal to the post-collision value of the distributions related to the opposite outward velocities, i.e. f_4^*, f_7^* and f_8^*

given by [92]

$$U_s = \frac{1}{4}\left(\frac{8}{s_q} - \frac{8 - s_\nu}{2 - s_\nu}\right)G\delta t, \qquad (5.2)$$

where $G = |\nabla p|/\rho$, s_ν and s_q are the relaxation parameters of the MRT model defined in Sec. 3.8. The slip velocity of different Bounce-Back schemes are properly analysed in [79]

From Eq. (5.2), it is clear that in general the Bounce-Back rule does not yield a zero slip velocity at the wall, which is what we would like to obtain in case of an incompressible flow. The velocity is actually zero somewhere between the last fluid node and the Bounce-Back node, but this position is function of s_ν and s_q. Hence, the geometry of the system varies with s_ν and s_q.

In porous media applications, this is a very annoying drawback, indeed. In fact, the permeability of a porous media, which is its main physical quantity, is function of the geometry only for Stokes flow, and consequently it is dependent on the relaxation parameters. Therefore, the value of the relaxation parameters shall be carefully tuned in order to obtain a low slip velocity at the half-way wall.

It is worth noting that Eq. (5.2) is valid in case of Hagen-Poiseuille flow and it is not general. However, it is good practice to take Eq. (5.2) as reference and to tune the relaxation parameters accordingly.

As we know from Sec. 3.8, the BGK model can be viewed as a MRT model with all the relaxation parameters equal to ω. In this case, Eq. (5.2) turns into:

$$U_s = \frac{1}{4}\left(\frac{\omega^2 - 16\omega + 16}{\omega(2 - \omega))}\right)G\delta t = \frac{48\nu^2 - 1}{8\nu}G\delta t, \qquad (5.3)$$

where we recall that $\nu = (1/\omega - 1/2)/3$. Thus, in this case, the condition which gives a zero slip velocity is $\nu^2 = 1/48$, corresponding to $\omega = 1,071796\ldots$ and $\tau = 1/\omega = 0.9330127\ldots$. In general it is good practice to choose ω approximately 1.

The MRT model allow us to tune the parameters so that U_s is always zero. This condition is obviously fulfilled when:

$$s_q = \frac{8(2 - s_\nu)}{8 - s_\nu}, \qquad (5.4)$$

which gives rise to the so-called Two-Relaxation-Time (TRT) model [30]: all the parameters are equal to s_ν, except for s_q given by Eq. (5.4). Hence, the TRT model allows more freedom in the choice of viscosity.

Anyway, if the refinement is carried out by means of a diffusive scaling in which $\delta t \sim \delta x^2$, from Eq. (5.2) it is straightforward that also $U_s \sim \delta x^2$ and

thus, the effect of this drawback rapidly decrease when $\delta x \to 0$ independently from the choice of s_ν and s_q.

As a concluding remark of this section, let us analyse the reason of the non-zero slip velocity provided by the Bounce-Back scheme. In Sec. 5.1 we have included the Bounce-Back rule into the category of boundary conditions that do not prescribe a macroscopic quantity at the relative node, but try to model the interaction with the external environment (in this case the wall). Thus, it is not surprising that the velocity is actually not zero. However, it is shown in [93], and also reported in [82], that the slip velocity of a gas is given by:

$$U_s = \sigma K n H \partial_y u|_w, \qquad (5.5)$$

where σ is a coefficient dependent on the model of interaction between gas particles and wall; H is the height of the channel; Kn is the Knudsen number that for an ideal gas is proportional to the ratio between Mach and Reynolds numbers:

$$Kn \sim \frac{Ma}{Re} = \frac{\nu}{Hc_s}. \qquad (5.6)$$

Hence, taking into account Eqs. (5.3), (5.5) and (5.6), two remarks should be pointed out:

- the velocity of a gas at wall is never exactly zero;

- the velocity of a gas at wall increases with Kn and thus with ν, as it happens for the slip velocity predicted by the Bounce-Back scheme (5.3), though the law is different.

Accordingly, we conclude that the slip velocity due to the Bounce-Back scheme shows common features with the real slip velocity of an ideal gas, since the BB rule somehow tries to model the wall-gas interaction.

5.3   Periodic boundary conditions

The periodic boundary conditions are very simple and should be applied when the system is periodic in one or more directions. In general in this kind of problems we are able to identify an elementary geometry which repeats itself infinite times. Thus, the study of the whole system reduces to the study of this fundamental cell.

Let us focus on Fig. 5.3. The periodic boundary conditions for the upper and lower boundary are represented by the following equations:

$$f_7(\boldsymbol{x_u}, t) = f_7(\boldsymbol{x_l}, t), \quad f_4(\boldsymbol{x_u}, t) = f_4(\boldsymbol{x_l}, t), \quad f_8(\boldsymbol{x_u}, t) = f_8(\boldsymbol{x_l}, t), \quad (5.7a)$$

$$f_5(\boldsymbol{x_l}, t) = f_5(\boldsymbol{x_u}, t), \quad f_2(\boldsymbol{x_l}, t) = f_2(\boldsymbol{x_u}, t), \quad f_6(\boldsymbol{x_l}, t) = f_6(\boldsymbol{x_u}, t), \quad (5.7b)$$
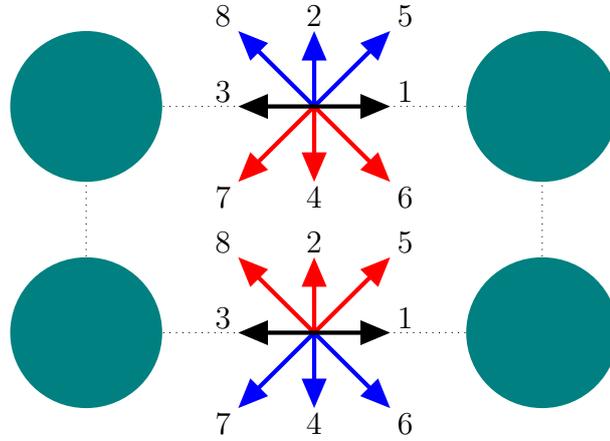
Figure 5.3. Graphical representation of periodic boundary conditions for a regular array of disks.

where $\boldsymbol{x_u}$ and $\boldsymbol{x_l}$ denote, respectively, the coordinates of a generic node belonging to the upper or lower boundary. It is clear that periodic boundary conditions consist in copying the unknown distribution functions with those at the opposite boundary.

5.4 Boundary conditions from moments' perspective

In Sec. 3.8, we have seen how the Lattice Boltzmann methods can be formulated in terms of appropriate independent moments of the distribution functions f_i. Therefore, the boundary conditions can also be expressed from the moments' point of view and not directly on the f_i. In what follows, we will analyse which moments can be prescribed simultaneously on a certain boundary and which not, exploiting the ideas suggested by Bennett in [88].

Let us consider an inlet node on a straight boundary like that portrayed in Fig. 5.1 and let us focus our attention on boundary conditions which provide the three unknown distribution functions f_1, f_5 and f_8 without modifying the others. Moreover, let us write how these distribution functions appear into the independent moments identified in Sec. 3.8 and in particular in Eq. (3.86):

$$\rho \to f_1 + f_5 + f_8, \tag{5.8a}$$

$$j_x \to f_1 + f_5 + f_8, \tag{5.8b}$$

$$j_y \to f_5 - f_8, \tag{5.8c}$$

$$\rho(e + 1/2u^2) \to f_1 + 2(f_5 + f_8), \tag{5.8d}$$

$$2p_{xx} \to f_1, \tag{5.8e}$$

$$p_{xy} \to f_5 - f_8, \tag{5.8f}$$

$$\phi_{xy} \to f_5 + f_8, \tag{5.8g}$$

$$\phi_{yx} \to f_5 - f_8, \tag{5.8h}$$

$$\varepsilon \to f_5 + f_8. \tag{5.8i}$$

Analysing these dependencies it is very easy to realize which set of moments cannot be imposed simultaneously. For example, it is clear that it is not possible to set both density ρ, i.e., pressure, from Eq. (3.34), and the x-component of momentum density j_x, because they fix the value of the group $f_1 + f_5 + f_8$, while it is possible to set ρ and j_y. For this reason, we are not allowed to fix pressure and the velocity vector at the same time.

Moreover, it is not sufficient to provide ρ and j_x, for example, because a further independent equation is needed in order to define f_1, f_5 and f_8 univocally. This additional equation might regard another moment or it might be just a modelling equation, as it happens with the Zou-He boundary conditions which we will be describing in the following section.

5.5   Zou-He boundary conditions

In what follows, we will refer directly to the original paper of Zou and He [24], in which this kind of boundary condition appeared for the first time.

Let us consider again the inlet node of Fig. 5.1. We will analyse the case of pressure boundary condition, in which the density ρ is imposed, while the component of the velocity parallel to the surface, in this case u_y, is set to zero. Let us write the equations for ρ, ρu_x and ρu_y:

$$\begin{cases} \rho = f_0 + f_1 + f_2 + f_3 + f_4 + f_5 + f_6 + f_7 + f_8, \\ \rho u_x = f_1 - f_3 + f_5 - f_6 - f_7 + f_8, \\ \rho u_y = f_2 - f_4 + f_5 + f_6 - f_7 - f_8. \end{cases} \tag{5.9}$$

Gathering together the unknown distributions and setting $u_y = 0$, we obtain:

$$\begin{cases} f_1 + f_5 + f_8 = \rho - (f_0 + f_2 + f_3 + f_4 + f_6 + f_7), \\ f_1 + f_5 + f_8 = \rho u_x + (f_3 + f_6 + f_7), \\ f_5 - f_8 = -f_2 + f_4 - f_6 + f_7. \end{cases} \qquad (5.10)$$

The subtraction of the first equation to the second one of Eqs. (5.10) yields:

$$u_x = 1 - \frac{f_0 + f_2 + f_4 + 2(f_3 + f_6 + f_7)}{\rho}. \qquad (5.11)$$

Hence, it is clear that imposing ρ implies fixing also the x-component of the velocity vector. However, we have only two independent equations so far and we need a further equation to close the system. Zou & He proposed to impose a Bounce-Back condition for the non-equilibrium component of the distribution normal to the surface, that in this case is f_1. This condition is translated mathematically by:

$$f_1(\boldsymbol{x_i}, t) - f_1^{eq}(\boldsymbol{x_i}, t) = f_3(\boldsymbol{x_i}, t) - f_3^{eq}(\boldsymbol{x_i}, t), \qquad (5.12)$$

where $\boldsymbol{x_i}$ denotes the coordinates of an inlet node. It should also be remarked that all the equilibrium distributions are determined once ρ and $\boldsymbol{u}$ are fixed, as in this case. Thus, it is straightforward to compute the equilibrium functions needed from Eq.(3.75).

Eventually, we obtain the three independent equations of the Zou-He scheme, for an inlet node with pressure boundary conditions:

$$\begin{cases} f_1 = f_1^{eq} + f_3 - f_3^{eq}, \\ f_1 + f_5 + f_8 = \rho - (f_0 + f_2 + f_3 + f_4 + f_6 + f_7), \\ f_5 - f_8 = -f_2 + f_4 - f_6 + f_7. \end{cases} \qquad (5.13)$$

Similar equations can be obtained for velocity boundary conditions in which u_x and u_y are fixed. The treatment of corner nodes and the extension to the $3D$ case are properly analysed in the original paper [24].

Although, the meaning and the idea behind the non-equilibrium Bounce-Back is not clear and, as also remarked by Bennett [88], they are not explained by Zou & He in [24], the Zou-He boundary conditions have proved to be very accurate and also very simple to code, especially for the two-dimensional case [24].

Chapter 6

Porous Media applications

In this chapter, we will start to get familiar with the Lattice Boltzmann simulations from a practical point of view, carrying out simulations for several geometries. In particular, we will deal with the issue of setting appropriate simulation parameters, keeping in mind the results of the previous chapters. For this reason, an accurate analysis of the error of the simulations will be given, comparing different types of collision models, different schemes of boundary conditions and also two ways of scaling the time and spatial steps. In order to carry out these analyses, we definitely need to study fluid dynamics problems whose solution is already known or well approximated.

Our first study will be the two-dimensional Hagen-Poiseuille flow already presented in Sec. 2.2. The reasons which have justified this choice are three-fold. First of all, the analytical solution of the flow is known and given by Eqs. (2.8), hence, the analysis of the error is straightforward. In the second instance, in Sec. 2.4, we have seen how the Carman-Kozeny model is based on the Hagen-Poiseuille equation, and thus this kind of flow plays an important role in porous media. In general, we are allowed to say that flow in porous media at low Reynolds number shows common features with the Hagen-Poiseuille flow and we can consider it as a preliminary reference case. Finally, in the LBM literature the flow in a two-dimensional straight channel is widely studied [79, 24, 94, 75, 95].

As a second test case, we will deal with a flow over a hexagonal and periodic array of disks (or disks in 2D). This is a first example of porous medium, whose study is simplified because of the periodic nature of the problem, which allows us to consider only an elementary geometry and to use periodic boundary conditions. Even for this geometry, there exists some analytical approximated formulas for permeability, so we can compare them with the Lattice Boltzmann simulations, as well. This study takes inspiration from the works of Yadzchi *et al.* [96] and Pan *et al.* [35]. In the former, the study of the hexagonal array of disks is carried out using a finite element

method, while in the latter LBM are used for a body-centred cubic array of spheres.

Finally, we will analyse a porous medium made up of a random array of disks. For this geometry, the Lattice Boltzmann method will be used mainly to verify the validity of the Carman-Kozeny model and to determine the Reynolds number for which the flow does not obey the Darcy's law any more. In addition, the issue of "*how to compute tortuosity*" is addressed.

In Sec. 6.1, a general description of Palabos, the open source library used to carry out the simulation is provided.

Before going into the results of the simulation, a detailed explanation of the simulation setup is provided, highlighting also the main difficulties in this process. Throughout this chapter, for the sake of generality, we will always use dimensionless quantities.

6.1 The tool: Palabos

All the simulations in this thesis are carried out by means of Palabos. Palabos is an open-source library written in C++, specifically developed for Lattice Boltzmann methods. Palabos implements the main lattice models and boundary conditions, and its open-source nature allows also the development of new models to be embedded in its framework of functions and classes. In the current versions, Palabos lacks a graphical interface, and consequently also the user needs to struggle with some programming. However, tutorials and showcases are available for several topics, which definitely helps in setting up new problems.

The programming paradigm of Palabos is to exploit the inherent parallelization of Lattice Boltzmann methods and at the same time to allow the development of new models. In fact, by following some programming rules, it is possible to write new Lattice Boltzmann schemes, without taking care of the issue of parallelization of the code, which is done automatically. The main development guideline is that the new models, or in general new contributions to the library, should be implemented by means of the functions and classes already present in the Palabos distribution, exploiting the object-oriented structure of the library itself.

6.2 Simulation setup

First of all, let us introduce the concept of lattice units. It is a system of units which is very convenient in case of regular structures, like typical lattice structure of LBM. In this system the spatial step δx and the time step δt

are both set to unity, $\delta x = \delta t = 1$. Sometimes, it is also convenient to set the density equal to unity at inlet, for example. Obviously, this establishes a direct correspondence between the mass in physical [1] or dimensionless units and the mass in lattice units, which is needed to convert the value of the distribution functions. We will refer to this units of mass as mu in this chapter.

Thus, considering the case of the D2Q9 lattice shown in Fig. 3.4, the distance between two neighbouring nodes in lattice units is equal to 1 or $\sqrt{2}$, and in addition, the number of iterations corresponds to the time in lattice units. Usually, the simulations are carried out numerically using these units, and then the results are converted in dimensionless units and, eventually, in physical units.

It is straightforward that in lattice units, the BGK Lattice Boltzmann equation Eq. (3.76) turns into:

$$f_i(\boldsymbol{x} + \boldsymbol{\xi_i}, t + 1) - f_i(\boldsymbol{x}, t) = -\frac{1}{\tau}(f_i(\boldsymbol{x}, t) - f_i^{eq}(\boldsymbol{x}, t)), \quad i = 0, 1, \ldots, 8, \quad (6.1)$$

where the discrete velocities $\boldsymbol{\xi_i}$ are of course given by Eqs. (3.68) with $c = \delta x/\delta t = 1$, and the equilibrium distribution functions f_i^{eq} are computed from Eq. (3.75) using quantities in lattice units.

From Eq. (3.69) and from Eq. (3.8), it is clear that in lattice units the speed of sound c_s and the kinematic viscosity ν are given by $c_s = 1/\sqrt{3}$ and $\nu = (2\tau - 1)/6$. From now on we will denote the quantities in lattice units with the subscript "lu".

Let us now focus our attention on the simulation setup. The simulations share the following five general features:

- the simulations are based on the lattice D2Q9;

- the steady state is assumed to be reached when the Value Tracer, an approriate parameter defined in Palabos to detect the steady state, falls below a user-defined value;

- the Bounce-Back rule described in Sec. 5.2 is used to model the gas-wall interaction. Accordingly, the geometry is provided simply in the form of a matrix of 0 and 1;

- constant pressure boundary conditions, like the Zou-He presented in Sec. 5.5, are imposed at inlet and outlet. Thus, we follow the approach of fixing the ΔP and obtaining the Darcy's velocity as a result of the simulations;

---

[1]By physical units, we mean the International System of Units

- at time $t = 0$ the flow is initialized with a linear pressure gradient, i.e., a linear density gradient, with ΔP between inlet and outlet equal to that imposed by the boundary conditions when $t \geq 0$; all the components of the velocity vector are initialized to zero. At $t = 0$, the distribution function f_i are evaluated at equilibrium;

In addition, it is worth pointing out that we want to simulate incompressible flows, using the Lattice Boltzmann method which is a compressible scheme.

In order to understand how to choose the parameters of the simulation, let us analyse the simple two dimensional Hagen-Poiseuille flow. As it was stated before, throughout this chapter we would like to obtain results in dimensionless units, as those introduced in Sec. 2.1, and therefore, the quantity without subscript are all intended as dimensionless. Let us suppose that we have a grid of $N_x = 51$ and $N_y = 52$ lattice nodes. Obviously the upper and lower nodes are Bounce-Back nodes, and in Sec. 5.2, we have seen in this scheme that the wall is placed half-way between the last fluid node and the Bounce-Back node. Thus, we are actually simulating a channel of height $H_{lu} = 50$ and length $L_{lu} = 50$. We take as reference length the height of the channel $L_0 = H$ and we obtain that the spatial step is $\delta x = 1/H = 0.02$.

As reference velocity, we need to relate a velocity to the ΔP imposed between inlet and outlet. From this velocity a Reynolds number is defined. In fact, in the opinion of the author, it would be awkward to compute the Reynolds number directly during the *post processing* phase, since it would be affected by error and it would depend on the parameters of the simulations, leading to a not univocally defined value. Hence, it is wise to establish a reference velocity known *ex ante* the numerical simulations.

For the case of Hagen-Poiseuille flow the choice is rather natural, and we set as reference velocity the Darcy's velocity predicted by the analytical solution of the flow given in Eq. (2.10):

$$U_{0lu} = -\frac{R_{lu}^2}{3\mu_{lu}}\frac{\Delta P_{lu}}{L_{lu}}, \qquad (6.2)$$

where we remember that $R_{lu} = H_{lu}/2$. We will see in the following section, that a similar choice will be made for the case of the hexagonal and random array of disks.

It is also clear that assuming the reference density to be unity in lattice units, it follows that $\mu_{lu} = \nu_{lu}$. The previous definitions allow to establish a direct correspondence between the Reynolds number and the ΔP if we fix the spatial step and the kinematic viscosity in lattice units, ı.e., τ.

In fact, let us suppose that we want to simulate a flow with a given Reynolds number Re. The kinematic viscosity in dimensionless units is def-

initely $\nu = 1/Re$, and the substitution into Eq. (3.8) yields:

$$\delta t = Re\,\nu_{lu}\,\delta x^2. \tag{6.3}$$

If we fix the relaxation parameter τ, we finally obtain the time step in dimensionless units δt. Accordingly, the reference velocity in lattice units is also determined:

$$U_{0lu} = \frac{\delta t}{\delta x}. \tag{6.4}$$

Now, we can use Eq. (6.2) to compute the ΔP between inlet and outlet in lattice units and finally complete the simulation setup.

However, we have to take into account that the error of the Lattice Boltzmann simulations is definitely associated also to the Mach number Ma given by:

$$Ma = \frac{U_{lu}}{c_{slu}} = \sqrt{3}\frac{\delta t}{\delta x} = \sqrt{3}\,Re\,\nu_{lu}\,\delta x. \tag{6.5}$$

The Mach number shall always be taken under control, since it could affect the results of the simulations. Thus, if the Mach number is considered too high we need to reduce either the δx or τ. Reducing the Reynolds number is in general not an option since it would change the problem. However, if we are interested in computing the permeability of a porous medium, we could change also the Reynolds number, as long as it is sufficiently low to preserve the validity of the Darcy's law.

From the previous description, we realise that the simulation setup of Lattice Boltzmann simulations could be tricky and from the users' point of view, a little of experience is required. The following simulations will help us to get familiar with this process.

6.3   Convective and diffusive scaling

In Sec. 4.5, we have seen how the sources of error δx, δt and Ma appear in the error formula for an incompressible flow Eq. (4.50). Furthermore, in Chap. 4, we have carried out the Chapman-Enskog expansion whose starting point was the convective scaling $\delta t \sim \delta x$.

However, two remarks should be emphasized for the convective scaling. First of all, since by definition $\delta t/\delta x = const.$, during this scaling the Mach number is kept constant, as well as the related error. Consequently, in the convective scaling, we cannot achieve a perfect convergence. For this reason, it is wise to assume a sufficiently low Mach number at the beginning of the simulations. In addition, if we consider Eq. (6.5) it is evident that if we want to keep Ma constant, and also the Reynolds number constant during the scaling, when δx is decreased, it is necessary to increase the viscosity, namely
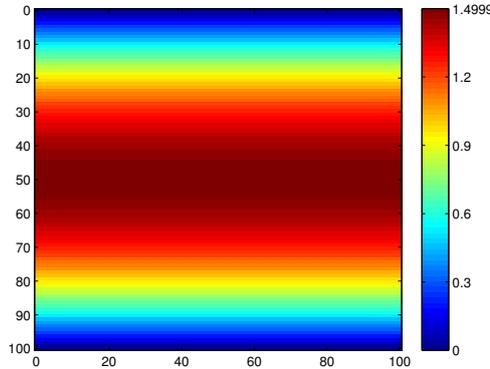
Figure 6.1. Velocity field of the Hagen-Poiseuille flow when the steady state is reached.

τ [2]. Nevertheless, we have to take into account the additional problem of the slip velocity at wall, when we use Bounce-Back boundary conditions. For instance, for the BGK model we have seen in Subsec. 5.2.1 that U_s is rigorously zero when $\tau = 0.9330127\ldots$, and considering Eq. (5.3), during the convective scaling we shall keep under control the value of τ, which shall not be much greater than unity.

Another possible scaling is the diffusive scaling, where $\delta t \sim \delta x^2$. In this case, also the Mach number tends to zero when $\delta x \to 0$. The error of the Lattice Boltzmann method becomes simply $\mathcal{O}(\delta x^2)$. Unlike the convective scaling, the diffusive scaling allow us to choose a fixed relaxation parameter τ and keep also constant the Reynolds number. In fact, from Eq. (6.3) if we fix the Reynolds number and the viscosity in lattice units, we obtain a diffusive scaling $\delta t = a\,\delta x^2$, with $a = Re\,\nu_{lu}$. Thus, we can choose τ minimizing for example the slip velocity at wall, or from stability considerations.

The diffusive scaling guarantees a perfect convergence of the error, since all the sources of error approach zero. Nevertheless, the condition $\delta t \sim \delta x^2$ increases dramatically the number of iterations needed to reach the steady state compared to the convective scaling.

6.4 Hagen-Poiseuille simulations

The Hagen-Poiseuille flow is investigated using three collision models:

---

[2]On the contrary, it should be remembered that we required a fixed τ in the Chapman-Enskog procedure, which lead to a variable viscosity.

1. the BGK model;

2. the TRT model we have described in Subsec. 5.2.1;

3. the Multiple-Relaxation-Time model with optimized stability introduced by Lallemand & Luo in [41]; this model makes use of the following relaxation parameters: $s_{p_{xx}} = s_{p_{xy}} = 1/\tau$, $s_e = 1.63$, $s_{\varepsilon} = 1.14$ $s_{q_x} = s_{q_y} = 1.92$.

The Zou-He boundary conditions are used to impose pressure at inlet and outlet. It would be interesting to analyse the error for different boundary condition scheme, but we will tackle this issue for the case of hexagonal array of cylinders in Sec. 6.5. Before starting to comment the results, it is worth pointing out that all the figures are related to quantities in dimensionless form, using as reference length the height of the channel H and as reference velocity the average cross sectional velocity U_0 obtained from Eq. (6.2).

Fig. 6.1 shows the visualization of the velocity field at the end of the simulation, and it has been obtained using the BGK model with $N_x = 101$, $N_y = 102$, $\tau = 1$ and $Ma = 0.0001$. In this figure, we can catch sight of the typical parabolic profile of the Hagen-Poiseuille flow, as well as we notice that the maximum velocity is very close to the theoretical value of 1.5 predicted by Eq. (2.10).

Figs. 6.2 are obtained with the BGK model keeping fixed $Ma = 0.0001$ and $\tau = 1$. In this case, according to Eq. (6.5), the Reynolds number is inversely proportional to δx, $Re \sim 1/\delta x$, and from Eq. (6.3) this leads to a convective scaling $\delta t \sim \delta x$, with variable Reynolds number. The variation of the Reynolds number is not a great issue as long as the flow remains laminar. In our simulations the maximum Reynolds number for $\delta x = 1/25$ is $Re = 0.00866025\ldots$, which is by far below the transition treshold of about 2000. Thus, a convective scaling with variable Reynolds number and constant τ is acceptable in this case.

In Fig. 6.2, we are able to see how the parabolic profile of the Hagen-Poiseuille flow is well recovered even for a very coarse grid with $N_x = 7$ and $N_y = 8$. This result is really helpful in case of porous media flow indeed. In fact, we know that the flow inside the pores of a porous medium shares common features with the Hagen-Poiseuille flow, and hence, we can establish as a general rule of thumb, that the distance between two walls in a porous medium should be at least 5 or 6 lattice units, while about 13 lattice units should be sufficient to ensure a good accuracy. Obviously, we have to keep the Mach number sufficiently low.

Fig. 6.3 is realized with the same Mach number and τ as before, but with $\delta x = 1/100$. On the y-axis the absolute value of the local relative error ϵ is plotted on a logarithmic scale. We see that the order of magnitude of ϵ is
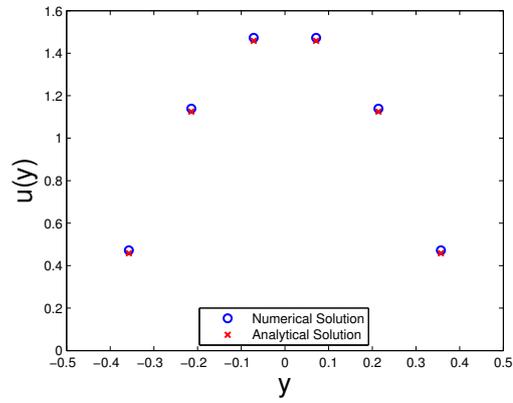
(a) $\delta x = 1/6$
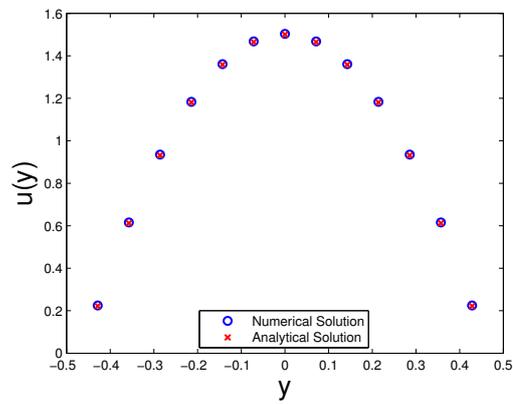
(b) $\delta x = 1/13$
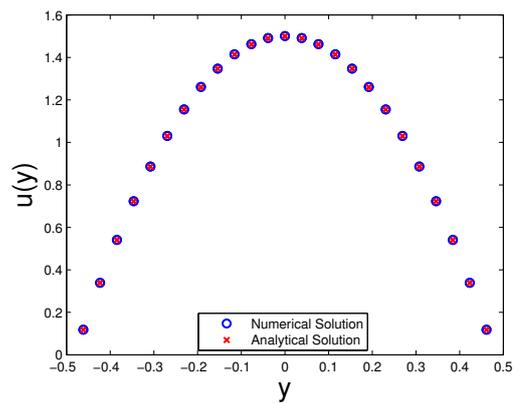
(c) $\delta x = 1/25$

Figure 6.2. Comparison between the analytical solution and the numerical results of the BGK model for different δx.
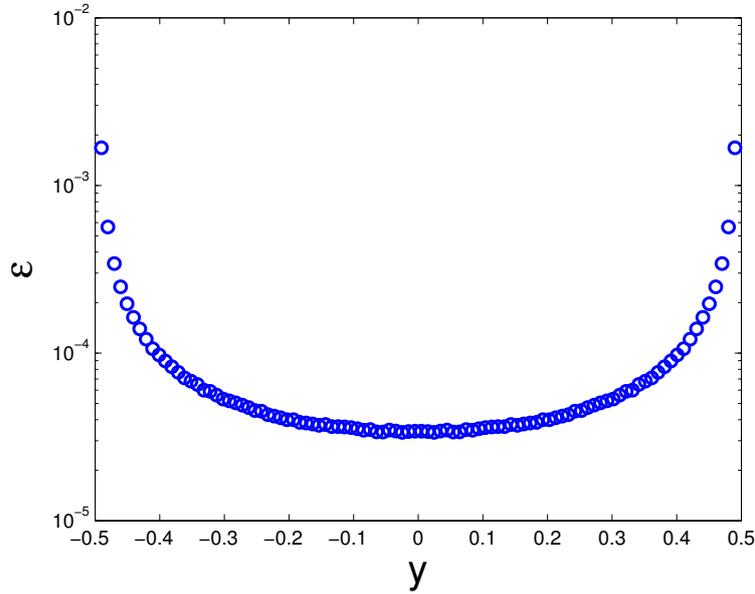
Figure 6.3. Relative velocity error profile when $\delta x = 1/100$.

10^{-3} for nodes close to the wall, while it is 10^{-4} at the centre of the channel. The obvious reason is that near the wall there are greater gradients respect to the central region, which cause the error to increase. For our particular case however, there is an additional explanation. As we know, when $\tau = 1$, the BGK model coupled with the Bounce-Back rule does not guarantee a zero slip velocity U_s. The non-zero slip velocity causes an error which weighs definitely more close to the wall, where the velocities are lower.

Let us now focus our attention on the permeability dependency on τ. In order to show this dependency, we wish to carry out a numerical experiment in which the effect of U_s is isolated from the other sources of error. The natural choice is to keep fixed the Mach number and the spatial step, and to simulate the flow with different relaxation times. In this way, from Eq. (6.5), it follows that the product $Re\,\nu_{lu}$ must remain constant. Accordingly, we need to accept a variation of the Reynolds number, which definitely does not change anything if the flow remains laminar. From Eq. (6.3), also the δt remains constant, and thus, all the sources of error in Eq. (4.50) are kept constant.

Fig. 6.4 shows the trend of the relative error on permeability $\Delta k/k_{th} = (k - k_{th})/k_{th}$ with τ, for the three models. The permeability has been obtained by computing the flow rate, and thus the Darcy's velocity, by means of a mid-
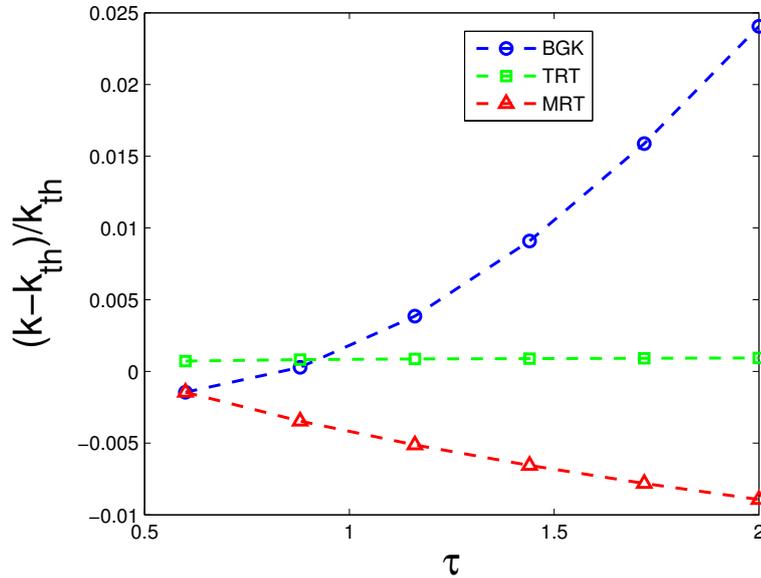
Figure 6.4. Permeability dependency on τ for different collision models.

point rule for integration [3], and then using its definition given by the Darcy's law Eq. 2.14. We can see how the TRT model basically provides a constant permeability as predicted by the theory. In addition, the BGK model exhibits an error very close to zero when $\tau \approx 0.9$, which is again in agreement with the theoretical results of Subsec. 5.2.1. The negative value of $\Delta k / k_{th}$ for the MRT model is due to the value of the relaxation parameter $s_q = 1.92$ assumed by this model. In fact, it is straightforward that the substitution of this value into Eq. (5.2), yields a negative slip velocity in the range of τ examined in Fig. 6.4, that is a lower permeability than the case $U_s = 0$.

In Fig. 6.5, we can see how this dependency is drastically reduced when $\delta x \to 0$. In particular, given a fixed τ, the scaling is carried out always assuming a fixed Mach number ($Ma = 0.0001$), and in turn, a constant value of the product $Re\,\delta x$. Even in this case the global result is a convective scaling $\delta t \sim \delta x$.

As a concluding test for the Hagen-Poiseuille flow we will make a comparison between the three models, in case of convective and diffusive scaling. We are able to see the results in Fig. 6.6. Differently from the previous cases, the convective scaling is carried out with a fixed Reynolds number and Mach number. This means that we need to scale $\nu_{lu} \sim 1/\delta x$ and consequently, τ will increase when δx is decreased. Obviously, we wish to keep the relaxation

---

[3]The error associated to this integration is $\mathcal{O}(\delta x^2)$
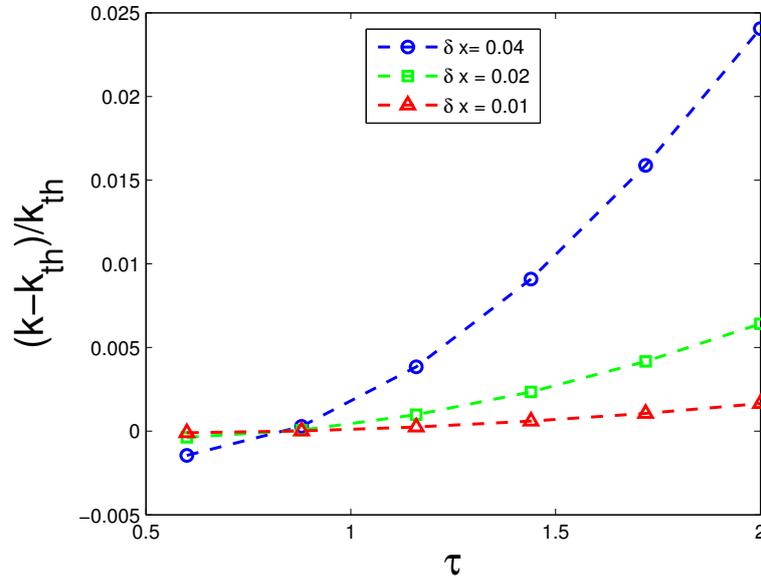
Figure 6.5. Permeability dependency on τ for the BGK model, with different δx.

parameter low, not much greater than unity, or the error due to the slip velocity will take over. For this reason, we decide to choose a Mach number low enough to guarantee that when δx is minimum, in this case $\delta x = 1/200$, the relaxation parameter is equal to one. Assuming that the Reynolds number is fixed to $Re = 0.1$, this means $Ma = 0.00014$.

As it can be seen in Fig. 6.6(a), in case of convective scaling, the TRT model is definitely the model which shows the lowest relative error, while the MRT model performs worse than the BGK when δx is lower than 0.02, but better when it is greater.

The diffusive scaling setup is definitely simpler than the convective one. The relaxation parameter τ and the Reynolds number can be kept fixed during the scaling. The simulations are carried out with $\tau = 1$ and $Re = 0.1$.

According to Fig. 6.6(b), even for the diffusive scaling the best performances in terms of accuracy belong to the TRT model, while the MRT is definitely the one which produces the greater error for any δx.

As pointed out in Sec. 6.3, the error of the Lattice Boltzmann simulations with diffusive scaling should be $\mathcal{O}(\delta x^2)$. It is easy to verify this statement in our case. In fact, in Fig. 6.7, we can notice how the error of the diffusive scaling is well approximated by a parabolic function. This function has been obtained using the Matlab function POLYFIT. In addition, Fig. 6.8 shows a comparison in logarithmic scale between the error on the permeability obtained with the diffusive scaling of the BGK model, and the curves in case
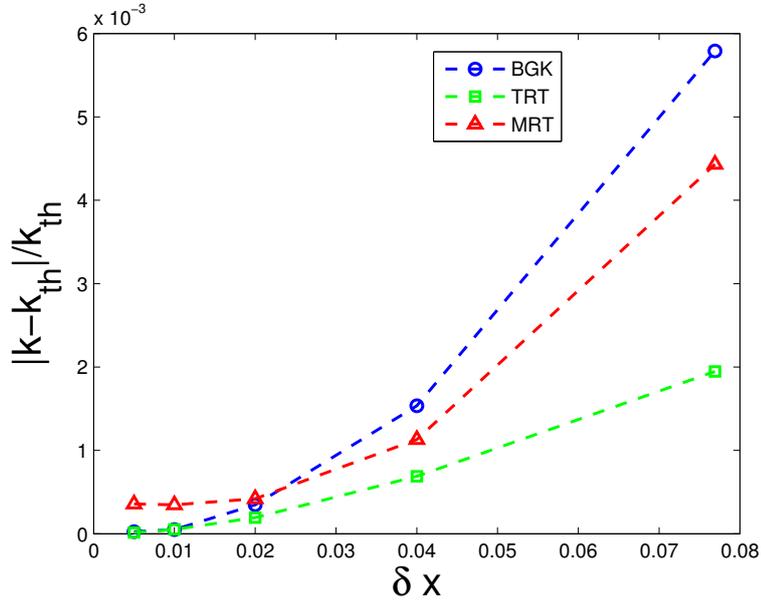
(a) *Convective scaling*
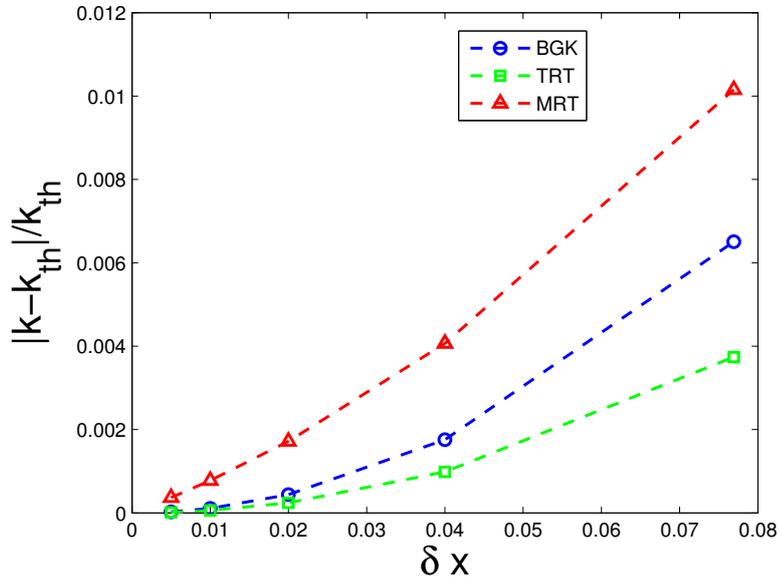
(b) *Diffusive scaling*

Figure 6.6. Comparison of the relative error on permeability between the BGK, TRT and MRT, in case of diffusive and convective scaling.
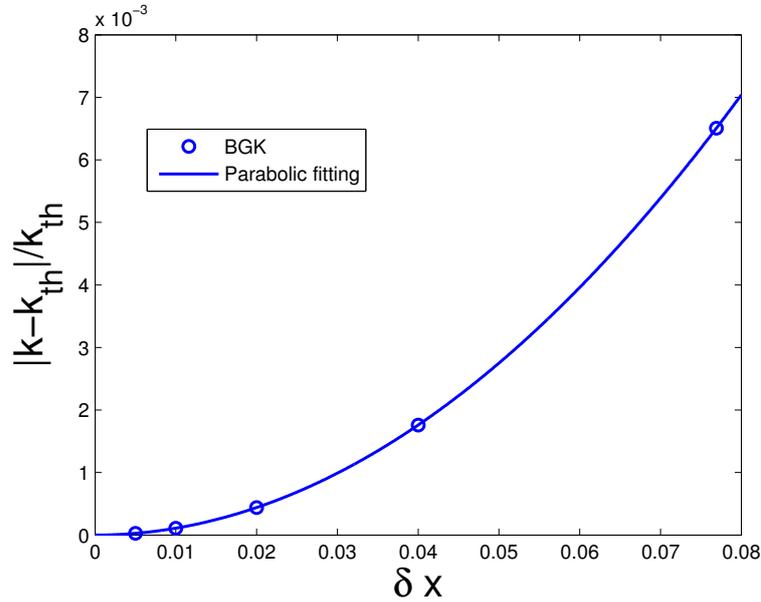
Figure 6.7. Parabolic fitting of the error on permeability obtained with the BGK model by means of diffusive scaling.

the error is $\sim \delta_x$ and $\sim \delta_x^2$. The error of the BGK model definitely follows the curve with error $\sim \delta_x^2$, and thus, the BGK model shows a second order accuracy in this case.

Finally, Fig. 6.9 displays the comparison between the error produced by the convective and diffusive scaling for the TRT model. In particular, the same simulations are carried out for $\delta x = 1/13, 1/25, 1/50, 1/100, 1/200$. The simulations parameters are exactly the same for the coarser case, that is $\delta x = 1/13$. The Reynolds number is kept fixed in both cases to the value $Re = 0.1$, while the relaxation parameter τ is constant only for the diffusive scaling, and it is chosen to be unity. From these values, it is easy to obtain the Mach number when $\delta x = 1/13$: $Ma = 0.00222058\ldots$. Thus, the convective scaling simulations are carried out using $Re = 0.1$ and $Ma = 0.00222058\ldots$.

The diffusive scaling performs definitely better in terms of accuracy. In fact, when $\delta x = 1/200$, we witness a difference of two orders of magnitude between the relative error of the simulation carried out with convective and diffusive scaling. Thus, the diffusive scaling should be used when accuracy is concerned.

Nevertheless, the time required by the simulations increases dramatically in case of diffusive scaling. As it can be seen from Fig. 6.10, when $\delta x = 1/200$ the computational time of the diffusive simulation is one order of magnitude the time required by the convective one. Thus, the diffusive scaling obtains
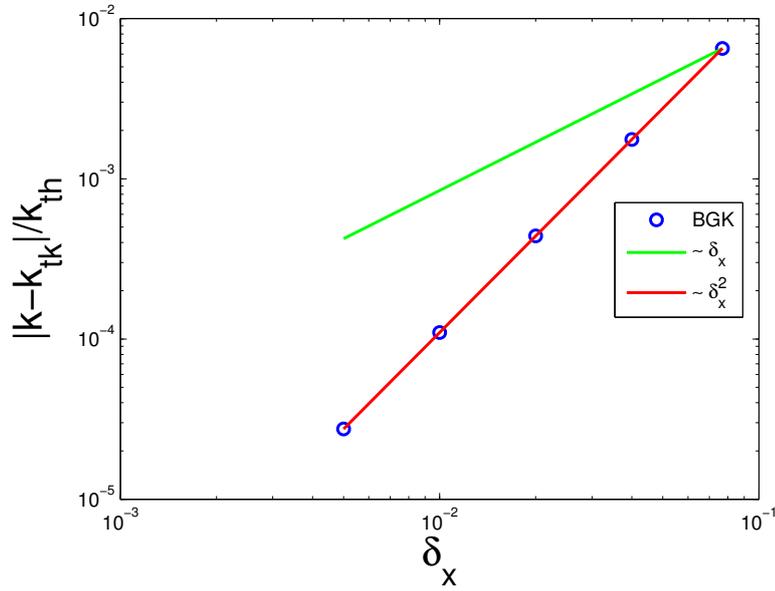
Figure 6.8. Comparison between the error on permeability obtained with the BGK model by means of diffusive scaling and the curves with error $\sim \delta_x$ and error $\sim \delta_x^2$.
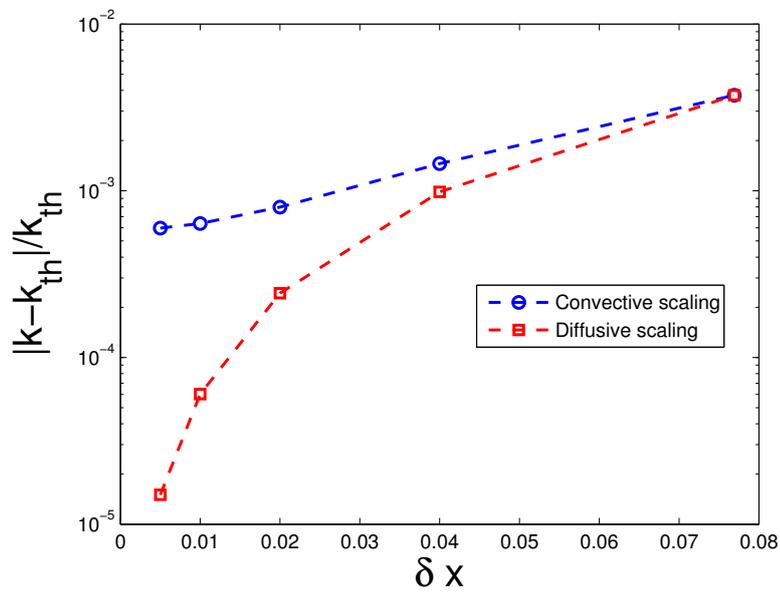
Figure 6.9. Comparison between convective and diffusive scaling for the TRT model.
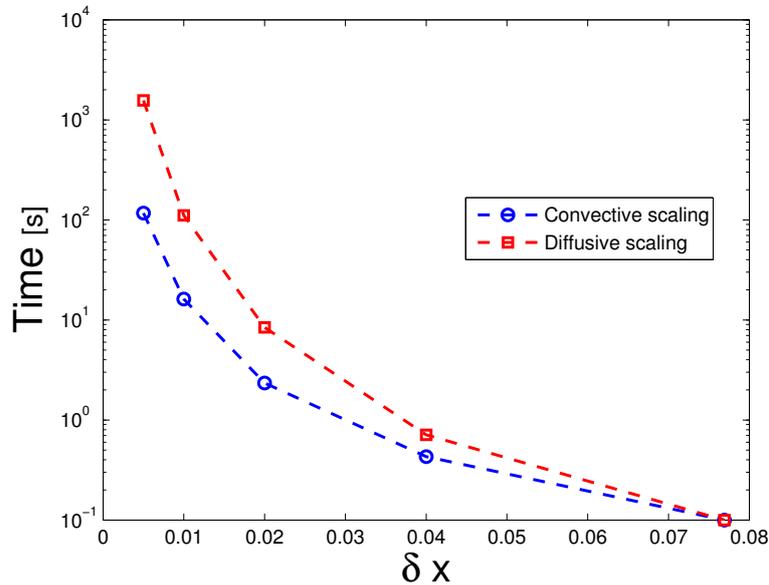
Figure 6.10. Computational time for convective and diffusive scaling with TRT model.

an accuracy two order of magnitude better with respect to the convective case, but it requires a computational time ten times longer.

6.5 Hexagonal array of disks

In this section, we will turn our attention to the study of the flow over an hexagonal array of disks represented in Fig. 6.11. In particular, from the periodicity of the medium, the analysis can be reduced to the elementary cell displayed in Fig. 6.11(b), leading to a first simplified study of a porous medium. The aim of this section is basically twofold:

1. introducing the Lattice Boltzmann methods for a more complex medium than the straight conduit of the Hagen-Poiseuille flow.

2. testing the Lattice Boltzmann methods by means of semi-analytical formulas available for this geometry.

In a certain sense, this section shall be considered as a transition from Sec. 6.4 to Sec. 6.6, in which the Lattice Boltzmann methods will be used as a tool to calculate the properties of a porous medium made up of a random array of disks.
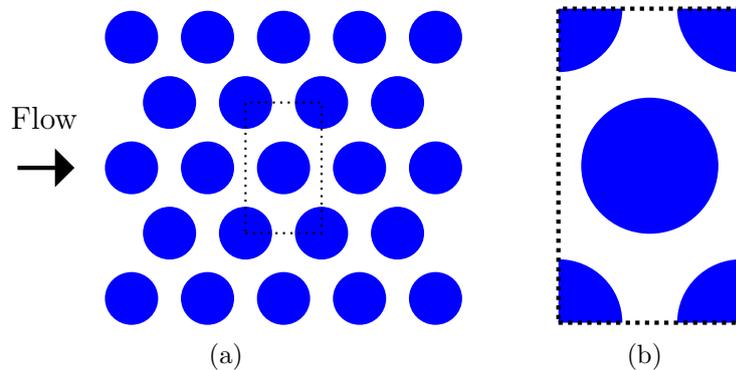
Figure 6.11. Hexagonal array of disks and elementary cell.
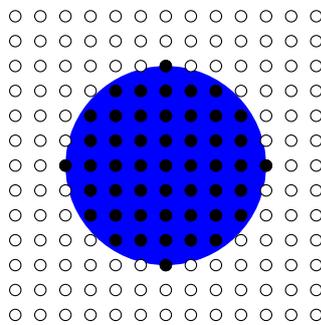
Figure 6.12. Example of geometry construction: the black dots represent the Bounce-Back nodes, while the white ones are fluid nodes.

Before starting to comment the results, few words are needed in order to understand how the geometry is generated and how the simulations are set up.

The geometry generation is very simple, indeed, thanks to the easy handling due to the Bounce-Back rule. Let us suppose that the radius of the disk is R. The Bounce-Back nodes are simply the nodes, whose distance from the relative centre is less than or equal to R. An example is displayed in Fig. 6.12. During the simulation setup, basically the same steps described in Sec. 6.2 are are carried out, but we need to define proper reference length and velocity. The reference length is chosen as the hydraulic diameter D_H defined by Eq. (2.16), with the factor 2 in place of 4. The factor 2 is more advisable for 2D cases, simply because for the reference flow in a straight conduit we would obtain that D_H is equal to the height of the channel [4].

---

[4]Obviously the choice of the factor in the hydraulic diameter definition does not change anything from our point of view.
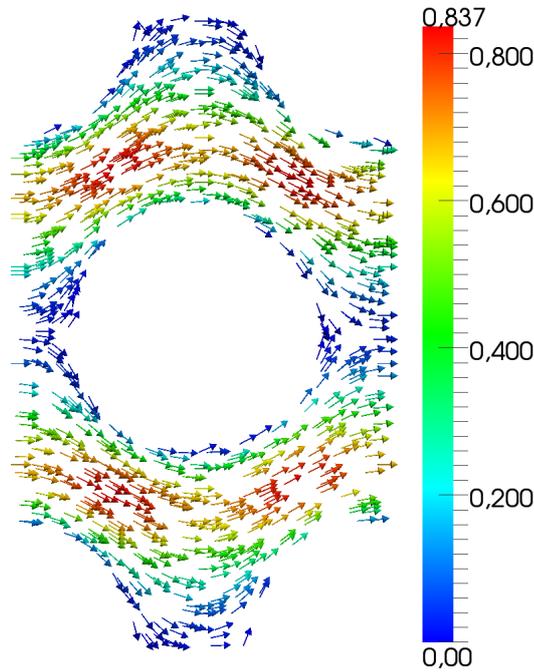
Figure 6.13. Velocity vectors for $\phi \simeq 0.6$

The reference velocity is in turn set as the average cross sectional velocity of an Hagen-Poiseuille flow whose height is equal to the hydraulic diameter.

These choices lead to a well defined Reynolds number, which we will use during the simulations.

The simulation setup is now totally similar to that described in Sec. 6.2, except for the need of periodic boundary conditions at the lower and upper boundary of the elementary cell Fig. 6.11(b).

In Fig. 6.13, we can appreciate a qualitative visualization of the numerical solution produced by the Lattice Boltzmann methods in this kind of medium.

The numerical experiment about the permeability dependency on τ has been repeated even with this geometry, as shown in Fig. 6.14. The reason was to evaluate this effect for the three models under consideration, when dealing with geometries for which analytical formulas, as Eq. (5.2), do not exist.

In particular, the simulations are carried out over an elementary cell with $N_x = 91$ and $N_y = 157$ lattice nodes made up of disks whose diameter is $d = 60$ lattice units, generating a porosity $\phi \simeq 0.6$. The Mach number is kept fixed to $Ma = 0.0001$. As we can see, the TRT model, basically maintain a constant permeability even in this case without straight boundaries, which is a very interesting feature, especially when we would like to use a convective
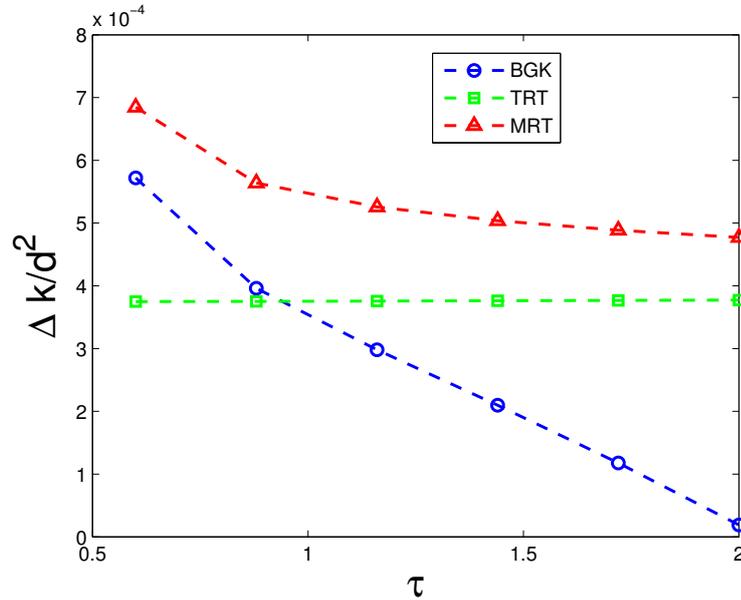
Figure 6.14. Permeability dependency on τ for an hexagonal array of disks with $\phi \simeq 0.6$; the y-coordinate represents the absolute difference between the result of the simulations and the permeability predicted by the Tamayol & Bahrami relation.

scaling.

Let us now introduce the analytical formulas with which we are going to compare the numerical results.

The first one is the equation proposed by Drummond & Tahir [2] (also analysed in [96]) and it is valid under the approximation of high porosities. Taking into account the elementary cell of Fig. 6.11(b), its formulation is:

$$\frac{k}{d^2} = \frac{1}{32\phi}\left(\ln\left(\frac{1}{\phi}\right) - 1.497 + 2\phi - \frac{\phi^2}{2} - 0.739\phi^4 + \frac{2.534\phi^5}{1 + 1.2758\phi}\right), \quad (6.6)$$

where d is the diameter of the disks.

The equation proposed by Tamayol and Bahrami [3] is more recent and it states that:

$$\frac{k}{d^2} = \frac{1}{32\phi}\left(\ln\left(\frac{1}{\phi}\right) - 1.498 + 2\phi - \frac{\phi^2}{2} - 0.0018\phi^6\right). \quad (6.7)$$

The prediction of these analytical formulas are compared to the numerical results of the Lattice Boltzmann simulations in Fig.6.15. The simulations are carried out by means of the TRT model and Zou-He pressure boundary conditions, with $Re = 0.01$ and $\tau = 0.9$ for all the porosities. The Darcy's
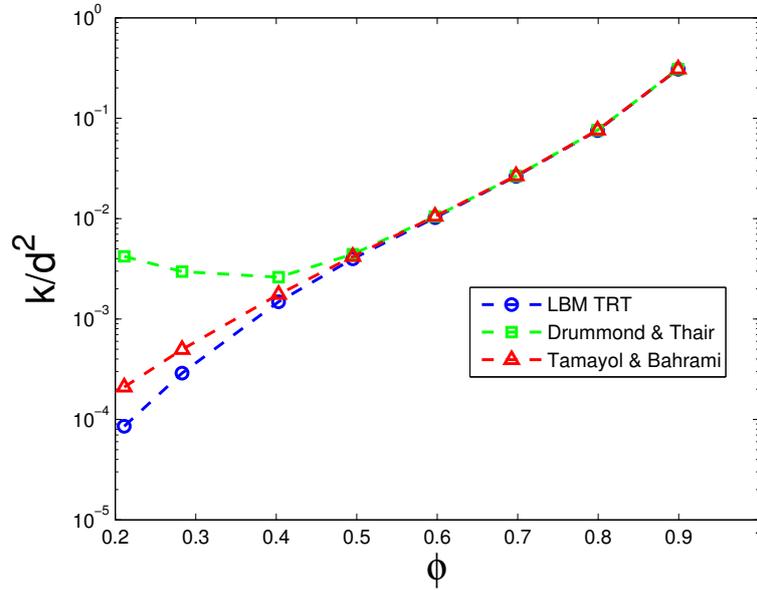
Figure 6.15. Comparison between the T&B and D&T formulas and the numerical LBM results on permeability for different porosities.

law is valid for this medium with such a low Reynolds number. Furthermore, the starting geometry for any porosity is generated fixing the diameter of the disks to $d = 60$ lattice units and the desired porosity. From this values, it is easy to obtain N_x and N_y [5].

The value $d = 60\,\text{lu}$ is chosen to adequately recover the disk shape by means of the aforementioned discrete approximation. Unlike other CFD schemes, we are not free to adapt the mesh to our geometry given the rigid lattice structure of the LBM grid.

In addition, when it was considered necessary, a grid refinement was carried out along with a diffusive scaling.

From the analysis of Fig. 6.15, we recognize a general agreement of the LBM simulations with the T&B, although some deviations are observed when $\phi < 0.5$. The D&T equation is valid with high porosities, but it definitely leads to an overestimated permeability with low porosities, as also suggested by the theory behind it.

Table 6.1 shows in details the numerical results and the predictions of the analytical formulas for the porosities taken into account. We notice that for $\phi \geq 0.5$, the agreement with the semi-analytical formulas is either up to

---

[5]It should be noted that for this medium there exists a minimum porosity $\phi = 1 - \pi/(2\sqrt{3})$

ϕ	k/d^2		
	LBM-TRT	D&T	T&B
0.21110	$0.85599 \cdot 10^{-4}$	$42.148 \cdot 10^{-4}$	$2.0094 \cdot 10^{-4}$
0.28311	$2.8894 \cdot 10^{-4}$	$29.670 \cdot 10^{-4}$	$4.9704 \cdot 10^{-4}$
0.402991	$1.4867 \cdot 10^{-3}$	$2.6090 \cdot 10^{-3}$	$1.7561 \cdot 10^{-3}$
0.49510	$3.9782 \cdot 10^{-3}$	$4.4117 \cdot 10^{-3}$	$4.1904 \cdot 10^{-3}$
0.59723	$1.0210 \cdot 10^{-2}$	$1.0483 \cdot 10^{-2}$	$1.0538 \cdot 10^{-2}$
0.69792	$2.6341 \cdot 10^{-2}$	$2.6592 \cdot 10^{-2}$	$2.6649 \cdot 10^{-2}$
0.79919	$7.5427 \cdot 10^{-2}$	$7.6145 \cdot 10^{-2}$	$7.6074 \cdot 10^{-2}$
0.89931	$3.0710 \cdot 10^{-1}$	$3.0879 \cdot 10^{-1}$	$3.0849 \cdot 10^{-1}$

Table 6.1. Numerical results of the LBM simulations on k/d^2 compared to the analytical formulas.
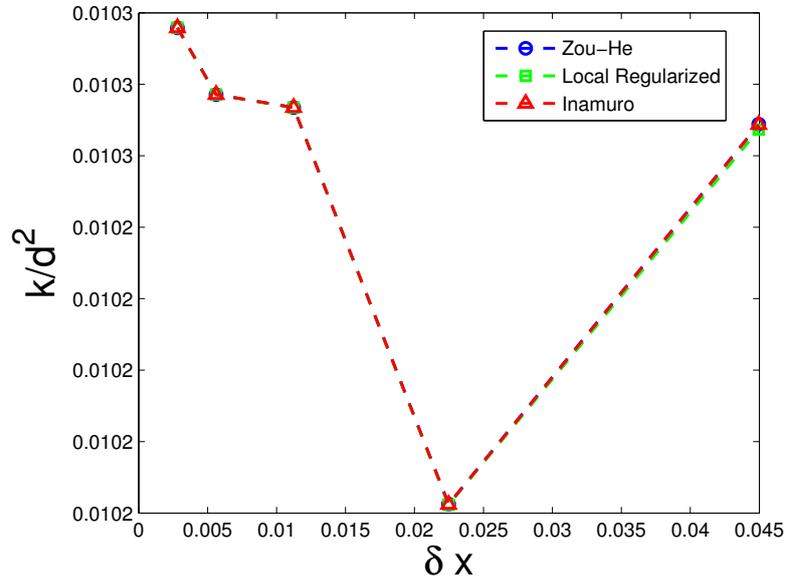
Figure 6.16. k/d^2 obtained with different schemes of pressure boundary conditions.

the first significant figures or even to the second significant figures. When $\phi < 0.5$, the D&T equation is not reliable, and the agreement between the LBM simulations and the T&B equation degrades only to the same order of magnitude. For low porosities, this discrepancy has been investigated through several grid refinements along with diffusive scaling, but the better results are those reported in Table 6.1.

Thus, we conclude that either the LBM simulations or the predictions of the T&B formula (or both!) are not reliable for low porosities. However, the T&B equation is obtained by means of approximations, while we know that in case of diffusive scaling the error of LBM should be $\mathcal{O}(\delta x^2)$, and consequently we are lead to assume the results of the simulations as the most reliable. Finally, Fig. 6.16 shows how basically there is a total agreement between the permeability obtained using the boundary conditions schemes proposed by Zou-He and Inamuro, and the Local Regularized scheme. In particular, the results are equal up to 5 or 6 significant figures. Fig. 6.16 is obtained by means of a convective scaling.

6.6   Random array of disks

In this section, we will study the flow over a random array of disks by means of the Lattice Boltzmann methods. In particular, we refer to a medium like that displayed in Fig. 6.20, in which we see a visualization of the velocity

field as well. Thus, the disks are not free to overlap. In addition, the random array is assumed to be periodic in both directions.

6.6.1 Geometry generation and simulation setup

The geometries are simply generated using Matlab and a possible algorithm is shown in Fig. 6.17.

This algorithm is called in [97] *"parking algorithm"*, considering the case of three-dimensional packing of disks. Despite its simplicity, this algorithm does not lack drawbacks. As reported in [98], the volume fraction limit for a random array of hard disks, called Random Close-Packing ϵ_c, should be $\epsilon_c \simeq 0.82$. Nevertheless, the parking algorithm has shown increasing difficulties in reaching porosities lower than $\phi \approx 0.4$, resulting in a very time consuming operation. For this reason, a different algorithm is needed in order to obtain geometries with porosities below this limit value.

The literature about random packings is very wide, and a brief analysis has shown that more efficient methods to generate random packings are based on Monte Carlo methods, and in particular on the Metropolis algorithm or the event-chain algorithm, which are well described in [99]. Though the event chain algorithm is more efficient, the Metropolis algorithm has been chosen for its simplicity. As a matter of fact, these methods were originated to study the thermodynamic properties of the system of hard spheres or hard disks, such as the identification of the volume fraction which delimits the transition from a disorderly to an orderly phase. However, they are a perfect instrument for our case as well.

The basic idea behind both Metropolis and event-chain algorithms is to instantiate a regular and orderly configuration, and then to mess it up randomly. In our case, we will initialize a square array of disks. In this way, we are able to fix the porosity *"ex-ante"*, falling below the threshold $\phi \approx 0.4$ imposed by the parking algorithm.

The key concept of the Metropolis algorithm is the definition of a "move". After the initialization, a disk k is picked randomly and in addition, a random vector $\boldsymbol{\delta_k}$ is generated randomly and associated to this disk. The random variables are all assumed with a uniform distribution. The maximum magnitude of the vector $\boldsymbol{\delta_k}$ is fixed to a certain value δ. A move consists in the attempt to displace the disk k by δ, obtaining the new position $\boldsymbol{r'_k} = \boldsymbol{r_k} + \boldsymbol{\delta_k}$. If this process does not induce an overlapping, the move is accepted, otherwise it is discarded. Starting from the initial configuration, a reasonable number T of moves is attempted in order to obtain a random structure [99]. The flow chart of the algorithm is shown in Fig. 6.18.

An example of geometry obtained through the Metropolis algorithm is displayed in Fig 6.19. The simulation setup is basically the same used in
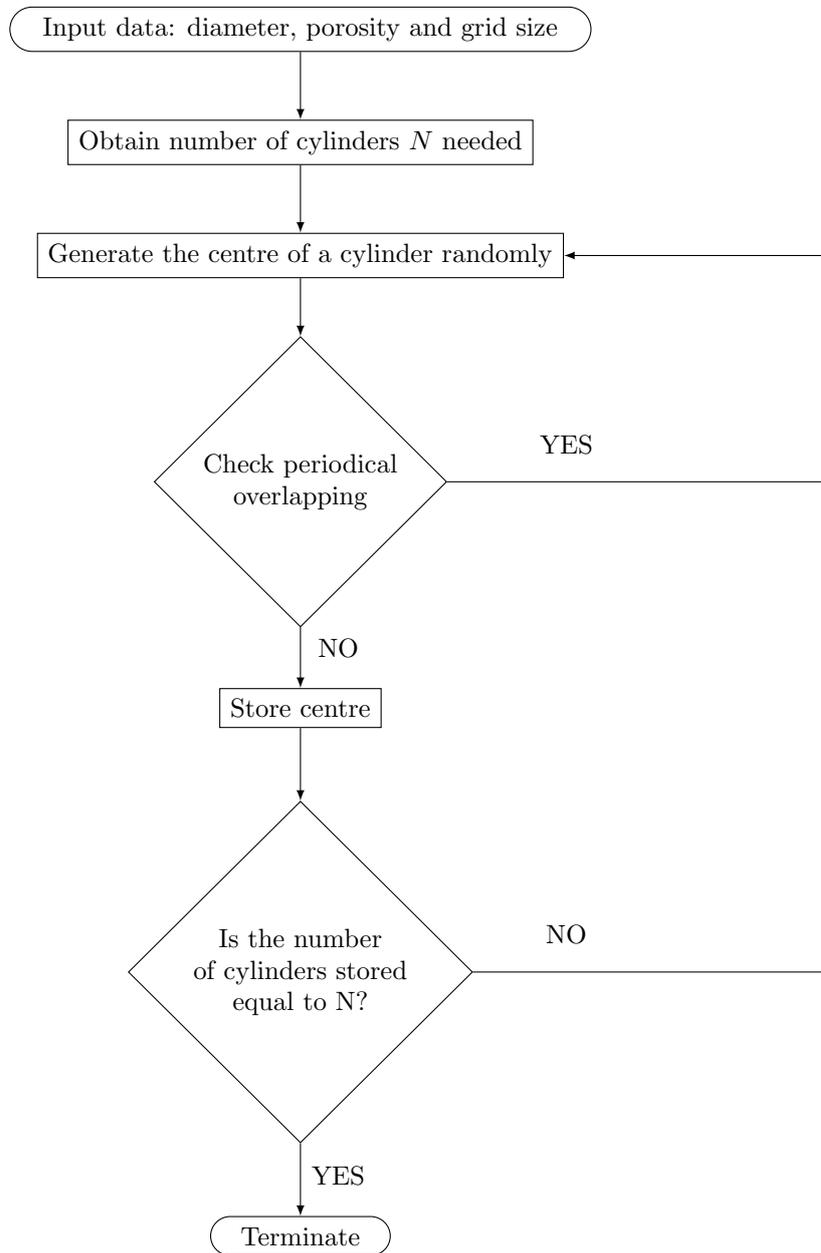
Figure 6.17. Random parking algorithm.
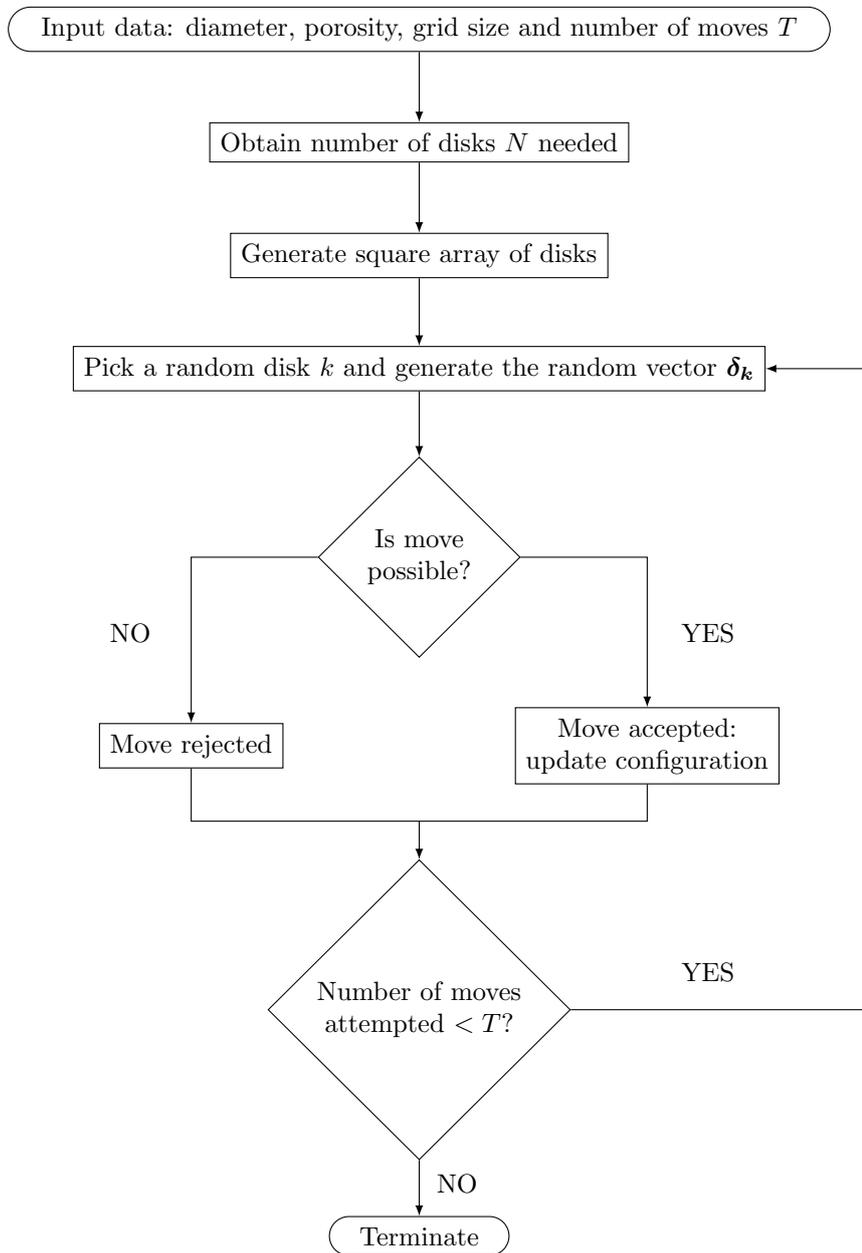
Figure 6.18. Metropolis algorithm

(a) Initial square configuration

(b) Configuration after 250000 attempted moves
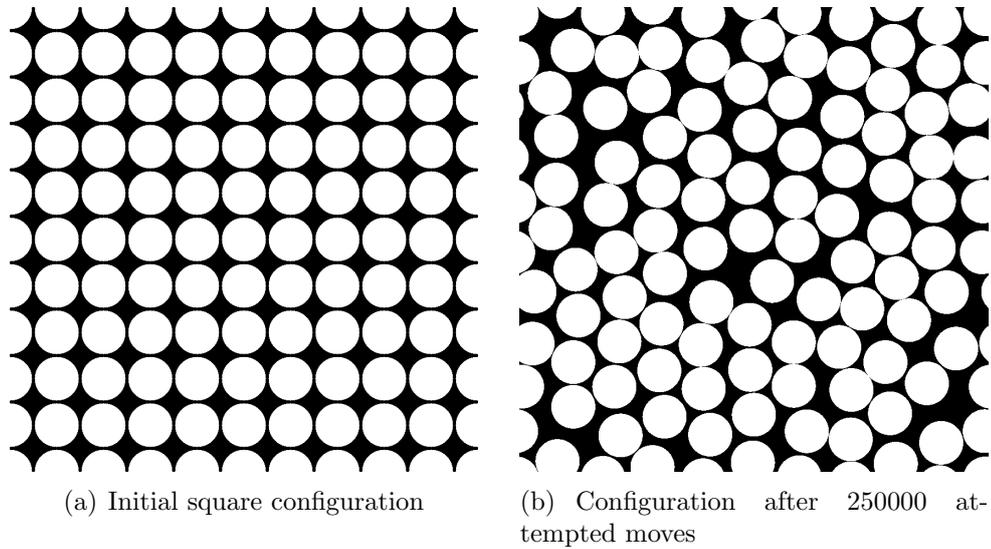
Figure 6.19. Evolution of the Metropolis algorithm for $\phi = 0.3$.

the case of the hexagonal array of disks. The reference length is chosen as the hydraulic diameter and the reference velocity is chosen as the average velocity of an Hagen-Poiseuille flow inside a conduit of height $H = D_H$ and length equal to the length of the porous medium. Since the geometry is considered periodic, even in this case, on the upper and lower boundaries we are allowed to prescribe periodic boundary conditions. In addition the TRT model is used to study these geometries, because as we know from the previous section, it ensures a higher flexibility in the choice of the relaxation parameter.

Since for each porosity, we may have different random distributions, which of course affects somehow the permeability of the medium even though not taken into account in the Carman-Kozeny equation, 10 geometries for each porosity are studied in order to obtain an averaged result. The range of porosity taken into account is $0.4 \leq \phi \leq 0.9$.

Initially, the simulations are all carried out with the following parameters:

- $N_x = N_y = 501$ lattice nodes;

- $Re = 0.1$;

- $\tau = 2$.

The choice $\tau = 2$ has been made to speed up convergence to the steady state, decreasing δt, with obviously a penalization in terms of accuracy. This choice is however possible for the TRT model, without modifying the slip velocity

at walls. In addition, when it was considered necessary, which in general might be the case of low porosities, a grid refinement is carried out assuming convective scaling.

6.6.2 How to compute tortuosity numerically

In this thesis, the tortuosity of a flow inside a porous medium is computed following the approach described in [100] by Duda *et al.*, which we will describe hereafter.

Sometimes in literature tortuosity is computed as a not well defined streamline length average, as done in [96] for instance. In general, the tortuosity is computed as:

$$T = \frac{1}{L} \frac{\sum_i \lambda_i w_i}{\sum_i w_i},$$
(6.8)

where i runs over discrete points of a cross section, L is the length of the channel, λ_i is the length of a streamline which passes through the relative discrete point, and w_i is a weight which tries to consider the flow associated to each streamline, according to the definition L_e given in Eq. (2.22).

However, the generation of streamlines and the computation of their lengths are very time consuming operations, which in turn introduces further numerical errors.

For this reason, Duda *et al.* tried to obtain in [100] a formula to calculating the tortuosity, starting directly from the velocity field, without generating streamlines. In their paper, they start directly from the definition Eq. (2.22) and they end up with the following formula:

$$T \leq \frac{\int_V |\boldsymbol{u}(\boldsymbol{r})| \, dv}{\int_V u(\boldsymbol{r}) \, dv},$$
(6.9)

where $u(\boldsymbol{r})$ is the velocity component along the direction in which we want to evaluate tortuosity[6] and the integral is evaluated over all the fluid volume (or area in two dimensions).

Eq. (6.9) is obtained under the assumptions of incompressible flow and the equality sign does not hold in general, because of the contribution of recirculation zones. Flow in porous media is in general characterized by recirculation zones indeed, as the flow is not irrotational because of viscous effects. However, Duda *et al.* argued in [100] that in porous media these zones take up only small regions, and in addition they are characterized by very small velocities. Thus, their contribution in the integrals of Eq. (6.9)

---

[6]It should be remembered that tortuosity is a tensor indeed, hence it can be evaluated also along other directions.
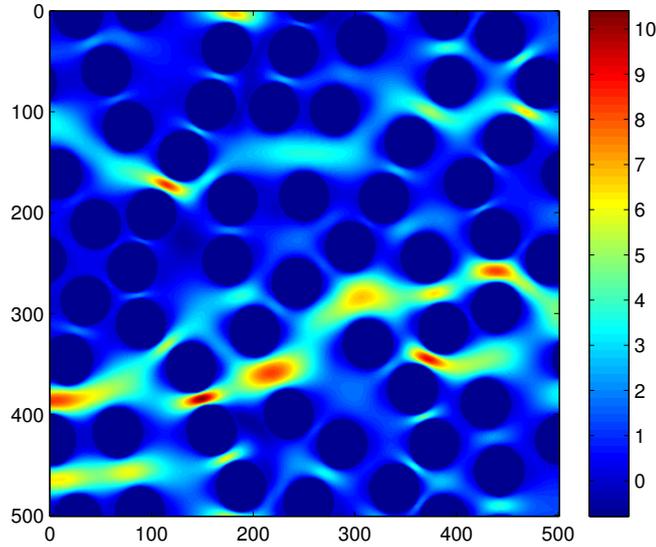
Figure 6.20. Example of velocity visualization (u_x/q) when $\phi = 0.6$.

is in general negligible, and the equality sign can be assumed to hold. Nevertheless, in this context a simple visualization of the streamlines may be helpful in order to evaluate whether Eq. (6.9) is reasonably valid or not.

Finally, the two integrals of Eq. (6.9) will be evaluated from the numerical velocity fields by means of the simple trapezoidal formula of integration of two variables.

6.6.3 Results

In the first instance, we need to understand the range of validity of the Darcy's law. The Darcy's law is valid under the assumptions of low Reynolds number, but we have to know how low the Reynolds number has to be. For this reason, we carried out simulations on a random geometry with $\phi = 0.6$, that we have considered as reference. In particular, the simulations were performed imposing a pressure gradient (or density gradient) between inlet and outlet, in the range $[0.001, 0.13]$, with reference density at inlet equal to unity and relaxation parameter $\tau = 1$ [7]. The results of the simulations are displayed in Fig. 6.21. The Darcy's law establishes a linear relationship between ΔP and Darcy's velocity q. The deviation from linearity is due to inertia effects, which begin to be important at $\Delta P \approx 0.06 \mathrm{mu}\,t s^{-2}$, which corresponds to $Re \approx 20$. As pointed out in Sec. 2.3, this does not mean

---

[7]Of course we are reasoning in lattice units.
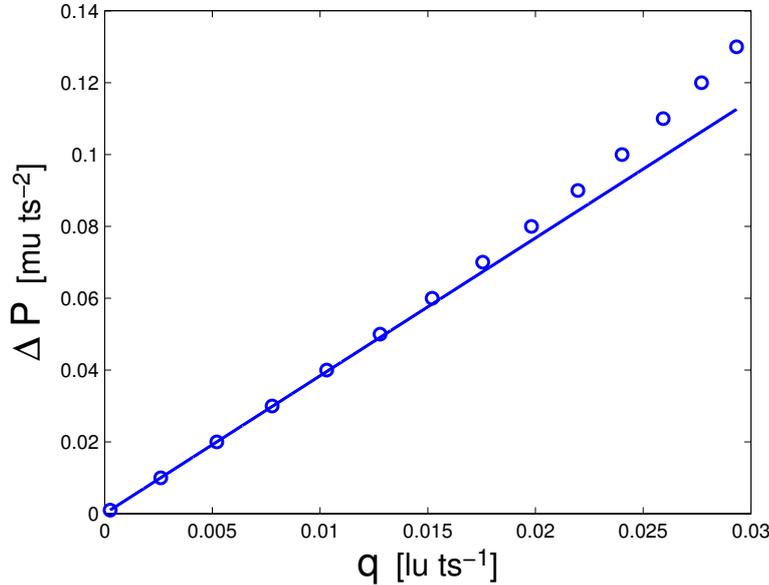
Figure 6.21. Pressure difference vs. Darcy's velocity relationship for a porous medium with $\phi = 0.6$. We see that when ΔP increases the linearity is lost.

that the flow is not laminar. In particular, we see that the Darcy's law underestimates the pressure difference needed to obtain a certain Darcy's velocity, when the q is sufficiently high. Hence, in all the following simulations we have assumed a Reynolds number $Re = 0.1$, which is definitely in the range of validity of Darcy's law also for the other geometries.

The Carman-Kozeny equation tries to take into account all the effects of geometry by means of the tortuosity and the shape factor. Obviously, we expect that these two parameters are not sufficient to describe properly all the variety of possible random geometries. For this reason, when dealing with random geometries, the shape factor of the Carman-Kozeny equation has to be intended as a fitting parameter.

Thus, we carried out a linear regression of the permeability k/d^2 with regressor $\phi^3/(T^2(1-\phi)^2)$. In particular, the linear regression was considered without the intercept: $k/d^2 = \gamma \phi^3/(T^2(1-\phi)^2)$, where $\gamma = 1/\beta$.

Initially, the linear regression was carried out in the range $0.4 \leq \phi \leq 0.9$. We can see the results of the regression in Fig. 6.22. The shape factor, obtained as a fitting parameter, was $\beta = 133.33\ldots$, while the adjusted R^2 of the regression was $R^2_{adj} = 0.9032$. Yadzchi *et al.* in [101] obtained a shape factor $\beta = 140$. An explanation for this discrepancy might be that in the present work we considered a minimum distance between disks of $0.1\,d$, while in Yadzchi *et al.*'s work, they took $0.05\,d$.
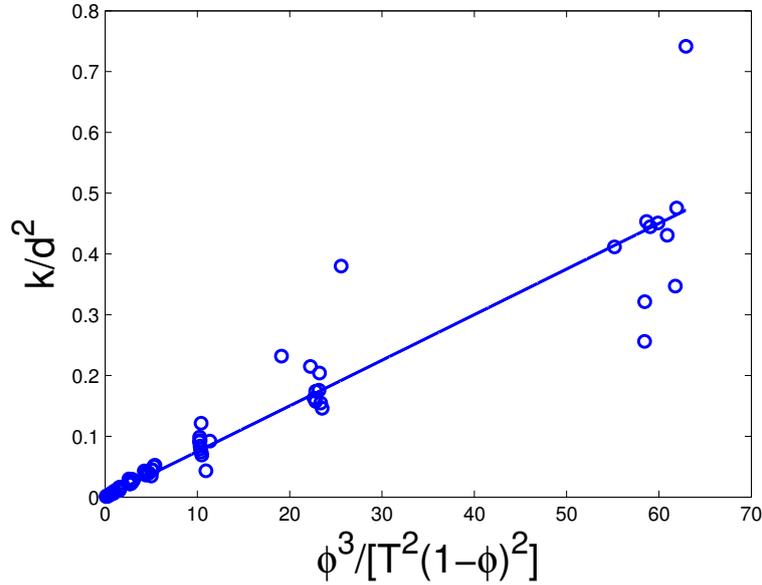
Figure 6.22. Linear regression k/d^2-$\phi^3/[T^2(1-\phi)^2]$ in the range $0.4 \le \phi \le 0.9$.

Even though the R^2_{adj} was relatively high, and thus the Carman-Kozeny equation can be considered a good approximation for this kind of geometry, we witnessed greater deviations from the CK behaviour at high porosities. This is not a surprise since, as it was explained in Chap. 2, the Carman-Kozeny model considers the flow in a porous medium as a flow inside small and intricate conduits, while at high porosities, the approach of "flow around many obstacles" is more suited.

Thus, other two linear regressions in the range $0.4 \le \phi \le 0.55$, and $0.6 \le \phi \le 0.9$, respectively have been carried out. In the range $0.4 \le \phi \le 0.55$, we witnessed a considerable improvement of the R^2_{adj}, which increased to $R^2_{adj} = 0.9775$. In addition, the shape factor becomes $\beta = 121.95$. In Fig. 6.23, we are able to see the graph of the regression. Instead, in the range $0.6 \le \phi \le 0.9$, the R^2_{adj} worsened: $R^2_{adj} = 0.8841$.

As expected, this means that the CK equation is better satisfied in the lower range of porosities.

A qualitative analysis of the results has shown two main cases in which the description in terms of tortuosity and shape factor are not sufficient to recover all the features of the geometry and do not explain the behaviour of the permeability.

Fig. 6.24 shows the case of geometry with $\phi = 0.85$ and relatively high tortuosity, $T = 1.20302$. Even though, the tortuosity is high, the porous medium shows a high permeability compared to those obtained for other
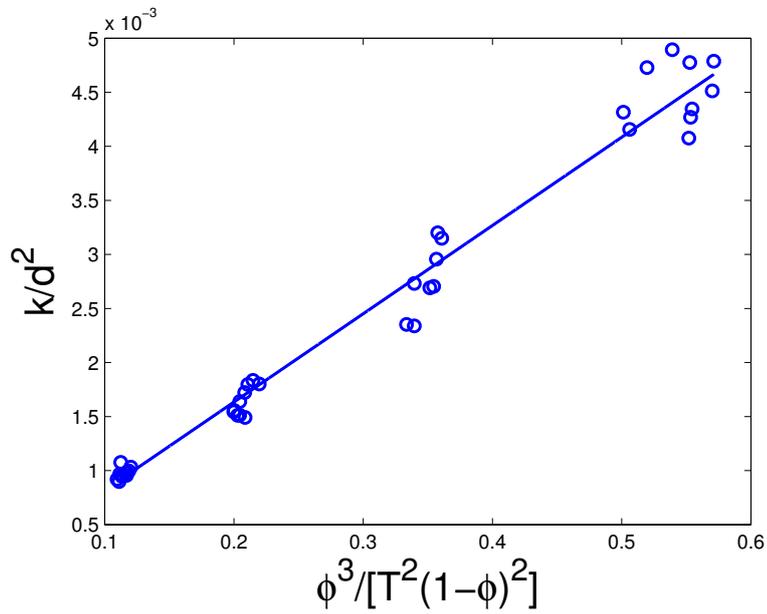
Figure 6.23. Linear regression k/d^2-$\phi^3/[T^2(1-\phi)^2]$ in the range $0.4 \leq \phi \leq 0.55$.
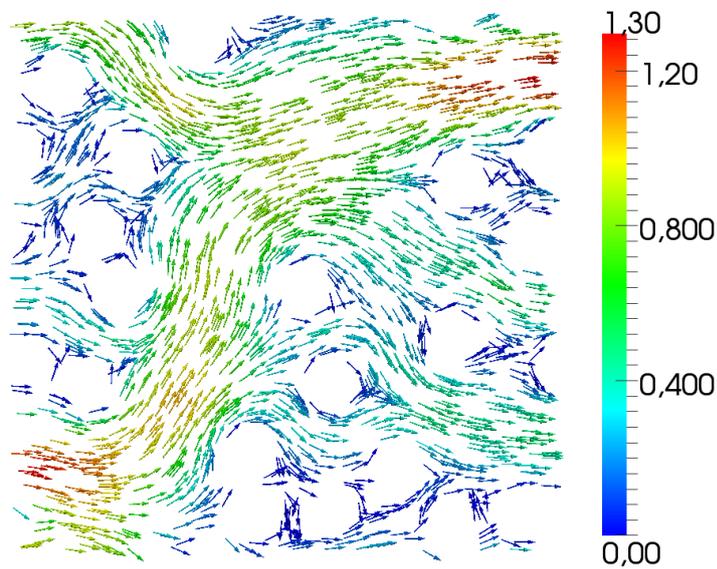
Figure 6.24. Dimensionless velocity vector field for a geometry with $\phi = 0.85$. The flow is tortuous, but there is a large channel and thus, the permeability is relatively high.
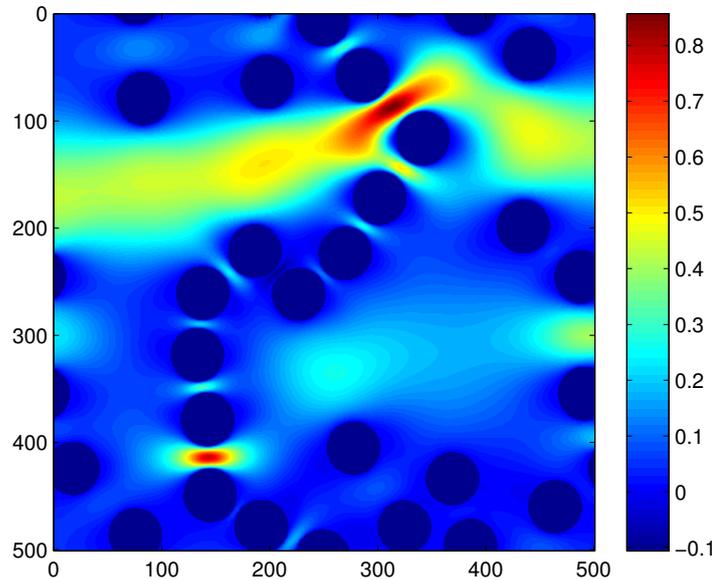
Figure 6.25. Dimensionless velocity magnitude along the x-direction for a geometry with $\phi = 0.8$. The flow is not tortuous, but it encounters a block situation and thus, the permeability is relatively low.

geometries with the same porosity. This is due to the formation of a main large channel which, even if tortuous, does not provide a great hindrance to the flow. The formation of such a channel is definitely more likely at high porosities.

Instead, in Fig. 6.25, we can see a flow that is not very tortuous, $T = 1.10989$, but suddenly encounters a section of local low porosity. The reduction of the permeability compared to the average for such porosity is not explained by the tortuosity. In addition, even this case is more likely to occur at high porosities.

Another reason for which the Carman-Kozeny model is more valid in the range of low porosities is the tendency of the random system to give rise to local ordered structure. Obviously, this is due to the transition from a totally disordered phase, i.e., the gas, to a typical liquid phase which is ordered in the short range, but disordered in the long range. In Fig. 6.26, it is easy to identify typical hexagonal structures. Thus, in the low range of porosities the structure is locally very similar for any random geometry, which obviously helps to explain the permeability by means of the tortuosity and the shape factor only.

If we think about the definition of tortuosity, we realize that it is some-
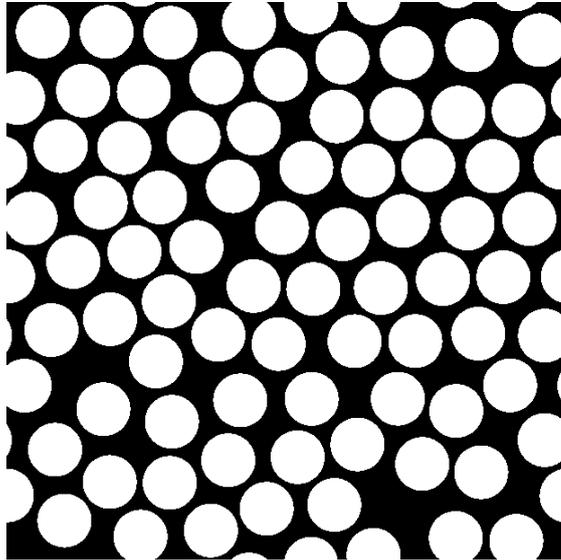
Figure 6.26. Random array of disks with $\phi = 0.4$. We are able to appreciate the tendency to form local hexagonal structures.

how connected to the porosity of the porous medium. In Fig. 6.27, we can appreciate how the tortuosity generally decreases with the increase of porosity. This is rather obvious, as when $\phi = 1$, the tortuosity is equal to unity. In addition, we see a stabilization of tortuosity at low porosity. The reason is, even this case, the tendency of the system to form orderly structures, which makes the random media very similar to each other.
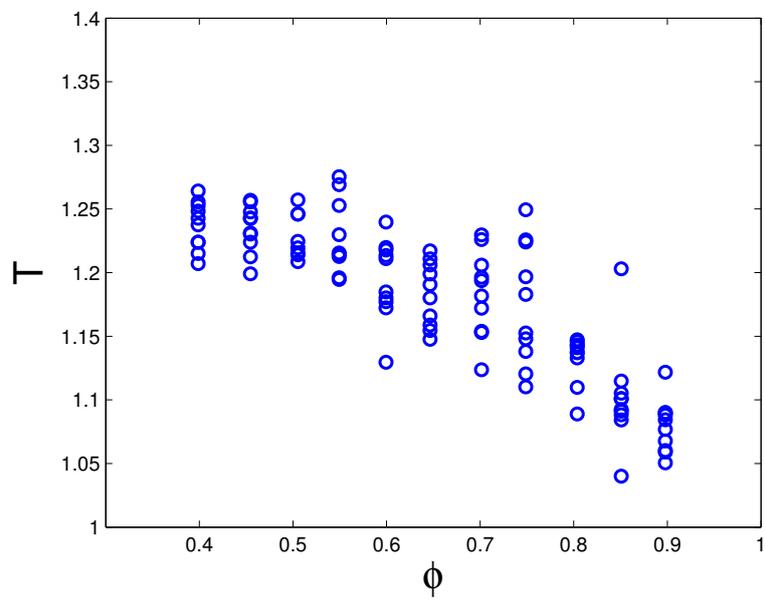
Figure 6.27. Dispersion graphs of tortuosity vs. porosity

Chapter 7

Lattice Boltzmann methods for multi-component and multi-phase flows: the Shan-Chen model

The capability of simulating multi-component and multi-phase flows is certainly one of the most striking features of Lattice Boltzmann methods. The separation between two or more phases arises naturally from the lattice mesoscopic description, and thus we do not need an interface tracking algorithm, such as Front Tracking, Level Set and Volume of Fluid methods (see [13] for an overview), which require a high computational effort.

The Lattice Boltzmann approaches for multi-component and multi-phase flows can be divided into three categories. The first one is based on the interpretation of the Lattice Boltzmann equation. Basically, in order to obtain a phase separation in a physical system, we need to include the interaction between molecules in our model. For example, the Van der Waals theory is based on the assumption of a system of hard spheres, characterized by a mean attractive potential acting upon molecules. For this reason, it is called a *mean-field* theory. In this way, the system shows the typical short-range repulsion, due to the not overlapping condition, and long-range-attraction, caused by the mean potential. As we know, the Van der Waals theory is capable of recovering a gas-liquid transition for a single-component system. Thus, the idea is to create a so-called *pseudo-potential* between the particles of the lattice, which, even though it is not a direct translation of a physical interaction, it shows a phase separation in proper conditions. The most popular model, which belongs to this class is certainly the Shan-Chen model [4], which we will describe in details in what follows.

The models based on a Free-Energy functional belongs to the second

113

category. In these models, two particle populations for each component are needed. One of them is used to approximate the Navier-Stokes equation as usual, while the other is related to the Cahn-Hilliard equation, which describes the phase separation [102]. The models based on these approach are basically improvements of the original model proposed by Swift *et al.* in [31], which lacked Galilean invariance. The problem of Galilean invariance of Free-Energy methods was solved by the model proposed by Zheng *et. al* in [33].

Finally, the last class of models incorporates the interaction directly into the continuous Boltzmann equation, and then obtain a Lattice Boltzmann equation in analogy with the procedure carried out in 3. The first of this class of models was introduced by He *et. al.* in [103], while one of the most popular is the model proposed by Lee & Lin [34]. This class of methods is certainly the most promising because they allow the simulation of higher density and viscosity ratio, compared to the Shan-Chen model and Free-Energy model. However, the simulations certainly require a higher computational effort compared to the Shan-Chen model, and also the easy implementation, typical of the Lattice Boltzmann methods, is definitely lost.

The current version of Palabos implements the Shan-Chen model for both two- and three-dimensional cases, for single- and multi-component flows, but an implementation of Free-Energy methods is missing. The Lee-Lin [34] model is implemented only for the three-dimensional case, and it is still in a development stage. Since, we intend to conduct simulations in two-dimensions to get in touch with Lattice Boltzmann methods for multi-phase flows, we are forced to use the Shan-Chen model, if we want to do it with the Palabos library. For this reason, in this chapter we will analyse the Shan-Chen model only. However, due to its easy implementation and the intuitive physical idea behind it, the Shan-Chen model is certainly the most suitable model to start studying multicomponent/multi-phase flow by via the Lattice Boltzmann methods.

In what follows, initially a description of the model is given in the general case of multi-component and multi-phase system. Then, the miscible/immiscible behaviour of the Shan-Chen model is investigated by means of a static bubble simulation, in which we will also show other features of the Shan-Chen model and begin to understand the need of calibrating the model by means of simple simulation tests. These tests allow also to identify the main drawbacks of the model. In order to overcome these problems, a modification of the interaction term, proposed by Yuan & Schaefer [5], is implemented, extending the Palabos library. The procedure basically consists in the incorporation of physical Equation Of State (EOS), in the Shan-Chen model. Finally, a first validation of the Shan-Chen model is carried out,

analysing the case of a 2D co-current flow, already described in Sec. 2.5.3.

7.1   Model description

Let us begin the description of the Shan-Chen model by considering a binary mixture. For each component, we can define Q distribution functions f_i^σ, where Q is the number of velocities of the lattice model. These distribution functions satisfy the usual Lattice Boltzmann equation:

$$f_i^\sigma(\boldsymbol{x} + \boldsymbol{\xi_i}, t + 1) - f_i^\sigma(\boldsymbol{x}, t) = -\frac{1}{\tau_\sigma}(f_i^\sigma(\boldsymbol{x}, t) - f_i^{\sigma(eq)}(\boldsymbol{x}, t)),$$

$$i = 0, 1, \ldots, Q - 1; \quad \sigma = 1, 2,$$

(7.1)

where of course we are using the BGK model. Here we have directly considered lattice unit for time $\delta t = 1$, while from now on we will call the lattice spacing $\delta x = c$. These assumptions have been done because the literature about the Shan-Chen model is mostly developed using this system of units.

The mesoscopic density and momentum for each component are obviously $\rho_\sigma = \sum_i f_i^\sigma$ and $\rho_\sigma \boldsymbol{u_\sigma} = \sum_i \boldsymbol{\xi_i} f_i^\sigma$. The equivalent mixture relaxation parameter τ_{mix} is the weighted average of the relaxation parameters of the single components, where the weights are the masses of the single components. If we denote by y_σ the mass fraction of the component σ [1], by the previous statement we can write $\tau_{mix} = \sum_\sigma y_\sigma \tau_\sigma$. Thus, according to Eq. (3.8), the viscosity of the mixture can be computed as [104]

$$\nu_{mix} = c_s^2\left(\tau_{mix} - \frac{1}{2}\right).$$

(7.2)

The introduction of the force term is done by means of the method of shifting velocity on the equilibrium velocities. The equilibrium distribution functions are computed by means of Eq. (3.75), in which the equilibrium velocities are given by [105]:

$$\boldsymbol{u_\sigma^{eq}} = \boldsymbol{u'} + \frac{\tau_\sigma \boldsymbol{F_\sigma}}{\rho_\sigma}.$$

(7.3)

The velocity $\boldsymbol{u'}$ represents the velocity of the mixture in the absence of interactions. The formula for $\boldsymbol{u'}$ can be obtained through a very simple reasoning. Let us consider a binary ideal mixture without interactions. As usual, in order to obtain a macroscopic equation for the mixture, we need to multiply Eq. (7.1) by $\boldsymbol{\xi}$ and then sum over the lattice velocities and components. In

---

[1]It is straightforward that $y_\sigma = \rho_\sigma/\rho$, where $\rho = \sum_\sigma \rho_\sigma$.

addition, the right side of the equation must be equal to zero. Thus, we obtain the following equation:

$$\sum_{\sigma=1}^{2} \frac{1}{\tau_\sigma} \left[\sum_{i=0}^{Q-1} \boldsymbol{\xi_i} f_i^\sigma - \sum_{i=0}^{Q-1} \boldsymbol{\xi_i} f_i^{\sigma,eq} \right] = 0. \tag{7.4}$$

However, at equilibrium both components share the same velocity $\boldsymbol{u'}$ and thus we are allowed to write:

$$\sum_{\sigma=1}^{2} \frac{1}{\tau_\sigma} \left[\rho_\sigma \boldsymbol{u_\sigma} - \rho_\sigma \boldsymbol{u'} \right] = 0, \tag{7.5}$$

which finally yields:

$$\boldsymbol{u'} = \frac{\sum_{\sigma=1}^{2} \rho_\sigma \boldsymbol{u_\sigma} / \tau_\sigma}{\sum_{\sigma=1}^{2} \rho_\sigma / \tau_\sigma}. \tag{7.6}$$

In case of a system of N components, the summation would be simply extended from $\sigma = 1$ to $\sigma = N$.

As it was discussed in Chap. 4, the macroscopic momentum of the component σ, which takes part to the Navier-Stokes equations is given by:

$$\rho_\sigma^m \boldsymbol{u_\sigma^m} = \sum_i \boldsymbol{\xi_i} f_i^\sigma + \frac{\boldsymbol{F_\sigma}}{2} = \rho_\sigma \boldsymbol{u_\sigma} + \frac{\boldsymbol{F_\sigma}}{2}. \tag{7.7}$$

Accordingly, the macroscopic momentum of the mixture is the sum of the momentum of each component $\rho^m \boldsymbol{u^m} = \sum_\sigma \rho_\sigma \boldsymbol{u_\sigma^m}$.

So far, we have reported the theory of the Lattice Boltzmann methods for mixtures, but we have not introduced the Shan-Chen model yet, whose main characteristic is the definition of an interaction force between particles. In the most general case, the force acting on the component σ is the sum of four contributions:

1. the interaction of the σ-th component with itself: $\boldsymbol{F_{\sigma\sigma}}$;

2. the interaction of the σ-th component with the $\bar{\sigma}$-th component: $\boldsymbol{F_{\sigma\bar{\sigma}}}$;

3. the adhesion forces on solid surfaces: $\boldsymbol{F_\sigma^{ad}}$;

4. the external forces (such as gravity): $\boldsymbol{F_\sigma^{ext}}$.

Hence $\boldsymbol{F_\sigma} = \boldsymbol{F_\sigma^{coh}} + \boldsymbol{F_\sigma^{ad}} + \boldsymbol{F_\sigma^{ext}}$, where the superscript "coh" stands for cohesion forces and $\boldsymbol{F_\sigma^{coh}} = \boldsymbol{F_{\sigma\sigma}} + \boldsymbol{F_{\sigma\bar{\sigma}}}$. From now on, for the sake of simplicity, we will denote by $\boldsymbol{F_{\sigma\bar{\sigma}}}$ also the single-component interaction, considering the subscripts σ and $\bar{\sigma}$ running over all the components.
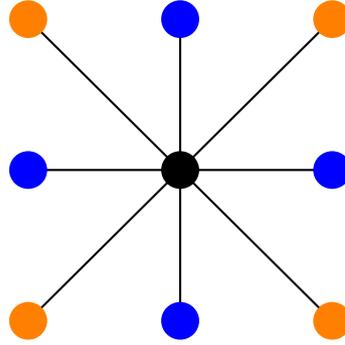
Figure 7.1. Nearest and next-nearest neighbour on the lattice D2Q9.

The Shan-Chen model [4] defines an interaction potential between particles at a certain position $\boldsymbol{x}$ as:

$$V_{\sigma\bar{\sigma}}(\boldsymbol{x}, \boldsymbol{x}') = G_{\sigma\bar{\sigma}}(\boldsymbol{x}, \boldsymbol{x}')\psi_\sigma(\rho_\sigma(\boldsymbol{x}))\psi_{\bar{\sigma}}(\rho_{\bar{\sigma}}(\boldsymbol{x}')), \qquad (7.8)$$

where ψ_σ is in general a function which increases with the density of the σ-th component and goes to zero when $\rho_\sigma \to 0$. It should be noted that this expression is basically a pair potential between two neighbours, which is only function of the distance $|\boldsymbol{x} - \boldsymbol{x}'|$. In addition, it recovers the typical long range interaction of liquids even though it is limited to the nearest nodes. When dealing with a single-component interaction, in order to recover the behaviour of a liquid, and thus allow phase separation, the long range interaction should be attractive, which corresponds to negative values of the interaction potential. The density function originally proposed by Shan & Chen in [4] is:

$$\psi_\sigma(\rho_\sigma(\boldsymbol{x})) = \rho_0(1 - e^{-\rho_\sigma/\rho_0}), \qquad (7.9)$$

where ρ_0 is an arbitrary parameter. However, different functions ψ_σ have been proposed for the single-component interaction in literature [105], while usually for the interaction between components ψ_σ is taken equal to ρ_σ. In addition, the original formulation of the Shan-Chen model was based on a hexagonal lattice and takes the following function $G_{\sigma\bar{\sigma}}(\boldsymbol{x}, \boldsymbol{x}')\psi_\sigma$.

$$G_{\sigma\bar{\sigma}}(|\boldsymbol{x} - \boldsymbol{x}'|) = \begin{cases} g_{\sigma\bar{\sigma}}, & |\boldsymbol{x} - \boldsymbol{x}'| = c, \\ 0, & |\boldsymbol{x} - \boldsymbol{x}'| > c. \end{cases} \qquad (7.10)$$

In this way, we are taking into account only the interaction between the nearest neighbours, which in a hexagonal lattice are all the nodes connected to the node located at $\boldsymbol{x}$. However, when dealing with regular lattices, like the D2Q9, we should consider also the interaction between the next-nearest neighbours (the orange ones in Fig. 7.1), in order to obtain an interaction

with all the connected nodes. According to [106], for the D2Q9 lattice the function $G_{\sigma\bar{\sigma}}(|\boldsymbol{x} - \boldsymbol{x}'|)$ should be defined as:

$$G_{\sigma\bar{\sigma}}(|\boldsymbol{x} - \boldsymbol{x}'|) = \begin{cases} 1/9\, g_{\sigma\bar{\sigma}}, & |\boldsymbol{x} - \boldsymbol{x}'| = c, \\ 1/36\, g_{\sigma\bar{\sigma}}, & |\boldsymbol{x} - \boldsymbol{x}'| = \sqrt{2}c \\ 0, & \text{otherwise.} \end{cases} \qquad (7.11)$$

The factors 1/9 and 1/36 reflects the weights introduced in Subsec. 3.7.3. Thus, the force $F_{\sigma\bar{\sigma}}$, acting on the component σ and caused by the component $\bar{\sigma}$, is equal to $-\nabla V_{\sigma\bar{\sigma}}$ and is given in the discretized form by:

$$\boldsymbol{F_{\sigma\bar{\sigma}}}(\boldsymbol{x}) = -\psi_\sigma(\rho_\sigma(\boldsymbol{x}))g_{\sigma\bar{\sigma}} \sum_{i=0}^{8} w_i\psi_{\bar{\sigma}}(\rho_{\bar{\sigma}}(\boldsymbol{x} + \boldsymbol{\xi_i}))\boldsymbol{\xi_i}. \qquad (7.12)$$

The interpretation of this formula is clear if we keep in mind the definition of the pair interaction potential Eq. (7.8). In fact, the particles at node $\boldsymbol{x}$ interacts with all the connected nodes (nearest and next-nearest neighbours), via the above-mentioned pair interactions. In Eq. (7.12), we are simply summing the forces due to each connected neighbour. These forces are evaluated as the gradient of the pair interaction potential, which of course has to be intended as function of the distance between the two nodes.

The total force acting on the σ-th component is simply the sum over all the components of these contributions.

Analysing Eq. (7.12), we understand the basic idea of the Shan-Chen model. Since, the function ψ is connected to density, and in particular it increases with density, we realize how a uniform density distribution would yield a null interaction force, because the summation into Eq. (7.12) would be zero by symmetry. However, if density fluctuations are present, depending on the sign of the parameter $g_{\sigma\bar{\sigma}}$, the cohesion force manifests itself either by hindering the density fluctuation or by promoting phase separation. The parameter $g_{\sigma\bar{\sigma}}$ determines also the strength of the interaction. In fact, it is easy to realize that high values of $g_{\sigma\bar{\sigma}}$ mean high surface tensions.

The Chapman-Enskog expansion for the Shan-Chen model is basically similar to the one carried out in Chap. 4, but, considering Eq. (4.49), the additional interaction terms $-\partial_\alpha V_{\sigma\bar{\sigma}}$ are added to the left side, leading to a momentum equation for the mixture [4]:

$$\partial_t(\rho^m u_\alpha^m) + \partial_\beta(\rho^m u_\alpha^m u_\beta^m) = -\partial_\alpha(c_s^2\rho^m) + \partial_\beta(\mu\partial_\beta u_\alpha^m) +$$
$$\partial_\beta(\mu\partial_\alpha u_\beta^m) + F_\alpha - \sum_{\sigma,\bar{\sigma}} \partial_\alpha V_{\sigma\bar{\sigma}}, \qquad (7.13)$$

where the terms $\mathcal{O}$ are not reported for the sake of simplicity [2]. Analysing

---

[2]If a mass source is not present $\rho^m = \rho = \sum_\sigma \rho_\sigma$

Eq. (7.13), it is straightforward to identify the macroscopic pressure as:

$$p = c_s^2 \rho + \sum_{\sigma, \bar{\sigma}} \partial_\alpha V_{\sigma \bar{\sigma}}. \qquad (7.14)$$

In this way, it is possible to obtain a non-ideal equation of state for the system, which links density and pressure. Since, in literature there is a bit of confusion on the form of the equation of state, depending on the type of lattice and how the Shan-Chen model is implemented, the derivation of the equation of state for the model described above is here reported. Using a correct equation of state is actually very important, because we will need to compute pressure in order to obtain the surface tension and also because it let us to better understand the immiscible behaviour of the Shan-Chen model, as it will be shown in the next section.

Thus, let us consider the Shan-Chen model applied to the lattice D2Q9 as described before. According to Eq. (7.12) the force acting on the σ-th component and caused by the $\bar{\sigma}$-th component is given by:

$$\boldsymbol{F_{\sigma \bar{\sigma}}} = -g_{\sigma \bar{\sigma}} \psi_\sigma(x, y) \left[\frac{1}{9} (\psi_{\bar{\sigma}}(x + c, y)\boldsymbol{\xi_1} + \psi_{\bar{\sigma}}(x, y + c)\boldsymbol{\xi_2} + \psi_{\bar{\sigma}}(x - c, y)\boldsymbol{\xi_3} + \right.$$

$$\psi_{\bar{\sigma}}(x, y - c)\boldsymbol{\xi_4}) + \frac{1}{36} (\psi_{\bar{\sigma}}(x + c, y + c)\boldsymbol{\xi_5} +$$

$$\left. \psi_{\bar{\sigma}}(x - c, y + c)\boldsymbol{\xi_6} + \psi_{\bar{\sigma}}(x - c, y - x)\boldsymbol{\xi_7} + \psi_{\bar{\sigma}}(x + c, y - c)\boldsymbol{\xi_8}) \right].$$

$$(7.15)$$

Now, by means of a Taylor expansion of the first order of the terms $\psi_{\bar{\sigma}}$, and remembering that $\boldsymbol{\xi_3} = -\boldsymbol{\xi_1}$, $\boldsymbol{\xi_4} = -\boldsymbol{\xi_2}$, $\boldsymbol{\xi_7} = -\boldsymbol{\xi_5}$ and $\boldsymbol{\xi_8} = -\boldsymbol{\xi_6}$, we are allowed to write [3]:

$$\boldsymbol{F_{\sigma \bar{\sigma}}} = -g_{\sigma \bar{\sigma}} \psi_\sigma \left[\frac{1}{9} \left(2 \frac{\partial \psi_{\bar{\sigma}}}{\partial x} \right) c \, \boldsymbol{\xi_1} + \frac{1}{9} \left(2 \frac{\partial \psi_{\bar{\sigma}}}{\partial y} \right) c \, \boldsymbol{\xi_2} + \right.$$

$$\left. \frac{1}{36} \left(2 \frac{\partial \psi_{\bar{\sigma}}}{\partial x} + 2 \frac{\partial \psi_{\bar{\sigma}}}{\partial y} \right) c \, \boldsymbol{\xi_5} + \frac{1}{36} \left(-2 \frac{\partial \psi_{\bar{\sigma}}}{\partial x} + 2 \frac{\partial \psi_{\bar{\sigma}}}{\partial y} \right) c \, \boldsymbol{\xi_6} \right].$$

$$(7.16)$$

Finally, the insertion of Eqs. (3.68) yields:

$$\boldsymbol{F_{\sigma \bar{\sigma}}} = -\frac{1}{3} g_{\sigma \bar{\sigma}} c^2 \psi_\sigma \begin{bmatrix} \frac{\partial \psi_{\bar{\sigma}}}{\partial x} \\ \frac{\partial \psi_{\bar{\sigma}}}{\partial y} \end{bmatrix}. \qquad (7.17)$$

After this derivation, we are able to compute the interaction potential $V_{\sigma \bar{\sigma}}$ since $F_{\sigma \bar{\sigma}, \alpha} = -\partial_\alpha V_{\sigma \bar{\sigma}}$. Thus, let us consider a single-component interaction,

---

[3]From now on, the arguments (x, y) will be omitted.

where $\bar{\sigma} = \sigma$. From Eq. (7.17), we obtain:

$$F_{\sigma\sigma,\alpha} = -\frac{1}{3}g_{\sigma\bar{\sigma}}c^2\psi_\sigma\frac{\partial\psi}{\partial x_\alpha}, \qquad (7.18)$$

and from its simple integration:

$$V_{\sigma\sigma} = \frac{1}{6}g_{\sigma\bar{\sigma}}c^2\psi^2. \qquad (7.19)$$

This result is basically the same obtained by Kuzmin in [1] and by Sbragaglia *et al.* in [32]. In addition, by applying the same procedure to the scheme proposed by Yuan & Schaefer in [5], in which the factors 1 and 1/4 are used in place of 1/9 and 1/36 into Eqs. (7.11), the equation of state is the same.

Let us now conclude the analysis of the equation of state of the Shan-Chen model by considering the interaction between different components. Let us consider a binary mixture in which $g_{12} = g_{21}$. According to Eq. (7.17), in this case the sum of the forces $F_{12,\alpha}$ and $F_{21,\alpha}$ is:

$$F_{12,\alpha} + F_{21,\alpha} = -\frac{1}{3}g_{12}c^2\left(\psi_1\frac{\partial\psi_2}{\partial x_\alpha} + \psi_2\frac{\partial\psi_1}{\partial x_\alpha}\right). \qquad (7.20)$$

Its easy integration yields:

$$V_{12} + V_{21} = \frac{1}{3}g_{12}c^2\psi_1\psi_2, \qquad (7.21)$$

which was correctly applied in [106].

Thus, if we consider the most general case of a binary mixture in which both single-component and multi-component interactions are taken into account, inserting Eqs. (7.19) and (7.21) into Eq. (7.14), we finally obtain the equation of state for the mixture:

$$p = c^2\left[\frac{\rho_1 + \rho_2}{3} + \frac{1}{6}\left(g_{11}\psi_1^2 + g_{22}\psi_2^2\right) + \frac{1}{3}g_{12}\psi_1\psi_2\right], \qquad (7.22)$$

where of course we have used $c_s^2 = c^2/3$, since we are dealing with the lattice D2Q9. Obviously, if we use also spatial lattice units $c = 1$.

7.2   Static tests

The starting points of any Shan-Chen study of multi-phase flows are definitely static tests. In particular, the static bubble, or drop, test plays a very important role in the Shan-Chen mode [4]. In two dimensions, the test basically consists in placing a disk, in the centre of a square domain, with density

---

[4]From now on we will call it static bubble, even if sometimes it might be a drop.

(a) *Bubble*

(b) *Drop*
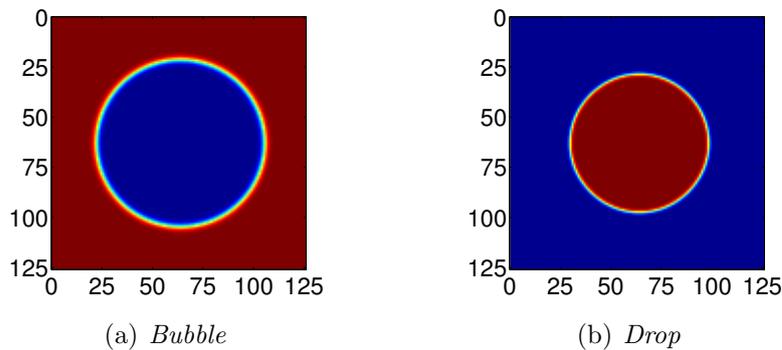
Figure 7.2. Examples of bubble and drop obtained with the single-component Shan-Chen model. The blue represents low density, while the red high density.

different from the one of the surrounding fluid. The domain is assumed to be periodic in all directions. As no external forces are applied to the fluid, we expect that the interface will remain circular and that the velocity field will be everywhere equal to zero. Obviously this test case may be applied to any computational method for multi-phase flow.

In addition, for reasons that will be clearer later on, also the flat interface test might be useful in the context of the Shan-Chen model. The test is similar to the static bubble, but now the interface is initialized flat in a periodic domain, as shown in Fig. 7.3.

However, for the Shan-Chen model the static tests fulfil another fundamental role. In fact, as the reader may have understood from the model description given in Sec. 7.1, in the Shan-Chen model we are not free to pass directly parameters such as the surface tension, or even the density or the dynamic viscosity of one phase to the simulation. Instead, in order to control the simulation, we need an additional phase of calibration of the model, which, as we will see, might be very tricky. This can surely be numbered among the drawbacks of the Shan-Chen model, even though it might be instructive for the understanding of multi-phase phenomena.

It is clear that the static tests are particularly suited for the calibration process. In fact they allow to evaluate the simulated surface tension easily, to investigate the immiscible behaviour of the Shan-Chen model and to highlight also other characteristics of the model. Thus, the static tests are always preparatory for more complex simulations to be carried out by means of the Shan-Chen model.

We begin our analysis of the Shan-Chen model by considering the single-component case, where a pseudo-potential $\psi_1(\rho)$ is present. According to
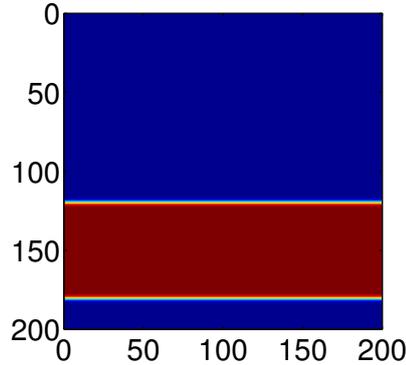
Figure 7.3. Flat interface test. The blue represents low density, while the red high density.

Eq. (7.22), the equation of state for this system becomes:

$$p = \frac{\rho}{3} + \frac{1}{6}g_{11}\psi_1^2(\rho), \tag{7.23}$$

where we are directly considering a system of lattice units, where the lattice spacing is set equal to unity. In addition, we will use the pseudo-potential originally proposed by Shan & Chen [4] and already reported in Eq.(7.9). The critical point of the system can be obtained by setting:

$$\frac{\partial p}{\partial \rho} = 0, \tag{7.24a}$$

$$\frac{\partial^2 p}{\partial \rho^2} = 0. \tag{7.24b}$$

It can be easily verified that this leads to the following critical parameters [1]:

$$\rho_c = \rho_0 \ln 2, \tag{7.25a}$$

$$(\rho_0 g_{11})_c = -4. \tag{7.25b}$$

However, in literature, it is common to set the density unit equal to ρ_0, which is definitely the natural density scale in this problem. Consequently, by fixing also the lattice spacing as unity, a mass unit is induced that from now on we will call mu_0. It should also be noted that the critical value of g_{11} is negative, which, as it was already mentioned, means attractive long-range interactions.

The critical value of g_{11} was verified numerically by means of a flat interface test. The flat interface test was preferred over the static bubble test,
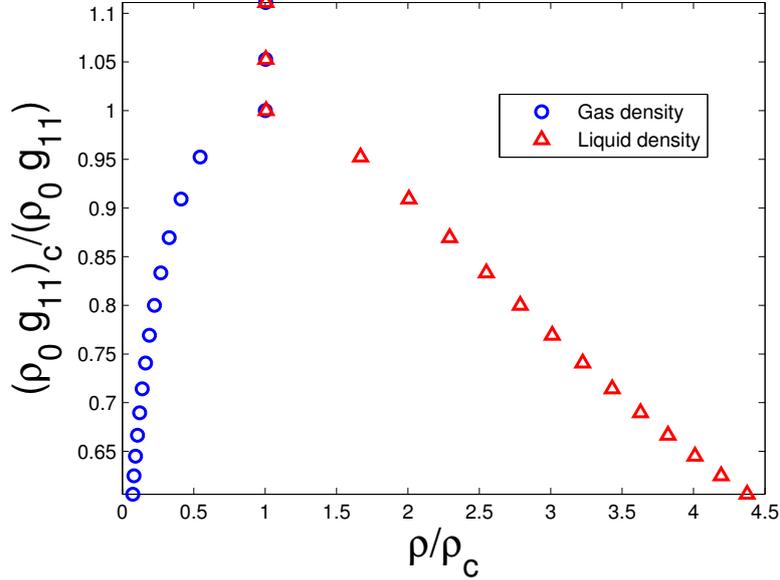
Figure 7.4. Phase separation for the single-component Shan-Chen model.

because in the second case the density values would have been surely influenced by the bubble radius. This has actually a physical sense. In fact, when a bubble of vapour is formed inside liquid water, we expect that it has a slightly higher pressure compared to the saturation value. This is due to the effect of mechanical equilibrium at the interface analysed in Subsec. 2.5.1 and translated by the Laplace's law Eq. (2.25).

The simulations are carried out over a domain of 200x200 lattice nodes. The flat interface was initialized by placing a density $\rho = 1 \, \mathrm{mu_0 \, lu^{-2}}$ on half domain, while $\rho = 0.3862 \, \mathrm{mu_0 lu^{-2}}$ was set on the other half of the domain [5]. In this way a total density $\rho = \ln 2 \, \mathrm{mu_0 \, lu^{-2}}$ was achieved in the system. A density difference is in general necessary in order to trigger phase separation. In all the simulations the relaxation parameter τ was set to unity. The parameter g_{11} is varied from a theoretical supercritical value to the stability limit. The simulations are stopped when an equilibrium condition is reached. The results are displayed in Fig. 7.4. We see that the theoretical critical value of g_{11} agrees well with the numerical results and the graph is definitely comparable with the one obtained by Kuzmin in [1]. The maximum simulated density ratio is $\rho_L/\rho_G \approx 100$, which corresponds to $\rho_0 g_{11} = -7.3$, where instability occurs. This ratio is well below the ratio ≈ 1000 of the air-water system, but it is however relatively high. However, this limit is valid for flat

---

[5]The quantities are obviously considered in two dimensions.

interfaces, while the situation worsens for circular interfaces.

In addition, an interpretation of the parameter g_{11} is suggested. In fact, increasing the parameter g_{11} in magnitude has the same effect of decreasing the temperature in a real system. This is due to the fact that in physical system the effect of any interacting potential must be weighted by the thermal energy $k_b T$ (see [107] for more insights). Thus, in our case we have that the effect of the interacting potential of the Shan-Chen model is governed by the ratio:

$$\frac{g_{11}\psi^2}{k_b T}.$$ (7.26)

However, $k_b T$ is a lattice constant equal to $1/3$ in lattice units, and therefore the weight is governed by the parameter g_{11}. From Fig. 7.2 and Fig. 7.3, we can readily identify a characteristic of the Shan-Chen model, that is the presence of a diffusive finite interface. The interface has a certain thickness in which the density assumes intermediate values between the gas and liquid condition. On the contrary, the interface is usually modelled with an infinitesimal thickness, as it is done in the derivation of the Laplace's law. In this case, the interface becomes a surface of discontinuity. However, we can imagine how this is just an approximation, and in general the interface has a certain thickness, indeed. The discontinuous modelling can be considered valid, when the typical thickness of the interface is much lower than the typical length scale of the problem under consideration, which is true in many cases.

In the context of diffusive interface, the thermodynamic definition of the surface tension was formulated by van der Waals during the nineteenth century and it states that [108]

$$\sigma = \int_{-\infty}^{+\infty} \Psi(z)\, dz,$$ (7.27)

where we are considering an infinite system with a flat interface and z identifies the direction perpendicular to the interface. $\Psi(z)$ represents the local excess free energy density, that is the difference between the free energy with and without the interface. Eq. (7.27) is the starting point of the Cahn-Hilliard theory of surface tension [102], from which other Lattice Boltzmann models are originated, as it was already mentioned at the beginning of this chapter. Nevertheless, the definition of a Free-Energy for the Shan-Chen model is not trivial, but it has been recently achieved by Sbragaglia *et al.* [109], which solves the problem of lack of thermodynamical basis of the Shan-Chen model.

In Fig. 7.5 we can better appreciate the diffusive behaviour of the Shan-Chen model at interface. The density slightly goes from density values typical
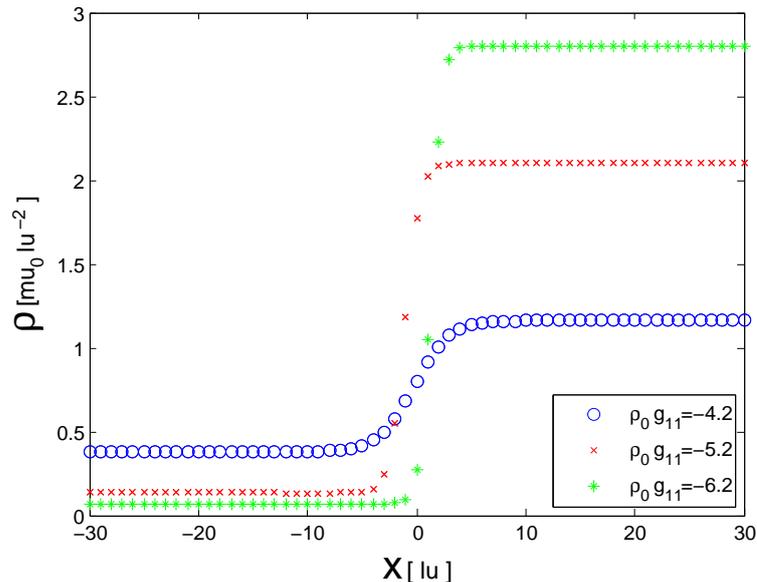
Figure 7.5. Density as a function of x for different values of the parameter $\rho_0 g_{11}$. The origin of the x-axis was placed approximately in the centre of the interface in each case. The domain was taken 200x200 lattice nodes.

of the gas phase to values typical of the liquid phase. Furthermore, it is clear that the thickness of the interface decreases with the magnitude of the parameter $\rho_0 g_{11}$. From a practical point of view, it is definitely easier to deal with thin interface thicknesses, which also represents the case of most applications, but, as we will see, the stability of the method is concerned when the interface is too thin.

As it was already stated, in this context, the Laplace's law is no longer rigorously valid, but it continues to represent a good approximation, especially at high values of $\rho_0 g_{11}$. Thus, the usual way to obtain the surface tension is to test the Laplace's law by running simulations with different bubble radii, keeping fixed the parameter $\rho_0 g_{11}$. Then, by means of a linear regression (without intercept) between the pressure difference P_c and the inverse of the radius $1/R$, the linear regression is obtained according to the Laplace's law in two dimensions Eq. (2.27). An example of this procedure is displayed in Fig. 7.6.

In particular the pressure inside the bubble is evaluated at the centre, while the outside pressure is computed in one point near one of the boundaries. It is worth noting that the radius of the disk is not an input parameter. The disk is initialized with a certain radius R_{in}, but it is then modified according to the mechanical equilibrium established by the simulation. Thus, the final radius has to be measured, at the end of the simulation
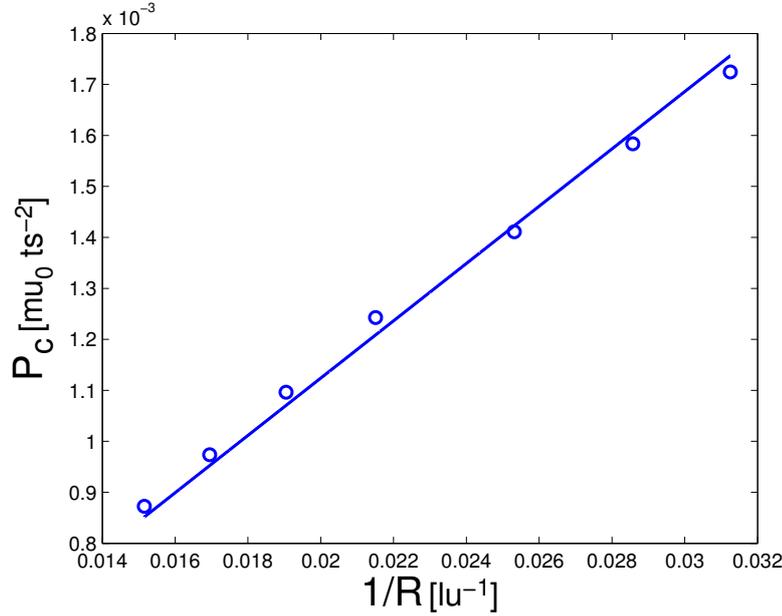
Figure 7.6. Laplace's law verification. The parameter $g_{11}\mathrm{lu}^2\,\mathrm{mu}_0^{-1}$ is set to $-5\,\mathrm{lu}^2\,\mathrm{mu}_0^{-1}$ and from the linear regression the surface tension was obtained $\sigma = 0.05620\,\mathrm{mu}_0\,\mathrm{lu}\,\mathrm{ts}^{-2}$.

and it is also not well defined, given the diffusive nature of the interface. In Fig. 7.6, the radius was assumed between the two nodes i and j, such that $\rho(i) \leq (\rho_L + \rho_G)/2 \leq \rho(j)$. When the magnitude of $\rho_0 g_{11}$ is relatively high, the surface tension obtained by considering the minimum or maximum radius of the interface are almost equal, which of course allow us to use the average radius. Fig. 7.6 shows a good agreement with the Laplace's law, which allows to obtain the surface tension of the system.

It is worth pointing out that another way of computing the surface tension is from its mechanical definition. Considering the case of an horizontal flat diffusive interface and an infinite system, the surface tension is given by[108]:

$$\sigma = \int_{-\infty}^{+\infty} (P_{yy} - P_{xx})\,dy \qquad (7.28)$$

where $P_{\alpha\alpha}$ are the diagonal components of the pressure tensor. In fact, when we have phase separation, we can imagine how the diagonal components of the pressure tensor at equilibrium are not all equal as usual at the interface (and equal to the common pressure). Basically, this is the inherent cause of the surface tension.

Shan [110] has recently obtained an expression to compute the additional components of the pressure tensor due to the Shan-Chen interaction. Starting
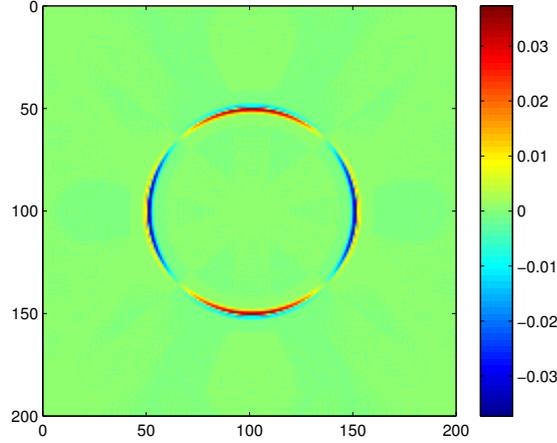
Figure 7.7. Difference between P_{yy} and P_{xx} ($[\mathrm{mu}_0\,\mathrm{ts}^{-2}]$) for a static bubble.

from the continuum description of the intermolecular forces in which the additional pressure tensor due to the force interaction is defined as:

$$\nabla \cdot \bar{\bar{\boldsymbol{P}}}^{\boldsymbol{I}} = \boldsymbol{F^I},\qquad(7.29)$$

where here with the superscript "I" we intend that the force is an interaction force. By applying this definition to the interaction of the Shan-Chen model and thus considering a discrete description, the Shan-Chen pressure tensor is obtained as [110]:

$$\bar{\bar{\boldsymbol{P}}}^{\boldsymbol{SC}} = -\frac{g_{11}}{2}\psi(\boldsymbol{x})\sum_i w_i \psi(\boldsymbol{x}+\boldsymbol{\xi_i})\boldsymbol{\xi_i}\boldsymbol{\xi_i}.\qquad(7.30)$$

This formula was used to compute P_{xx}^{SC} and P_{yy}^{SC}. In Fig. 7.7 we can appreciate how the difference between the two diagonal components of the stress tensor assumes non zero values at the interface.

Thus, the computation of the surface tension was attempted through Eqs. (7.28) and (7.30) and compared to the results of the Laplace's test for different values of the parameter g_{11}, keeping fixed ρ_0. In particular, the theoretical surface tension was evaluated through Eq. (7.28) for a series of numerical experiments with flat interface, where the integral was evaluated along one of the interfaces of Fig. 7.3:

$$\sigma = \int_{interface}(P_{yy}-P_{xx})\,dy.\qquad(7.31)$$

The integral is evaluated through the trapezoidal rule.
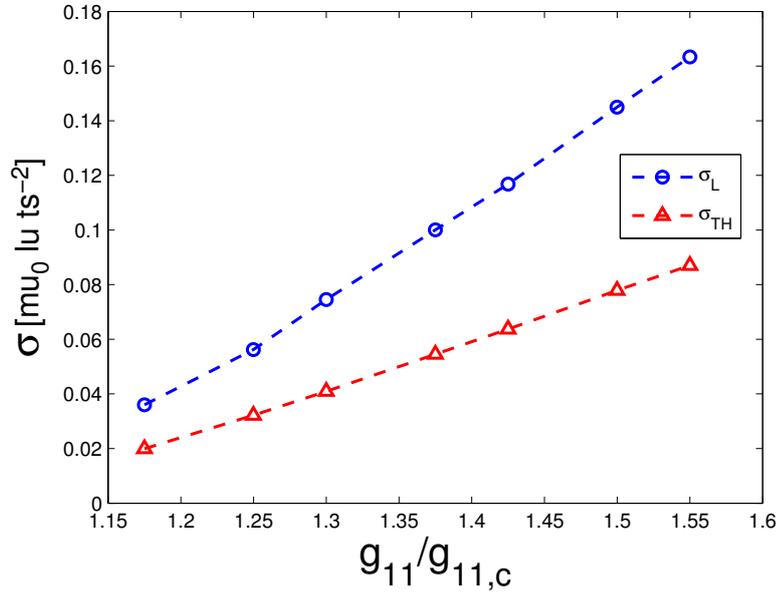
Figure 7.8. Laplace's law surface tension and theoretical surface tension as a function of $g_{11}/g_{11,c}$.

Simulations with the same parameter g_{11} are carried out for the static bubble test with different radii and the simulated surface tension is obtained through the Laplace's law as described before. In these simulations $\rho_0 = 1\mathrm{mu}_0\,\mathrm{lu}^{-2}$.

The results are displayed in Fig. 7.8. We can appreciate how both the simulated surface tension and the theoretical surface tension increase linearly with the parameter $g_{11}/g_{11,c}$. However, a discrepancy between the two values is clear, as well. In addition, Fig. 7.8 shows clearly a proportionality relationship between σ_L and σ_{TH}. The proportionality constant was found to be 1.8493 by the linear regression.

This discrepancy has been studied by Huang *et al.* in [85] and the reason behind it has been found in the inclusion of the interaction force term by the methods of the shifting velocity of the original Shan-Chen model. In particular, as shown in Fig., in the original formulation the Shan-Chen model the surface tension, and the density ratio as well, strongly depends on the relaxation parameter τ. However, this feature seems to be shared also by other forcing schemes and by other choice of the pseudo-potential ψ [85]. The dependency of the surface tension and the density ratio τ is clearly unphysical and it is thermodynamically inconsistent. Nevertheless, as it was argued by Kuzmin [1], this effect should be eliminated if the proper scheme proposed by Guo *et al.* [84] is applied to the Shan-Chen model. This agrees
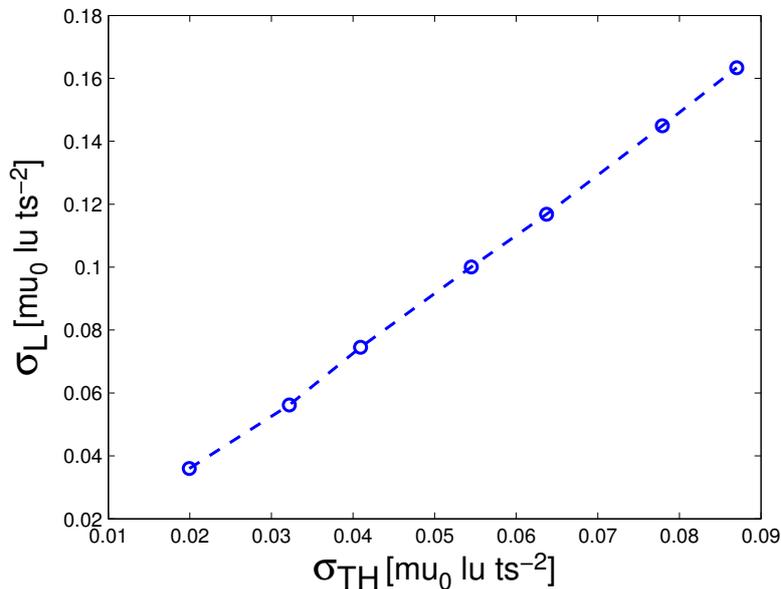
Figure 7.9. Simulated surface tension vs. theoretical surface tension.

with the proof given in Chap. 4 and allows to identify the cause of the unphysical dependency on τ of the surface tension in the additional terms neglected in the momentum equation by other schemes, but forced to zero by the Guo's scheme.

Unfortunately, the Shan-Chen model is implemented in Palabos only with the original method of the shifting velocity on the equilibrium distribution. The implementation of the Guo's scheme would have required a considerable modification of the code that has been avoided in this thesis and left for an eventual future work.

It is worth pointing out that the dependency of the density ratio and the surface tension on τ are not the only inconsistencies of the Shan-Chen model. We have already mentioned the lack of a free-energy in the original formulation and in addition, it is shown [105], that the only form of the pseudopotential ψ which is consistent with the Maxwell's equal area reconstruction is:

$$\psi(\rho) = \psi_0 e^{-\rho_0/\rho}. \tag{7.32}$$

All these problems of the Shan-Chen model should be taken into account when dealing with concrete simulations, but in general do not affect its applicability. For example, the simulated surface tension of the model can always be computed with the Laplace's test without considering its discrepancy from the theoretical value. Anyway, from this introduction of the single-component Shan-Chen model, we can understand how a constraint of the

model is that the density ratio and the surface tension cannot be tuned independently. Moreover, if the relaxation parameter is kept fixed, the dynamic viscosity ratio is always equal to the density ratio. A further complication would be to relate vary the relaxation parameter with density, in order to tune the dynamic viscosity ratio, but even this possibility will not be analysed in what follows. However, we here report that Sbragaglia *et al.* have suggested that the surface tension and the density ratio can be tuned independently by considering also the interaction with the second layer of neighbours [32], giving rise to the so-called multi-range model.

Let us now focus on another interesting feature of the Shan-Chen model for single-component fluid that is the behaviour nearby the critical point. It is known that different critical phenomena such as gas-liquid transition and ferromagnetic transition shares similar critical behaviour as a function of the parameter that governs the transition, which is typically temperature. In critical transitions, an order parameter can be identified, which takes into account the phase separation. For example, in gas-liquid transition, the role of the order parameter is accomplished by the difference between liquid and gas density, while in ferromagnetic transition it is carried out by the magnetization. The order parameter goes to zero at the critical point and it shows a power law behaviour as a function of the parameter governing the transition:

$$\Lambda \sim \theta^{\beta_\Lambda}, \tag{7.33}$$

where here we are denoting by Λ a certain order parameter and by θ the associated transition parameter. Surprisingly enough, order parameters from different phenomena not only behaves as a power law, but seem to share also the same exponent β_Λ. The critical behaviour of the Shan-Chen transition has been investigated considering the order parameter $\Lambda^{SC} = (\rho_L - \rho_G)/\rho_L$ and as transition parameter $\theta^{SC} = (\rho_0 g_{11})_c [1/(\rho_0 g_{11})_c - 1/(\rho_0 g_{11})]$. In Fig. 7.10, we are able to see how the power law behaviour is perfectly recovered by the Shan-Chen model. Furthermore, the exponent of the transition is found $\beta_{SC} \approx 0.5$. This definitely puts the Shan-Chen model in the framework of mean field theory. In fact, the mean-field theories of van der Waals and Curie-Weiss for gas-liquid transition and ferromagnetic transition respectively, predict both a critical exponent equal to $1/2$ [107]. For more insights on the critical behaviour of the Shan-Chen model see [111].

As a final issue for the single-component Shan-Chen model we deal with the effective verification of the static bubble test. As we have previously mentioned we expect the velocity field to be everywhere zero and the bubble to remain at the centre of the domain, where it is initially placed with a symmetrical disk shape in two dimensions. Obviously, the radius of the bubble generally varies from the initial value, unless we have correctly guessed
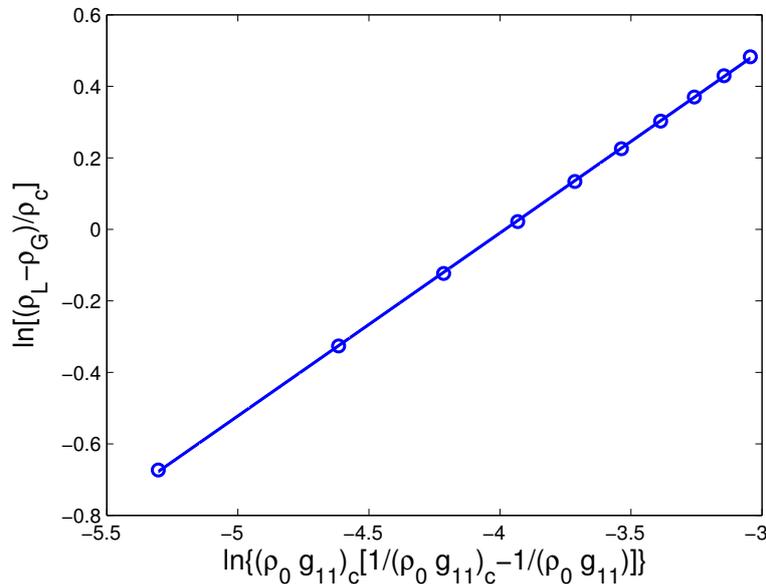
Figure 7.10. Order parameter as a function of the transition parameter for the single-component Shan-Chen model.

the equilibrium gas and liquid density at the beginning of the simulations, which is of course a very unlikely event.

Fig. 7.11(a) shows the velocity norm field scaled by $c_s = 1/\sqrt{3}$, that is the Mach number. The velocity is basically everywhere zero, except at the interface where we have high velocities. These unphysical velocities are usually called spurious currents and are definitely one of the main concern of the Shan-Chen model. It should be noted that the structure of the velocity field resembles that of the underlying lattice. The velocity vectors shown in Fig. 7.11(b) allow us to identify the presence of circulating flows through the interface. In Fig. 7.12, we can grasp how the spurious velocities are normal to the interface, when the x-axis or the y-axis are perpendicular to the interface [6]. The spurious currents are not only a feature of the Shan-Chen model, but they are also present in multi-phase schemes based on free-energy.

The spurious currents not only complicates the analysis of the result of the simulations, but are also the cause of the instability of the simulations when the parameter $\rho_0 g_{11}$ increases in magnitude. In fact, the spurious velocities are connected to the density gradient at interface and thus when $\rho_0 g_{11}$ becomes more negative [7], leading to higher density ratios and lower

---

[6]Actually, we are able to notice it also in Fig. 7.11(b), if we look carefully at it

[7]In this case we are obviously considering the pseudopotential $\psi = 1 - e^{-\rho/\rho_0}$, but
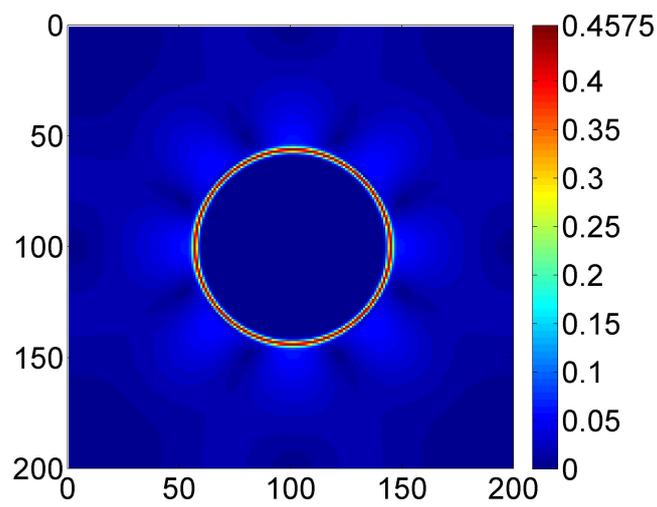
(a) *Mach number field u/c_s.*
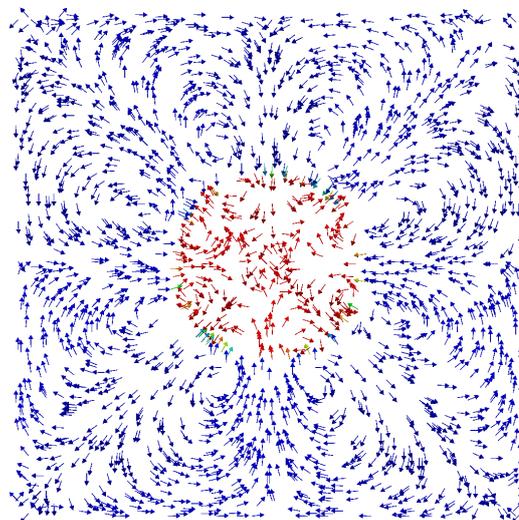
(b) *Velocity vectors.*

Figure 7.11. Spurious velocities for the static bubble test.

(a) U_x/c_s (b) U_y/c_s
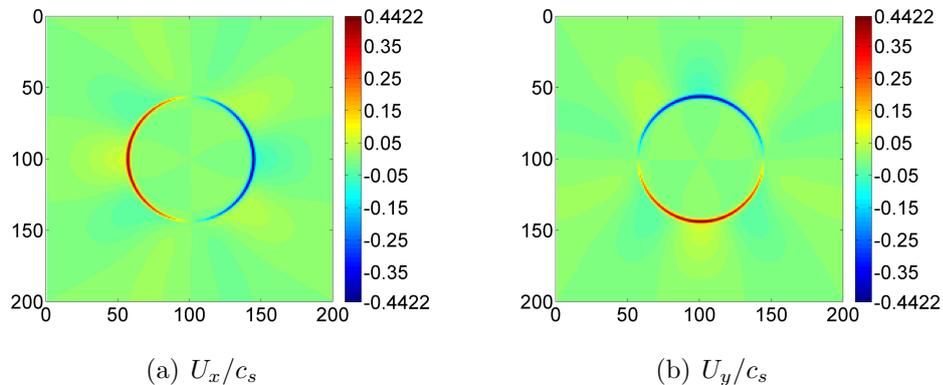
Figure 7.12. Scaled velocity components.

interface thickness, we expect the spurious currents to increase in magnitude leading to instability [1], whose main origin lays in the expansion of the Maxwellian distribution function for low Mach number Eq. (3.53). In fact, this is the reason of the limited density ratios of the Shan-Chen model.

It is established in literature that the origin of the spurious currents is the not sufficient isotropy of the interaction force term and are present only when the interface has a certain curvature [112]. Great effort has been made in recent years in order to reduce the spurious currents. The interpretation of the spurious currents given by Shan in [112] has been further investigated in [32] by Sbragaglia *et al.*, which has proposed the already mentioned multi-range potential model, which increases the isotropy of the force term and allows to reduce the spurious currents. However, another method of dealing with the spurious currents has been proposed by Yuan & Schaefer in [5] and consists in incorporating different equation of state (EOS) in the Shan-Chen model. We will come back to this approach in the following section, since it has also other interesting feature.

After the analysis of the static test for the single-component Shan-Chen model, we will now treat the multi-component Shan-Chen model. Since the main features of the Shan-Chen model have been already highlighted by the single-component case, and are basically shared by the multi-component case, we will just briefly tackle the issue of the multi-component Shan-Chen model, focusing on its immiscible behaviour.

Thus, let us consider a multi-component system where only the interaction between the two components is considered, which means $g_{11} = g_{22} = 0$.

---

analogous considerations can be made for different choices of ψ.
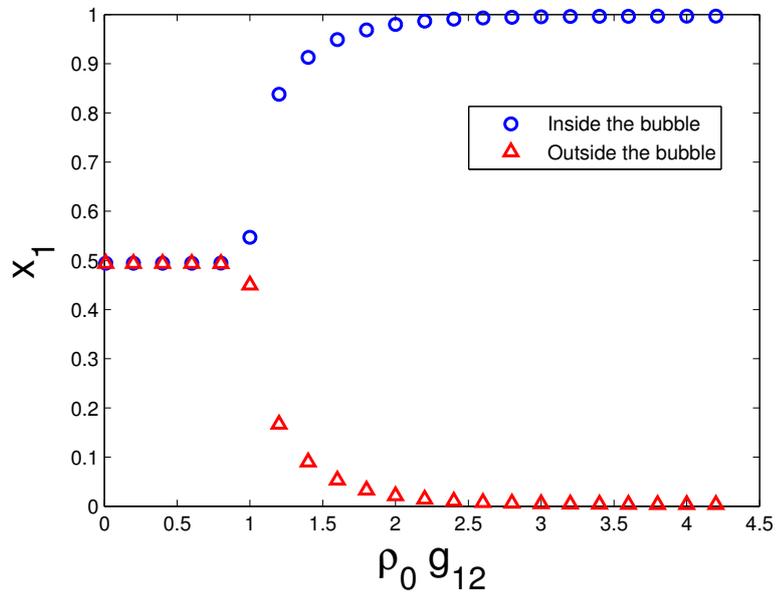
(a) *Mass fraction of component* 1
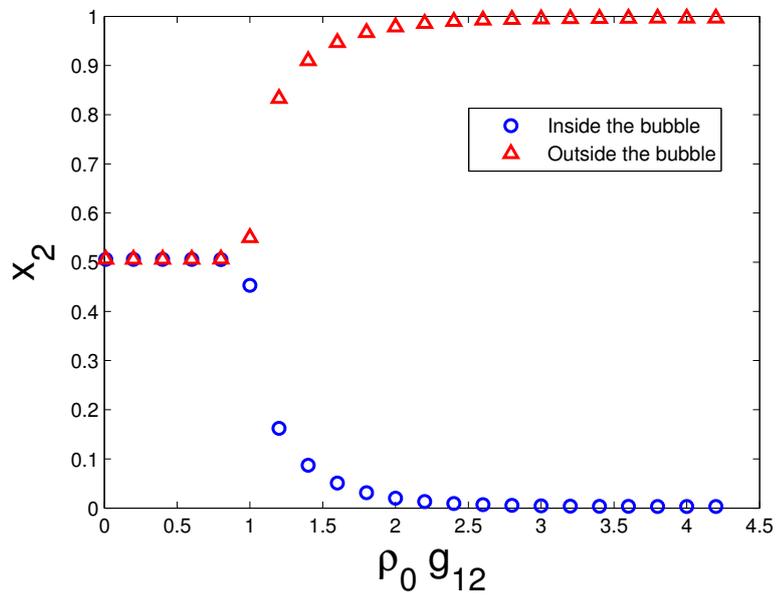
(b) *Mass fraction of component* 2

Figure 7.13. Immiscible behaviour of the multi-component Shan-Chen model.

According to Eq.(7.22), the equation of state for the system becomes:

$$p = \frac{\rho_1 + \rho_2}{3} + \frac{1}{3}g_{12}\rho_1\rho_2, \tag{7.34}$$

where we are considering lattice units and we have set the multi-component pseudopotential ψ_σ equal to ρ_σ for both components as usual in literature and how it is implemented in Palabos.

The immiscible behaviour of the multi-component case is investigated in the case of a static bubble. In fact in this case, the flat interface and the static bubble do not differ too much, since we are actually interested in the mass fractions of each component. In this case, the results are scaled by the total density of the system which has now the role of ρ_0 and fixes the mass scale mu_0 [106]. In addition, the critical value of the parameter $\rho_0 g_{12}$ is equal to unity [106].

Thus, in order to initialize the simulation, a disk is placed at the centre of a 126x126 lattice nodes. The radius of the disk is equal to $50\,\mathrm{lu}$ and the density of component 1 and 2 are set respectively to $\rho_1 = 1\,\mathrm{mu_0}\,\mathrm{lu}^{-2}$ and $\rho_2 = 0\,\mathrm{mu_0}\,\mathrm{lu}^{-2}$. On the contrary, outside the disk the densities are set $\rho_1 = 0\,\mathrm{mu_0}\,\mathrm{lu}^{-2}$, $\rho_2 = 1\,\mathrm{mu_0}\,\mathrm{lu}^{-2}$. In this way the total mass fractions are approximately equal to $1/2$, i.e., the critical mass fractions. By varying g_{12} we obtain different mass fractions as usual. In all the simulations the relaxation parameter τ is set to 1. When the mass fractions of the fluids become stationary the simulation is stopped as usual. The results are shown in Fig. 7.13.

We are able to see that the numerical critical value of the parameter $\rho_0 g_{12}$ matches the theoretical findings. For $\rho_0 g_{12}$ greater than the critical value $(\rho_0 g_{12})_{crit} = 1$, the system separates itself in two phases with different mass fractions. The separation curve is now strictly symmetric.

It should be noted that, in this case, it is possible to tune the kinematic viscosity ratio taking different values of τ for the two components. However, only viscosity ratios close to unity are allowed due to instability.

Analogously to the single-component case, the computation of the surface tension can be made by means of the Laplace's law and the surface tension increases with $\rho_0 g_{12}$. Nevertheless, a serious limitation of the multi-component Shan-Chen model is that the density ratios are always very close to 1. In general, it is very difficult to tell whether the higher density will be inside the disk or outside it. A further complication would be to include also the single-component interactions in the multi-component model, which lead to the general equation of state reported in Eq. (7.22).

7.3 Incorporating EOS

In Sec. 7.2 we have started to become familiar with the Shan-Chen model in its original formulation. The main criticalities have also been highlighted and they can be summarized in:

- spurious currents;

- coupling between density ratio and surface tension;

- unphysical dependency of the surface tension on the relaxation parameter.

We have also seen that recent the literature on the Shan-Chen model has focused on the solution of these problems. Basically two approaches have been proposed to deal with these issues:

1. the introduction of a multi-range pseudopotential (Sbragaglia *et. al* [32]);

2. the incorporation of physical Equation of State (EOS) (Yuan & Schaefer [5]).

In particular, the multi-range potential method, in which the interaction is extended to the next layers of neighbours, seems to reduce all the above-mentioned problems, but the price to be paid is an higher computational cost. On the other hand, the usage of physical EOS seems to allow a great reduction of the spurious currents, achieving much higher density ratio when compared to the original formulation of the Shan-Chen pseudopotential with basically the same computational cost. Furthermore, dealing with common EOS is definitely easier and leads to more physical situations.

It is worth pointing out that the idea behind the multi-range potential is supported in [32] by the theoretical interpretation of the nature of the spurious currents, that is the insufficient isotropy of the interaction force term. The multi-range potential implies an improvement of isotropy and thus, a reduction of spurious currents. On the contrary, the introduction of a physical EOS on the Shan-Chen model seems to yield improvements, but theoretical basis lack and they are limited to the more physical behaviour of the system.

Neither the method of the multi-range potential, nor the introduction of an EOS is implemented in the current version of the Palabos library. Thus, in order to test one of the two methods a bit of coding was needed. Since the incorporation of the EOS was considered more easily feasible, this approach has been chosen. The implementation of the multi-range potential seems

also feasible, even though it requires a greater modification of the source code, and for this reason it is left as an eventual future work. Thus, we now introduce the main ideas behind the method of the incorporation of physical EOS.

Let us begin by considering the single-component equation of state of the Shan-Chen model Eq. (7.23). Now, the idea is very simple, indeed. This equation can be recast in order to obtain an explicit formula for the interaction potential:

$$\psi = \sqrt{\frac{6(p - c_s^2 \rho)}{g_{11}}}. \tag{7.35}$$

This allows an *ad hoc* construction of the pseudopotential in order to match the desired EOS. In fact, considering for example the van der Waals equation of state:

$$p = \frac{\rho RT}{1 - b\rho} - a\rho^2, \tag{7.36}$$

we can compute the pressure as a function of ρ in each point of the lattice and then inserting it into Eq. (7.35) to obtain the pseudopotential in that point. Afterwards, the pseudopotentials can be used in Eq. (7.12) to obtain the interaction force as usual.

The first new feature of this approach is the direct introduction of a temperature in the system. In the original scheme, we have seen that the concept of temperature was connected to the parameter g_{11}. An increase of g_{11} in magnitude meant a decrease of temperature. In this case, the temperature is incorporated into the pseudopotential, carrying out the same qualitative role of g_{11}. In addition, it is worth noticing that the role of the parameter g_{11} in this scheme is only to guarantee that the argument of the square root remains positive. Since, g_{11} needs to be negative to ensure phase separation in the original SC model, we expect the same behaviour in this case.

In Yuan & Schaefer's [5] paper, the two EOS which gave the best performances were the Carnahan-Starling (CS) and the Peng-Robinson (PR). Hence, we will now focus on these equations of state.

The Carnahan-Starling EOS [43] is basically the evolution of the van der Waals EOS:

$$p = \rho RT \frac{1 + b\rho/4 + (b\rho/4)^2 - (b\rho/4)^3}{(1 - b\rho/4)^3} - a\rho^2, \tag{7.37}$$

where a and b are the two parameters of the equation. The parameters of the simulations are of course connected to the critical temperature T_c and pressure p_c:

$$a = 0.4963 \frac{T_c^2 R^2}{p_c}, \qquad b = 0.18727 \frac{RT_c}{p_c}, \tag{7.38}$$
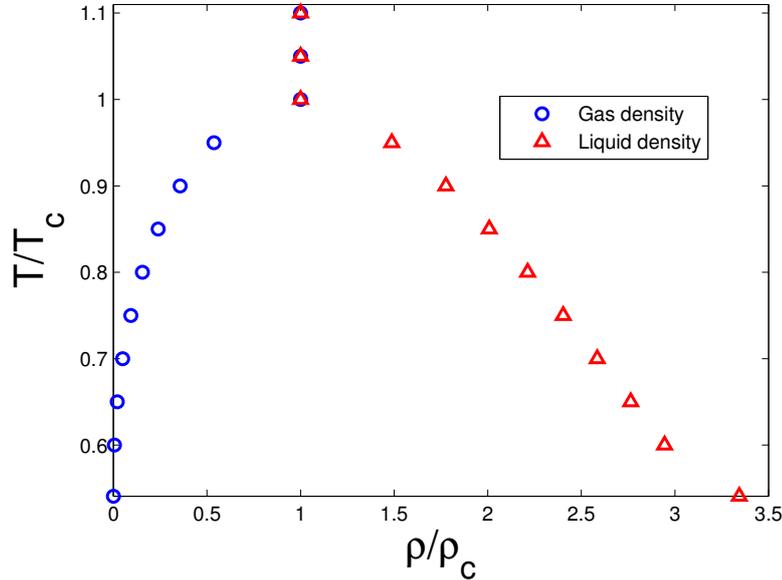
Figure 7.14. Phase separation for the Carnahan-Starling EOS.

from which we can obtain the critical compressibility factor $Z_c = p_c/(\rho_c R T_c) = 0.35930763$ [113] and consequently the critical density ρ_c. We will use the same parameter chosen in [5], that is $R = 1\,[\mathrm{lu}^2\,\mathrm{ts}^{-2}\,\mathrm{K}_0^{-1}]$, $a = 1\,[\mathrm{mu}_0^{-1}\,\mathrm{lu}^3\,\mathrm{ts}^{-2}]$ and $b = 4\,[\mathrm{lu}^2\,\mathrm{mu}_0^{-1}]$ [8]. These choices fixes a mass scale mu_0 and an absolute temperature scale K_0, when converting to physical units. However, in what follows we will always report the result in a reduced quantity system for the sake of clarity. The reduced temperature, pressure and density are obviously defined:

$$\tilde{T} = \frac{T}{T_c}, \quad \tilde{p} = \frac{p}{p_c}, \quad \tilde{\rho} = \frac{\rho}{\rho_c}. \tag{7.39}$$

In order to explore the immiscible behaviour of the CS, simulations were carried out for the case of a flat interface, similarly to what has been done for the original SC model in Sec. 7.2. The domain size was 200x200 lattice nodes. A small density difference is initialized in the two halves of the domain and the total density of the system is kept equal to the critical one in all the simulations. In all the simulations the relaxation parameter τ was set to unity. In this case the temperature is varied in place of the parameter g_{11} from supercritical to subcritical values. The results are shown in Fig. 7.14.

The minimum value of the reduced temperature achieved was $T/T_c = 0.5408$, which corresponds to a density ratio $\rho_L/\rho_G = 53\,827$. This result

---

[8]Of course, the units are for the 2D case.
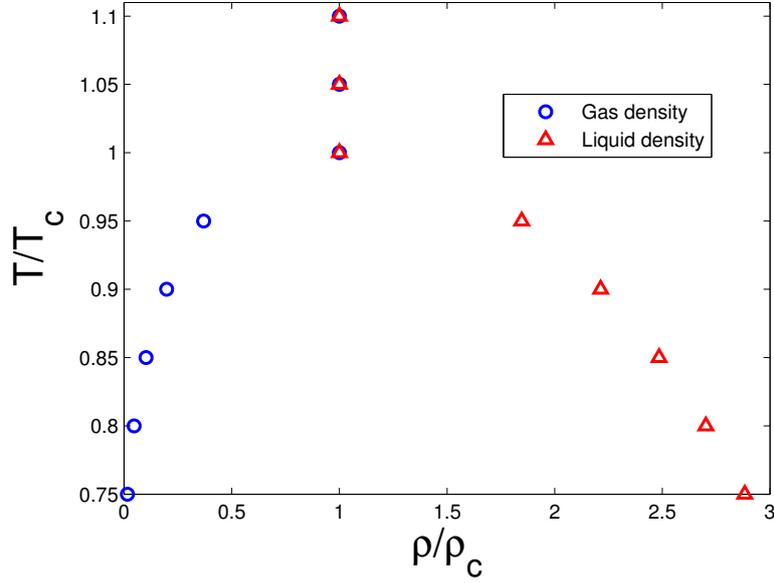
Figure 7.15. Phase separation for the Peng-Robinson EOS.

is valid for flat interfaces where the spurious currents are lower than the static drop/bubble case. However, it is definitely much higher than the value $\rho_L/\rho_G \approx 100$, reported in Sec. 7.2 for the original SC pseudopotential.

The Peng-Robinson EOS belongs to the family of cubic equations of state [42]. Its formulation is:

$$p = \frac{\rho RT}{1 - b\rho} - \frac{a\alpha(T)\rho^2}{1 + 2b\rho - b^2\rho^2},$$
(7.40)

$$\alpha(T) = [1 + (0.37464 + 1.54226\omega - 0.26992\omega^2)(1 - \sqrt{T/T_c})]^2.$$

The parameter ω is called acentric factor and is dependent on the species under consideration. In case of water it is equal to 0.344. The parameters a and b of the EOS are connected to the critical temperature and pressure by the following relationships:

$$a = 0.45724\frac{R^2 T_c^2}{p_c}, \qquad b = 0.0778\frac{RT_c}{p_c}.$$
(7.41)

This yields a critical compressibility factor $Z_c = 0.307$ [42]. Similarly to the case of CS equation we set the same parameter a and b of [5]: $R = 1\,[\text{lu}^2\,\text{ts}^{-2}\,\text{K}_0^{-1}]$, $a = 2/49\,[\text{mu}_0^{-1}\,\text{lu}^3\,\text{ts}^{-2}]$ and $b = 2/21\,[\text{lu}^2\,\text{mu}_0^{-1}]$.

In Fig.7.15, we can see the phase diagram for the PR EOS. The acentric factor in this case is $\omega = 0.344$, which is the acentric factor of water. In this

139

	R_{in}[lu]	ρ_L^{in}/ρ_c	ρ_G^{in}/ρ_c	$(\rho_0 g_{11})_c/(\rho_0 g_{11})$	T/T_c	u_{max}/c_s
SC	30	2.913	0.2040	0.7825	/	0.2653
CS	30	2.213	0.1548	/	0.8	0.1921
PR	30	2.307	0.1616	/	0.88418	0.1428

Table 7.1. Numerical parameters and results of the fixed density ratio test. Here, SC denotes the original Shan-Chen model, CS the Carnahan-Starling EOS and PR the Peng-Robinson EOS.

case, the maximum density ratio achieved in this case is $\rho_L/\rho_G = 767$, which is related to $T/T_c = 0.75$. This value is lower than the maximum density ratio of the CS EOS. This is a first evidence of an initialization problem, which affects the Shan-Chen model.

So far, we have only dealt with flat interfaces, but in reality we are interested in curved interfaces. The Shan-Chen model for curved interfaces yields always higher spurious currents than the flat interface test. Thus, in order to compare the Carnahan-Starling EOS, the Peng-Robinson and the original Shan-Chen pseudopotential we need to consider the static circular test. In particular, two tests will be conducted in order to evaluate which is the best model between the three alternatives. Considering always a fully periodic domain of 200x200 lattice units, a circular interface of radius 30 lattice units is initialized, with the liquid phase inside it. Reasonable values for the liquid and the gas phase can be obtained from the simulations for flat interfaces. Accordingly, at the interface we have a jump discontinuity. In the first test, the parameters governing the phase separation, that is $\rho_0 g_{11}$ for the original SC model, and T/T_c for the CS and PR equations of state, are tuned in order to achieve the same density ratio. Then, the static drop simulations are carried out for the three models and the results compared in terms of maximum magnitude of the spurious currents. Each simulation has been run for 50 000 iterations. It is worth noticing that the final radius will never be exactly the same for the three phases due to compressibility. The density ratio was fixed to ≈ 14.28, which is the equilibrium density ratio of the CS equation when $T/T_c = 0.8$. The parameters of the other two equations are then adjusted to obtain this ratio. The acentric factor of the Peng-Robinson is fixed and equal to that of water $\omega = 0.344$.

We can see the velocity field of the different models in Fig. 7.16. The input parameters and the numerical result in terms of maximum magnitude of the spurious currents are shown in Table 7.1. Both the CS and PR equations of state show a lower maximum velocity compared to the original SC, even though they remain of the same order of magnitude. In particular, the PR is the EOS which performs the best result, decreasing the maximum velocity of

(a) u/c_s for the original SC.

(b) u/c_s for the CS EOS.

(c) u/c_s for the PR EOS.
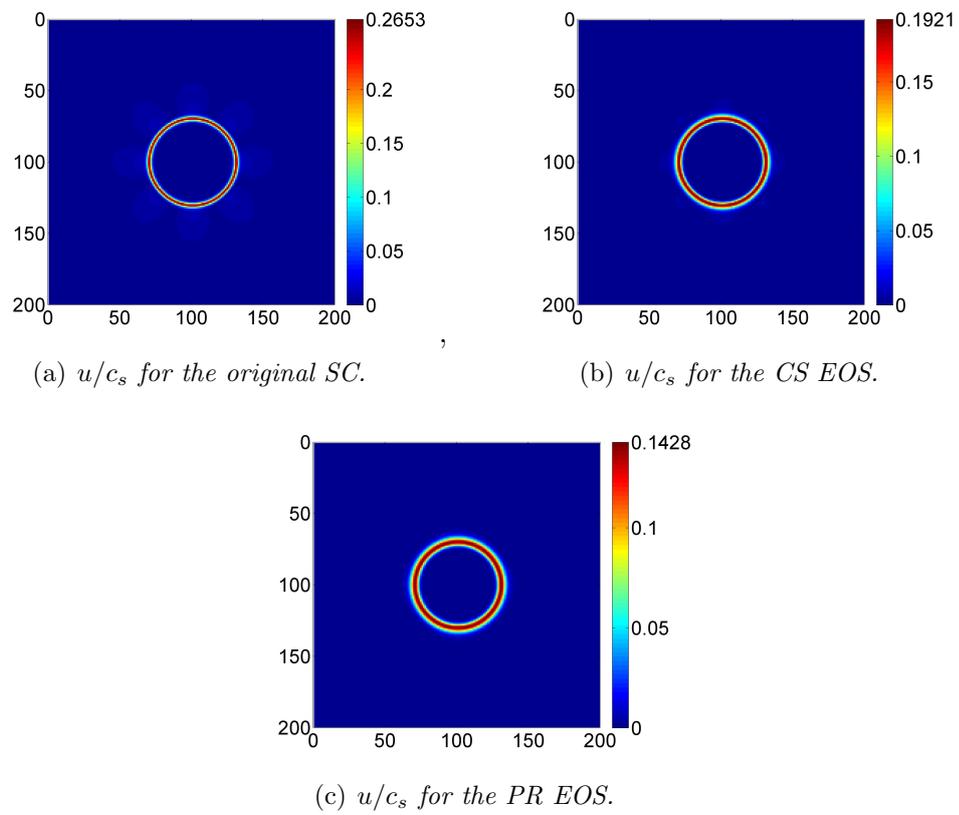
Figure 7.16. u/c_s field for the different pseudopotentials.

	ρ_L^{in}/ρ_c	ρ_G^{in}/ρ_c	ρ_L/ρ_G	$(\rho_0 g_{11})_c/(\rho_0 g_{11})$	T/T_c	u_{max}/c_s	Reason
SC	4.194	0.08195	47.46	0.625	/	0.5413	Drop movement
CS	2.621	0.06410	37.49	/	0.73	0.2694	Initial instability
PR	2.622	0.06472	37.37	/	0.82	0.2289	Initial instability

Table 7.2. Numerical parameters and results of the limiting density ratio test. Here, SC denotes the original Shan-Chen model, CS the Carnahan-Starling EOS and PR the Peng-Robinson EOS.

the original SC by almost a factor 2. From, Fig. 7.16, we can grasp the reason of this reduction in the higher interface thickness of the PR EOS. The density gradients of the PR EOS are smoother than the others, leading to lower spurious currents. On the other hand, as we know, high interface thicknesses rather complicate the analysis of the result and the application to physical systems, in which the interface is usually negligible. It is worth pointing out that, here we witness higher spurious currents than those reported in [5], where a similar test was conducted in three dimensions.

In the second test, the density ratios are pushed over their limits for the three models, until instability occurs. In particular, this instability may be numerical or physical. In fact, it has been witnessed that even though the simulations where numerically stable, at high density ratio the simulations showed an odd behaviour. For instance, phenomenon like movement of the drop towards a certain direction or loss of sphericity have been observed, which took place even after many time steps. Since, this behaviour has no physical sense, and the model cannot be applied in this regime for practical purposes, it was decided to reject these results.

The size of the domain remains the same of the previous test, as well as the relaxation parameter and the number of iterations. In order to carry out a "fair" test, the initial gas and liquid densities are taken in each case from the relative flat interface test. Thus, a *sharp* initialization has been used, where the interface is discontinuous. The reason of this clarification will become understandable in what follows. The initial radius in each test is $r_{in} = 30$ lu. Little differences have been observed between the final and initial radius. The limiting results of this test are summarized in Table 7.2. In particular, in Table 7.2 all the results are physically and numerically. The cause of instability at higher density ratio is also reported, as well as the initial liquid and gas densities.

From Table 7.2, we see that in this test, the highest density ratio has been obtained with the original Shan-Chen model. In particular, we notice that both the CS and PR EOS show lower spurious velocities with respect to the original SC model, but suffer a problem of initialization, probably due to

	ρ_L^{in}/ρ_c	ρ_G^{in}/ρ_c	ρ_L/ρ_G	T/T_c	u_{max}/c_s	Reason
CS	2.767	0.02073	146.36	0.65	0.3731	Initial instability
PR	2.883	0.01556	185.29	0.75	0.3343	Initial instability

Table 7.3. Numerical parameters and results for the CS and PR EOS when they are initialized with a diffusive interface. The interface thickness in this case is of 10 lu. In the interface the density varies linearly from ρ_L to ρ_G.

	ρ_L^{in}/ρ_c	ρ_G^{in}/ρ_c	ρ_L/ρ_G	T/T_c	u_{max}/c_s
CS	3.142	0.1139	518.6	0.6	0.4491

Table 7.4. Example of density ratio achieved with the CS EOS.

the high spurious velocities at the beginning of the simulation. We see also, that this happens for the CS and the PR for a similar density ratio. This initialization issue might be very annoying in practice, but it may be worth the effort, since it allows to achieve higher density ratios. In fact, by means of a smoother initialization, in which also the diffusive interface is initialized, higher density ratios can be obtained. We can see in Table 7.3, that the CS and and PR allows to simulate higher density ratios. In these cases no physical instability have been observed. In addition, the values here reported are the respective limiting cases, when the interface thickness is initialized with 10 lu.

Even higher density ratios can be achieved by not matching the initial values of the flat interface test and initializing with intermediate densities. In this case, the main shortcoming is that the final radius will very inevitably from the initial one. As an example, we report the result that has been obtained for the CS EOS, which has proved to be more flexible than the PR EOS from this point of view, in Table 7.4, which should not be intended as a limiting value.

From this simple tests, we conclude that the EOS approach in the Shan-Chen model allows to reduce the spurious velocities given a fixed density ratio and to achieve higher density ratios, compared to those of the original Shan-Chen model. However, if we want to use EOS at high density ratios we have to cope with the initialization issue.

In Sec. 7.5, we will see that there is also another issue, which is for now hidden in the use of EOS.
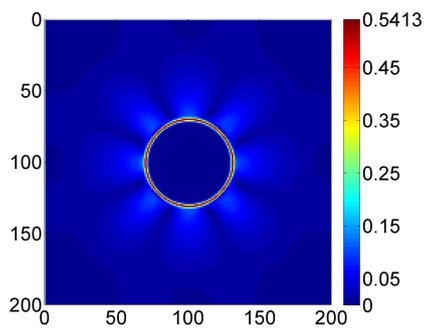
(a) u/c_s for the original SC.
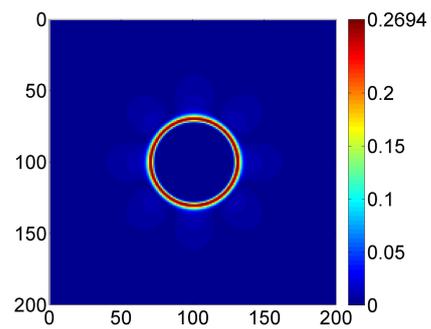
(b) u/c_s for the CS EOS.
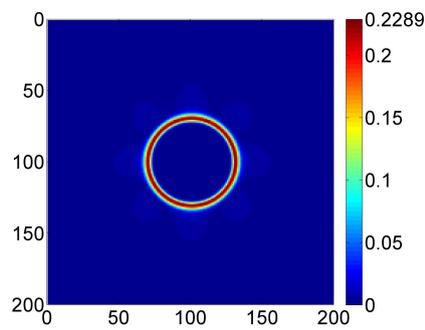
(c) u/c_s for the PR EOS.

Figure 7.17. u/c_s field for the different pseudopotentials at the stability limit (Table7.2).

(a) *Total wet: $\rho_W/\rho_c = 2.170$.*

(b) *Wet: $\rho_W/\rho_c = 1.4738$.*

(c) *Non-wet: $\rho_W/\rho_c = 0.3684$.*

(d) *Total non-wet: $\rho_W/\rho_c = 0.1936$.*
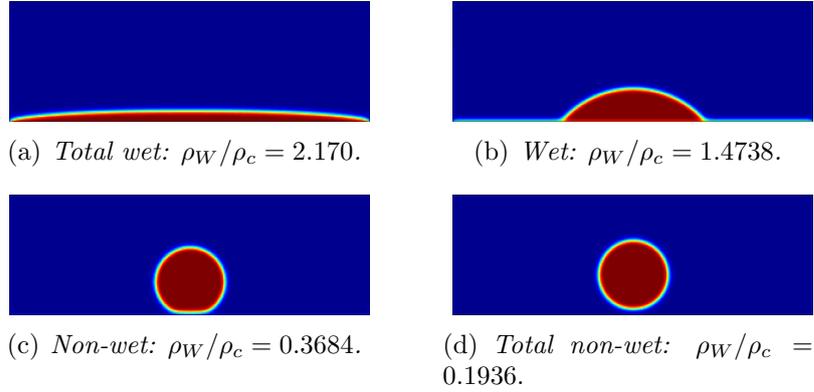
Figure 7.18. Different wetting conditions for the liquid phase.

7.4 Determination of the contact angle

So far, we have only seen how the Shan-Chen model allows to take into account the interparticle forces by means of a fictitious pseudopotential. However, when dealing with flows in porous media, we need also to incorporate the interaction of the two phases with the surface in order to obtain different contact angles. Even this task can be surprisingly carried out by means of a fictitious additional interaction with the solid boundaries. The form of the interaction is the following for the single component case [114]

$$\boldsymbol{F^{ad}} = -g_{11}\psi(\rho(\boldsymbol{x})) \sum_i w_i \psi(\rho_W)s(\boldsymbol{x} + \boldsymbol{\xi_i})\boldsymbol{\xi_i}, \qquad (7.42)$$

where s is a function that is equal to 1 if the node $\boldsymbol{x} + \boldsymbol{\xi_i}$ is a solid node (a Bounce-Back node for example) and 0 if it is a fluid node. The density ρ_W is a fictitious density attributed to the boundary node. By changing its value it is possible to achieve different contact angles and wetting conditions. In particular, we expect that values of ρ_W close to the gas/liquid density would mean that the gas/liquid is the wetting phase. Even in this case the contact angle can be evaluated by means of a simple test.

In Fig. 7.18, we can see how different wetting conditions can be achieved by tuning the wall density ρ_W. In particular, Fig. 7.18 has been obtained for the PR EOS with $T/T_c = 0.9$. In this condition, the liquid and gas density are respectively $\rho_L/\rho_c = 2.170$ and $\rho_G/\rho_c = 0.1936$. In fact, when ρ_W/ρ_c equals these values, we obtain total wetting/non-wetting conditions.

It is worth noticing that by changing the value of ρ_w in the domain we can easily achieve also space dependent wetting conditions. In particular, this situation may occur in oil reservoir in which there might be water-wet zones, as well as oil-wet zones.

An important observation is that the contact angle can definitely be adjusted at will with the Shan-Chen model to match that of real physical systems.

7.5 Relative permeability in a 2D co-current channel

In Sec. 7.3, we have seen how the incorporation of physical EOS, such as the the Peng-Robinson or the Carnahan-Starling, in the Shan-Chen pseudopotential, allows to achieve higher density ratio, reducing the magnitude of the spurious currents. In the fixed density ratio test, the Peng-Robinson EOS was the one that produced the lowest spurious currents. For this reason, we will consider the PR form of the SC pseudopotential at the beginning of this section.

The aim of this section is to validate the Shan-Chen model in the simple case of a two-dimensional co-current channel, already described in Sec. 2.5.3. A similar validation has been carried out in [37, 49, 115, 50] for the respective LBM models.

Indeed, in the context of porous media, we are interested in achieving high density ratios, in order to obtain a wider range of dynamic viscosity ratios (M). In fact, in Sec. 2.5.3 we have pointed out the influence of the parameter M in the relative permeability curves. The magnitude of this effect is particularly strong in the 2D co-current channel as we can see from Eqs-(2.35).

We have seen also that in the Shan-Chen model the relaxation parameter τ is in general fixed for both phases, and consequently the kinematic viscosity ratio is fixed and equal to 1. This obviously means that the dynamic viscosity ratio M is equal to the density ratio:

$$M = \frac{\mu_{nw}}{\mu_w} = \frac{\rho_{nw}}{\rho_w}.$$ (7.43)

Being aware of this constraint, let us begin our validation by considering the case of a 2D co-current flow, where the wetting phase is the one with the highest dynamic viscosity, that is the liquid phase. The domain is similar to that displayed in Fig. 2.6 and it is composed of 201x102 lattice nodes. The Peng-Robinson EOS has been used with the same parameters reported in Sec. 7.3. The reduced temperature is equal to $T/T_c = 0.9$, and yields a density ratio $\rho_L/\rho_G = 11.21$. According to the definition given in Eq. (7.43), the dynamic viscosity ratio is $M = 0.08921$. The fictitious density at walls is equal to $\rho_w = \rho_L$, where Bounce-Back boundary conditions are applied. The
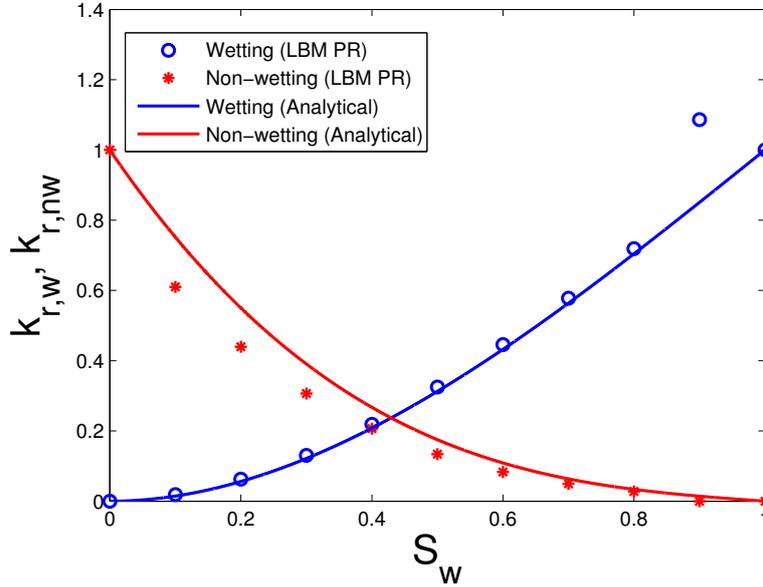
Figure 7.19. Comparison between the analytical and numerical relative permeabilities of the PR EOS. $M = 0.08921$: the liquid is the wetting phase.

relaxation parameter is always equal to 1^9. The numerical experiment has been carried similarly to [37, 49, 115, 50]. Periodic boundary conditions are applied in the x-direction. The role of the pressure gradient in Eqs. (2.33) and (2.34) is carried out by a constant force per unit of area $\boldsymbol{F}$ [10], applied to both fluids, and obviously directed in the x-direction [11]. In all the simulations $F = 10^{-8} \mathrm{mu_0 lu^{-1} ts^{-2}}$. The liquid and the gas densities are initialized taking the corresponding results of the flat interface test. The position of the interface is assumed between the two nodes i and j such that $\rho(i) \leq (\rho_L + \rho_G)/2 \leq \rho(j)$. Of course, the inherent diffusive nature of the interface may generate ambiguities in this definition. The relative permeabilities of the wetting and the non-wetting phases can be simply obtained as the ratio between the Darcy's velocity of the present experiment, and the Darcy's velocity in case the channel is occupied either by only the wetting phase or only by the non-wetting phase.

The results are shown in Fig. 7.19. We can see a clear tendency of the LBM simulations to underestimate the relative permeability of the non-wetting phase, while the agreement seems better achieved for the wetting

---

[9]This specification will be omitted in what follows

[10]It would be per unit of volume in 3D.

[11]From now on we will call it F being aware of its direction.
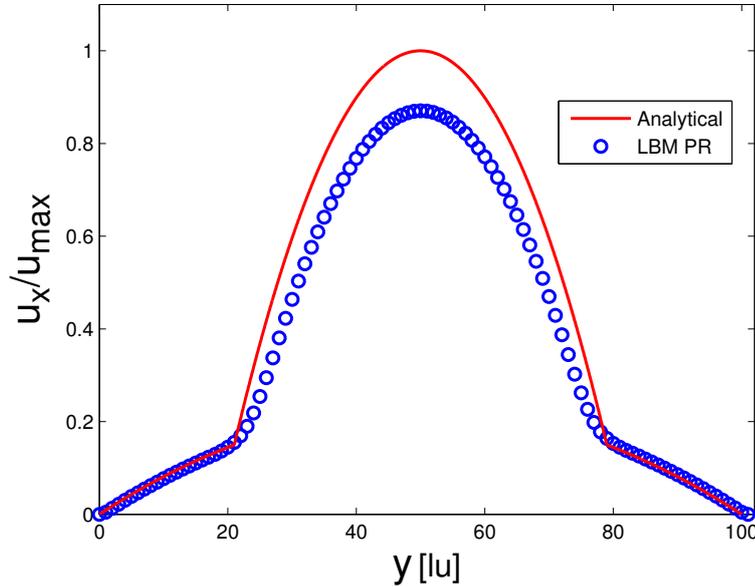
Figure 7.20. Comparison between the analytical and numerical velocity profiles for the PR EOS. $S_w \approx 0.4$ and $M = 0.08921$: the liquid is the wetting phase.

phase, except for the case $S_w = 0.9$. This observation is further supported by Fig. 7.20, where the predicted velocity of the non-wetting phase is definitely lower than the analytical one. The reason of this behaviour has been found in the diffusive nature of the interface obtained with Shan-Chen model. In fact, we can expect the velocity gradients of a diffusive interface to be smoother than those of a sharp interface. This effects seems to influence mostly the the non-wetting phase in this case. It seems also that there is a slight loss of symmetry. A similar behaviour has been obtained in [37], but not supported by explanations.

Nevertheless, we have previously observed in Sec. 7.3, and in particular in the analysis of Fig. 7.16, that the PR EOS was certainly the one that produces the greatest interface thicknesses given a fixed density ratio. From this observation, we are lead to expect that the best results should be obtained with the original SC, which was the model with the lowest interface thickness, while intermediate results are expected from the CS EOS.

For this reason, also the CS and the original SC model (which we will simply denote by SC) have been tested by matching the same dynamic viscosity ratio. In particular this corresponds to $T/T_c = 0.8335$ for the CS EOS, and $(\rho_0 g_{11})/(\rho_0 g_{11})_c = 1.230$ for the SC model.

The comparison between the three models and the analytical solution is shown in Fig. 7.21. As it was foretold, the SC model shows the best agreement
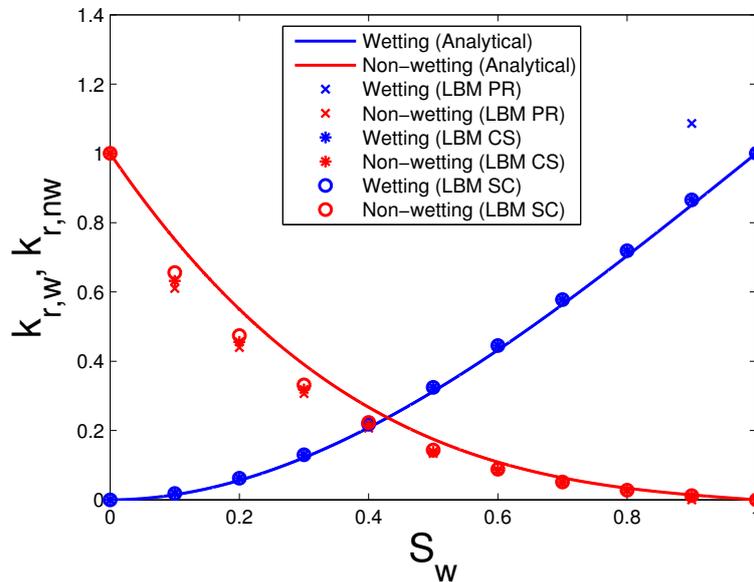
Figure 7.21. Comparison between the analytical and numerical relative permeabilities of the PR, CS and SC. $M = 0.08921$: the liquid is the wetting phase.

with the analytical solution due to its thin interface, followed by the CS and the PR EOS. In addition, also the comparison between the velocity profiles is reported in Fig.7.22, where the velocities are made dimensionless using the maximum analytical velocity, which in turn shows the better agreement of the original SC. Here we are able to appreciate the smoother velocity gradients of the PR and CS compared to the original SC.

For the sake of completeness, we considered also the case with $M > 1$, in which the liquid is the non-wetting case and the gas the wetting phase. The parameters are basically the same as before, with the exception that the fictitious density at wall is now equal to ρ_G. We can see the results in terms of relative permeabilities in Fig. 7.23. Even in this case, the tendency to underestimate the relative permeability of the non-wetting phase is clear. In turn, the original SC model shows better results than the CS and PR EOS. In Fig. 7.24, we can see the comparison with the analytical result for the case $S_w \approx 0.4$. Basically, the same phenomenon as before can be observed regarding the velocity gradients at the interface. However, we can also see a strange behaviour of the SC model at the beginning of the interface, where the velocity seems to decrease. This is also slightly shown by the CS model, while the PR model does not show this effect. An interpretation of this effect might be the influence of the spurious velocity along the y-direction, which may cause a first inertia effect. This also explains why this behaviour is more
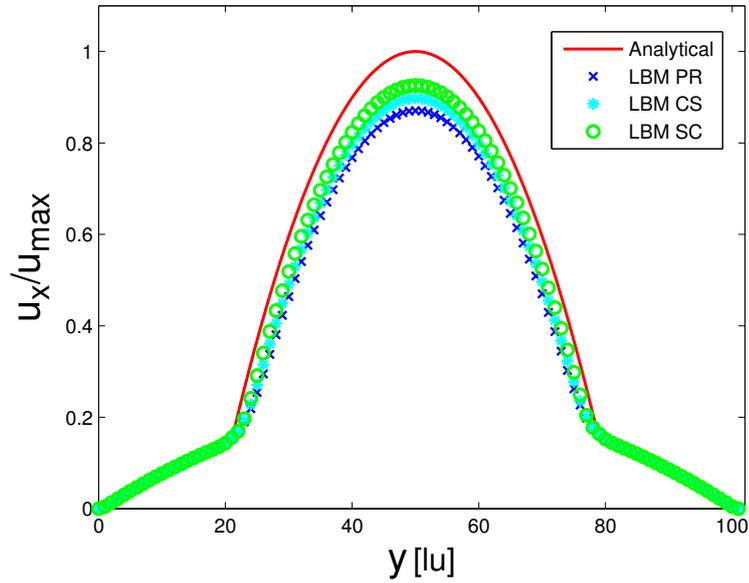
Figure 7.22. Comparison between the analytical and numerical velocities of the PR, CS and SC. The velocity profiles are scaled with the maximum analytical velocity, in order to allow a comparison. $S_w \approx 0.4$ and $M = 0.08921$: the liquid is the wetting phase.
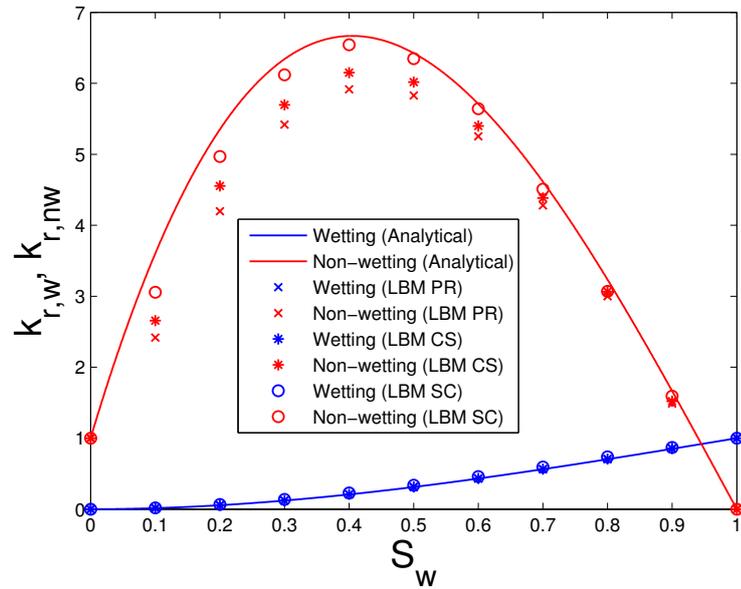
Figure 7.23. Comparison between the analytical and numerical relative permeabilities of the PR, CS and SC. $M = 11.21$: the gas is the wetting phase.
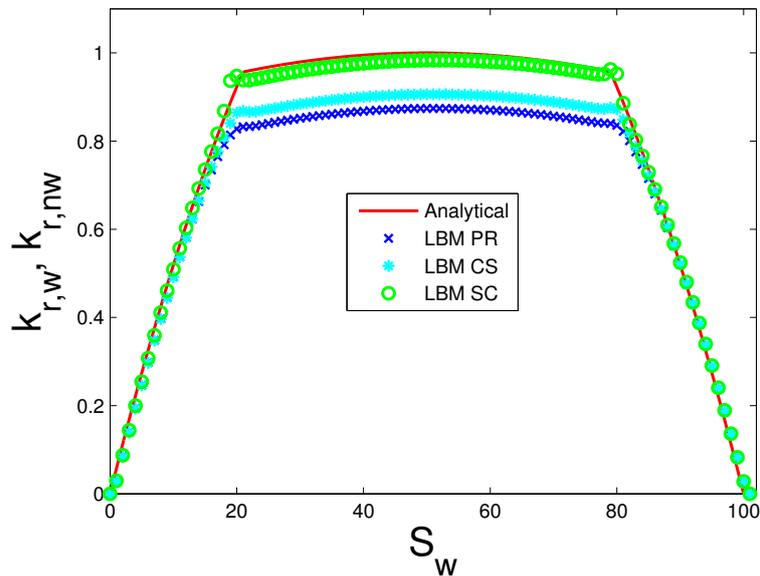
Figure 7.24. Comparison between the analytical and numerical velocities of the PR, CS and SC. The velocity profiles are scaled with the maximum analytical velocity, in order to allow a comparison. $S_w \approx 0.4$ and $M = 11.21$: the gas is the wetting phase

pronounced for the original SC model.

Finally, Fig.7.25 shows how the CS EOS can be used to simulate flows with higher density ratios. In this case, $\rho_L/\rho_G = 65.83$, and since the liquid is the wetting phase $M = 1/65.83 = 0.01519$. This ratios begin to be unattainable by the original Shan-Chen model. Basically, the analysis is the same as before. Anyway, we expect that at higher density ratios the CS EOS would take advantage of the reduction of the interface thickness and thus, the agreement with the analytical solution should be improved. Indeed, we have also to take into account that the velocity gradients become sharper. Consequently, the presence of a diffusive interface weights more in this problem and we do not witness a definite improvement of the agreement with the analytical solution.

From this test case, we conclude that if the density ratios are relatively low the original Shan-Chen model should be preferred over the EOS models, while the CS and PR EOS should be employed to explore higher density ratios. However, it is worth pointing out that the 2D co-current channel is a particularly favourable test case, since we are dealing with flat interfaces and the spurious velocities are consequently directed in the y-direction. The situation may change when considering curved interfaces, in which case the
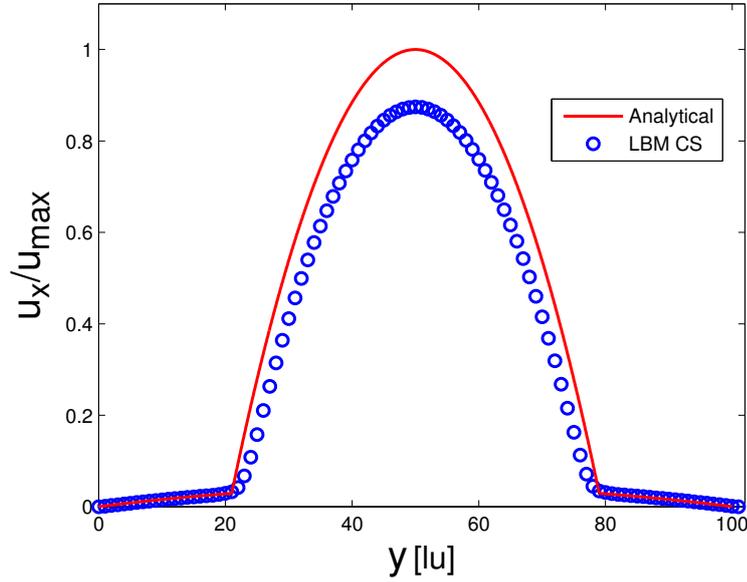
Figure 7.25. Comparison between the analytical and numerical velocity profiles for the CS EOS. $S_w \approx 0.4$ and $M = 0.01519$: the liquid is the wetting phase.

models should be subjected to a further validation, that has not been carried out neither in this thesis, nor in other similar works [37, 49, 115, 50]. We here report that some validation has been achieved for the rising bubble test in [116], while a comparison with experimental data has been carried out in [38], although both with limited density ratios.

Chapter 8

Conclusions

In this thesis, the Lattice Boltzmann methods for fluid dynamics have been discussed theoretically and practically, with particular attention to flows in porous media. We have reported how the Lattice Boltzmann equation can be obtained as a proper discretization of the Boltzmann equation, which definitely set the methods in the framework of Statistical Mechanics. The connection between the Navier-Stokes equations have been shown by means of the Chapman-Enskog expansion, where we have also identified the method proposed by Guo *et al.* [84], as the correct way of including the forcing term in the LBE.

All the numerical simulations in this thesis have been carried out by means of the Palabos library. In addition, all the simulations were related to two-dimensional problems. The numerical study of single-phase flows has definitely shown that the LBMs are a valid tool in the context of porous media. In particular, in this context the easy handling of complex geometries by means of the Bounce-Back boundary conditions is a key element in the success of the methods. Moreover, the TRT model should be preferred over the BGK model and other versions of the MRT model in porous media applications, because it allows to annul the unphysical dependency of the permeability on the viscosity. A validation has been carried out for the Hagen-Poiseuille flow and the flow over a hexagonal array of disks showing good agreement with the analytical or semi-analytical formulas available. In addition, the LBM with the TRT collision term has been used to verify the Carman-Kozeny model to predict the permeability, in a random array of disks. The simulations have shown a general validity of the model, especially at moderate porosities.

The study of two-phase flows has been introduced considering the Shan-Chen model, which is the first multi-phase model proposed in the LBM literature. The main characteristics of the original model have been discussed and shown using the numerical simulations, highlighting also the limitations

of the model. These are basically caused by the presence of artificial velocities at the interface, which may trigger instability and cause a general ambiguity between physical and artificial velocities. In order to reduce these problems, the method of incorporating physical Equations Of State in the Shan-Chen model has been implemented in the Palabos library. The Carnahan-Starling and the Peng-Robinson EOS have been considered. In this way, by means of static tests, we have seen that the magnitude of the spurious currents can be reduced given a fixed density ratio, and higher density ratios can be simulated, even though with some initialization problems.

Finally, a first validation of the model has been achieved by simulating the two-phase flow in a co-current channel, for which the analytical solution is available. In particular, this has shown that the original formulation of the Shan-Chen model may be more appropriate compared to the EOS models when the density ratios are limited, due to the lower thickness of the interface. However, it was also pointed out that this may be valid for the specific case of the co-current flow, but may not be true for more complex cases. In addition, at higher density ratios only the EOS models can be employed.

8.1   Future perspectives

Starting from this thesis, several future work may be envisaged. We now list some of them:

- the Lattice Boltzmann methods may be applied to study the flow in real three-dimensional porous media and compare the results with experimental data;

- the theoretical findings obtained by means of the Chapman-Enskog procedure may be tested numerically in a test case, comparing the results of different schemes for the inclusion of the forcing term;

- the typical problems of the Shan-Chen model can be further reduced by employing some other improvements proposed in literature, such as the multi-range potential introduced by Sbragaglia *et al.* [32];

- the correct way of including the interaction force could be implemented for the Shan-Chen model;

- the Shan-Chen model shall be validated for a more complex case than the co-current flow.

Appendix A

A.1   Gauss-Hermite Quadrature

The aim of this Appendix is to provide insights about the Gauss-Hermite quadrature used in Subsec. 3.7.3 to obtain the Lattice Boltzmann equation (for reference see [70, 117]). In general a *Gaussian quadrature formula* to approximate integrals has the following form:

$$\int_a^b w(x)f(x)dx \simeq \sum_i^n \omega_i f(x_i), \tag{A.1}$$

where $w(x)$ is a *weight function* such that

$$c_k = \int_a^b w(x)x^k dx, \qquad (k = 0, 1, 2, \dots) \tag{A.2}$$

are defined and finite, and in addition $c_0 > 0$. The ω_i in Eq. (A.1) are usually called the weights associated to x_i, which in turn are the root of certain polynomials. The definition of these polynomials depends on the function $w(x)$ taken into account. An important characteristic of Gaussian quadrature formulas is that if n is the number of nodes, they are rigorously exact for all the polynomials of degree $m \leq 2n-1$. In fact, we have exploited this properties in Subsec. 3.7.3.

The Gaussian quadrature formulas are closely connected to the theory of orthogonal polynomials. In fact, the polynomials related to the weight function $w(x)$ are defined as the set of polynomials such that:

$$\int_a^b w(x)P_n(x)P_m(x)dx = 0, \qquad (m \neq n; m, n = 0, 1, 2, \dots), \tag{A.3}$$

where P_n and P_m denote respectively polynomials of degree n and m. It is intuitive that the left side of Eq. (A.3) can be considered a scalar product in

this context, and thus, Eq. (A.3) introduces notion of orthogonality between these polynomials. It can be shown that these polynomials are unique.

In the Gauss-Hermite quadrature the role of the weight function is carried out by the function $w_{GH}(x) = \exp[-x^2]$, and the interval of integration is $(-\infty, +\infty)$. Thus, it can be used to compute integrals of the following form:

$$\int_{-\infty}^{+\infty} f(x)e^{-x^2}dx \simeq \sum_{i}^{n} \omega_i f(x_i).$$ (A.4)

The orthogonal polynomials related to the weight function $\exp[-x^2]$ are called *Hermite polynomials*, and are given by the following formula:

$$H_n = (-1)^n e^{x^2} \frac{d^n(e^{-x^2})}{dx^n}.$$ (A.5)

It is easy to verify that this formula yields a polynomial of degree n. In case of n nodes of integration the abscissas x_i are the roots of the Hermite polynomials of degree n, while the associated weights are given by:

$$w_i = \frac{2^{n-1}n!\sqrt{\pi}}{n^2[H_{n-1}(x_i)]^2}.$$ (A.6)

A.2 Moments of the Maxwellian

Here, we show that the second and third order moments of the equilibrium distribution functions (Eq. (3.75)) f_i^{eq} of the Lattice Boltzmann equation are given by Eqs. (4.36). Thus, the moments we would like to compute are:

$$m_{d,\alpha\beta}^{eq} = \sum_i \xi_{i\alpha}\xi_{i\beta}f_i^{eq}, \qquad (A.7a)$$

$$m_{d,\alpha\beta\gamma}^{eq} = \sum_i \xi_{i\alpha}\xi_{i\beta}\xi_{i\gamma}f_i^{eq}, \qquad (A.7b)$$

where the subscript d stands for "discrete" moments. The discrete velocity are obviously those of Eqs. (3.68). In particular, the computations of these moments can be done either by considering the summation directly, or by computing the moments of the continuous Maxwellian equilibrium distribution function of the Boltzmann equation Eq. (3.39). We know from Chap. 3, that the first step to obtain the Lattice Boltzmann equation is an expansion of the Maxwellian distribution function in the low Mach number limit, which yields an error $\mathcal{O}(Ma^3)$. In addition, we have also required that the moments of this approximated distribution function must be preserved by the Gauss-Hermite quadrature up to third order. Thus, we realize that the discrete moments of up to third order are equal to those of a Maxwellian if we neglect terms $\mathcal{O}(Ma^3)$. Consequently we are allowed to write:

$$m_{c,\alpha\beta}^{eq} = m_{d,\alpha\beta}^{eq} + \mathcal{O}(Ma^3), \qquad (A.8a)$$
$$m_{c,\alpha\beta\gamma}^{eq} = m_{d,\alpha\beta\gamma}^{eq} + \mathcal{O}(Ma^3), \qquad (A.8b)$$

where the subscript c denotes the continuous moments of the Maxwellian distribution function, defined as:

$$m_{c,\alpha\beta}^{eq} = \int \xi_\alpha\xi_\beta f^{eq}\,d\boldsymbol{\xi}, \qquad (A.9a)$$

$$m_{c,\alpha\beta\gamma}^{eq} = \int \xi_\alpha\xi_\beta\xi_\gamma f^{eq}\,d\boldsymbol{\xi}. \qquad (A.9b)$$

We will follow the second approach, since it is definitely more general and explicative. In addition, we will always consider the two-dimensional case, as done throughout this thesis.

Thus, let us consider the second order moment of the Maxwellian where $\alpha = \beta$:

$$m_{c,\alpha\alpha}^{eq} = \frac{\rho}{2\pi\theta}\int \xi_\alpha^2 \exp\left[-\frac{(\boldsymbol{\xi}-\boldsymbol{u})^2}{2\theta}\right] d\boldsymbol{\xi}, \qquad (A.10)$$

where we have already inserted the definition of the Maxwellian distribution function Eq. 3.39. The integral of Eq. (A.10) can be divided into two independent contributions:

$$m_{c,\alpha\alpha}^{eq} = \frac{\rho}{2\pi\theta} \left\{ \int_{-\infty}^{+\infty} \xi_\alpha^2 \exp\left[-\frac{(\xi_\alpha - u_\alpha)^2}{2\theta}\right] d\xi_\alpha \right\} \left\{ \int_{-\infty}^{+\infty} \exp\left[-\frac{(\xi_\beta - u_\beta)^2}{2\theta}\right] d\xi_\beta \right\}$$
(A.11)

Let us start from the first integral in $d\xi_\alpha$:

$$I_{\alpha\alpha} = \int_{-\infty}^{+\infty} \xi_\alpha^2 \exp\left[-\frac{(\xi_\alpha - u_\alpha)^2}{2\theta}\right] d\xi_\alpha.$$
(A.12)

Now, it is natural to operate the change of variable $\zeta_\alpha^2 = (\xi_\alpha - u_\alpha)^2/2\theta$:

$$I_{\alpha\alpha} = \sqrt{2\theta} \int_{-\infty}^{+\infty} (u_\alpha + \sqrt{2\theta}\zeta_\alpha)^2 \exp[-\zeta_\alpha^2] d\zeta_\alpha,$$
(A.13)

which in turn can be written as:

$$I_{\alpha\alpha} = \sqrt{2\theta}\{ \int_{-\infty}^{+\infty} u_\alpha^2 \exp[-\zeta_\alpha^2] d\zeta_\alpha +$$
$$\int_{-\infty}^{+\infty} 2\sqrt{2\theta}\zeta_\alpha \exp[-\zeta_\alpha^2] d\zeta_\alpha + \int_{-\infty}^{+\infty} 2\theta\zeta_\alpha^2 \exp[-\zeta_\alpha^2] d\zeta_\alpha \}.$$
(A.14)

In the previous equation, the second integral is clearly equal to zero, since the integrand is an odd function. Remembering that:

$$\int_{-\infty}^{+\infty} \exp[-\zeta^2] d\zeta = \sqrt{\pi},$$

which is known as the Gaussian integral, we can readily obtain:

$$I_{\alpha\alpha} = \sqrt{2\pi\theta}(u_\alpha^2 + \theta).$$
(A.15)

Instead, the second integral in $d\xi_\beta$ of Eq. (A.11) is even easier to compute and it is given by:

$$I_0 = \int_{-\infty}^{+\infty} \exp\left[-\frac{(\xi_\beta - u_\beta)^2}{2\theta}\right] d\xi_\beta = \sqrt{2\pi\theta}.$$
(A.16)

Finally, the insertion of Eqs. (A.15) and (A.16) into Eq. (A.11) yields:

$$m_{c,\alpha\alpha}^{eq} = \rho\theta + \rho u_x^2.$$
(A.17)

By means of a similar procedure, we can also obtain the moment for the case $\alpha \neq \beta$:

$$m_{c,\alpha\beta}^{eq} = \frac{\rho}{2\pi\theta} \int \xi_\alpha \xi_\beta \exp\left[-\frac{(\boldsymbol{\xi} - \boldsymbol{u})^2}{2\theta}\right] d\boldsymbol{\xi} = \rho u_\alpha u_\beta.$$
(A.18)

Now, we can gather Eqs. (A.17) and (A.18) into a single formula as:

$$m_{c,\alpha\beta}^{eq} = \delta_{\alpha\beta}c_s^2\rho + \rho u_\alpha u_\beta, \tag{A.19}$$

where we have used the definition $c_s^2 = \theta$, introduced in Chap. 3. From Eq. (A.19), we notice that no terms $\mathcal{O}(u^3)$, i.e., $\mathcal{O}(Ma^3)$ are present, which means that the discrete moments of second order are equal to those of a Maxwellian. Thus, we have obtained Eq. (4.36a).

The same procedure can be applied to the third order moments. When $\alpha = \beta = \gamma$:

$$m_{c,\alpha\alpha\alpha}^{eq} = \frac{\rho}{2\pi\theta} \int \xi_\alpha^3 \exp\left[-\frac{(\boldsymbol{\xi} - \boldsymbol{u})^2}{2\theta}\right] d\boldsymbol{\xi} = 3\rho c_s^2 u_\alpha + \rho u_\alpha^3, \tag{A.20}$$

while for the case $\alpha = \gamma$ and $\alpha \neq \beta$:

$$m_{c,\alpha\alpha\beta}^{eq} = \frac{\rho}{2\pi\theta} \int \xi_\alpha^2 \xi_\beta \exp\left[-\frac{(\boldsymbol{\xi} - \boldsymbol{u})^2}{2\theta}\right] d\boldsymbol{\xi} = \rho c_s^2 u_\beta + \rho u_\alpha^2 u_\beta. \tag{A.21}$$

Unlike the case of the second order moments, both Eq. (A.20) and Eq. (A.21) show terms $\mathcal{O}(Ma^3)$, which are not recovered by the discrete moments. This means that the discrete third order moments are equal to those of the Maxwellian, neglecting the terms $\mathcal{O}(Ma^3)$. Thus, it is easy to verify that by neglecting these terms, we obtain Eq. (4.36b).

Bibliography

[1] A. Kuzmin. *Multiphase simulations with lattice Boltzmann scheme.* PhD thesis, University of Calgary, 2009.

[2] J.E. Drummond and M.I. Tahir. Laminar viscous flow through regular arrays of parallel solid cylinders. *International Journal of Multiphase Flow*, 10(5):pp. 515–540, 1984.

[3] A. Tamayol and M.Bahrami. Parallel Flow Through Ordered Fibers: An Analytical Approach. *Journal of Fluids Engineering*, 132:114502, 2010.

[4] X. Shan and H. Chen. Lattice Boltzmann models for simulating flows with multiple phases and components. *Physical Review E*, 47:pp. 1815–1820, 1993.

[5] P. Yuan and L. Schaefer. Equations of state in a lattice Boltzmann model. *Physics of Fluids*, 18:042101, 2006.

[6] X. He and L.-S. Luo. A priori derivation of the lattice boltzmann equation. *Physical Review E*, 55(6):pp. R6333–R6336, 1997.

[7] X. He and L.-S. Luo. Theory of the lattice Boltzmann method: From the Boltzmann equation to the lattice Boltzmann equation. *Physical Review E*, 56(6):pp. 6811–6817, 1997.

[8] F.A.L. Dullien. *Porous Media, Fluid Transport and Pore Structure.* Academic Press, Inc, San Diego, 1991.

[9] George V. Chilingarian Erle C. Donaldson and Teh Fu Yen. Advisory editor. In *Enhanced Oil Recovew, I Fundamentals and Analyses*, volume 17, Part A of *Developments in Petroleum Science.* Elsevier, 1985.

[10] D.B. Ingham and I. Pop. *Transport Phenomena in Porous Media II.* Pergamon, Oxford, 2002.

[11] J.S. Rowlinson and B. Widom. *Porous Media, Applictions in Biological Systems and Biotechnology*. CRC Press Taylor & Francis Group, Boca Raton, 2011.

[12] A. R. A. Khaled and K. Vafai. The role of porous media in modeling flow and heat transfer in biological tissues. *International Journal of Heat and Mass Transfer*, 46(26):pp. 4989–5003, 2003.

[13] F. Chen and H. Hagen. A Survey of Interface Tracking Methods in Multi-phase Fluid Visualization. In Ariane Middel, Inga Scheler, and Hans Hagen, editors, *Visualization of Large and Unstructured Data Sets - Applications in Geospatial Planning, Modeling and Engineering (IRTG 1131 Workshop)*, volume 19 of *OpenAccess Series in Informatics (OASIcs)*, pages 11–19, Dagstuhl, Germany, 2011. Schloss Dagstuhl–Leibniz-Zentrum fuer Informatik.

[14] S. Wolfram. *Theory and applications of cellular automata*. World Scientific, Singapore, 1986.

[15] J. Hardy, Y. Pomeau, and O. de Pazzis. Time evolution of a two-dimensional model system. I. Invariant states and time correlation functions. *Journal of Mathematical Physics*, 14(12):pp. 1746–1759, 1973.

[16] U. Frisch, B. Hasslacher, and Y. Pomeau. Lattice-gas automata for the Navier-Stokes equation. *Physical Review Letters*, 56:pp. 1505–1508, 1986.

[17] G. McNamara and G. Zanetti. Use of the Boltzmann equation to simulate lattice-gas automata. *Physical Review Letters*, 61:pp. 2332–2335, 1988.

[18] L. Boltzmann. *Lectures on Gas Theory*. University of California Press, Berkeley, 1964.

[19] C. Cercignani. *The Boltzmann Equation and Its Applications*. Springer-Verlag, New York, 1988.

[20] S. Chapman and T.G. Cowling. *The Mathematical Theory of Nonuniform Gases*. Cambridge University Press, Cambridge, 1970.

[21] X. He and L.-S. Luo. Lattice Boltzmann Model for the Incompressible Navier-Stokes Equation. *Journal of Statistical Physica*, 88:pp. 927–944, 1997.

[22] A.A. Mohamad. *Lattice Boltzmann Method, Fundamentals and Engineering Applications with Computer Codes*. Springer-Verlag, London, 2011.

[23] D. d'Humiéres and I. Ginzburg. Multi-reflection boundary conditions for lattice Boltzmann models. Technical report, Fraunhofer-Institut fr Techno- und Wirtschaftsmathematik, 2002.

[24] Q. Zou and X. He. On pressure and velocity boundary conditions for the lattice Boltzmann BGK model. *Physics of Fluids*, 9:pp. 1591–1598, 1997.

[25] P. A. Skordos. Initial and boundary-conditions for the lattice Boltzmann method. *Physical Review E*, 48(6):pp. 4823–4842, 1993.

[26] T. Inamuro, M. Yoshino, and F. Ogino. Non-slip boundary-condition for lattice Boltzmann simulations. *Physics of Fluids*, 7(12):pp. 2928–2930, 1995.

[27] J. Lätt. *Hydrodynamic Limit of Lattice Boltzmann Equations*. PhD thesis, University of Geneve, 2007.

[28] D. d'Humiéres. Generalized lattice boltzmann equations. In *Rarefied gas dynamics: theory and simulations*, volume 159, pages pp. 450–458. Progress in Aeronautics and Astronautics, 1992. ed. B.D. Shizgal & D.P. Weaver.

[29] D. d'Humiéres, I. Ginzburg, M. Krafczyk, P. Lallemand, and L.-S. Luo. Multiple-relaxation-time lattice Boltzmann models in three dimensions. *Philosophical Transactions of the Royal Society of London A*, 360:pp. 437–451, 2001.

[30] I. Ginzburg, F. Verhaeghe, and D. d'Humiéres. Study of simple hydrodynamic solutions with the two-relaxation-times lattice Boltzmann scheme. *Communications in Computational Physics*, 3:pp. 519–581, 2008.

[31] M.R. Swift, W.R. Osborn, and J.M. Yeomans. Lattice Boltzmann Simulation of Non-Ideal Fluids. *Journal of Chemical Physics*, 28:pp. 258–267, 1958.

[32] M. Sbragaglia, R. Benzi, L. Biferale, S. Succi, K. Sugiyama, and F. Toschi. Generalized lattice boltzmann method with multirange pseudopotential. *Physical Review E*, 75:026702, 2007.

[33] H.W. Zheng, C. Shu, and R.Y. Zhang. A lattice boltzmann model for multiphase flows with large density ratio. *Journal of computational physics*, 218:pp. 352–371, 2006.

[34] T. Lee and C.-L. Lin. A stable discretization of the lattice Boltzmann equation for simulation of incompressible two-phase flows at high density ratio. *Journal of computational physics*, 206:pp. 16–47, 2005.

[35] C. Pan, L.-S. Luo, and C.T. Miller. An evaluation of lattice Boltzmann schemes for porous medium flow simulation. *Computer & Fluids*, 35:pp. 898–909, 2006.

[36] U. Aaltosalmi. *Fluid flow in porous media with the Lattice-Boltzmann method.* PhD thesis, University of Jiväskilä, 2005.

[37] H. Huang, Z. Li, L. Shuaishuai, and X. Lu. Shan-and-Chen-type multiphase lattice boltzmann study of viscous coupling effects for two-phase flow in porous media. *International Journal of Numerical Methods in Fluids*, 61:pp. 341–354, 2009.

[38] C. Pan, M. Hilpert, and C. T. Miller. Lattice-Boltzmann simulation of two-phase flow in porous media. *Water Resources Research*, 40:W01501, 2004.

[39] L. Hao and P. Cheng. Pore-scale simulations on relative permeabilities of porous media by lattice Boltzmann method. *International Journal of Heat and Mass Transfer*, 53:pp. 1908–1913, 2010.

[40] H. Liu, A. J. Valocchi, Q. Kang, and C. Werth. Pore-Scale Simulations of Gas Displacing Liquid in a Homogeneous Pore Network Using the Lattice Boltzmann Method. *Transport in Porous Media*, 99:pp. 555–580, 2013.

[41] P. Lallemand and L.-S. Luo. Theory of the Lattice Boltzmann Method: Dispersion, Dissipation, Isotropy, Galilean Invariance, and Stability. *Physical Review E*, 61:pp. 6546–6562, 2000.

[42] D.-Y. Peng and D. B. Robinson. A New Two Constant Equation of State. *Industrial & Engineering Chemistry Fundamentals*, 15(1):pp. 59–64, 1976.

[43] N. F. Carnahan and K. E. Starling. Equation of state for nonattracting rigid spheres. *The Journal of Chemical Physics*, 51(2):pp. 635–636, 1969.

[44] L.D. Landau and E.M. Lifschitz. *Fluid Mechanics*. Pergamon Press, Oxford, 1987.

[45] P.K. Kundu and I.M. Cohen. *Fluid Mechanics*. Elsevier, Oxford, 2008.

[46] O. Reynolds. An Experimental Investigation of the Circumstances Which Determine Whether the Motion of Water Shall Be Direct or Sinuous, and of the Law of Resistance in Parallel Channels. *Philosophical Transactions of the Royal Society of London*, 174:pp. 935–982, 1883.

[47] S. Whitacker. Flow in Porous Media i: a Theoretical Derivation of Darcy's Law. *Transport in Porous Media*, 1:pp. 3–25, 1986.

[48] M. Matyka, A. Khalili, and Z. Koza. Tortuosity-porosity relation in porous media flow. *Physical Review E*, 78:026306, 2008.

[49] A.G. Yiotis, J. Psihogios, M.E. Kainourgiakis, A. Papaioannou, and A.K. Stubos. A lattice Boltzmann study of viscous coupling effects in immiscible two-phase flow in porous media. *Colloids and Surfaces A-physicochemical and Engineering Aspects*, 300:pp. 35–49, 2007.

[50] Z. Dou and Z.-F. Zhou. Numerical study of non-uniqueness of the factors influencing relative permeability in heterogeneous porous media by lattice Boltzmann method. *International Journal of Heat and Fluid Flow*, 42:pp. 23–32, 2013.

[51] E.C. Donaldson, B.P. Lorenz, and R.D. Thomas. The effects of viscosity and wettability on oil and water relative permeabilities. In *Fall SPE Meet*, 1966.

[52] E.J.L Du Prey. Factors affecting liquid-liquid relative permeabilities of a consolidated porous medium. *Society of Petroleum Engineers Journal*, pages pp. 39–47, 1973.

[53] G.F. Pinder and W.G. Gray. *Essentials of Multiphase Flow and Transport in Porous Media*. Johan Wiley & Sons, Inc, Hoboken, 2008.

[54] U. Frisch, D. d'Humiéres, B. Hasslacher, P. Lallemand, and Y. Pomeau. Lattice Gas Hydrodynamics in Two and Three Dimensions. *Complex Systems*, 1:pp. 649–707, 1987.

[55] D.A. Wolf-Gladrow. *Lattice-Gas Cellular Automata and Lattice Boltzmann Models*. Springer-Verlag, Berlin, 2000.

[56] S. Succi. *The Lattice Boltzmann Equation for Fluid Dynamics and Beyond.* Oxford Scientific Publications, Oxford, 2001.

[57] P.E. Bhatnagar, P. Gross, and M.K. Krook. A model for collision processes in gases. I. Small amplitude processes in charged and neutral one-component systems. *Physical Review*, 94(3):pp. 511–525, 1954.

[58] J.-P. Rivet and J.B. Boon. *Lattice Gas Hydrodynamics.* Cambridge University Press, Cambridge, 2001.

[59] L.-S. Luo. Lattice Boltzmann Methods for Computational Fluid Dynamics. Lectures at Institut für Computeranwendungen im Bauingenieurwesen (CAB), Universität Braunschweig, available at http://research.nianet.org/∼luo/talks.html, August 2003.

[60] J.M.V.A. Koelman. A simple lattice Boltzmann scheme for Navier-Stokes fluid flow. *Europhysics Letters*, 15(6):pp. 603–607, 1991.

[61] C. Cercignani. *Ludwig Boltzmann, The Man Who Trusted Atoms.* Oxford University Press, Oxford, 1988.

[62] C. Cercignani. *Mathematical Methods in Kinetic Theory.* Plenum Press, New York, 1990.

[63] B.R. Martin. *Statistics for Physical Sciences, An Introduction.* Elsevier, Oxford, 2012.

[64] F.P. Incropera, D.P. Dewitt, T.L. Bergman, and A.S. Lavine. *Fundamentals of Heat and Mass Transfer.* John Wiley & Sons, Hoboken, 2007.

[65] H. Struchtrup. *Macroscopic Transport Equation for Rarefied Gas Flow.* Springer-Verlag, Berlin, 2005.

[66] E.J. Hinch. *Perturbation Methods.* Cambridge University Press, Cambridge, 1991.

[67] A.H. Nayfeh. *Perturbation Methods.* Wiley-VCH Verlag GmbH & Co. KGaA, Weinheim, 2004.

[68] E.A. Coddington. *An Introduction to Ordinary Differential Equations.* Dover Publications, Inc, New York, 1989.

[69] P.J. Dellar. Compound waves in a thermohydrodynamic lattice BGK using non-perturbative equilibria. *Europhysics Letter*, 57:pp. 690–696, 2002.

[70] A.H. Stroud and D. Secrest. *Gaussian Quadrature Formulas*. Prentice-Hall, London, 1966.

[71] A. Caiazzo. Analysis of lattice boltzmann initialization routines. *Journal of Statistical Physics*, 121:pp. 37–48, 2005.

[72] H.K. Versteeg and W. Malalasekera. *An Introduction to Computational Fluid Dynamics, The Finite Volume Method*. Pearson Education Limited, Harlow, 2007.

[73] O. Filippova and D. Hänel. Grid Refinement for Lattice-BGK. *Journal of Statistical Physics*, 147:pp. 219–228, 1998.

[74] M. Rohde, D. Kandhai, J.J. Derksen1, and H.E.A. van den Akker. A generic, mass conservative local grid refinement technique for lattice-Boltzmann schemes. *International Journal for Numerical Methods in Fluids*, 51:pp. 439–468, 2006.

[75] P. Chen. The Lattice Boltzmann Method for Fluid Dynamics. Master's thesis, École Polytechnique Fédérale de Lausanne, 2011.

[76] R.R. Nourgaliev, T.N. Dinh, T.G. Theofanous, and D. Joseph b. The lattice Boltzmann equation method: theoretical interpretation, numerics and implications. *International Journal of Multiphase Flow*, 29:pp. 117–169, 2002.

[77] A. Chorin. A numerical method for solving the incompressible viscous flow problems. *Journal of Computational Physics*, 135:pp. 118–125, 1997.

[78] X. He and L.S. Luo. Lattice Boltzmann Model for the Incompressible Navier-Stokes Equation. *Journal of Statistical Physics*, 88:pp. 927–944, 1997.

[79] X. He, Q. Zou, L.-S. Luo, and M. Dembo. Analytic Solutions of Simple Flows and Analysis of Nonslip Boundary Conditions for the Lattice Boltzmann BGK Model. *Journal of Statistical Physics*, 87:pp. 115–136, 1997.

[80] R. Rubinstein and L.-S. Luo. Theory of the lattice Boltzmann Equation: Symmetry properties of discrete velocity sets. *Physical Review E*, 77:pp. 1–11, 2008.

[81] P. Asinari. *Multi-Scale Analysis of Heat and Mass Transfer in Mini/Micro Structures*. PhD thesis, Politecnico di Torino, 2005.

[82] F. Verhaeghe, L.-S. Luo, and B. Blanpain. Lattice Boltzmann modeling of microchannel flow in slip flow regime. *Journal of Computational Physics*, 228:pp. 147–157, 2009.

[83] I. Ginzburg, F. Verhaeghe, and D. d'Humiéres. Study of Simple Hydrodynamic Solutions with the Two-Relaxation-Times Lattice Boltzmann Scheme. *Communications in Computational Physics*, 3:pp. 519–581, 2008.

[84] Z. Guo, C. Zheng, and B. Shi. Discrete lattice effects on the forcing term in the lattice Boltzmann method. *Physical Review E*, 65:pp. 1–6, 2002.

[85] H. Huang, M. Krafczyk, and X. Lu. Forcing term in single-phase and Shan-Chen-type multiphase lattice Boltzmann models. *Physical Review E*, 84:046710, 2011.

[86] M. Junk. A finite difference interpretation of the lattice Boltzmann method. *Numerical Methods for Partial Differential Equations*, 193:pp. 383–402, 2001.

[87] D.J. Holdych, D.R. Noble, J.G. Georgiadis, and R.O. Buckius. A finite difference interpretation of the lattice Boltzmann method. *Journal of Computational Physics*, 193:pp. 595–619, 2004.

[88] S. Bennett. *A Lattice Boltzmann Model for Diffusion of Binary Gas Mixtures*. PhD thesis, University of Cambridge, 2010.

[89] I. Ginzburg and D. d'Humiéres. Multireflection boundary conditions for lattice Boltzmann models. *Physical Review E*, 68, 2003.

[90] R. Mei, L.-S. Luo, and W. Shyy. An Accurate Curved Boundary Treatment in the Lattice Boltzmann Method. *Journal Computational Physics*, 155:pp. 307–330, 1999.

[91] M. Bouzidi, M. Firdaouss, and P. Lallemand. Momentum transfer of a Boltzmann-lattice fluid with boundaries. *Physics of Fluids*, 13:pp. 3452–3459, 2001.

[92] I. Ginzbourg and P.M. Adler. Boundary flow condition analysis for the three-dimensional lattice Boltzmann model. *Journal de Physique II*, 4:pp. 191–214, 1994.

[93] A. Beskok, G. Em Karniadakis, and W. Trimmer. Rarefaction and compressibility effects in gas microflows. *Journal of Fluids Engineering*, 118:pp. 448–456, 1996.

[94] P. Neumann and T. Rohrmann. Lattice Boltzmann Simulations in the Slip and Transition Flow Regime with the Peano Framework. *Open Journal of Fluid Dynamics*, 2:pp. 101–110, 2012.

[95] M. Bouzidi, D. d'Humiéres, P. Lallemand, and L.-S. Luo. Lattice Boltzmann Equation on a Two-Dimensional Rectangular Grid. *Journal of Computational Physics*, 172:pp. 704–717, 2001.

[96] K. Yadzchi, S. Srivastava, and S. Luding. Microstructural effects on the permeability of periodic fibrous porous media. *International Journal of Multiphase Flow*, 38(8):pp. 956–966, 2011.

[97] W. Zhang. *Experimental and computational analysis of random cylinder packings with applications.* PhD thesis, Lousiana State University, 2006.

[98] S. Torquato. Nearest-neighbor statistics for packing of hard spheres and disks. *Physical Review E*, 51(4):pp. 3170–3182, 1995.

[99] E. Bernard. *Algorithms and applications of the Monte Carlo method: Two-dimensional melting and perfect sampling.* PhD thesis, École Normale Supérieure, 2011.

[100] A. Duda, Z. Koza, and M. Matyka. Hydraulic tortuosity in arbitrary porous media flow. *Physical Review E*, 84:036319, 2011.

[101] K. Yazdchi, S. Srivastava, and S. Luding. On the validity of the carman-kozeny equation in random fibrous media. In E. Onate and D.R.J. Owen, editors, *Particle-based Methods II : fundamentals and applications.* Eccomas, 2011.

[102] J.W. Cahn and J.E. Hilliard. Free energy of a nonuniform system. i. interfacial energy. *Journal of Chemical Physics*, 28:pp. 258–267, 1958.

[103] X. He, X. Chen, and G.D. Doolean. Discrete boltzmann equation model for non-ideal gases. *Physical Review E*, 57(1):R13–R16, 1998.

[104] X. Shan and G. Doolean. Multicomponent Lattice-Boltzmann Model with Interparticle Interaction. *Journal of Statistical Physics*, 81:pp. 379–393, 1995.

[105] X. Shan and H. Chen. Simulation of nonideal gases and liquid-gas phase transitions by the lattice boltzmann equation. *Physical Review E*, 49(4):pp. 2941–2948, 1994.

[106] H. Huang, D.T. Thorne, M.G. Schaap, and M.C. Sukop. Proposed approximation for contact angles in Shan-and-Chen-type multicomponent multiphase lattice Boltzmann models. *Physical Review E*, 76:066701, 2007.

[107] R. Piazza. *Note di fisica statistica*. Springer-Verlag, Milano, 2011.

[108] J.S. Rowlinson and B. Widom. *Molecular Theory of Capillarity*. Dover Publications, Inc, Mineola, New York, 2002.

[109] M. Sbragaglia, H. Chen, X. Shan, and S. Succi. Continuum Free-Energy formulation for a class of Lattice Boltz- mann multiphase models. *Europhysics Letters*, 86(2):24005, 2009.

[110] X. Shan. Pressure tensor calculation in a class of nonideal gas lattice boltzmann models. *Physical Review E*, 77:066702, 2008.

[111] N.S. Martys. Critical properties and phase separation in lattice Boltzmann fluid mixtures. *Physical Review E*, 63:031205, 2001.

[112] X. Shan. Analysis and reduction of the spurious current in a class of multiphase lattice Boltzmann models. *Physical Review E*, 73:047701, 2006.

[113] L.W. Yelash, T. Kraska, and U. K. Deiters. Closed-loop critical curves in simple hard-sphere van der Waals-fluid models consistent with the packing fraction limit. *Journal of Chemical Physics*, 110(6):pp. 3079–3084, 1999.

[114] R. Benzi, L. Biferale, M. Sbragaglia, S. Succi, and F. Toschi. Mesoscopic modeling of a two-phase flow in the presence of boundaries: the contact angle. *Physical Review E*, 74(2):021509, 2006.

[115] A. Ghassemi and A. Pak. Numerical study of factors influencing relative permeabilities of two immiscible fluids flowing through porous media using lattice Boltzmann method. *Journal of Petroleum Science and Engineering*, 77:pp. 135–145, 2011.

[116] A. Gupta and R. Kumar. Lattice Boltzmann simulation to study multiple bubble dynamics. *International Journal of Heat and Mass Transfer*, 51:pp. 5192–5203, 2008.

[117] A. Ghizzetti and A. Ossicini. *Quadrature Formulae*. Academie-Verlag,, Berlin, 1970.